HEAT TRANSFER AND EVAPORATION IN SPRAY COOLING OF HOT GAS FLOWS, INCLUDING THE EFFECT OF NOZZLE DESIGN

Olaf Schmidt

A thesis submitted to Middlesex University in partial fulfilment of the degree of Doctor of Philosophy.

School of Engineering Systems

Middlesex University

December 2001

Declaration

This thesis has been written by myself and its contents have not been submitted for any other degree or publication. The work described in it is my own except were specific reference has been made to other authors.

Olaf Schmidt

Acknowledgements

The efforts of many people have made it possible for the work described here to be carried out and others have assisted with the thesis production. I would like to thank everyone who helped for their invaluable contributions. In particular, I thank Prof. J. Kubie of Napier University for introducing me into this field, suggesting the topic for research and his role as 1st Director of Studies. His advice at the experimental stage was greatly appreciated.

I would like to express my particular gratitude to Dr. J. Lewis of Middlesex University, who was my 2nd Director of Studies and provided guidance, support and encouragement throughout the research period covering the numerical modelling. I would also like to thank Prof. A. S. White my 3rd director of studies and Prof. G Goldspink who have maintained a keen interest in my work and without those help, advice and encouragement this thesis would never have been finished.

The support of the University technical staff was vital to the research programme, and my special thanks are due to the whole workshop team and Mr. J Mueller who manufactured the nozzle parts as required.

My thanks are further offered to all my colleagues at the Middlesex University for sharing university life. In particular my thanks are due to my fellow researcher and lifetime friend D. Gopaul, who was the best office mate.

And last, but certainly not least, I would like to take this opportunity to thank my mother Mrs. Christa Friedrichs for her help, encouragement and support during these years of studying and research.

Abstract

This study investigates the influence of spray nozzle internal geometry on heat transfer performance and the resultant power requirements. An experimental apparatus was designed and built, which allowed for close control of the heat transfer from air to water and the required energy for droplet production. The apparatus allowed for simultaneous measurements of heat transfer rate from the gas to the spray droplets and the pumping power requirements for the sprayed liquid. A spray chamber was constructed in the form of a Perspex cylinder, 372 mm internal diameter and 372 mm height, mounted on its vertical axis. Thermocouples, humidity sensors, and pressure sensors were used to measure the temperature difference of the air and water, the humidity difference of the air, and the pressure drop across the nozzle. The spray nozzles have been installed at the centre of the upper cover plate directed along the cylinder axis. The heat and mass transfer process was carried out in a counter current flow. Two different nozzle designs were the subject of this investigation.

The pressure swirl nozzle works on liquid pressure alone. Droplet formation and size is influenced by changes of the internal geometry and liquid pressure.

An effervescent two fluid atomiser with internal mixing was tested. The influence of changes in gas bubble and exit orifice geometry on droplet size and formation was investigated.

Analysis of the heat transfer process is based on the energy balance for the whole cylinder. This analysis allows for the determination of the nozzle with the best performance characteristics. From the required energy to produce the droplets and the rate of heat transfer, a new equation for the index of energy performance, was defined.

A Laser Doppler Analyser was used to determine the droplet size and velocity for the low pressure nozzles and this data was compared with the existing theory. The droplet distribution of the spray nozzles was determined for various configuration. The measured droplet size was below the calculated droplet size using the derived equations from the literature. Photographs of the spray angle at different liquid pressures were taken for digital analysis. The spray angle showed reasonable agreement with the literature.

A three dimensional numerical model was designed to simulate the heat transfer process inside the spray chamber using PHOENICS, a Computational Fluid Dynamics (CFD) software. The software modelled the heat and mass transfer inside the spray chamber. This model then allowed for the testing of different droplet distributions, formations, and their influence on the heat transfer process. In order to validate the results, the necessary variables such as the gas mass flow, liquid mass flow rate, droplet size, spray angle and scatter, hot air inlet temperature, were obtained from the experimental data. The result of the simulation is the air outlet temperature and humidity of the spray chamber. The internal 3D flow field is solved with the Lagrangian and Eulerian equation including the disturbance, solved with the k-ε turbulence model, created by the spray droplets.

Four different pressure swirl configurations were simulated. Every configuration had five different pressure points. Every pressure point was simulated individually in order to find out if the numerical simulation software was able to predict the correct result for different liquid mass flow rates without altering the boundary setting and parameters.

The heat transfer process was found to depend on the droplet size and distribution produced by the spray nozzle. A comparison of the experimental data with the simulation results demonstrated the accuracy of the CFD model. The temperature accuracy was ±5.9% and for the humidity ±12% on average for all simulations.

It was found that the heat transfer of the effervescent atomiser depends on the mass ALR and that the highest heat transfer was measured when it was operating with an ALR of 0.1. The tested effervescent atomiser was found to be strongly influenced by the atomising air, an effectiveness of 93% achieved. The change of the internal geometries had no significant influence on the heat transfer rates.

The change of the internal geometry, especially the exit orifice diameter, had a strong influence on the pressure swirl nozzle performance, which started at 85% and reached a maximum of 95%. It was found that the pressure requirement for the 4.7 mm exit orifice was only 20% of the pressure requirement of the 2.5 mm exit orifice in order to achieve the same cooling performance. The pressure swirl needed for all flow rates approximately 20 times less energy to achieve the same cooling as the effervescent nozzle.

Table of Contents

Nomenclature

$\dot{m}$	[kg/s]	mass flow rate
$\dot{V}$	[m^3/s]	volume flow rate
A	[m^2]	area
B_M	[-]	mass transfer number
B_T	[-]	thermal transfer number
C_D	[-]	discharge coefficient
c_p	[J/kg K]	specific heat capacity at constant pressure
D	[m]	diameter
D_{32}	[µm]	Sauter Mean Diameter
D_{AB}	[m^2/s]	Diffusion coefficient [m^2/s]
d_L	[m]	diameter of ligaments
FN	[-]	flow number
H	[m]	Height
h	[W/m^2 K]	Heat transfer coefficient
k	[J/m s K]	thermal conductivity
k_{vm}	[mole/s m^2]	Mean mass transfer of vapour
L	[m]	length
$\dot{m}$	[kg/s]	mass flow rate
M	[kg/kmol]	molar mass
NTS	[-]	Number of tangential slots
Nu	[-]	Nusselt number
p	[Pa]	Differential pressure
P	[W]	Power
Pr	[-]	Prandtl number
Q	[W]	heat transfer rate
Q	[-]	Fraction of the total volume
R	[m]	radius
Re	[-]	Reynolds number
SMD	[µm]	Sauter Mean Diameter
T	[°C]	temperature
t_s	[m]	film thickness
U	[m/s]	velocity

u	[m/s]	axial velocity
$\dot{V}$	[m^3/s]	volume flow rate
v	[m/s]	local flow velocity
v_i	[m/s]	inlet velocity to swirl chamber
v_r	[m/s]	radial velocity
Y	[-]	mass fraction
Δt_{hu}	[s]	duration of heating up period
Δt_{st}	[s]	duration of steady state period
ϑ	[W/K]	heat transfer per temperature driving force
β	[-]	number that determines growth rate of disturbance
η	[%]	effectiveness
φ	[%]	relative humidity
λ	[m^2/s]	evaporation constant
λ_w	[m]	wavelength of disturbance
μ	[kg/m s]	dynamic viscosity
θ	[°]	half spray angle
ρ	[kg/m^3]	density
σ	[N/m]	surface tension
ω	$\left[\frac{kg\,H_2O}{kg\,dry\,air}\right]$	specific humidity
ψ	[1/K]	index of performance

Subscripts

∞	ambient value
a	air
am	mixed air
aw	air for mixing with water
b	boiling temperature
e	exit orifice
g	gas
hu	mean or effective value during heat-up period
L	liquid
p	tangential inlet slots

r	reference value
S	value at drop surface
s	swirl chamber
st	steady-state value
v	vapour
w	water
BP	Bottom plate
TP	Top plate
T	Tube
P	Perspex
S	polystyrene
A	Aluminium
ch	Spray chamber
D	Droplet
fwf	Falling water film
ac	Critical air value
wc	Critical water value
0	initial value

Note: Symbols that are not defined here are defined in the text

Non-dimensional numbers

Weber number $$We = \frac{U^2 D_e \rho_w}{\sigma_w}$$

Reynolds number $$\mathrm{Re} = \frac{\rho_w U D_{32}}{\mu_w}$$

Ohnesorge-number $$Oh = \frac{\mu_w}{\sqrt{D_e \rho_w \sigma_w}}$$

Sherwood number $$Sh = \frac{h x}{D_{AB}}$$

Prandtl number $$\mathrm{Pr} = \frac{c_p \mu}{k}$$

Chapter 1. Introduction

This thesis explores an effective and inexpensive way of cooling down hot gas with water. The atomisation of liquids to form spray droplets is used in a wide variety of application areas including cooling of hot gases, cleaning of exhaust gas, liquid fuel combustion, spray drying, and fire protection using sprinkler sprays (Hino et al., 2000). Extremely large liquid surface areas are created by the atomisation of bulk liquid, thus enhancing the heat and mass transfer processes between the liquid and the adjacent gas. A further benefit of using sprays is that a more even distribution of liquid can be achieved throughout a gas or over a solid surface.

Two examples of where liquid sprays are used for the objective of heat transfer (with phase change) are:

- Condensation of steam: by direct contact with a cold atomised liquid in a spray condenser (Schlick, 1995, Buglayev et. al., 1985).
- Cooling of hot gas; by the use of evaporation enthalpy of the atomised liquid (Kachhwaha et. al., 1998a & 1998b).

Other applications where combined heat and mass transfer processes involve spray droplets are:

- Spray drying: where a solid-liquid mixture is injected into a hot air stream. The liquid evaporates leaving the solid substance in powder form. Many common products such as washing powder, milk powder, soup and coffee granulates are produced by spray drying.
- Dissolving of gas into an atomised liquid by absorption (Schlick, 1995).
- Humidification by atomisation of water into a gas stream.
- Liquid fuel injection systems in internal combustion engines, including diesel engines, gas turbines, and other liquid fuelled systems, such as furnaces where the liquid is atomised with the aim of rapid evaporation and complete combustion (Babu et. al., 1982, Chin and Lefebvre, 1985).

Different techniques require particular types of nozzles. Many special types of nozzles and atomisers are available for this purpose. Atomisers with relatively large exit orifices are preferred for applications where the liquid carries solid particles, because the chances of a blockage are minimised. Pressure swirl nozzles and effervescent atomisers are the preferred devices for this technique.

Surface heat exchangers are often used to cool air in industry. The problem with surface heat exchangers is the large pressure drop required to drive the gas flow. Other problems are the size, flexibility and cost involved with this technique. A new type, the direct contact heat exchanger, can operate on a liquid-liquid (Inaba et. al., 2000) or gas-liquid basis. For this research, water droplets are used for the heat transfer of a gas-liquid. Injecting liquid in the form of spray is an effective method of promoting liquid-gas heat transfer since a large interfacial area per unit volume is achieved with a very small gas phase pressure drop. Suzuki et. al. (1985) and Buglayev et. al.(1985) showed that liquid sprays provide an efficient mechanism for heat transfer between liquids and surrounding gases. An important factor in the design of the direct heat transfer exchanger is the type of nozzle that is used to produce the droplets. The droplet size and the droplet distribution also have an influence on the performance. Lefebvre (1989) and Bayvel (1989) presented the different methods for generating spray droplets and their likely uses. They found that pressure swirl nozzles and two fluid nozzles, such as the effervescent atomiser, usually produce smaller droplets and therefore operate more effectively than other types, such as rotary atomisers. These nozzles are used in many industrial applications in which high heat and mass transfer rates between the injected liquid and surrounding medium are required. Another important factor depends on the internal geometry of the spray chamber. The compactness of heat exchangers is defined as the ratio of the heat exchanger surface area used to the volume of the heat exchange. Conventional heat exchangers compactness ratios start at about 700 m^2/m^3. This value depends on the water flow rate and the droplet size. The compactness for the direct heat exchanger used for this research varies with the water pressure. For the flight time of one droplet, the compactness is between 13 to 29 m^2/m^3. With reference to a time frame the compactness lies between 142 to 2204 m^2/m^3.

Pressure swirl nozzles operate with a water pressure of the order of 1 MPa to produce droplets small enough to produce a complete surface coating. Commercial pressure swirl nozzles described in the catalogues of Spraying System (1994), Delavan (1993), and BETA (1995) operating with a minimum of 0.35 MPa differential water pressure and producing a droplet size distribution of 120 to 400 μm. An increased differential water pressure results in a higher mass flow rate of water and smaller droplets. Smaller droplets have a larger surface area volume ratio that enhances the energy transfer. Higher differential water pressure results in higher operating cost.

The effervescent atomiser is a twin fluid atomiser with internal mixing. Gas is injected in the flowing liquid. This novel type of twin fluid atomiser has not been used for spray cooling to date. The work of, e.g. Yule (1994), on melts and internal combustion engines is not related to this work.

1.1 Aims and Objectives

The work described in this thesis has been undertaken to examine the factors that affect the overall efficiency of the spray cooling of a gas flow. The research does not investigate the heat transfer from the gas to a single droplet (Antar et. al., 2000) or the droplet behaviour under various conditions (Feng and Michaelides, 2000). The main aims of this work are to:

- to determine nozzle power per unit heat transfer from gas.
- optimise the design of nozzles required for cooling gas by minimising the energy consumption.
- model gas flow, temperature and humidity distribution inside a spray chamber.

To accomplish these aims, the following objectives were identified:

- design, test and optimise pressure swirl nozzles.
- design, test and optimise effervescent atomisers, in order to satisfy the first aim.
- investigate the spray cooling processes and energy requirements.

- measure the droplet sizes and compare with available data and predictive techniques.
- model the process with a Computational Fluid Dynamics (CFD) software to satisfy the second aim.

To satisfy the second aim a three-dimensional Computational Fluid Dynamics (CFD) finite element (FE) model was derived that solves the fundamental equation for heat and mass transfer, and momentum energy. The results of the 3D FE model are compared with experimental results to verify the accuracy of the simulation.

The exact internal geometry and boundary conditions of the spray chamber are replicated in the layout of the model. The initial inlet conditions and locations of water droplets and hot air properties are specified. Some assumptions have to be made due to the software restrictions, e.g., the radiation and the heat loss through boundary walls are ignored. Literature review articles on two-dimensional FE models have been reported by Crowe et al. and 1977, Jicha et al. 1994. The asymmetrical layout of the spray chamber made it necessary to design a three-dimensional model. The Eulerian approach solved flow field and the droplet trajectory is solved with the Lagrangian approach. The model solves the steady-state conditions for constant inlet conditions. This is useful to examine the flow field, temperature and humidity distributions, and droplet trajectory inside the spray chamber. Based on the results it is possible to optimise the spray chamber to gain a higher heat and mass transfer. The time to achieve these steady-state conditions has been examined experimentally. The results of the air outlet temperature and humidity are compared with the experimental results.

1.2 Outline of Thesis

The thesis contains seven chapters. In this introductory chapter, a general background has been given and the aims and objectives of the research project identified.

A review of relevant literature is given in chapter 2. Literature describing the different types of nozzles used for the research and how the droplets are produced is included. The formation of droplets and droplet-gas interaction is explained.

Chapter 3 describes in detail the design and manufacture of the experimental test rig. The designs of our pressure swirl nozzle and effervescent atomiser are presented, illustrating the internal geometry and the associated variables. Parts used to vary the internal geometry are described. Assembly drawings of these nozzles are given and layouts show how they are finally used. A test schedule for the nozzles is given. A review of droplet size measurement techniques is included.

Experimental results are presented and discussed in chapter 4. The data is interpreted for use in subsequent calculations. A summary of the nozzles used in these tests is also given.

Chapter 5 contains the results of the CFD model. An introduction of background information related to the theory employed with this technique is included. Particular attention is given to the Eulerian and Lagrangian formulation. The software and the required numerical settings are briefly described and followed by an analysis of the results obtained with the CFD model. Equations for the numerical analysis are presented. The chapter includes a basic review of the theory used in the Computational Fluid Dynamics (CFD) code.

The predictions of the CFD model are then, in chapter 6, compared with the experimental data. An uncertainty calculation is made for the CFD model and the experimental data. Subchapter 6.5 discusses and compares the design of the tested nozzles with derived nozzles equations that are available in the literature. The numerical results and the experimental data, both including their uncertainties, are then compared.

Conclusions are drawn about the design of nozzles for the specific use in a direct contact heat exchanger and of the numerical simulation system. Recommendations and new aims for further research are given in chapter 7.

A unique part of this research is the establishment of a new test rig that produces repeatable measurements of heat and mass transfer rates and simultaneously the

power requirement to produce the droplets that are directly responsible for the heat and mass transfer. A number of design principals are established:

- For improved heat transfer in cooling appliances
- Economic use of nozzles that should be applied to these processes
- Proof that a simplified model can predict results with relative close agreements to the experimental data (±15%)

A range of non-dimensional design parameters that should be used for pressure swirl nozzles operating in cooling devices was established from the experimental results. These design parameters are used to build a nozzle that operates most effectively in the direct contact cooling devices. The experimental results extended published work in the areas of:

- Liquid nozzle pressure
- Previously untested nozzle sizes and expansion ratios
- Investigation of nozzle geometry with low power requirements
- Internal geometry for nozzles that are used in cooling appliances

A simplified 3D CFD model was created with PHOENIX 2.2.2 software. The CFD software was not able to simulate a falling water film and this was compensated for by a wall coefficient of restitution. The outlet conditions of both mediums were predicted with this model. Comparison of the numerical and experimental results showed close agreement for both mediums. This model can be used to simulate cooling performances for various droplet sizes.

Chapter 2 Literature Overview

2.1 Introduction

The literature review for this thesis is focused on the relevant work carried out in past research. The aim of this chapter is to review the basic knowledge of the specific area of research that represent the basis of this work. Only relevant research carried out after 1960 is reviewed. Many sources for these topics in this thesis are readily available, for instance Lefebvre's book, "Atomisation and Sprays" (Lefebvre, 1989), is a very comprehensive work reviewing a wide variety of journal articles, conference proceedings and other related works in connection with spray technology and droplet interaction. Another useful source is "Transport Phenomena" by Bird, Stewart, and Lightfoot. A useful journal is Atomizer and Sprays, which is published by the Institution of Liquid Atomisation and Spray Systems (ILASS). This presents articles, which are all related to spray systems and atomisation techniques also involving numerical simulations. There is also an annual European conference held by the European division of the ILASS. The international Institution holds a conference every 3 years.

Many different atomisation methods exist, such as the rotary atomiser, electrostatic atomiser, whistle atomiser, airblast atomiser, air-assist atomiser, pressure atomiser, and effervescent atomiser. These are listed in Table 2-1. This review considers only the methods that are relevant for this work. Therefore, the literature review concentrates on pressure atomisers, and in particular the pressure swirl nozzle, and the effervescent atomiser, which belongs to the twin fluid category.

Firstly, the atomiser terminology and the definition of droplets are explained. Secondly, different atomiser technologies are presented, namely pressure swirl nozzle and effervescent atomiser, which are the main interest in this research. The droplet behaviour in suspension with air, including the principles of the heat transfer from gas to liquid droplets is discussed.

To understand how droplets are produced, it is necessary to review in section 2.2.1 the process of liquid sheet disintegration. The droplets are used for the purpose of heat transfer. A review of the heat transfer and evaporation of droplets in suspension with air is given in section 2.4. The main emphasis of section 5.2 is to explain the

methodology of the simulation technique. Finally, a brief review of existing droplet size measurement techniques is presented in Chapter 3.4.1.

Table 2-1: Types of Atomisers

Atomiser		
Pressure Atomiser	Twin Fluid	Other Types
• Plain Orifice	• Air Assist - internal mixing	• Electrostatic
• Pressure Swirl	• Air Assist - external mixing	• Ultrasonic
• Square Spray	• Air Blast – pre-film	• Sonic (whistle)
• Duplex	• Air Blast – plain jet	• Vibrating Capillary
• Dual Orifice	• Effervescent	• Flashing Liquid
• Spill Return		

2.1.1 Definition of Spray Droplets and Atomiser Terminology

The term 'atomisation process' expresses the conversion of a bulk liquid into droplets. Liquid pressure nozzles produce a liquid sheet or a jet. The disintegration of this liquid sheet or jet results in droplets and is described later in chapter 2.2.1. Droplets of various sizes originate in this disintegration process. The size of droplets is important for various techniques, where a certain droplet size is required, e.g., coating, cooling, spray drying. Several empirical and mathematical distribution functions are developed to describe the droplet size distribution in a spray. The most commonly used expression for droplet size distribution is the Rosin-Rammler distribution, which can be expressed in the form

$$1 - Q = \exp - \left(\frac{D}{X} \right)^q \qquad [1]$$

where X and q are constants, which depend on the measured droplet size and spray distribution. X is a representative droplet size of the maximum measured droplet diameter, e.g. 63.2%. Therefore, 63.2% of all droplets are smaller. Q represents the

fraction of the total volume contained in the droplets with a smaller diameter than D (Lefebvre, 1989).

Representative droplet diameters can be defined. These representative droplet diameters define the percentage of droplets that are smaller within the droplet diameter distribution produced by the nozzle. The index *ab* at the *D*, equation [2] varies from 0 to 1, where 1 represents 100%. For example, $D_{0.9}$ denotes that 90% of total liquid volume is in droplets with a smaller diameter.

Different mean diameters exist for various techniques and are defined in general as

$$D_{ab} = \left[\frac{\Sigma N_i D_i^a}{\Sigma N_i D_i^b} \right]^{1/(a-b)} \quad [2]$$

The equation to calculate the mean diameter, *D*, has two subscripts where a=3 and b=2 are used to calculate the Sauter mean diameter. These two subscripts appear also in the equation.

The mean droplet size for heat and mass transfer application is mostly expressed as a Sauter Mean Diameter (SMD or D_{32}) and is used later for work described in this thesis. The SMD represents the size of the droplet that is 32% of the maximum droplet diameter of the spray. This is the diameter of a droplet whose ratio of volume to surface area is the same as that of the entire spray. Other mean diameters for different applications are available to represent the mean diameter and the droplet size distribution. There is for example Jones (1982) who specified an equation for the mass median diameter, $D_{0.5}$, also known as MMD, where the 0.5 means that 50% of the total liquid volume is in drops of smaller diameter. Bouse (1994) tested different nozzle types and showed that the pressure swirl nozzle produced the smallest droplets with the same amount of pressure energy. The droplet size is dependent on the physical properties of the fluid used. Walzel (1990) calculated by physically based dimensionless equations that the mean droplet size increases with increase of the viscosity of the fluid. The result of an increased liquid viscosity is that a thicker liquid sheet leaves the exit orifice. The other factor is the higher surface tension that prevents the easy disintegration of the ligaments. The friction factor was neglected in this correlation, which leads to an inaccurate solution for the SMD.

To describe pressure atomisers, industry uses the Flow Number (FN), which indicate the effective flow area of nozzle. The Flow Number describes the nozzle flow rate

divided by the square root of pressure differential times the liquid density and is expressed as

$$FN = \frac{\dot{m}_L}{(p_L)^{0.5}(\rho_L)^{0.5}} \quad [3]$$

The American standard use different units to SI Units and the flow number therefore needs to be redefined, if American units are to be used (Lefebvre, 1989).

2.2 Review of the past work on spray cooling systems.

High heat flux cooling techniques have assumed an important role in modern industrial and technological applications. Failure of electronic devices can be prevented with an efficient heat removal technique. In metallurgical processes, for example, it is necessary to remove high heat fluxes in a controlled manner in order to obtain products with optimum metallurgical properties. In addition, in optical applications such as laser diodes, a large amount of heat must be dissipated to provide for appropriate operation. As a result of the growing demand for effective and controlled high heat flux removal, and the limitations of conventional cooling techniques such as single phase forced convection, alternative cooling techniques that involve phase change are receiving greater attention. Phase change heat transfer is characterised by very high heat fluxes for a small temperature differential between the hot fluid and the cooling fluid. One of these high heat flux cooling techniques that takes advantage of phase change is spray cooling. Spray cooling is able to remove large amounts of heat at low superheat levels. As a result, spray cooling has been considered as one of the most effective alternatives to remove heat flux.

Spray cooling can broadly divided into two categories depending on the mode of Spray generation:

- Pressure atomisation, where the high-pressure liquid is atomised by the pressure differential across a nozzle.
- Secondary gas assisted atomisation, where a stream of high velocity secondary gas is used to atomise the liquid into fine spay

The difference between the spray cooling physics for the two methods is caused by the presence of the secondary gas flow superimposed on the spray of the first method.

The applications range from removal of heat from solidifying metals (Fritsching et al, 1995; Fritsching and Bauckhage, 1994; Rogers and Katgerman, 1989), spray drier (Hino et al, 2000), heating up of fuel spray (Godsave, 1953; Vervisch, 1999; Choi and Baek, 1999; Su and Zhou, 2000), sprinkler systems (Nam, 1993; Back, 1995, McLean et al, 2000), space heating (Kang et al, 1995), charge droplets to transfer currency (Shrimpton and Yule, 1999), and liquid-liquid direct contact heat exchanger for waste heat recovery (Inaba et al, 2000). The similarity of all these appliances is the energy exchange via the particle surface.

Spray deposition is a novel technology that allows producing solid billets, tubes, coatings and difficult shapes directly from the melt. Advantages of this technology are the control of the structural density as well as providing the porosity used for filters and self-lubricating bearings. The atomisation of molten metals for metal powder production or spray forming applications is often achieved by means of two-fluid atomisation nozzles, where the disintegration of the melt is due to impinging high kinetic energy inert gas jets.

Spray drying has been widely used so far in pharmaceutical, chemical, food and cosmetic industries. Hino et al (2000) present their work in which a new four-phase nozzle has been developed. At average condition is the nozzle is capable of blowing 776 g min^{-1} of airflow and 500 ml min^{-1} in liquid flow. Air inlet temperature is between 180° and 200°C while the outlet temperature is between 70° to 80°C at an air flow rate of 19 to 24 kg min^{-1}. With an air-liquid ratio of 1.55 was it possible to produce with a mean diameter of 13.3 μm. With this new type of nozzle is it possible to produce very fine powder. The powder produced with this nozzle has a size of less than 2 μm. The dryer has got a height of 2072 mm and a maximum diameter of 1640 mm. Because of the small droplet size produced by this nozzle it is possible to design such a compact size spray dryer. The surface area of the droplets is now large enough to evaporate all the liquid before the powder leaves the apparatus.

Every spark ignition engine with fuel injection heats up fuel during the compression time and fuel droplets evaporate. The flammable air-fuel mixture is ignited by means of a spark plug. Droplets that are not fully evaporated are evaporating during the combustion. This ensures a smooth combustion and eliminates a spontaneous explosion in the combustion chamber. The complete vaporisation, and thus the combustion timing, is dependent on the drop size.

Godsave (1953) recognized the problem and started to investigate the field of the drop heating up and evaporation. The outcome of the research was a mathematical solution that considers the boundary condition of the droplets. The mathematical model considered this fact and had therefore both a heating up and evaporation phase. Choi and Baek (1999), Vervisch (1999), Su and Zhou (2000) used this theory for their numerical modelling. Choi and Baek (1999) developed a numerical model to simulate the auto ignition of the air-fuel mixture inside a cylindrical combustor. With this numerical model is it possible to predict the heating up and ignition behaviours of fuel droplets in a changing environment. Different parameters, such as injection type, initial gas temperature and droplet size can be varied and optimised for the process used.

Rogers and Katgerman (1989) developed a mathematical code and established an axisymmetric steady state PHOENICS model that was able to simulate the motion of the droplets and the interaction of the two phases including the friction loss, turbulence and gas compressibility effects. They used the particle-in-cell technique where the gas is considered to be the continuous phase. The motion of the droplet in the gas is calculated by the Langrangian integration of the equation of motion while the gas motion is calculated by using a standard Eulerian technique. The model was used to simulate the effect of gas pressure and particle size distribution. The simulation revealed that the maximum velocity is not in the centre of the particle stream and that the distribution is higher at increased pressure. Fritsching and Bauckhage (1994) developed the same model and confirmed the result of Rogers and Katgerman. Fritsching et al (1995) used the result of the simulation as a basis to design a test rig to validate the numerical model. The aim of the work was to optimise the nozzle geometry. The nozzles of the earlier applications have been blocked due to the back splashing of particles, where the simulation did not detected any back splashing. Fritsching et al (1995) investigated several geometric shapes of

nozzles. During the spray forming process, a stream of atomised metal droplets is collected on a substrate to form a pre-shaped deposit. By means of a numerical analysis of the heat transfer process in the transient growing deposit, the solidification history and therefore at least the material properties of the resulting product were derived. The numerical description is based on a non-orthogonal transient grid transformation and the solution of the heat transfer mechanism and suitable boundary conditions within this frame. Various numbers of nozzle designs have been tested and the experimental and numerical result were compared. The comparison of the results revealed that due to the k-ε turbulence model the spreading rate of the round free jet is overestimated by approximately 20%. The coefficient $C\mu$ in equation [4] of the k-ε turbulence model was modified with regard to the flow configuration, rather then being taken as a constant and then substituted into the transport equations of the standard $k-\varepsilon$ model

$$\mu_t = \rho\, C\mu \frac{k^2}{\varepsilon} \qquad [4]$$

$$\frac{\partial(\rho k)}{\partial t} + div(\rho k \mathrm{U}) = div\left[\frac{\mu_t}{\sigma_k} grad\, k\right] + 2\mu_t E_{ij}.E_{ij} - \rho\varepsilon \qquad [5]$$

$$\frac{\partial(\rho \varepsilon)}{\partial t} + div(\rho \varepsilon \mathrm{U}) = div\left[\frac{\mu_t}{\sigma_k} grad\, \varepsilon\right] + C_{1\varepsilon}\frac{\varepsilon}{k} 2\mu_t E_{ij}.E_{ij} - C_{2\varepsilon}\frac{\varepsilon^2}{k}\rho\varepsilon \qquad [6]$$

The standing vortex is underestimated in the simulation. As a result of this is the pressure maximum at a different location in the jet stream. The combination of this failure results in a higher radial velocity component and causes larger pressure differences within the particle stream.

Vervisch (1999), and Su and Zhou (2000) developed a model to predict combustion in a gas turbine combustion chamber. Both wrote their own numerical code. Both were based on the Navier-Stokes equation and included the model of Godsave. The numerical solutions are in reasonable agreement with those from semi-empirical correlation and experimental data. All three numerical models did not solve the internal droplet flow. The droplets treated as local sources of fuel and their properties are calculated in a Langrangian context, whereas the compressible Navier Stockes equations are solved in the Eulerian context.

The possibility of numerical prediction of droplet trajectories was used by Nam (1993) to simulate the actual delivering density of sprinkler spays. Nam used two sets of equations, gas phase and the liquid phase, that were solved in conjunction with the "Particle-In-Cell". The task was to simulate the penetration of a steady water spray along the centre region of a steady thermal plume. For sprinkler sprays it is necessary to produce droplets large enough to withstand the buoyancy forces created by the burning material. If the droplets are too small their motion is reversed and the droplet does not reach the burning surface. Nam used a mass flow rate of 1.14 kg s^{-1} and assigned 10 different droplet sizes along 250 trajectories to simulate the spray. The ten different droplet sizes ranged from 290 μm to 1100 μm which were based on the cumulative volume fraction. Each droplet represented 10% of the water spray flow rate. The tests where conducted on a 3.05 and 4.57 meter high ceiling cases. The results of the simulations were compared with experimental results. The results of the simulation are less than 45% in error. The numerical simulation actual predicted higher delivery density in the outer region as measured in the experiments. It was assumed that this is due to the lack of coherent experimental data to determine the sprinkler spray conditions.

McLean et al. (2000) used the sprinkler system for the purpose of an irrigation system instead of a fire protection system. They conducted research on the evaporation of droplets and used an electrical conductivity method. Evaporation of water droplets is a problem in countries where hot weather conditions required wetting of the crops and the availability of water is limited. The task was to find a method to minimise the evaporation of the droplets. Various techniques were tested and a maximum of 12% evaporation was measured. Accuracy of the electrical conductivity method was calculated to be ±0.5%. They found out that all techniques have a disadvantage and that primarily the droplet size is responsible for the evaporation. Larger droplets produced at lower pressure had the smallest amount of evaporation and should therefore be used. An increase of 25% in pressure results in smaller droplets and increases the evaporation by 25% as found by Frost and Schwalen (1955).

Direct heat transfer from a dispersed phase to a continuous phase also works with immiscible fluids. This technology is used preferably for alternative energy recovery. Kang et al (1995) and Inaba et al (2000) used liquid-to-liquid direct contact heat

exchanger to heat up water storage tanks that were used for space heating at night. Kang et al used solar energy to heat up the dispersed phase. Hydrocarbon was used as a continues phase and three different mediums, phthalates, oil, and water, for the dispersed phase were tested. The advantage of this system was the ability to work with lower temperature differences than common used systems (tube-and-shell type heat exchanger) and that the heat transfer was not reduced by corrosion and scaling. The experiments have shown that heat transfer rates are strongly influenced by the flow rate. At higher flow rates of the dispersed phase the faster the heat exchanger reached its thermal equilibrium. The maximum storage temperature was approximately 55°C.

Inaba et al (2000) used Perfluorocarbon (PFC) as a dispersed phase, with a density of 1830 kg m^{-3}, which was released in a hot water stream. They also found that an increase of water differential pressure across the nozzle produces smaller droplets. This increased the heat transfer surface per volume and lead finally to higher heat transfer. The incoming temperature of the hot water stream, heated by the waste, was between 30° to 40°C. the incoming temperature of the dispersed phase was between 5° to 15°C. Their analysis of the experimental data showed that the Nusselt number depends on the droplet diameter and the Reynolds number. This research paper is more focused on the derivation of correlations rather than the optimisation of this method and proves the usefulness of this technique.

2.3 *Pressure swirl nozzle*

Outstanding performance and reliability make the pressure swirl nozzle the most commonly used nozzle. At the pressure swirl nozzle the liquid is injected through tangential slots into a swirl chamber. It emerges with both tangential and axial velocity components to form a thin conical sheet at the nozzle exit (Figure 2-1). The pressure energy is converted into kinetic energy to achieve a high relative velocity between the liquid and the surrounding gas. This sheet extends rapidly, finally disintegrating into ligaments and then droplets.

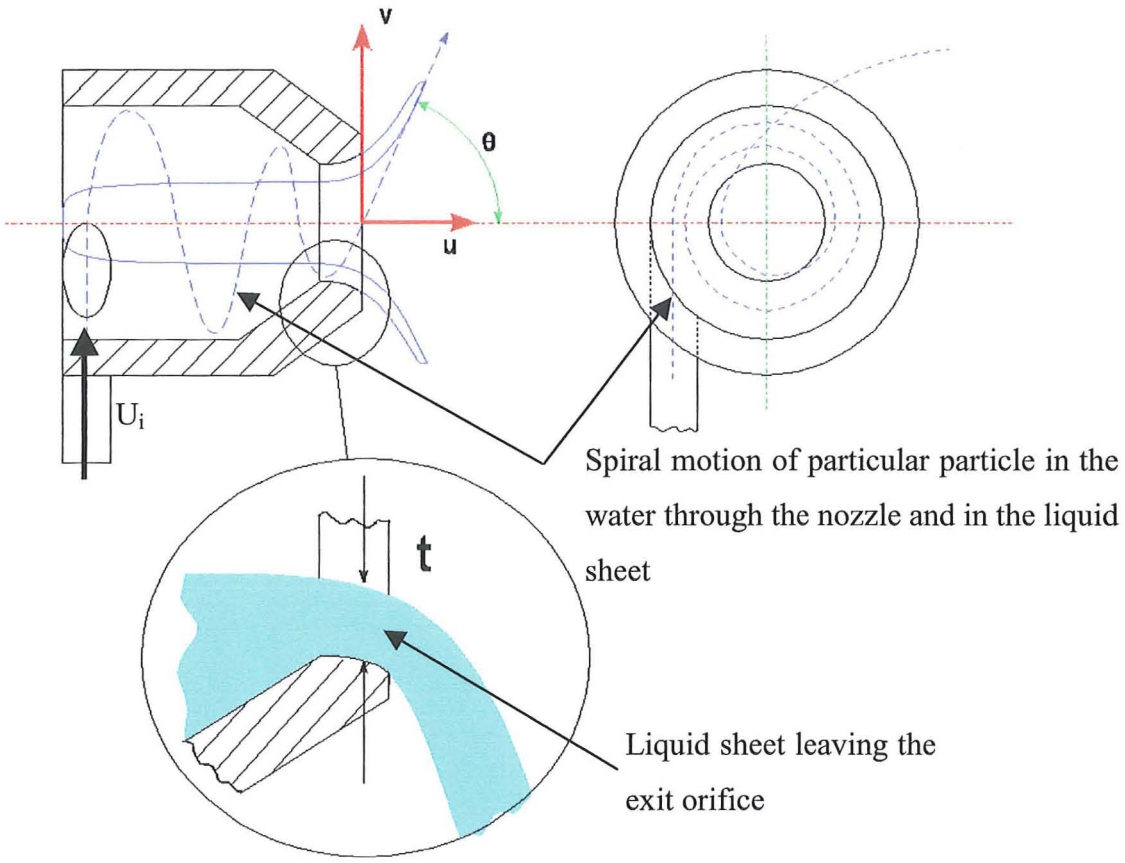

Figure 2-1: General layout of the flow mechanism in a pressure swirl nozzle

The mechanism of disintegration of the liquid depends on the outlet velocity at the nozzle, which can be broken down to the radial, *v*, and axial velocity, u. These velocities, *u* and *v* can be calculated with the following equations.

$$u_e = \frac{\dot{m}_L}{\rho_L (A_e - A_a)} \quad [7]$$

$$v_e = \frac{\dot{m}_L R_s}{\rho_L A_p R_a} \quad [8]$$

The velocity of the liquid sheet leaving the exit orifice is calculated from these two components and also can be used to determine the spray angle.

The internal flow characteristics of pressure swirl nozzles govern the thickness and uniformity of the annular liquid film formed at the final discharge orifice. The characteristics affect the relative magnitude of the axial and tangential components of velocity of this film. An understanding of the interrelationships between internal

flow characteristics, nozzle design variables, and important spray features such as the spray angle and Sauter mean diameter is of great practical interest.

2.3.1 Research in nozzle design and disintegration of the liquid sheet

The pressure swirl nozzle does not produce droplets, it produces a liquid sheet that disintegrates into ligaments, and the ligaments disintegrate into droplets. The break-up process, studied by Dombrowski and Johns (1963), is dependent on ambient conditions and on the thickness of the liquid sheet emerging from the exit orifice.

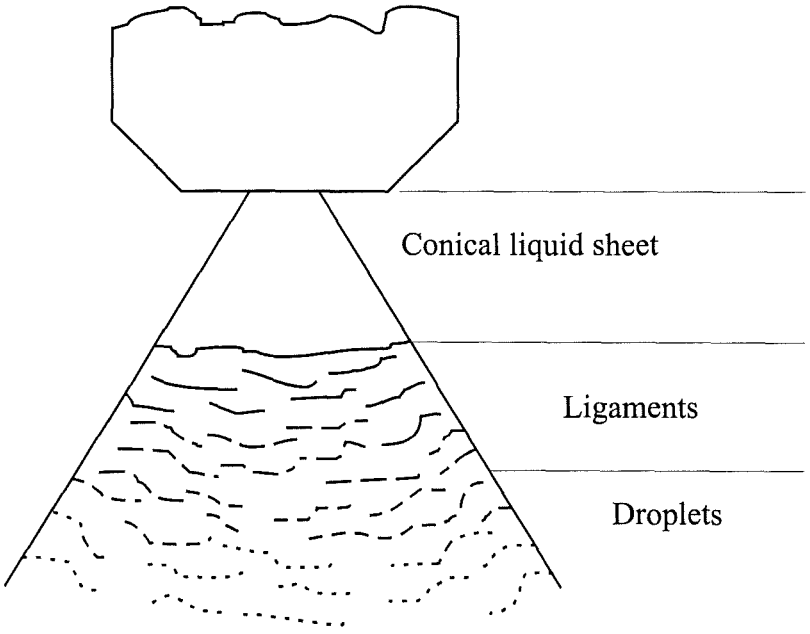

Figure 2-2: Break up process of liquid sheets

They observed that first a conical liquid sheet will be formed. The thickness of this sheet is reduced with the increase of the diameter of the hollow cone pattern. Due to the aerodynamic forces, which are dependent on the relative velocity U_R (between the sheet and the surrounding gas), waves appear on the liquid sheet (Figure 2-2). These waves then break up the sheets into ligaments. These ligaments, which are thin tubes of water, then break up into droplets due to the surface tension.

Dombrowski and Johns found that at low velocities the disintegration of the water film takes place under the influence of aerodynamic forces forming sinusoidal waves. If the outlet velocity exceeds a certain value, the disintegration is due to turbulent forces in the liquid. The droplet size is influenced by the thickness of the liquid sheet. A late break-up of the expanding liquid sheet results in smaller droplets.

This behaviour agrees with Squire (1953), who used a suitable expression of the anti-symmetric oscillations that satisfy Laplace's equation. An equation to calculate the wavelength, λ, of the sheet disintegration, for Weber numbers We >> 1, was developed.

$$\lambda_w = \frac{2\pi t_s \rho_L}{\rho_a (We-1)} \qquad [9]$$

The Weber number is defined as

$$We = \frac{\rho_L U^2 t_s}{2\sigma} \qquad [10]$$

The growth rate of the amplitude of the liquid sheet follows the function of e^{Φ_A}, where Φ_A is defined as

$$\Phi_A = \frac{\rho_A \lambda_w (1-We)^2}{\rho_L \lambda_w t_s (1-We) We^{0.5}} \qquad [11]$$

The thickness of the liquid film influences its break-up process. Giffen and Muraszew (1953) have proven that the film leaving the exit orifice is not passing through the full cross section of the exit orifice. Their analysis refers to a simplex atomiser where internal guiding plates create the swirling motion of the liquid. Their analysis applies also to other types of pressure swirl nozzles. The liquid flow pattern is produced by the imposition of a spiral motion on a free vortex (see Figure 2-1). Conservation of the angular momentum provides the following relationship between tangential velocity v and radius r:

$$vr = U_i R_s \qquad [12]$$

where U_i is the inlet velocity to the swirl chamber and R_s is its radius. The inlet velocity is calculated with the following equation

$$U_i = \frac{\dot{m}_L}{\rho_L A_P} \qquad [13]$$

where A_p the total cross sectional area of the tangential inlet slots. Equation [9] implies the existence of a gas core at the centre of the swirl chamber, which is always observed in practice, since with $r = 0$ the velocity v would otherwise be infinite.

The characteristics of a pressure swirl nozzle can be determined if the dimensions of the diameter of the inlet ports, D_p, density of liquid, ρ_L, diameter of the swirl

chamber, D_s, and exit orifice, D_e, and the spray angle of the liquid sheet at the orifice, θ, are known (Figure 2-3). If the pressure drop across the nozzle, Δp_L, is known, it is then possible to calculate the flow number, *FN*, and atomiser constant, *K*.

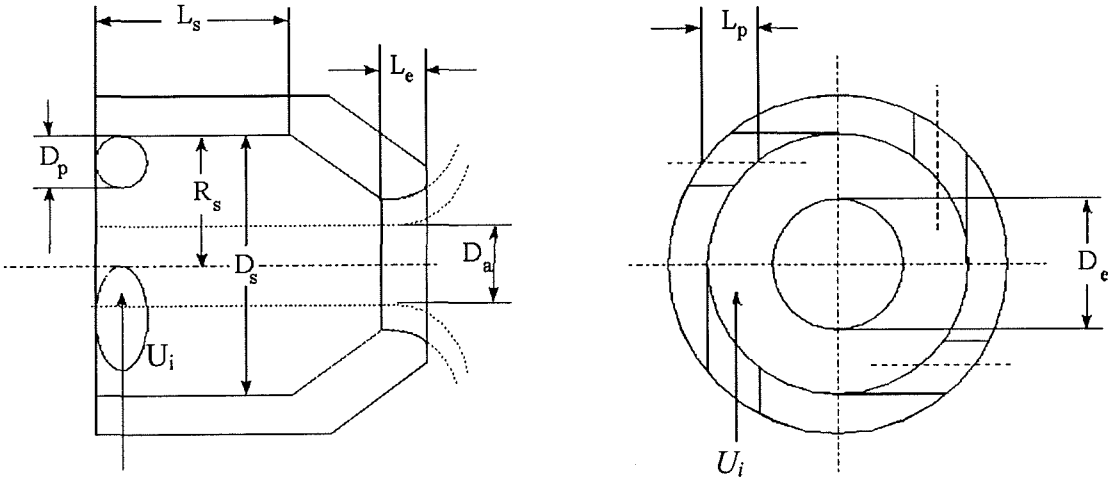

Figure 2-3: Notation for the internal dimensions of a pressure swirl nozzle

A major consideration in the design of a pressure swirl nozzle is the loss of energy. For the nozzle design it is desirable to reduce the surface area which is in contact with the flowing liquid to minimise the frictional losses. Frictional loss results in a decreased velocity of swirling liquid. This reduced velocity results in a smaller air core and a thicker liquid sheet leaving the exit orifice. A thicker liquid sheet results in bigger droplets. Frictional losses are the main causes of decreasing efficiency of pressure swirl nozzles. The smoother the wetted surface inside the pressure swirl nozzles, the smaller is the friction loss. The kinetic energy of the liquid is not decreased and results in a higher liquid velocity leaving through the exit orifice. In large atomisers L_e/D_e can be as small as 0.2, but with small atomisers the difficulty of manufacturing small-scale components to the required degree of accuracy usually dictates minimum values for L_e/D_e of around 0.5.

Tipler and Wilson (1959) recommended that the length/diameter ratio of the swirl ports should not be less then 1.3. Short slots discharge the liquid in a diffused manner and may result in an uneven spray.

The influence of swirl chamber dimension on discharge coefficient was examined by Carlisle (1955). Figure 2-4 shows the effect of the ratio D_s/D_e on the discharge

coefficient. Carlisle (1955) and Tipler and Wilson (1959) recommend a ratio of 3.3 for D_s/D_e. A ratio of 3.3 is the best match between the experimental and theoretical values, as shown in Figure 2-4, which has at this point only a minimum deviation.

The ratio length/diameter of the swirl chamber should be as small as possible to reduce the frictional loss. However, it must allow the liquid jets to coalesce into a uniform vortex sheet. The normal ratio of L_s/D_s is between 0.5 and 1.0. Higher values of L_s/D_s, up to 2.75, would result in an improved atomisation but very high frictional losses.

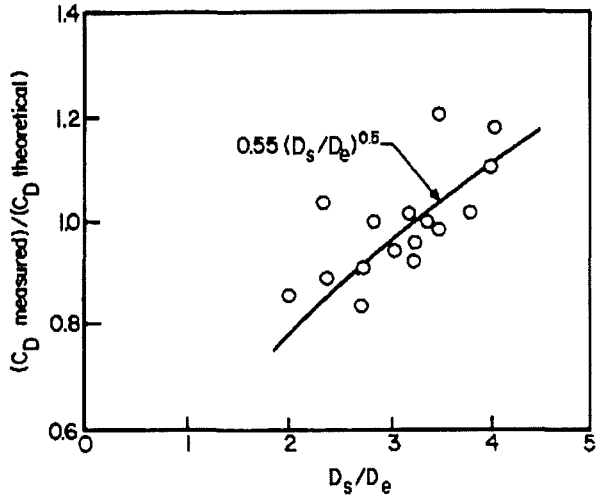

Figure 2-4: Ratio agreement of the measured to theoretical discharge coefficient over the diameter ratio from swirl chamber to exit orifice (Tipler and Wilson, 1959)

Atomisers can be broadly characterised by their flow number, which Lefebvre (1989) expressed as the ratio of the nozzle mass flow rate to the square root of the liquid injection pressure. The influence of nozzle dimensions on flow number was studied experimentally by Kutty et al. (1978), who found that the air core diameter increases with an increase in orifice diameter and a decrease in the diameter of the inlet ports into the swirl chamber. He also found that there is a connection between the mass flow rate and liquid density and the pressure differential across the nozzle and the internal nozzle dimensions which was presented in the form of equations by Rizk and Lefebvre (1985). The influence of swirl atomiser geometry on the droplet size was studied by Elkotb et al. (1978) who developed an empirical mean drop size equation based on the Tanasawa-Tesima distribution, which depends on the aspect ratio of the

atomiser while keeping the shape similar. The developed equation [14] depend on the dimension of the swirl chamber, the exit orifice, the inlet ports and discharge coefficient. In this work by Elkotb, the discharge coefficients, and the liquid properties, which have influence on the calculation of the droplet size, are not defined. The nozzle geometry was varied in the range of L_s/D_s = 0.083 to 2.75, L_e/D_e from 0.77 to 2.82, and the inlet ports ranged from 2 to 5. The pressure drop across the nozzle was between 1 to 3 MPa. The L_s/D_s ratio, the L_e/D_e ratio of nozzle geometry and the number of inlet ports were varied and included in the analyses. The droplet size was measured using the slide sample technique. The empirical equation developed was

$$\frac{D_{32}}{D_e} = 8.343 \frac{C_D^3 \left(\frac{L_s}{D_e}\right)^{0.546} \left(\frac{L_e}{D_e}\right)^{0.0673}}{\left(\frac{D_s}{D_e}\right)^{0.678} \left(\frac{D_p}{D_e}\right)^{1.785}} \qquad [14]$$

The wide range of measurements taken resulted in the conclusion that the Sauter mean drop size

a) decreases with the increase of the liquid pressure,

b) decreases with the decrease of L_e/D_e ratio.

The experiments have also shown that the number of the tangential inlet ports has only a slight effect on the atomisation quality.

Jones (1982) optimised a large pressure swirl jet atomiser for a power plant to improve the droplet size and spray quality for better combustion to reduce the unburned carbon. He developed an empirical correlation, which included the mean droplet size, operational parameters, design and liquid parameters. The experimental data was obtained by using a Polaroid black-and-white camera and a high-speed photographic technique. Jones investigated and compared the values of the non-dimensional groups that are typical for pressure swirl atomisers. The range of the values of these groups is shown in Table 2-2.

Jones obtained two empirical correlations, for the discharge coefficient [15] and for the mass median diameter [16], and used this to optimise the pressure swirl jet atomiser. The discharge coefficient was found to be

$$C_D = 0.45\left(\frac{D_e\rho_L U_u}{\eta_L}\right)^{-0.02}\left(\frac{L_e}{D_e}\right)^{-0.03}\left(\frac{L_s}{D_s}\right)^{0.05}\left(\frac{A_i}{D_eD_s}\right)^{0.52}\left(\frac{D_s}{D_e}\right)^{0.23} \quad [15]$$

where

$$D_{0.5} = 2.47 m_L^{0.315} P_L^{-0.47} \eta_L^{0.16} \eta_A^{-0.04} \sigma_L^{0.25} \rho_L^{-0.22} \times\left(\frac{L_e}{D_e}\right)^{0.03}\left(\frac{L_s}{D_s}\right)^{0.07}\left(\frac{A_i}{D_eD_s}\right)^{-0.13}\left(\frac{D_s}{D_e}\right)^{0.21} \quad [16]$$

Table 2-2: Range of non-dimensional groups covered by Jones (1982)

Dimensionless group	Range covered	Typical value	
$\frac{L_e}{D_e}$	0.1 - 0.9	0.15	
$\frac{L_s}{D_s}$	0.31 - 1.26	0.7	
$\frac{L_p}{D_p}$	0.79 - 3.02	1.2	
$\frac{A_p}{D_eD_s}$	0.19 - 1.21	0.52	
$\frac{D_s}{D_e}$	1.41 - 8.13	2.7	
$\frac{D_e\rho_L U^2}{\sigma}$	$11.5\times10^3 - 3.55\times10^5$	Low pressure 2.4 MPa (350 psi) 1.08 x 105	High pressure 6.3 MPa (900 psi) 3.88 x 105
$\frac{D_e\rho_L U}{\mu_L}$	$1.913\times10^3 - 21.14\times10^5$	6.45 x 105	23.64 x 105
$\frac{\mu_L}{\mu_A}$	279 - 2235	750	
$\frac{\rho_L}{\rho_A}$	694 - 964	700	

The result showed that the optimised pressure swirl nozzle produces a spray with a 12% smaller mass median diameter of comparable commercially available atomisers and this results in about a 26% drop in furnace solids in the exhaust gas.

The flow number is used to express the nozzle throughput to the square root of the liquid injection pressure and liquid density. Rizk and Lefebvre (1985) developed an equation from research conducted by Kutty et al. (1978). Their analysis of data yielded the following expression for the flow number, *FN*, now based on the internal geometric nozzle dimensions:

$$FN = 0.395\left(\frac{A_p^{0.5} D_e^{1.25}}{D_s^{0.25}}\right) \quad [17]$$

where A_p is the total area of the tangential inlet ports. It is then possible to calculate the film thickness, t_s, formed by the liquid emerging from the nozzle as a thin conical sheet with the equation

$$t_s = 2.7\left[\frac{D_e FN \mu_L}{(\Delta p_L \rho_L)^{0.5}}\right]^{0.25} \quad [18]$$

where the liquid properties density and viscosity, and the pressure drop across the nozzle are included. Rizk and Lefebvre (1985) found that the discharge coefficient can be expressed with the following equation

$$C_D = 0.35\left(\frac{A_p}{D_s D_e}\right)^{0.25}\left(\frac{D_s}{D_e}\right)^{0.25} \quad [19]$$

which is similar to that of Dombrowski and Hasson (1969). How the constant of 0.35 from the regression of experimental data was found is not explained. The half spray angle, θ, can be calculated with

$$\theta = 3K^{-0.15}\left(\frac{\Delta p_L D_e^2 \rho_L}{\mu_L^2}\right)^{0.11} \quad [20]$$

where K is the atomiser constant and defined as

$$K = \frac{A_p}{D_e D_s} \quad [21]$$

Mao and Chuech (1991) investigated the liquid break-up process and used for their analysis a "FILM" code. This "FILM" code combines a film dynamics model with wave instability theory. The study, focused on the liquid break-up process, led to the prediction of the film trajectory, film thickness, film velocity, spray angle, break-up length and droplet size as a function of flow conditions, fluid properties and nozzle geometry. Two different methods established by Giffen and Muraszew (1953) and

Rizk and Lefebvre (1985), were used to estimate the initial film thickness emerging from the exit orifice of the pressure swirl nozzle. The comparison of the results shows good agreement. Experiments carried out with three pressure swirl nozzles verified the results of the two methods and showed that the initial film properties estimated after the "FILM" code prediction were in agreement. The thickness of the film varies as a function of downstream distance. The study shows that a thinner film thickness and larger film angle results in a shorter break-up length. A good agreement was obtained for the prediction of the droplet size distribution function, which is in good agreement with the research conducted by Arai and Hashimoto (1985), Wang and Lefebvre (1987) and Richter and Walzel (1989). It should be mentioned that the Sauter Mean Diameter (D_{32}) measured with the Phase Doppler Partical Analyser (PDPA) during the experiments was constantly lower than those of the model prediction.

2.3.2 Formation of droplets

The droplets are formed by the disintegration of the ligaments. Various definitions of the mean drop size are available. The Sauter mean diameter (SMD), which is based on the volume/surface ratio of the spray, is the most used definition. The Sauter mean diameter of droplets definition has a special significance for heat transfer applications, such as spray drying and the combustion of liquid fuel spray. Knowing that there is a relationship between the internal nozzle dimension and the droplet size, different researchers have presented empirical functions that predict the droplet size of their tested nozzles. The developed equations of this research are summarised in Table 2-3.

Radcliffe (1960) presented an equation to predict the droplet size of experiments carried out on different nozzles. This equation did not include effects of the nozzle dimensions and air properties. This equation was further developed by Jasuja (1979) generalising the equation for a higher bandwidth of nozzle variations. Babu et al. (1982) included the Flow Number in the equation and the differential pressure across the nozzle. Jones (1982) obtained an equation for the mean drop size, which is suitable for large capacity nozzles. Further development was done by Lefebvre (1983) who developed the following equation to calculate the Sauter Mean Diameter

$$SMD = 2.25\sigma^{0.25}\mu_L^{0.25}\dot{m}_L^{0.25}\Delta P_L^{-0.5}\rho_A^{-0.25} \quad [22]$$

This equation does not consider the spray cone angle nor the film thickness of the liquid sheet. Kennedy (1985) presented an equation to calculate the Sauter mean diameter involving the Flow number, liquid properties and the pressure differential across the nozzle. In an attempt to overcome some deficiencies of the existing SMD formulas and to explain some of the apparent anomalies that careful measurements often reveal, Wang and Lefebvre (1987) proposed an alternative form of the equation for the mean drop sizes produced by pressure swirl nozzles. This equation is not the result of a mathematical treatment of the subject but is based on consideration of the basic mechanisms involved in pressure swirl atomisation. They made the assumption that the SMD equation exists in two parts.

$$SMD = SMD_1 + SMD_2 \quad [23]$$

SMD_1 represents the first stage of atomisation. Its magnitude depends partly on the disruptive forces present within the liquid sheet and the development of capillary waves (ripples) on the liquid surface. The term SMD_2 represents the final stage of the atomisation process, in which the relative velocity induced at the liquid/air interface by the rapidly evolving conical sheet causes the surface protuberances generated in the first stage to become detached and break down into ligaments and then into drops. Surface tension forces oppose this final disintegration. Thus we have

$$SMD = 4.52\left(\frac{\theta\mu_L^2}{\rho_A\Delta p_L^2}\right)^{0.25}(t\cos\theta)^{0.25} + 0.39\left(\frac{\sigma_L}{\rho_A\Delta p_L}\right)^{0.25}(t\cos\theta)^{0.75} \quad [24]$$

The number 4.52 and 0.39 are constants that are only usable with the tested nozzle. Wang and Lefebvre did not give any information how this number was obtained.

Richter and Walzel (1989) presented an equation where the Sauter Mean Number is calculated with the Weber and Ohnesorge number. They defined the Weber Number as

$$We = \frac{2\Delta p\left(\frac{U}{\sqrt{\frac{2p_w}{\rho_w}}}\right)^2 D_e}{\sigma_w} \quad [25]$$

Dahl and Muschelknautz (1991) presented an equation to calculate the representative Maximum Droplet Diameter, $D_{0.99}$, which included the spray angle, liquid and gas properties and the nozzle geometry. Dorfner et al. (1995) presented an equation including the same variables as Dahl and Muschelknautz (1991) but presented it in a way which leaves the option open to calculate the Sauter Mean Diameter based on the Weber or Reynolds number. The idea that the droplet size depend on the relative velocity of the liquid sheet provided Sidahmed (1996a and 1996b) with two models to calculate the droplet size. The first model is based on the assumption that the velocity of the liquid sheet, U_L, is constant and the air velocity, U_A, is variable. The second model is based on the assumption that U_A, is constant and U_L, is variable. The maximum droplet size (deviation of 10%) and the diameter in still air (deviation of 7.5%) were predicted.

2.3.3 Techniques combined with pressure swirl nozzles

To optimise the pressure swirl nozzle and achieve a further reduction of the SMD some researchers tried to combine nozzle techniques. Nielsen et al. (1991) used a mixed fluid (water and carbon dioxide) and operated with a high pressure drop across the nozzle. The fluid temperature was between 40° to 70°C and the spray pressure was varied between 8 to 11 MPa. The reason for this high liquid pressure is that the solution has to be pressurised above the critical pressure to increase carbon dioxide solubility. The dissolved (supercritical) carbon dioxide creates inside the exit orifice an expansive force that overcomes liquid cohesion and surface tension forces that oppose atomisation. The dissolved supercritical carbon dioxide then becomes supersaturated as the spray solution leaves the nozzle. Due to this super-saturation it is possible to cool down warm water droplets quickly. The rapid expansion of the carbon dioxide leads to smaller droplets with higher velocity, and up to 3 times wider spray angle and spray pattern deposition keeps its uniformity.

Friedman and Renksizbulut (1994) concentrated their research on a pressure swirl nozzle where a concentric annular air jet was blasting into the hollow cone spray pattern under isothermal conditions. A Delavan 1.25-60° nozzle was used to produce the hollow cone spray at a constant flow rate of 0.063 l/s. The airflow rate was varied from 4.77 to 14.3 l/s and the droplet size was measured with a Laser Phase Doppler analyser system (LPDA). The observation showed that the initial spray cone widens substantially with increasing Airflow, and that the overall spray envelope remains

essentially the same. It was also observed that the smallest droplets in the 'high flux central core' have the highest velocity and give a very dense spray pattern.

The analysis of the data leads to the conclusion that the length of the 're-circulation zone' is basically unaffected by the liquid spray, furthermore its length is a function of the recirculation zone. The spray cone angle in the 're-circulation zone' widens substantially with the increase of airflow. The measurements of the LPDA system showed that the annular air jet entrains smaller droplets to the centreline of the spray and creates a high flux central core region.

Takahashi et al. (1995) attached a pressure swirl nozzle to a novel high amplitude piezoelectric driver. The influence of a high amplitude velocity of a hollow cone jet was studied. A modulation frequency from 4 to 52 kHz was tested. Two distinctive break-up modes were found at different resonant frequencies, ~17 and ~19 kHz, which resulted in a coherent roll-up and break-down process. Sections of the fluid jet moved with different relative velocities and collided with each other. This impact created radial velocity perturbations, formed circular discs and atomised the fluid. Hence a better spray quality was achieved, where a larger droplet number is caused because of the driver's pumping action. At approximately 17 kHz, the liquid sheet atomised and bifurcated in two major directions and dispensed droplets more evenly within the spray. At approximately 19 kHz, the spray angle narrowed and the droplets in the air core accelerated because of the driver's pumping action. The large droplet number flux caused by the driver's pumping action was helpful in maintaining a good spray quality at low pressure.

Table 2-3: Summarised droplet size equation for pressure swirl nozzle

Investigators	Equation	Remarks
Radcliffe (1960)	$SMD = 7.3\sigma^{0.6} v_L^{0.2} \dot{m}_L^{0.25} \Delta p_L^{-0.4}$	No effect of nozzle dimension or air properties
Jasuja (1979)	$SMD = 4.4\sigma^{0.6} v_L^{0.16} \dot{m}_L^{0.22} \Delta p_L^{-0.43}$	No effect of nozzle dimension or air properties
Babu et al. (1982)	$SMD = 133\frac{FN^{0.64291}}{\Delta p_L^{0.22565} \rho_L^{0.3215}}$	For $\Delta p_L < 2.8$ MPa
Babu et al. (1982)	$SMD = 607\frac{FN^{0.75344}}{\Delta p_L^{0.19936} \rho_L^{0.3767}}$	For $\Delta p_L > 2.8$ MPa
Jones (1982)	$MMD = 2.47\dot{m}_L^{0.315} \Delta p_L^{0.47} \mu_L^{0.16} \mu_A^{-0.04} \sigma_L^{0.25} \rho_L^{-0.22} \times \left(\frac{L_e}{D_e}\right)^{0.03} \left(\frac{L_s}{D_s}\right)^{0.07} \left(\frac{A_P}{D_s D_e}\right)^{-0.13} \left(\frac{D_s}{D_e}\right)^{0.21}$	Suitable for large capacity nozzles
Lefebvre (1983)	$SMD = 2.25\sigma^{0.25} \mu_L^{0.25} \dot{m}_L^{0.25} \Delta P_L^{-0.5} \rho_A^{-0.25}$	

Table 2-3 (continued): Summarised droplet size equation for pressure swirl nozzle

Kennedy (1985)	$SMD = 10^{-3}\sigma_l(6.11 + 0.32\times10^5 FN\sqrt{\rho_L} - 6.973\times10^{-3}\sqrt{\Delta p_L} + 1.89\times10^{-6}\Delta p_L)$	Suitable only for nozzles operating at Weber number larger than 10
Wang and Lefebvre (1987)	$SMD = 4.52\left(\frac{\sigma\mu_L^2}{\rho_A \Delta P_L^2}\right)^{0.25}(t\cos\theta)^{0.25} + 0.39\left(\frac{\sigma\rho_L}{\rho_A \Delta P_L}\right)^{0.25}(t\cos\theta)^{0.75}$	Includes effect of spray cone angle Values of film thickness obtained from Eq. 11, 12
Richter and Walzel (1989)	$SMD = \frac{1.6}{D_e}We^{-1/3}\chi^{0.4}(1+5Oh)^{1.2}$	
Dahl and Muschelknautz (1991)	$D_{0.99} = 1.13 t_s\left(\frac{\rho_L}{\rho_G}\right)^{1/6}\left(\frac{\sigma}{\rho_L W^2 t_s}\right)^{1/3}\left(\frac{0.5D_e}{t_s\tan\theta}\right)^{1/3}\left(\frac{\rho_G U t_s}{\eta_G}\right)^{1/5}$	
Dorfner et al. (1995)	$D_{FH} = \left[\frac{L_F\sin\theta + \sqrt{(L_F\sin\theta)^2 + 4\left(t_s^2 + 2t_s\frac{D_e}{2}\right)}}{2}\right]\cos\theta$ $SMD = 3.8204\, We_F^{-0.6297}\, D_{FH}$ $SMD = 18.94\ \mathrm{Re}_F^{-0.2983}\, D_{FH}$	
Sidahmed (1996)	$D = D_{\max} e^{\lvert 1-U\rvert^n Ln\left(\frac{D_0}{D_{\max}}\right)}$ U_L = constant U_A = variable $D = D_{\max} e^{\left\lvert 1-\frac{1}{U}\right\rvert^n Ln\left(\frac{D_{L0}}{D_{\max}}\right)}$ U_A = constant U_L = variable	

2.4 Atomisation process in effervescent atomisers

2.4.1 Introduction

The effervescent atomiser is a product of further development with regard to the twin-fluid atomiser. Rizkalla and Lefebvre (1975) made an experimental study of air-blast atomisation where the liquid sheet outside the atomiser was exposed to high-velocity air. They realised that the kinetic energy of a gas, preferably air, can be used to transform bulk liquid into small droplets. Extensive research by Lefebvre et al. (1988) led to a novel form of atomisation, the effervescent atomiser. The novel method is, that small gas bubbles are induced into the bulk liquid before leaving the atomiser through the exit orifice. In consequence, the pressure differential between the gas and the liquid is very small, only sufficient to inject the gas into the flowing liquid. The bulk liquid then carries the suspended gas bubble, which has at this stage the same pressure as the liquid, downstream to the exit orifice. Photographs show that when the air bubble leaves the atomiser through in the exit orifice, the air bubbles are "squeezed" and as they reach the ambient pressure they expand rapidly. This rapid expansion shreds the water into ligaments and small drops as shown in Figure 2-5.

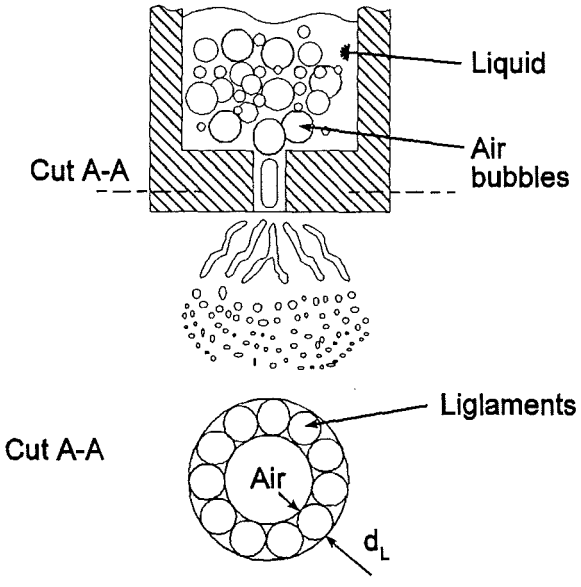

Figure 2-5: Formation process of droplets at the exit orifice of an effervescent atomiser

A ratio, called the Gas Liquid Ratio (GLR), has been derived to distinguish the amount of gas used from the amount of liquid. This ratio is calculated by dividing the mass of the injected gas by the mass feed of liquid to the atomiser.

$$GLR = \frac{\dot{m}_G}{\dot{m}_L} \qquad [26]$$

The dimensionless number is used to classify the amount of gas used to atomise the liquid. In every twin-fluid atomiser the atomisation process is influenced by the amount of gas used (Lefebvre, 1990), which compared to a twin-fluid atomiser is very small. Twin-fluid atomisers have a GLR of 0.4 to 1.4, and the effervescent atomiser from 0.002 to 0.20 (Lefebvre et. al., 1988).

The advantages offered by the effervescent atomisation include the following:

- At low pressure and small GLR the droplet distribution and spray pattern is satisfactory. Mean drop sizes are smaller compared to those obtained with air-assist atomisers for the same air/liquid ratio (Chin and Lefebvre, 1993).
- The atomiser has a relatively large exit orifice compared with other nozzles, which produce the same droplet size. Therefore, it is possible to use them for combustion devices that burn residual fuels, slurry fuels, or any type of fuel where atomisation is impeded by the necessity of using large hole and passage size to avoid plugging of the nozzle.
- The presence of air bubbles can prove very beneficial in alleviating soot formation and exhaust smoke (Li et. al., 1994).
- The simple design of this device leads itself to good reliability, easy maintenance and low manufacturing costs.

The separate supply of air, which must be provided at essentially the same pressure as that of the liquid, is the only apparent drawback of this method.

The different flow regimes, shown in Figure 2-5, that can be achieved in an effervescent atomiser by exceeding the recommended GLR was studied by Chin and Lefebvre (1993). A bubbly flow regime is obtained where air bubbles with a more or less uniform size are closely packed in the flowing liquid but do not coalesce. An increase of the GLR leads away from a bubbly flow toward slug, falling bubbly film, frothy, churning, and finally at high GLR's, to annular flow. In the exit orifice is a

frothy flow that becomes annular at high GLR's. A bubbly flow pattern is required for efficient use of the effervescent atomisers. A GLR of 0, no air bubbles at all, would produce a liquid jet that would break up as studied by Hiroyasu et al. (1991).

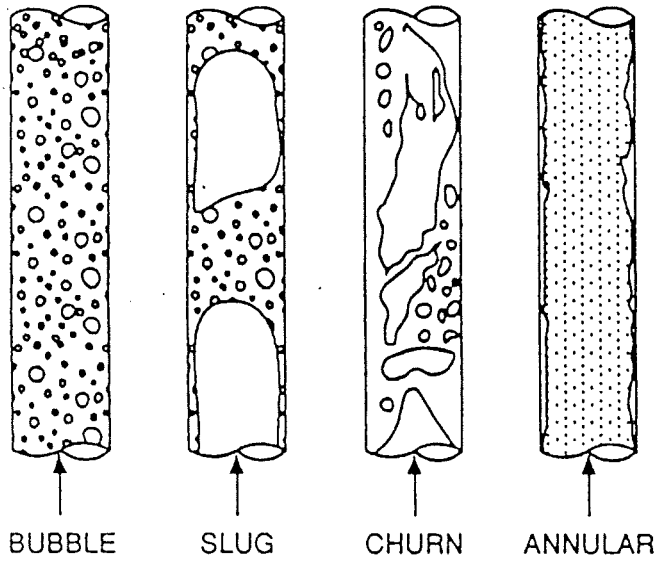

Figure 2-5: Flow pattern in vertical flow (Chin and Lefebvre, 1993)

There are two main configurations existing for effervescent atomiser:

The first method, referred to as type 1, where the air is forced from an aerator tube into the surrounding water is mounted horizontally and is shown in Figure 2-6.

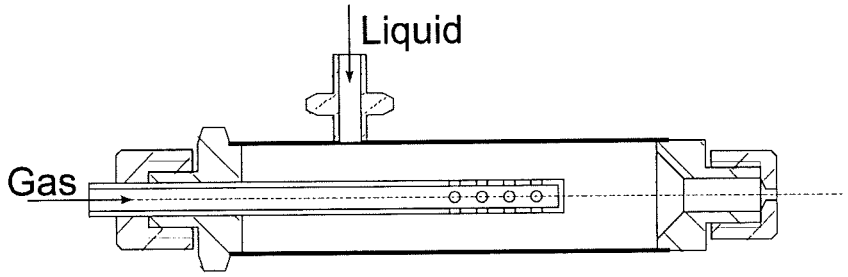

Figure 2-6: Effervescent atomiser (type 1)

The second method (type 2) is forcing air through air injection holes into the water as shown in Figure 2-7. The results of the first test with this arrangement were published by Roesler and Lefebvre (1989). The difference between type 1 and 2 is a) that the movement from a horizontal position to a vertical position and b) that the inner pipe for type 2 contains water instead of gas.

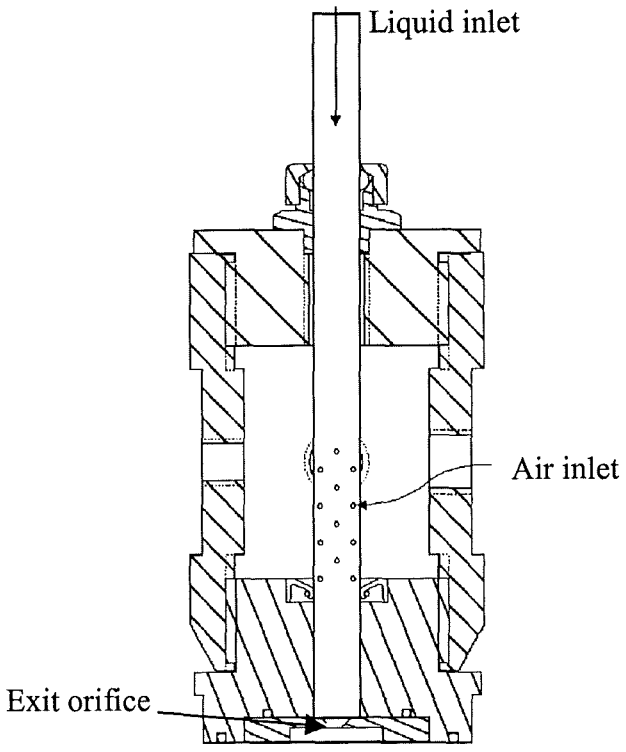

Figure 2-7: Effervescent atomiser (type 2)

The second method was used in the present work. The first method encountered some problems with the droplet distribution in the liquid. The liquid velocity was not fast enough to carry the droplet to the exit orifice. The air bubbles floated to the top and coalesced.

2.4.2 Droplet formation in an effervescent atomiser depending on the GLR

Lefebvre et al. (1988) studied the atomising performance of a novel type effervescent atomiser that they termed an "aerated-liquid atomiser". The tests were carried out at a liquid pressure varied from 34.5 to 690 kPa and a gas/liquid mass ratio (GLR) from 0.002 to 0.22. This was achieved by varying both mass flow rates. Three different exit orifice diameters were used, 0.8, 1.6, and 2.44 mm. The liquid employed was water and the atomising gas used was nitrogen. All tests were carried out under normal atmospheric pressure. The atomiser type 1 used for the test is shown in Figure 2-6.

The inner pipe containing the gas has an inside diameter of 6.3 mm and contains 20 holes with a diameter of 0.5 mm through which gas is injected into the flowing

water. The result of the tests was that the small pressure difference between the gas and liquid depended on the GLR and that the droplet size is depended on the GLR. The variation of the exit orifice diameter has only a negligible effect on the droplet size. An equation to calculate the minimum liquid thickness between adjacent gas bubbles, denoted as t_s, is:

$$t_s = D_{ai}\left\{\left[\frac{\pi}{6}\left(1+\frac{\rho_G}{\rho_L GLR}\right)\right]^{\frac{1}{3}}\right\} \qquad [27]$$

and suggests that an increase of the GLR improves the atomisation quality. The diameter of the exit orifice is not included in this equation and implies that the SMD is independent of it.

Roesler and Lefebvre (1989) continued the study of the effervescent atomiser. Modifications were made, which led to type 2. The method of atomisation was the same as reported in type 1. The liquid pressure was varied from 173 to 690 kPa and the GLR was varied from 0.001 to 0.05. The gas employed in this test was air. Equations were developed, considering the geometry of the atomiser and physics of the fluids. With the assumption that all gas bubbles are of spherical shape, and all of the same size, and if they are so closely packed that the volume of liquid in the intervening spaces is the minimum geometrically possible, the maximum GLR is given by the expression:

$$GLR_{\max} = 2.85\left(\frac{\rho_G}{\rho_L}\right) \qquad [28]$$

Roesler and Lefebvre's (1989) results of the SMD measurement correspond with the results of Lefebvre et al. (1988) and an empirical equation to calculate the energy of the atomising air, called bubble energy, was developed. The term bubble energy represents the amount of energy released by the injected air downstream of the exit orifice and used to break the water jet into ligaments and small droplets. The bubble energy is a function of GLR and the ratios of ambient air to liquid pressure.

$$E = RT\left(\frac{\dot{m}_G}{\dot{m}_L}\right)\ln\left(\frac{p_\infty}{p_L}\right) \qquad [29]$$

Therefore, at high GLR´s and/or high pressure difference across the atomiser, the injected gas has sufficient energy to break the water jet into fine droplets. At low

GLR and low pressure difference the effect of the bubble explosion is much smaller and therefore the droplets and ligaments are thicker. Lefebvre (1991) found from further investigation that the maximum GLR depends on the physical properties of the gas and liquid used. The result of his work led to the following equation to calculate maximum GLR:

$$GLR_{\max} = 4.80\left(\frac{\rho_G}{\rho_L}\right) \qquad [30]$$

Whitlow and Lefebvre (1993) examined experimentally the influence of a varying GLR on the droplet distribution. They used the q value of the Rosin-Rammler distribution as a parameter. Their research showed that the q value over the variation of the GLR is constant. Hence, the droplet distribution is not affected by the GLR as long as the effervescent atomiser operates in the bubbly flow regime.

Lefebvre (1991) examined the principal factors influencing the droplet size at the effervescent atomiser. He presented an equation to calculate the droplet size with the assumption that the spherical air bubbles are uniform in size and that the volume of liquid in the intervening spaces is the minimum geometrically possible. Lefebvre found also that the SMD is influenced by the flow regime and that the mean drop size increased with the increase of liquid viscosity.

Chen et al. (1993) concentrated the research on the drop size distribution at different ambient air pressures. The type 2 effervescent atomiser was used in that research, because the vertical position allows a better control of the gas bubbles and the mixing chamber, where the gas bubbles are injected into the flowing liquid, is smaller. The advantage of a long cylindrical mixing chamber with a small diameter is that the air bubbles are dragged with the water stream towards the exit orifice. The result of the experimental data of the SMD at different air pressures inside the spray chamber showed that a continuous increase in pressure causes the SMD to first increase up to a maximum value and then gradually decline. Chen had no explanation for this.

Nielsen et al. (1991) tested the effervescent atomiser with carbon dioxide to atomise the liquid jet. It is used in supercritical fluid spray processes where the volatile organic solvent content at coating formulations needs to be replaced. He claimed that he had found a new way of airless spraying with a new enormously vigorous

atomisation mechanism, which needed less supercritical carbon dioxide than air as the driving force. The energy in supercritical carbon dioxide is much higher that in air and this results in good atomisation.

2.4.3 Formation of droplets in an effervescent atomiser depending on the mass flow rate and liquid properties

Lefebvre et al. (1988) have shown that the size of the exit orifice has a negligible effect on the SMD. The SMD and the pressure difference of the injected gas into the liquid are mainly influenced by the GLR. A limitation of the previous work was the absence of the influence of liquid properties. Lund et al. (1993a) used for his research seven different fluids with viscosity ranging from 0.001 to 0.080 kg m^{-1} s^{-1} and surface tension ranging from 0.030 to 0.072 kg s^{-2}. He was using a small exit orifice, (he did not mentioned the diameter), to achieve mass flow rates of up to 1.5 g s^{-1} at liquid pressures of 239 kPa to 515 kPa. The result showed that the atomiser was producing a SMD of 70 μm at a GLR of less then 0.02. Another very interesting result of this research is that the atomiser performance was nearly independent of the viscosity of non-Newtonian liquids, and that a significant decrease in droplet size occurred with an increase in surface tension. Geckler and Sojka (1993) used the effervescent atomiser to spray a viscoelastic fluid, a solution of glycerine and water with dissolved Polyethylene oxide polymer, at a constant mass flow rate of 10 g s^{-1} and varying GLR for five different liquid mixtures. The result showed that at this mass flow rate the viscoelasticity was responsible for the increase of the SMD when added to a Newtonian liquid. The break-up of the liquid jet had changed and was producing a viscoelastic net downstream the exit orifice. This viscoelastic net was disintegrating first into ligaments and then into droplets further downstream. Lee and Sojka (1993) confirmed this result.

Lund et al. (1993b) investigated the atomisation performance with different molecular weights of the atomising gas. He replaced the air, which was used by others as the atomising gas, and used a mixture of CO_2 and He. The result showed that the droplet size increased with the increase in molecular weight of the atomising gas at a constant GLR. Lund did not find any systematic influence of GLR on the relationship between the Rosin-Rammler distribution coefficient q and the molecular weight. These results are contrary to the findings of Nielson et al. (1991).

A methodology for the design of an effervescent atomiser was given by Chin and Lefebvre (1993) with the objective to achieve a minimum spray droplet size. Chen and Lefebvre (1994a) showed that the GLR and the air/liquid density ratio primarily influence the discharge coefficient of the exit orifice. With an increase of the GLR the discharge coefficient decreased. Chen and Lefebvre (1994b) reported that the effervescent atomiser, produced due to the rapid expansion of the atomising gas, a much wider spray cone angle than plain-orifice atomisers. They also found that the spray angle depended on the GLR, which was confirmed by Lefebvre (1996). Bush and Sojka (1993 and 1994) studied the positive effect of entrainment by effervescent sprays downstream of the exit orifice. This entrainment was a useful mass addition that occurs in a spray due to turbulent mixing at its boundary. The air mass entrainment was found to be 17.5% of the liquid mass flow rate. This is an advantage and enhances the use of an effervescent atomiser in a gas turbine as described by Li et al. (1994).

No reference has yet been found for any article, on pressure swirl nozzles or effervescent atomisers, in which the energy to produce the spray was considered.

No one has yet:

- calculated the energy used to produce the spray droplet
- determined the nozzle power per unit heat transfer from gas
- optimised the design required for cooling gases by minimising the energy consumption
- simulated the gas flow, temperature and humidity distribution inside a 3-dimensional spray chamber with a non-axial air outlet

2.5 Gas-liquid phase interaction

2.5.1 Introduction

If a drop of liquid moves through air an interaction occurs. This interaction involves mass, momentum, and energy transfer between phases. Analysis of energy and mass transfer is obtained from inlet and outlet conditions of both liquid and gas media. The following measurements of both media at the inlet and outlet needs to be taken for the calculation:

- Temperature
- Humidity
- Mass flow rate

Applying the steady flow energy equation with velocity and level terms neglected in an adiabatic system gives

$$0 = \underbrace{\dot{m}_a\left(Cp_{a2}t_{a2} - Cp_{a1}t_{a1}\right)}_{\text{Change in air}} + \underbrace{\left(\dot{m}_{w2}h_{w2} - \dot{m}_{w1}h_{w1}\right)}_{\text{Change in water}} + \underbrace{\dot{m}_a\left(\omega_2 h_{v2} - \omega_1 h_{v1}\right)}_{\text{Change of vapour}} \quad [31]$$

where Cp_a is the specific heat at constant pressure for air at the temperature t_a. The subscript 1 denotes the incoming and 2 the outlet value. h_w are the enthalpies for water at the measured temperature, and h_v are the enthalpies for vapour at the measured temperature. The value of h_w and h_v are a function of temperature and taken from Rogers and Mayhew (1994). $\dot{m}_a$ is the mass flow rate of dry air and $\dot{m}_w$ the mass flow rate of water. ω_1 is the specific humidity at air inlet conditions and ω_2 is the specific humidity at air outlet conditions. The equation neglects kinetic and potential energy terms which are very small.

2.5.2 Heat transfer

If a cold liquid droplet travels with a relative velocity, U, through a hot gas, the heat transfer process is termed forced convection. Equation [32] is used to determine the heat transfer rates

$$\Delta q_a = h_a \Delta T_a \Sigma A_D \quad [32]$$

whereby the convective heat transfer coefficient from air to droplets, h_a, is determined from standard correlation as shown below. The Nusselt number used to determine the heat transfer coefficient for droplets is defined as

$$Nu_a = \frac{h_a D}{k_a} \quad [33]$$

For forced convection from droplets to surrounding gas the following popular correlation from Ranz Marshall (1952) can be used.

$$Nu_a = 2 + 0.6\,\mathrm{Re}^{1/2}\,\mathrm{Pr}^{1/3} \quad [34]$$

while the Reynolds number is defined as

$$\mathrm{Re} = \frac{\rho_f \left|U_D - U_a\right| D_{32}}{\mu_f} \quad [35]$$

Faeth (1977) used this theory for the analysis of his one-dimensional model of droplet evaporation and verified the correlation.

2.5.3 Mass transfer

The evaporation of droplets in a spray involves simultaneous heat and mass transfer processes. The overall rate of evaporation depends on the pressure, temperature, and transport properties of the gas: the temperature, volatility, and diameter of the droplets in the spray and the velocity of the drops relative to that of the surrounding gas. Suzuki et al. (1985) came to the conclusion that the cooling of the inlet air is dominated by the evaporation. Buglayev et al. (1985) stated that the distance of droplet travel distance and the temperature difference between the droplet and the gas affects the evaporation. Chin and Lefebvre (1985) studied analytically the heating-up and evaporation period of a fuel droplet. They found that a fuel droplet starts with a heating-up period before starting to evaporate. The importance of a numerical model due to the improvement of computer resources caused Kachhwaha et al. (1998) to develop a numerical model. This numerical model was used to predict the evaporative cooling of air with a water spray on a hot horizontal plate for parallel and counter flow. The amount of energy to keep the hot plate at a constant temperature was measured and was equal with the amount of energy of the evaporative cooling. This numerical model agrees with the experimental data to within ±15%.

The heat transfer of evaporation is calculated by

$$\dot{Q}_e = \dot{m}_e h_v \quad [36]$$

where h_v is the enthalpy difference from liquid inlet to vapour outlet. The mass of evaporation can be calculated with different methods.

• Firstly, Bird et al. (1960) defined the mass of evaporation as [37] where the molar mass flow rate of vapour, W_v, is defined as [38].

$$\dot{m}_e = M_W \dot{W}_v \quad [37]$$

$$\dot{W}_v = k_{vm} \dot{A}_D \frac{X_{A0} - X_{A\infty}}{1 - X_{A0}} \quad [38]$$

The variable A_D is the droplet surface and X_{A0} is the vapour pressure at droplet surface and $X_{A\infty}$ in air. The mean mass transfer coefficient, k_{vm} for vapour is defined as

$$k_{vm} = \frac{\rho_w D_{AB} Sh}{M_w D_{32}} \quad [39]$$

where the Sherwood number is analogously defined as the Nusselt number (Bird,1960)

$$Sh = 2 + 0.6 \mathrm{Re}^{1/2} Sc^{1/3} \quad [40]$$

and D_{AB} is the binary diffusivity for water-gas system, which is defined as

$$D_{AB} = 0.996\, a \left(\frac{T_D + T_a}{2\sqrt{T_{ac} T_{wc}}} \right)^b \left(\frac{1}{M_a} + \frac{1}{M_w} \right)^{1/2} \frac{(p_{ac} p_{wc})^{1/3} (T_{ac} T_{wc})^{5/12}}{p} \quad [41]$$

T_{ac}, T_{wc} represent the critical temperatures and p_{ac}, p_{wc} the critical pressures for the substances. Analysis of experimental data for a water-air system resulted in a=3.640 10^{-4} and b=2.334. Equation [40] requires the Schmidt number to be calculated, which is defined as

$$Sc = \frac{\mu_w}{\rho_w D_{AB}} \quad [42]$$

• A second method to determine the mass transfer is presented by Holman (1968) which defines a control volume around the droplet and calculates the concentration through which diffusion occurs. The equation to calculate the mass of evaporation depends also on the droplet surface and is defined as

$$\dot{m}_e = h_{Dw}\, A_D \left(C_{w1} - C_{w2}\right) \quad [43]$$

where A_D is the droplet surface and $C_{w1/2}$ is the concentration of vapour through which diffusion occurs and is defined by [44].

$$C_{wx} = \frac{M_w\, \rho_{vx}}{R_o\, T_{vx}} \quad [44]$$

The mass transfer coefficient h_{Dw} is defined by [45]

$$h_{Dw} = \frac{2\, Sh\, D_{AB}}{D_{CV} - D_{32}} \quad [45]$$

where D_{CV} denotes the diameter of the control volume and D_{32} the diameter of the droplet. The Sherwood number is given by equation [40]. Holman used Gilliland's semi-empirical equation for the diffusion coefficient in gases

$$D_{AB} = 18.01310^{-4} \frac{\left(1.8\, T_f\right)^{1.5}}{p_\infty \left(V_A^{1/3} + V_B^{1/3}\right)^2} \sqrt{\frac{1}{M_A} + \frac{1}{M_B}} \quad [46]$$

where M_A, M_B is the molecular weight, V_A, V_B the molecular volume of e.g. A = air and B = vapour, p_∞ the ambient pressure and T_f is the film temperature in which diffusion occurs and is defined as

$$T_f = \frac{T_D + T_a}{2} \quad [47]$$

where T_D is the temperature of the droplet and T_a the temperature of the surrounding air.

• The third method is presented by Crowe et al. (1977) where the mass of evaporation is calculated along the trajectory to incorporate the decreasing droplet diameter and the change of the drag coefficient into the calculation. The mass of evaporation is defined as

$$\dot{m}_e = h_{Dx}\, A \left(X_{vDs} - X_{va}\right) \quad [48]$$

where A is the droplet surface and the mass transfer coefficient h_{Dx} is defined as

$$h_{Dx} = \frac{Sh\left(\rho_a\, D_{AB}\right)}{D_{32}} \quad [49]$$

X_{vDs} indicates the mass fraction of vapour at droplet surface and the ambient air stream, p_v is the partial vapour pressure, M_w and M_a the molar weight of water and air.

$$X_{vDs} = \frac{p_v M_w}{M_a - (M_a - M_0)p_v} \qquad [50]$$

X_{va} is the sum of mass evaporation of each calculation after the time increment of Δt. In the case of a slow evaporating droplet the vapour pressure at the droplet surface corresponds to saturation conditions at the temperature of the drop.

2.5.4 Drag coefficient for a sphere

The drag coefficient is a function of the Reynolds number. There are three different regions known for the drag coefficient (Eastop and McConkey, 1986). Stokes's law is valid for a Reynolds number smaller than 0.1 and such flow is known as creeping flow around a sphere. The function of the friction coefficient is a straight-line portion of the log f versus log Re curve. The friction coefficient is given as (Rogers and Mayhew, 1967)

$$f = \frac{24}{\mathrm{Re}} \qquad \mathrm{Re} < 0.1 \qquad [51]$$

The region for a Reynolds number between 2 and 500 is called the intermediate region and indicates lesser dependence on the Reynolds number than in Stokes's law. The friction coefficient for this region is given as (Rogers and Mayhew, 1967)

$$f = \frac{18.5}{\mathrm{Re}^{0.6}} \quad 2 < \mathrm{Re} < 500 \qquad [52]$$

If the Reynolds number becomes higher, the drag coefficient becomes constant. This region is known as the Newton's law region. The equation (Rogers and Mayhew, 1967) that describes this region is

$$f = 0.44 \qquad 500 < \mathrm{Re} < 2\ 10^5 \qquad [53]$$

2.5.5 Droplet-wall interaction

The collision of a droplet onto a solid target is important in the heat and mass transfer process. Most of the droplets hit the column wall. When the droplet hits the wall, it breaks-up. Part of it sticks to the wall and the rest forms smaller droplets. The part that sticks to the wall forms a falling liquid film. The part that is splattered back into the gas flow as smaller droplets has a significant influence on the heat and mass transfer process. The impact of a droplet is divided into three main groups:

- Droplet impingement on heated surfaces, in which the temperature is above evaporation temperature of the liquid
- Droplet impingement on cold surfaces
- Droplet impingement on liquid films with the same physical properties

Group three is the main interest for this research (Levin and Hobbs (1971)). Their research was focussed on the impingement of 2.9 mm spherical droplets with low velocities normal to the dry surface. They discovered that if the kinetic energy of primary droplets was high enough, the droplets formed a cylindrical sheet. This occurrence was called corona formation. They found that thin droplets appear at the upper rim when the corona was unstable. Levin and Hobbs evaluated the diameter of droplets greater than 50 μm and discovered that the average diameter of splashing droplets lies between 10 to 20 % of the primary droplet diameter. When the kinetic energy was relatively low, the droplet was deformed during the impact and splashing did not occur and the fluid was completely deposited on the surface.

Stow and Hadfield (1981) continued the research of Levin and Hobbs (1971) with the difference that droplets with a diameter smaller then 50 μm were investigated. They determined that the splashing droplets of the unstable corona are about 10% of the primary droplet diameter and that the droplets were distributed according to a log-normal function.

Naber and Reitz (1988) investigated three different possible outcomes of the drop impingement:

- the deposition, or stick case,
- the rebound (reflection) and
- the "jet" case.

In the first case no secondary droplets are generated, in the second the primary droplet leaves the surface with a given angle, as for an elastic impact. In the third case the primary droplet rolls along the surface. In every case no lost of kinetic energy or mass is considered. For example the drop that reflects on the surface has the velocity components (u, v) before the impact and after the impact ($-u$, v). Wang

and Watkins (1993) had a slightly different version of the previous model. They based their model on the work of Wachters and Westerling (1966) for heated walls. For surface temperatures above the Leidenfrost threshold rebound of the droplets is observed for We < 30. For a Weber number from 30 to 80 the primary droplet disintegrated into two or three smaller drops rebounding from the surface. For We > 80 a splash is observed and various numbers of droplets emerging from the corona formation. Wang and Watkins proposed the scheme in Table 2-4 with

$$\omega = \left(1 - 0.95\cos^2 \varphi_{be}\right)^2 \qquad [54]$$

where φ_{be} is the impact angle respect to the normal to the wall. The value ω is needed to calculate the droplet properties after the impact listed in the table below depending on the Weber number.

Table 2-4: Correlations of Wang and Watkins (1993)

We < 80	We > 80
$u_{af} = \omega\, u_{be}$	$u_{af} = \omega\, u_{be}$
$v_{af} = \omega\, v_{be}$	$v_{af} = 0$
$D_{af} = D_{be}$	$D_{af} = 0.25 D_{be}$
n = 1	n = 64

The subscription "*af*" and "*be*" mean after and before impact. This model gives the same results for normal impacts as determined from the correlation by Naber and Reitz (1988).

The first attempt to build a complete empirical model for drop impacts on dry walls at ambient temperature was made by Mundo et al. (1995). They used a Phase Doppler Analyser (PDA) technique to find a splash threshold in term of the $K = Oh\, Re^{1.25}$ number. The mean secondary droplet diameter, D_{af}, and number, n_{af}, the deposited mass, m_{dep}, and two components, u_{af} & v_{af}, of the secondary droplet (SD) velocity are given as functions of the primary drop diameter and velocity in a small range of K after the threshold of 57.7.

Secondary droplets mean diameter $$D_{af} = \min[8.72\exp(-0.0281\,\mathrm{K}), 1.0]\, D_b e \quad [55]$$

Secondary droplets number $$n_{af} = (1.676\,10^{-5}\ \mathrm{K}^{2.539})\, n_{be} \quad [56]$$

Deposited mass fraction $$m_{dep}/m_{be} = \max\left[\frac{1 - n_{af}}{n_{be}(d_{af}/d_{be})^3}, 0.0\right] \quad [57]$$

Secondary droplets mean velocity

$$u_{af} = [1.337 - 1.318\ \xi + 2.339\ \xi^2]\, u_{be}$$
$$v_{af} = [-0.249\ - 2.959\ \xi + 7.794\ \xi^2]\, v_{be} \quad [58]$$

with $\xi = \frac{D_{af}}{D_{be}}$.

Marengo and Tropea (1999) concentrated their research on the experimental analysis of secondary droplet characteristics. A single water drop impacted onto a moving liquid film. The time integral value of the diameter and velocities was measured using a PDA technique. The authors used water droplets in their experiments only and introduced a dimensionless number. Their correlation is based on the ratio between the K_r number ($We\ Oh^{-0.4}$) and its critical value K_{cr}.

The results of the secondary droplet parameters (π_{af}) were fitted in the form

$$\pi_{af} = (C_1 + C_2\delta) + (C_3 + C_4\delta)(K_r - K_{cr})\,10^{-3} \quad [59]$$

where π is substituted by the parameter which should be calculated. The parameter δ is the non-dimensional film thickness and is calculated as $\delta = \frac{t_s}{D_{be}}$. The critical value is defined by Stanton and Rutland (1996) for splashing as $K_r = 13^{3.2}\ We\ Oh^{0.4}\ f'^{1.2}$ where f is the dimensionless impact frequency defined by $f' = f\,D\,u^{-1}$. The Table 2-5 contains the coefficients a, b, c, d, used to calculate the dimensionless velocities $u_{af}^{*} = \frac{u}{U}$ and $v_{af}^{*} = \frac{v}{V}$, mean diameter $D_{10af}^{*} = \frac{D_{10be}}{D}$ and Sauter mean diameter $D_{32af}^{*} = \frac{D_{32be}}{D}$ of the secondary droplets. The range of validity for the following set of coefficients a, b, c, d for almost normal impacts is ($\alpha > 80°$, $0.5 < \delta < 2$, $K_r < 4$).

The correlations of the experimental data was completed with three nondimensional equations to calculate the deposited mass, the concentration and the number of secondary droplets and are fitted in the form:

$$\frac{m_{af\,s}}{m_{be}} = (C_5 + C_6\delta)(K_r - K_0)^{(C_7+C_8\delta)} \quad [60]$$

$$\frac{N_{af\,s}}{N_{be}} = \max\left(0{,}1 + C_5 + \frac{C_5(K_r - K_0)}{1 - e^{(K_r - K_0)}} 2^{(C_6+C_7\delta)(K_r-K_0)}\right) \quad K_r \neq K_0 \quad [61]$$

$$C_{af\,s} = (C_5 + C_6\delta)(K_r - K_0)^{(C_7+C_8\delta)} \quad [62]$$

where $m_{af\,s}$ is the mass of the liquid spheres that bounces of the wall, $N_{af\,s}$ the total number of droplets emerging due to the splashing, and $C_{af\,s}$ is the concentration of droplets per impact. Table 2-5 contains the coefficients C1 to C8 to determine the deposited mass, the concentration and the number.

Table 2-5: The fitting coefficients for the empirical model of Marengo and Tropea (1999)

	C_1	C_2	C_3	C_4	C_5	C_6	C_7	C_8
u_{af}^*	0.056	0.057	0.038	0.000				
v_{af}^*	0.311	-0.077	-0.009	-0.024				
$D_{10\,af}^*$	0.209	0.100	-0.096	0.005				
$D_{32\,af}^*$	0.250	0.238	-0.022	-0.128				
$m_{af\,s}/m_{be}$					0.363	0.242	2.928	-1.521
$N_{af\,s}/N_{be}$					640.8	0.685	0.036	
$C_{af\,s}$					0.285	0.073	0.630	-0.100

2.5.6 Momentum, heat and mass transfer correlations for numerical modeling

The use of a commercial code (PHOENIX 2.2.2) is the basis of the numerical model. The governing equations comprise momentum, heat and mass transfer as well as the turbulence transport. These equations are coupled both hydrodynamically and via thermo-physical of the fluids. The basics of the momentum, heat and mass transfer correlations for numerical modelling are explained in this chapter. The continuation in Chapter 5.2 shows how these equations are used and implemented in the code. Furthermore in Chapter 5.2 the turbulence model is explained and its relations to the equations shown.

A number of articles and books are available which report and explain the used theory. Comprehensive sources are Versteeg and Malalasekera, "An Introduction to Computational Fluid Dynamics", and S.V. Patankar, "Numerical Heat Transfer and Fluid Flow". Useful information is also provided in the articles of Crowe et al. (1977), Nam (1993), and Jicha et al. (1994).

The calculation is based on a cell that contains as specified volume. A 3D model has the cell with six surfaces, which are labelled N, S, E, W, T, B, on three axis (x, y, z). The change of mass, momentum and energy of the fluid element contained in the cell is also depending on the time. Therefore, all terms of the resulting mass balance can be arranged on the left hand side of the equation and divided by $\delta x \delta y \delta z$. The rate of increase of mass in fluid element and net rate of flow of mass into fluid element can be written as

$$\frac{\partial \rho}{\partial t} + \frac{\partial(\rho u)}{\partial x} + \frac{\partial(\rho v)}{\partial y} + \frac{\partial(\rho w)}{\partial z} = 0 \qquad [63]$$

or in a more compact vector notation for the unsteady three dimensional mass conservation for a point in a compressible flow

$$\frac{\partial \rho}{\partial t} + div(\rho U) = 0 \qquad [64]$$

For incompressible flow, the density is constant and the equation becomes

$$divU = \frac{\partial u}{\partial x} + \frac{\partial v}{\partial y} + \frac{\partial w}{\partial z} = 0 \qquad [65]$$

Every change in a flowing fluid or fluid particle is calculated by using the momentum and energy conservation law were the property of such particle is a function of the position (x, y, z) and time t. The momentum and energy conservation law is defined as

Rate of increase of ϕ of fluid element	+	Net rate of flow of ϕ out of fluid element	=	Rate of increase of ϕ for a fluid particle

A fluid particle follows the flow, so that $\frac{dx}{dt} = u, \frac{dy}{dt} = v, \frac{dy}{dt} = w$. Now let ϕ be the property per unit mass that changes and is defined by $\frac{D\phi}{Dt}$. The change of ϕ per unit volume is then derived by $\frac{D\phi}{Dt}$ and the density ρ, which leads to the following equation

$$\rho \frac{D\phi}{Dt} = \rho\left(\frac{\partial \phi}{\partial t} + U \cdot grad\, \phi\right) \qquad [66]$$

The mass conservation equation contains the mass per unit volume as the conserved quantity and is the expressed in general

$$\rho \frac{D\phi}{Dt} = \frac{\partial(\rho\phi)}{\partial t} + div(\rho\phi U) \qquad [67]$$

The above function represents now the change of ϕ per unit volume and the net flow of ϕ out of the fluid element per unit volume. The mass conservation did not include the net rate of flow of ϕ out of the fluid element, which is obvious if the above equation is written in the form of

$$\rho \frac{D\phi}{Dt} = \frac{\partial(\rho\phi)}{\partial t} + div(\rho\phi U) = \rho\left[\frac{\partial \phi}{\partial t} + U \cdot grad\phi\right] + \phi\left[\frac{\partial \rho}{\partial t} + div(\rho U)\right] \qquad [68]$$

The momentum and energy equation can be used for three-dimensional calculation where ϕ is replaced by the relevant variables. An example is shown in the table below.

Table 2-6: Variation of ϕ at different components for momentum and energy conservation laws

x-momentum	U	$\rho\frac{Du}{Dt}$	$\frac{\partial(\rho u)}{\partial t}+div(\rho uU)$
y-momentum	V	$\rho\frac{Dv}{Dt}$	$\frac{\partial(\rho v)}{\partial t}+div(\rho vU)$
z-momentum	W	$\rho\frac{Dw}{Dt}$	$\frac{\partial(\rho w)}{\partial t}+div(\rho wU)$
Energy	E	$\rho\frac{DE}{Dt}$	$\frac{\partial(\rho E)}{\partial t}+div(\rho EU)$

The change of the momentum is defined by Newton's second law, which states that the rate of change of momentum of a fluid particle equals the sum of the forces on the particle.

Rate of increase of momentum of fluid particle = Sum of forces on fluid particle

The mass flux of this cell is calculated with the mass conversation equation, which is defined as

Rate of increase of mass in fluid element = Net rate of flow of mass into fluid element

The mathematically equation for the rate of increase of mass in the fluid element is defined as

$$\frac{\partial}{\partial t}(\rho\delta x\delta y\delta z)=\frac{\partial\rho}{\partial t}\delta x\delta y\delta z \qquad [69]$$

The rates of increase of momentum of a fluid particle is given by

$$\rho\frac{Du}{Dt} \qquad \rho\frac{Dv}{Dt} \qquad \rho\frac{Dw}{Dt} \qquad [70]$$

The sum of forces on fluid particle is represented by nine different stress components on the boundary's of the cell, which can be defined as

$$\begin{matrix} \tau_{xx} & \tau_{xy} & \tau_{xz} \\ \tau_{yx} & \tau_{yy} & \tau_{yz} \\ \tau_{zx} & \tau_{zy} & \tau_{zz} \end{matrix}$$

The sum of the total forces per unit volume on the fluid due to surface stress is expressed for the x-component as

$$\rho\frac{Du}{Dt} = \frac{\partial(-p+\tau_{xx})}{\partial x} + \frac{\partial\tau_{zy}}{\partial y} + \frac{\partial\tau_{zz}}{\partial z} + S_{Mx} \qquad [71]$$

and for the y- component

$$\rho\frac{Dv}{Dt} = \frac{\partial\tau_{xy}}{\partial x} + \frac{\partial(-p+\tau_{yy})}{\partial y} + \frac{\partial\tau_{zy}}{\partial z} + S_{My} \qquad [72]$$

and for the z- component

$$\rho\frac{Dv}{Dt} = \frac{\partial\tau_{xz}}{\partial x} + \frac{\partial\tau_{yz}}{\partial y} + \frac{\partial(-p+\tau_{zz})}{\partial z} + S_{Mz} \qquad [73]$$

The term S_M represents the gravity force for each component and is defined as $S_M = -\rho g$.

The energy equation is derived from the first law of thermodynamics and is used to derive the rate of increase of energy of a fluid particle calculated from the net rate of heat added to a fluid particle and the work done on the fluid particle by surface force.

Rate of increase of energy of a fluid particle	=	Net rate of heat added to a fluid particle	+	Net rate of work done on the fluid particle	+	Rate of increase of energy due to sources

The energy equation is depending on a large number of variables if it is written in its general form. It is very common to specify the energy equation and dismiss the parts that are not needed for a specific calculation.

The rate of increase of energy of a fluid particle was previously derived from the momentum and energy conservation law and is found in Table 2-6 and is $\rho\frac{DE}{Dt}$

The net rate of heat added to a fluid particle has, similar to the mass conservation, three components were the energy flux due to heat conduction is across the cell boundaries. The heat flux for the x-component is defined as

$$\left[\left(q_x - \frac{\partial q_x}{\partial x}\frac{1}{2}\delta x\right) - \left(q_x + \frac{\partial q_x}{\partial x}\frac{1}{2}\delta x\right)\right]\delta y\delta z = -\frac{\partial q_x}{\partial x}\delta x\delta y\delta z \qquad [74]$$

The y- and z-components are defined in the same way. If all three components are divided by the volume of the cell, δxδyδz, the total rate of heat added to the fluid particle can be written as

$$-\frac{\partial q_x}{\partial x} - \frac{\partial q_y}{\partial y} - \frac{\partial q_z}{\partial z} = -div\ q = div(k\ grad\ T) \qquad [75]$$

The total rate of work done on the fluid particle is expressed as

$$[-div(pU)] + \begin{bmatrix} \frac{\partial(u\tau_{xx})}{\partial x} + \frac{\partial(u\tau_{yx})}{\partial y} + \frac{\partial(u\tau_{zx})}{\partial z} + \\ \frac{\partial(u\tau_{xy})}{\partial x} + \frac{\partial(u\tau_{yy})}{\partial y} + \frac{\partial(u\tau_{zy})}{\partial z} + \\ \frac{\partial(u\tau_{xz})}{\partial x} + \frac{\partial(u\tau_{yz})}{\partial y} + \frac{\partial(u\tau_{zz})}{\partial z} \end{bmatrix} \qquad [76]$$

where the first term expresses the pressure in a vector form and the second term gives the work done by surface force.

Every particle in the flow has got a specific energy, E, which is up to now not defined. The specific energy is the sum of the internal energy, the kinetic energy, and the gravitational potential energy. The kinetic energy is defined as $\frac{1}{2}(u^2 + v^2 + w^2)$ and the gravitational potential energy is S_M. The internal energy is the thermal energy and the gravitational potential energy. Because of the many unknown, a term, rate of increase of energy due to sources, S_E, is created that contains this information. To calculate the rate of increase of energy due to sources is each component of the momentum equations multiplied by its velocity and subtracts it from equation [76] to remove the kinetic energy. This creates a new source term, S_i, which yields the internal energy, which is defined as

$$\rho\frac{Di}{Dt} = -p\,divU + div(k\,grad\,T) + \tau_{xx}\frac{\partial u}{\partial x} + \tau_{yx}\frac{\partial u}{\partial y} + \tau_{zx}\frac{\partial u}{\partial z} + \tau_{xy}\frac{\partial v}{\partial x} + \tau_{yy}\frac{\partial v}{\partial y} + \tau_{zy}\frac{\partial v}{\partial z} + \tau_{xz}\frac{\partial w}{\partial x} + \tau_{yz}\frac{\partial w}{\partial y} + \tau_{zz}\frac{\partial w}{\partial z} + S_i \qquad [77]$$

The energy equation is presented in a general form. Depending of the property of the fluid, compressible or uncompressible, different possibilities of simplification and alternation of the result are possible. If the fluid is incompressible the internal energy becomes $i=cT$, where c is the specific heat and T the temperature. The net flow of mass across the boundaries, *div* $\boldsymbol{U}$, becomes *div* $\boldsymbol{U}=0$. The energy equation can then be converted into a temperature equation. If the fluid is compressible, the energy equation can be rearranged to calculate the total specific enthalpy, h_0, because in a compressible fluid is

$$h = i + \frac{p}{\rho} \qquad \text{and} \qquad h_0 = h + \tfrac{1}{2}\left(u^2 + v^2 + w^2\right) \qquad [78]$$

To solve the shear stresses in equation [77], which are undefined so far, Newton's law of viscosity for compressible flows is used, which depends on the dynamic viscosity, μ, and the second viscosity, λ, that is related to stresses of the volumetric deformation. Not much is known about the second viscosity and Schlichting (1979) gave as a good approximation $\lambda = -\tfrac{2}{3}\mu$.

The nine stress components are defined with six independent functions and shown below.

$$\tau_{xx} = 2\mu\frac{\partial u}{\partial x} + \lambda\,div\,U \qquad \tau_{yy} = 2\mu\frac{\partial v}{\partial y} + \lambda\,div\,U \qquad \tau_{zz} = 2\mu\frac{\partial w}{\partial z} + \lambda\,div\,U$$

$$\tau_{xy} = \tau_{yx} = \mu\left(\frac{\partial u}{\partial y} + \frac{\partial v}{\partial x}\right) \qquad \tau_{xz} = \tau_{zx} = \mu\left(\frac{\partial u}{\partial z} + \frac{\partial w}{\partial x}\right) \qquad [79]$$

$$\tau_{yz} = \tau_{zy} = \mu\left(\frac{\partial v}{\partial z} + \frac{\partial w}{\partial y}\right)$$

After substitution of these shear stresses into equation and rearranging the equation it can be expressed as

$$\rho\frac{Di}{Dt} = -p\,divU + div(k\,grad\,T) + \Phi + S_i \qquad [80]$$

where Φ represents the dissipation function which yields all effects due to viscous stresses in the internal energy equation and is described as

$$\Phi = \mu\left\{\begin{array}{l} 2\left[\left(\frac{\partial u}{\partial x}\right)^2+\left(\frac{\partial v}{\partial y}\right)^2+\left(\frac{\partial w}{\partial z}\right)^2\right] \\ +\left(\frac{\partial u}{\partial y}+\frac{\partial v}{\partial x}\right)^2+\left(\frac{\partial u}{\partial z}+\frac{\partial w}{\partial x}\right)^2+\left(\frac{\partial v}{\partial z}+\frac{\partial w}{\partial y}\right)^2 \end{array}\right\}+\lambda\,(divU)^2 \qquad [81]$$

Substitution of these shear stresses into the momentum equation [71]-[73] gives the Navier-Stokes equation, where each component after rearranging can be written in the most useful form for the finite volume method as follows.

$$\rho\frac{Du}{Dt} = -\frac{\partial p}{\partial x} + div(\mu\ grad\,u) + S_M \qquad [82]$$

$$\rho\frac{Dv}{Dt} = -\frac{\partial p}{\partial y} + div(\mu\ grad\,v) + S_M \qquad [83]$$

$$\rho\frac{Dw}{Dt} = -\frac{\partial p}{\partial z} + div(\mu\ grad\,w) + S_M \qquad [84]$$

The transport equation for the property ϕ, where ϕ represents a general variable, is the first equation that is solved for computational procedures in the finite volume method. The conservation equations are used with this transport equation, which integrates them over a three-dimensional control volume. The transport equation in its integrated form can be expressed as

$$\int_{CV}\frac{\partial(\rho\phi)}{\partial t}dV + \int_{CV} div(\rho\phi U)dV = \int_{CV} div(\Gamma\ grad\,\phi)dV + \int_{CV} S_\phi dV \qquad [85]$$

On the left hand side represents the first term the rate of change on the particle and the second term is the convective term on the particle. The table below summarises the governing equations for the flow of compressible Newtonian fluid.

Table 2-7: Conservation equation of the flow for compressible Newtonian fluid

Mass	$\frac{\partial \rho}{\partial t} + div(\rho U) = 0$	[86]
x-component of momentum	$\frac{\partial(\rho u)}{\partial t} + div(\rho u U) = \frac{\partial p}{\partial x} + div(\mu\, grad\, u) + S_{Mx}$	[87]
y-component of momentum	$\frac{\partial(\rho v)}{\partial t} + div(\rho v U) = \frac{\partial p}{\partial y} + div(\mu\, grad\, v) + S_{My}$	[88]
z-component of momentum	$\frac{\partial(\rho w)}{\partial t} + div(\rho w U) = \frac{\partial p}{\partial z} + div(\mu\, grad\, w) + S_{Mz}$	[89]
Internal energy	$\frac{\partial(\rho i)}{\partial t} + div(\rho i U) = -p\, div U + div(k\, grad\, T) + \Phi + S_{Mx}$	[90]

On the right hand side is the diffusion and source term. The diffusion coefficient is shown as Γ. The diffusion term and the convective term is rewritten by applying Gauss divergence theory. For the steady state problem becomes the rate of change term zero and the transport equation can be written as

$$\int_A N \cdot (\rho \phi U) dA = \int_A div(\Gamma\, grad\, \phi) dA + \int_{CV} S_\phi dV \qquad [91]$$

The discretised equation for a three dimensional grid to calculate interior nodes is

$$a_P \phi_P = a_W \phi_W + a_S \phi_S + a_E \phi_E + a_W \phi_W + a_T \phi_T + a_B \phi_B + S_u \qquad [92]$$

where the index P stands for the node in the centre of the control volume, N, S, E, W, T, B, are representing the nodes beyond the boundaries of the predefined name (see Figure 5-1). The letter *a* stands for the neighbour coefficients of the control volume integrated conservation equation and ϕ represents the variable that needs to be solved.

Chapter 3 Experimental Apparatus and Test Program

3.1 Introduction

This chapter provides a detailed description of the equipment assembled for the experimental aspects of this work. As discussed in Chapter 1, the main objective of the experimental investigation was to obtain data on the cooling of a hot gas flow using a liquid spray, for the following purposes:

- assessing the cooling performance and energy consumption of different spray nozzle types and designs,

- comparison with the predictions of the computational fluid dynamics and heat transfer model described in Chapter 6.

The testing programme covered two types of spray nozzle; a pressure swirl atomiser and an effervescent atomiser. As flexibility in varying the internal geometry of the nozzles was required, commercial spray nozzles could not be used. The nozzles tested were designed and manufactured particularly for this investigation and are described in Section 3.2. The experimental program is described in section 3.6.

Supplementary testing, fully described in section 3.5, was performed to characterise the sprays generated by the pressure swirl nozzles. A LPDA became available at a later stage of the project. At this time all these experiments were stopped and the test rig was converted for the measurement of the spray characteristics. The equipment used for these tests and the set-up is described in Section 3.5.1.

3.2 Spray Nozzles

3.2.1 Pressure swirl atomiser

A multiplex pressure swirl nozzle was designed that allows the internal dimensions to be changed (Figure 3-1). The nozzle consists of a main body, a threaded rod, and a top and bottom cap. Inside the main body are a swirl chamber and exit orifice held in place by the threaded rod.

The nozzle body itself is a tube with two inside threads at both ends. In the middle of the nozzle body are three threaded holes to accommodate the K-type thermocouple and a pressure sensors and for the water supply. Copper washers and Teflon tape were used to ensure that the nozzle was watertight. A temperature sensor and a pressure sensor were used to obtain the required parameters (temperature and liquid pressure) of the fluid before it enters the swirl chamber.

The top cap has an outside thread, so that it can screw into the nozzle body and be made watertight. An 'O' ring was used to make the top plate watertight. In the centre is a 12 mm threaded hole that accommodates the threaded rod. The function of this rod is to clamp the swirl chamber and the exit orifice together, hold them in a fixed position, and avoid water bypassing the swirl chamber.

The bottom cap also has an outside thread that can be screwed into the nozzle body. A groove in the bottom plate is used to hold the exit orifice and the swirl chamber in a fixed position. Additionally there are four holes to screw the bottom cap to the top plate of the spray chamber.

The chosen ratios and the diameter of the swirl chamber were made to give 6561 combinations of the internal geometry depending on the swirl chamber and the exit orifice. It was planned to continue research following this programme and be the basis for further projects at Middlesex University. A nozzle coding was developed consisted of three parts, two numerical and one alphabetical, that describe the current nozzle configuration. The first numerical part of the code combined the diameter of the swirl chamber and the number of tangential slots. The second part was the alphanumerical which denotes the length of the swirl chamber. The third and last part is related to the exit orifice. The following pages describe the size of these parts. The bold printed values at Table 3-1 are used for the coding. For example, 9b20 is a

nozzle with a 7.5 mm swirl chamber diameter and 2 tangential slots with a length of 4.5 mm and an exit orifice diameter of 2.5 mm and a length of 1.25 mm.

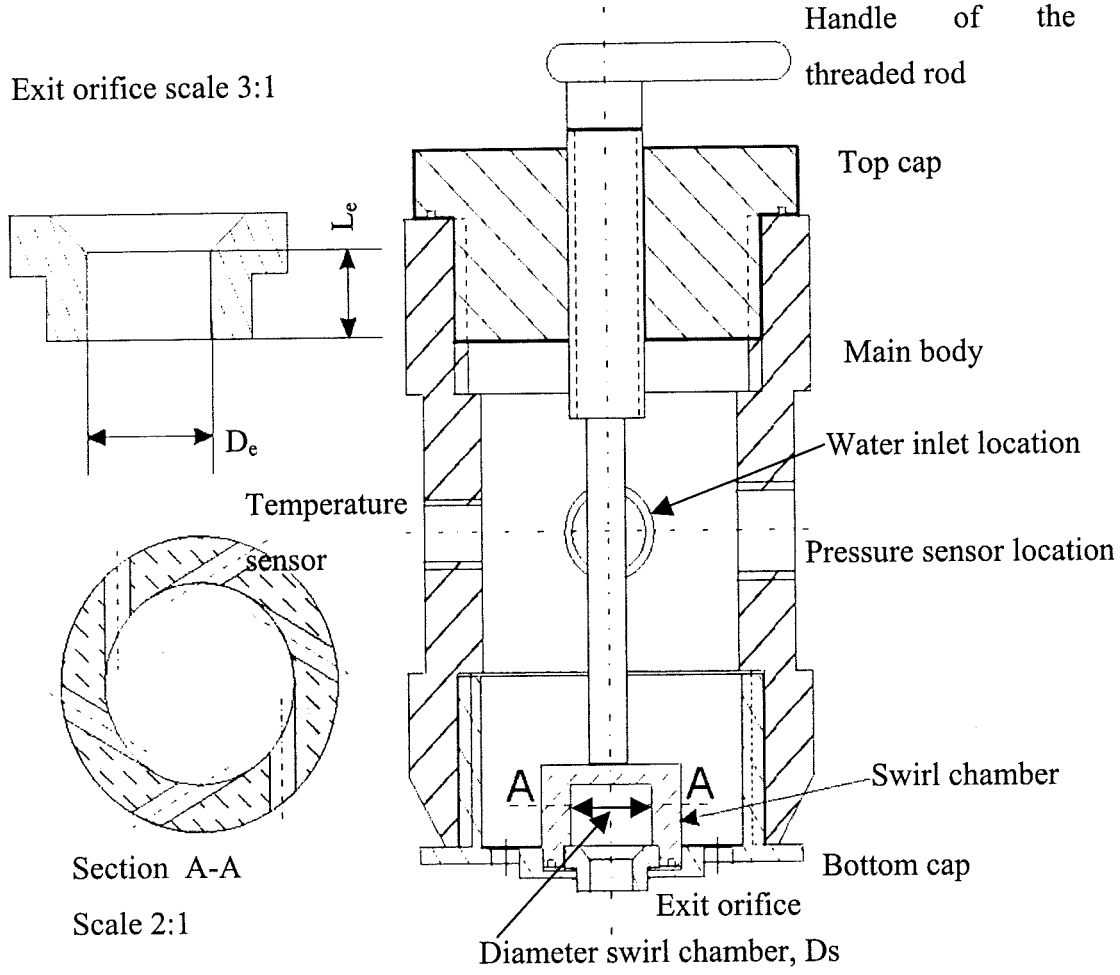

Figure 3-1: Pressure swirl nozzle

Nine different swirl chambers were manufactured. Each swirl chamber has its own number, which is constant for the number of slots. The tangential slots (NTS) have a constant inlet area irrespective of the number of slots. In all cases the swirl chamber has an inside diameter of 7.5 mm (D_s) and an outside diameter of 22 mm. To evaluate the effect of the swirl chamber length the ratios (L_s/ D_s) of 0.8, 0.6 and 0.4 were chosen. The letters a, b or c describe the length of the swirl chamber. The details are shown in Table 3-1 and in Figure 3-2.

Table 3-1: Dimensions of the swirl chambers /mm

No.	NTS	D_s	D_s/D_e	D_p	L_p	B	E	Y	H	L_s a	L_s b	L_s c
9	2	7.5	1.6	3.41	15.33	10.59	2.02	8.98	4.71	6.00	4.50	3.00
18	4	7.5	1.6	2.41	15.89	13.13	2.50	8.50	4.21			
27	6	7.5	1.6	1.97	16.23	14.26	2.71	8.29	3.98			

The diameter of the exit (D_e) orifice is designed by the pre-chosen ratio (D_s/D_e) of the swirl chamber diameter (D_s). The diameter of the swirl chamber, D_s, with 7.5 mm, is the variable from where everything is calculated. The ratios D_s/D_e are selected as 3 or 1.6. The ratio L_e/D_e to calculate the length of the exit orifice is in respect to the exit orifice diameter is chosen as 0.7, 0.5 and 0.3. The length of the exit orifice (L_e) is calculated from the chosen ratio (0.7, 0.5, or 0.3 (L_e/D_e). The diameter of the exit orifice and the length of the exit orifice are summarised at Table 3-2.

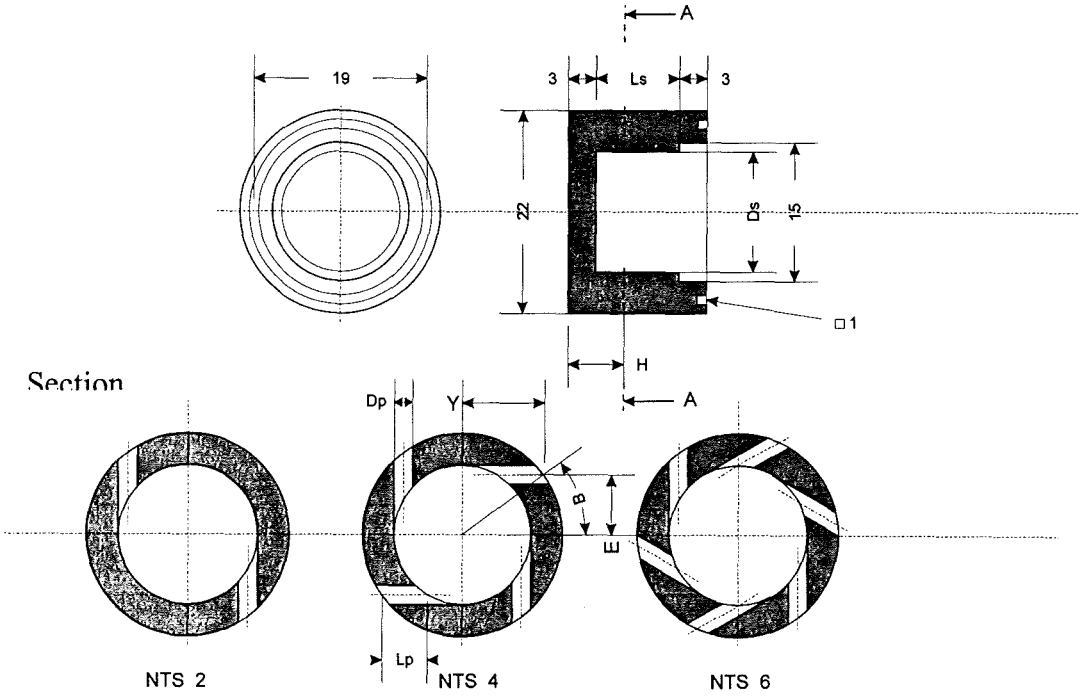

Figure 3-2: Layout of a swirl chamber

Hence, nine different exit orifices were built that can be used in any spray chamber configuration. Each orifice is tapered at an angle of 45° to aid the removal of water from the swirl chamber to the exit orifice. There are 81 different configurations possible with the 9 different swirl chambers.

Table 3-2: Length and diameter of the pressure swirl exit orifice depending on the D_s/D_e and L_e/D_e ratios and the numbering of these configurations

D_s/D_e ratio	D_e mm	L_e at L_e/D_e ratio		
		0.7	0.5	0.3
3	2.5	1.75 (No. **19**)	1.25 (No. **20**)	0.75 (No. **21**)
1.6	4.7	3.29 (No. **25**)	2.35 (No. **26**)	1.41 (No. **27**)

3.2.2 Effervescent atomiser

The effervescent atomiser (Figure 2-7) is a twin fluid atomiser, which needs an extra supply for the atomising air. The effervescent atomiser consists of a main body, a top and bottom cap, an exit orifice and a mixing tube.

The main body is the same as that used for the pressure swirl atomiser. Three threaded holes in the main body accommodate the air supply, the temperature sensor, and pressure sensor. The temperature sensor measures the atomising air temperature just before it is inserted into the liquid. The pressure sensor is mounted at this position to provide the best record of the atomising air pressure to avoid errors due to friction loss in pipes. The atomising air supply is positioned at an angle of 90° to the pressure sensor, so that the momentum of the air is not influencing the result of the pressure sensor.

The top cap has an outside thread so that it can screw into the main body and the use of an 'O'-ring makes it water and airtight. In addition to this Teflon tape was used on the thread. In the centre is a 12 mm threaded hole that accommodates a joint. The joint at the top plate is used to clamp the mixing tube.

The bottom cap has an outside thread that is screwed into the main body to make it water and airtight. The centre has a tight fit sleeve for the mixing tube and additionally a packing ring to prevent air passing by the mixing tube. The exit orifice is mounted in a 4.7 mm deep groove at the outside of the bottom cap and allows a quick and easy change.

The stainless steel mixing tube with an outside diameter of 10 mm is used to induce the air into the liquid stream. The liquid flows through the inside of the mixing tube, where the diameter is 8.8 mm, and the air enters through a hole pattern in the tube. The hole pattern has five rows of four holes and they are 6.4 mm apart along the

where the diameter is 8.8 mm, and the air enters through a hole pattern in the tube. The hole pattern has five rows of four holes and they are 6.4 mm apart along the length of the tube perpendicular to its axis. Each row is rotated 45° from the previous one. The last row is located 51 mm upstream of the exit orifice. Five different air inlet diameters were chosen. The smallest air inlet diameter was 0.5 mm and increased in steps of 0.2 mm up to 1.3 mm.

The notation used for the effervescent atomiser consists of four parts. The first part is a two-digit number that provides information about the exit orifice diameter. The number '47' stands for a 4.7 mm exit orifice. The 4.7 mm exit orifice is the only one that is tested.

The second part is a two-digit number that indicates the size of the air holes. The tested sizes were 0.5 mm and 1.3 mm and are indicated by the digits '05' and '13' respectively.

The third part is the ratio of the length to diameter of the exit orifice. Two different L_e/D_e ratios were manufactured. The ratio L_e/D_e selected for testing were, 0.7 and 0, and hence the notation is '07' and '00'. Part number four is separated by a slash and represents the GLR.

To compare the pressure swirl nozzle and effervescent atomiser performance the same exit orifice diameter was chosen for both nozzles. The L_e/D_e ratios at the effervescent exit orifices were selected as 0.7 and 0 as shown in Figure 3-3. The ratio of 0 was chosen, because it widens the spray angle substantially.

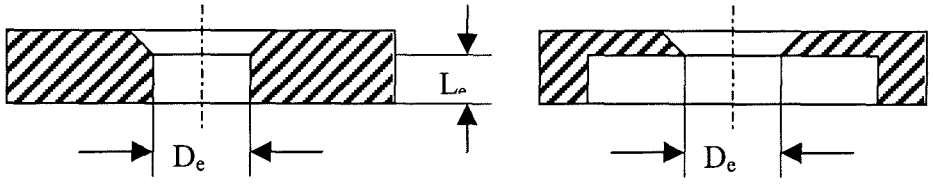

Figure 3-3: Cross section of the exit orifice with the L_e/D_e ratio of 0.7 and 0

3.3 Spray Heat Transfer Test Rig

A schematic diagram of the apparatus used for the spray heat transfer experiments is shown in Figure 3-4. The central component of the test rig is a thermally insulated spray chamber in which an unsaturated hot air stream is brought into direct contact, in overall counter flow, with cold water droplets generated by a single spray nozzle. For these inlet conditions, simultaneous heat and mass transfer occur between the two streams, giving rise to cooling and humidification of the air stream, and the associated heating and partial evaporation of the sprayed water. Measurements of the air stream temperature and humidity at inlet and outlet, together with the air mass flow rate, enable the rates of energy and mass exchange between the two streams to be determined. Additional measurements of the spray water mass flow rate and the liquid temperature rise across the chamber allows the overall energy balance for the test chamber to be checked.

Full descriptions of the spray chamber, the air and water supply systems and the associated instrumentation fitted to the test rig are given in the following sections.

3.3.1 Spray chamber

The spray chamber is constructed from a Perspex cylinder, 372 mm internal diameter and 10 mm wall thickness, mounted with its axis vertical. The height of the cylinder is 382 mm. Aluminium plates of 400 by 400 mm and a thickness of 10 mm close the chamber at both ends. A 5 mm deep circular O-ring groove is machined into both end plates to locate the Perspex cylinder, which leaves an internal height of 372 mm for the cylinder. A clamping device attached to the supporting frame holds the chamber assembly firmly together in order to prevent air or water leakages. The enclosed volume of the chamber is approximately 40 litres.

The spray nozzle under test is installed through the centre of the upper cover plate, pointing downwards along the axis of the chamber. The nozzle is mounted so that its exit plane is recessed 5 mm into the inside surface of the upper cover plate.

The hot air stream supplied to the chamber passes through a 50 mm internal diameter pipe that is connected to an opening at the centre of the lower cover plate. The air supply pipe protrudes 30 mm into the spray chamber, and prevents water running into the supply pipe. A 60 mm diameter baffle located just downstream and directly opposite this opening is profiled, as shown in Figure 3-4, to assist the air to turn through 90° and to pass through a 12.5 mm annular gap as it enters the chamber. The baffle prevents spray droplets from entering the air supply pipe and helps distribute the air over the chamber cross-section; rather than as a central vertical jet flow. The temperature of the entering air is measured by a 3 mm diameter mineral insulated Type K (nickel-chromium/nickel-aluminium) thermocouple probe mounted in the supply pipe approximately 20 mm upstream of the chamber entry.

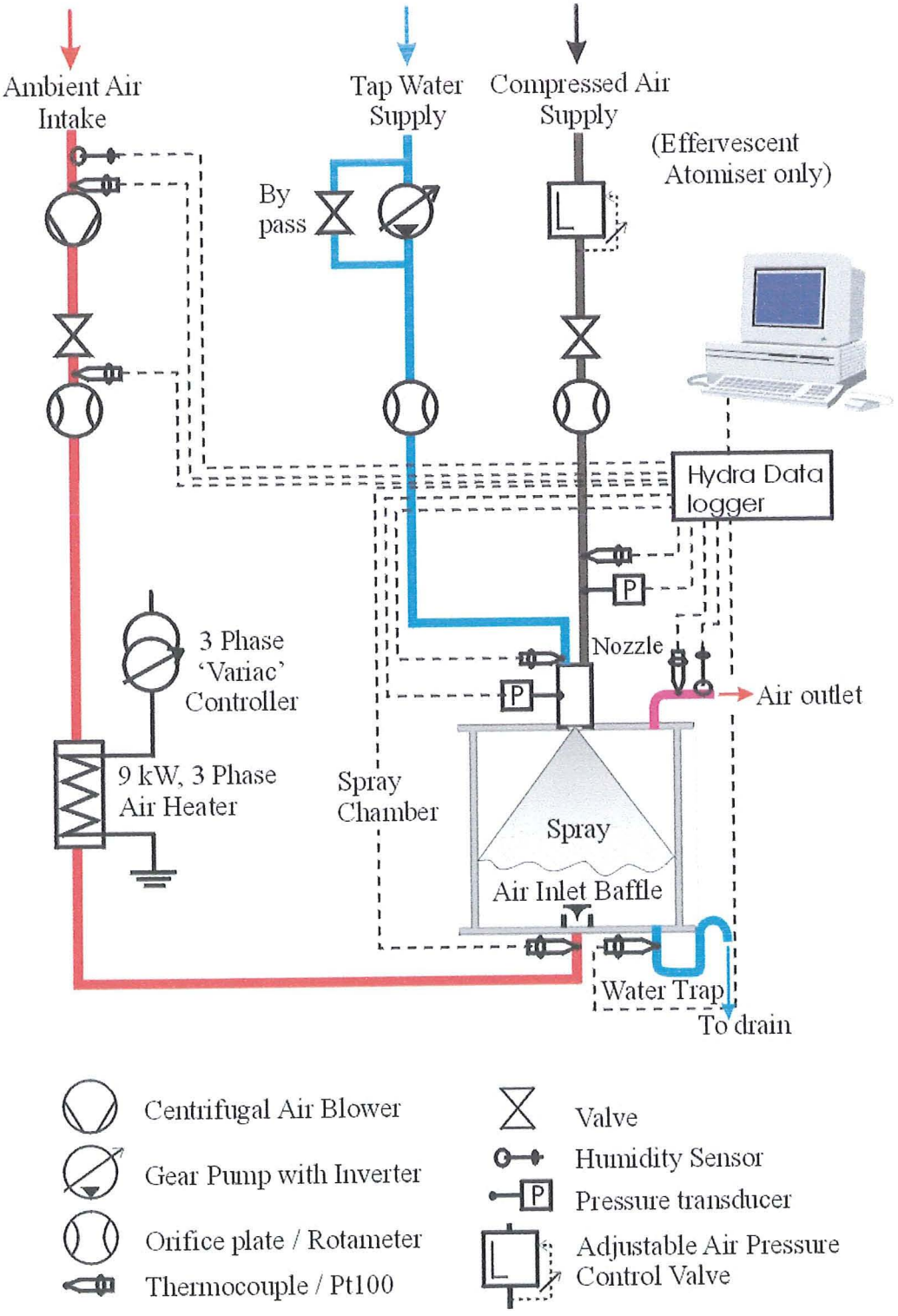

Figure 3-4:Schematic diagram of the test rig with nomenclature of instrumentation

A 50 mm diameter opening is provided in the upper cover plate with its centre located 150 mm from the chamber axis to allow the cooled (and humidified) air to leave the spray chamber. A single hole was the only practical solution due to the location of the humidity sensor. As shown in Figure 3-4, the exiting air passes immediately through

90° bend with a 50 mm internal diameter, before exhausting to atmosphere. A Vaisala HMD30YB digital transmitter probe, incorporating a relative humidity sensor and a platinum resistance element, is fitted in the downstream section of this bend to determine the relative humidity and temperature of the air leaving the spray chamber. The digital humidity transmitter probe and the platinum resistance element are powered by a DC source, which supplies a voltage of 20 V DC with 5mA. The output signal is set for the digital humidity transmitter and the platinum resistance element to 0-10 V DC. The purpose of the 90° bend and the internal vane fitted therein is to eliminate entrained liquid droplets to ensure that they cannot impact on the humidity sensor. The air exit duct offers negligible resistance and hence the pressure inside the spray chamber is effectively equal to the external ambient pressure.

A 50 mm diameter hole in the lower base plate, 150 mm from the chamber axis, allowed non-evaporated water to drain from the spray chamber. A 150 mm deep U-trap was fitted below this outlet to prevent air escaping from the chamber via this route. The outlet temperature of the water was measured by a 3 mm diameter mineral insulated Type K (nickel-chromium/nickel-aluminium) thermocouple probe installed in this water trap. The manufactures accuracy of this thermocouple was ±3% of the measured temperature. To minimise the random error, all K-type thermocouples used in this test rig were tested against each other. Ten K-type thermocouples were tested, from which the five with the smallest deviation to each other were chosen for use on the test rig. During the test the thermocouples were bundled together in such a way that their tips were located within a one cubic centimetre volume. All thermocouples were connected to the Hydra Data Logger, which was set to a scanning rate of 5 seconds. This was the fastest scanning rate for the Hydra Data Logger and was chosen to detect which thermocouples had the fastest response time.

Tests were performed successively in ice water with a temperature of approximately 0°C, in water at an ambient temperature of 20°C, and finally in boiling water. The maximum deviation of the thermocouples was ±0.1°C at all three temperatures. The five thermocouples selected for use on the test rig had a maximum deviation of ±0.05°C. The error was reduced to ±0.2°C and repeatability of ±0.1°C.

To minimise heat losses from the spray chamber, the exposed external surfaces are thermally insulated. The cylindrical surface of the spray chamber is wrapped with three layers of polystyrene foam sheets. Each of the sheets has a thickness of 2 mm, which results to an overall thickness of approximately 6 mm. A 25 mm thick polystyrene foam sheet insulation covers the top and bottom plates completely. Please see section 3.3.6. All polystyrene foam sheets have a thermal conductivity of k=0.036 W $m^{-1}K^{-1}$.

3.3.2 Air flow system

The hot air pipe is used to provide a constant heated and measured air into the spray chamber. This system consists of a blower with HANSEN 2-phase motor, an orifice plate, a butterfly valve, a Vaisala HMD30YB digital humidity sensor, and a 9 kW air heater. Steel pipes with 50 mm inside diameter and threaded ends connect these items.

A Vaisala HMD30YB digital transmitter probe, incorporating a relative humidity sensor and a platinum resistance element, is fitted at the intake of the blower to determine the relative ambient humidity and temperature of the air entering the air flow system. The voltage supply source and the output settings are identical to the previously described digital transmitter probe and platinum resistance element. The blower supplies 2.5 kg air min^{-1} of ambient air. A HANSEN 2-phase 0.5 kW AC motor drives the blower. An orifice plate, manufactured to BS 1042 standard, is used to measure the mass flow rate of the air. The butterfly valve gives the option to adjust the airflow. The design of the orifice plate and the calculation of the mass flow rate follow the British Standard 1042 Section 1.1.

The inlet air was heated up to the required temperature in an air heater. The 9 kW air heater was controlled by a variac that is connected to a 3-phase supply. The power input to the heater was not measured, because the main interest was to adjust the air temperature to a required value.

3.3.3 Water flow system

On the frame of the test rig the gear pump with associated motor was mounted. A 0.5 kW 3-phase motor was connected to a frequency inverter. An adjustable flow rate can be achieved with the control of frequency. The motor was connected to the gear pump via a plastic coupling. This type of pump was chosen because of the ability to pump water and to have a specific mass flow rate of water independent of pressure. This pump provided a steady flow that did not oscillate. The mass flow rate was adjusted between 1 to 15 kg min^{-1}. The maximum pressure difference was limited to 6 kPa and the maximum flow rate to 15 kg min^{-1}. The flow rate was measured by a flow meter that operates in the range of 2 – 20 kg min^{-1} and has an accuracy of ±2% of full-scale divisions and a repeatability of ±1%. The UCC rotameter, type FR5000 series, order number 361-0212 and 361-0228 were calibrated by measuring the mass flow through the rotameter. The mass flow rate was preset and a container, which was placed on a scale, was filled with water. The time needed to fill the container with the measured mass of water was used to calculate the accuracy of the rotameter. These tests were performed and repeated for various mass flow rate to determine the accuracy and the repeatability. Pulsation of the flow rate was averaged. The results are presented in Table 3-4.

The water and air (at effervescent atomiser) pressure was measured at the nozzle body. Two Druck PDCR 810 pressure sensors with a silicon diaphragm, operating between 0 - 0.7 MPa gauge, are used for this purpose. The accuracy of this pressure sensor was ±0.5% and the repeatability ±0.1% full scale division. The water and air (at effervescent atomiser) temperature was taken by two stainless steel mineral insulated K-type thermocouples at the nozzle body.

Table 3-3: Configuration, input and output of connected channels to Hydra Data Logger

Channe 1	Measurement	Setting
1	Upstream air temperature at orifice plate	Thermocouple K-type, °C
2	Air temperature at spray chamber entry	Thermocouple K-type, °C
3	Air temperature at spray chamber exit	Thermocouple Pt 100, °C U =0 - 10 V DC Temp =10 U + 20 [°C]
4	Humidity of air at spray chamber exit	V DC U = 0 -10 V DC Humidity = 10 U [%]
5	Water temperature at nozzle body	Thermocouple K-type, °C
6	Water pressure at nozzle body	V DC U = 0 - 0.1 V DC Pressure = 35 U + 1,01325
7	Water temperature at spray chamber exit	Thermocouple K-type, °C
8	Pressure of atomising air in the effervescent atomiser	V DC U = 0 - 0.1 V DC Pressure = 70 U + 1,01325
9	Temperature of the atomising air	Thermocouple K-type, °C
10	Humidity of ambient air	V DC U = 0 -10 V DC Humidity = 10 U [%]
11	Temperature of ambient air	PRT 100, °C U =0 - 10 V DC Temp =10 U + 20 [°C]

U stands for the expected voltage signal that will be used at the functions predefined at the user manual of the Hydra Data Logger to convert reading to physical values, e.g., V DC into °C.

3.3.4 Data acquisition system

A portable programmable Hydra Data Logger, which could record up to 20 channels, was used to record the readings of the instrumentation at 30 seconds intervals. The Hydra Data Logger incorporates a cold junction compensation for thermocouples, which are pre-calibrated by the manufacturer. It was possible to display and switch through all of the channels during the experiments. Every channel had to be configured separately and the set-up during experiments is shown in Table 3-3. Additionally it is possible to insert a linear function, m x + b, so that the data could be displayed as real values (e.g. VDC converted to relative humidity [%]). The data logger operates at 240 Volt and is connected via a RS232 to an IBM 286 computer located next to the test rig. This computer was used to download and store the data from the Hydra Data Logger. Readings were taken every 30 seconds and recording started as soon as steady state temperature conditions at air outlet were reached. To judge when steady state was reached the last air outlet temperature reading was subtracted from the actual air outlet temperature reading. If the difference was smaller than 0.1°C then recording was started.

3.3.5 Measurement uncertainty estimates

The minimum and maximum error of the instrumentation is between ±0.2% and ±3%. The list below shows the instruments used and their error as supplied by the manufacturers. Only the flow meter and the thermocouples are calibrated to minimise the random error and to validate the accuracy given by the supplier. The thermocouples as well as the flow meter lay inside the accuracy supplied by the manufactures. The humidity sensors have been tested against each other and had an accuracy of ±0.2% of the measured relative humidity and ±0.3°C for the temperature readings of the PT-thermocouples. For the remaining instrumentation no facility to measure the accuracy within the lab was available.

Table 3-4: Summary of instrumental errors

Thermocouples K-Type: PTR 100:	±3% between 0 to 100°C of measured temperature ±0.2°C Accuracy of electronics of measurement ±0.02 °C/°C (typical) Temperature dependence of measurement
Pressure transducer Druck 810 range of $\Delta p \leq 600$ kPa (at 20°C)	±0.5% FS total error over a temperature range of 0 to 50°C of measurement
Humidity sensor Vaisala HMD30YB 0-100% RH digital	±2% RH (0...90% RH) of measurement ±3% RH (90...100% RH) of measurement
UCC Rotameter, FR5000 Series order no. 361-0212 range 0.2–2.0 kg min^{-1} order no. 361-0228 range 2.0–20.0 kg min^{-1}	±2% Accuracy Full Scale Division (FSD) ±1% Repeatability FSD
Orifice plate (homemade) with a range of $\Delta p \leq 9807$ Pa (at 20°C)	±0.5 mm H_2O U-tube monometer

3.3.6 Heat loss estimate

The heat loss of the spray chamber is calculated for air inlet temperatures of 80° and 150°C to determine how significant the heat loss is for the result. The average outlet temperature of the cylinder at steady state droplet-gas heat transfer for an inlet temperature of 80°C is approximately 40°C and for 150°C approximately 55°C. The Perspex tube and the insulated outside surface of the aluminium top and bottom plates are the objects of this calculation including the insulation of these parts. Other losses are neglected. The total heat loss is derived from the sum of these three objects as follows.

$$Q = Q_T + Q_{TP} + Q_{BP} = 2\pi k_T \Delta T H_T R_T + k_{TP} \Delta T A_{TP} + k_{BP} \Delta T A_{BP} \qquad [93]$$

The overall heat transfer for the radial steady conduction through the wall of insulated Perspex tube, k_T, is calculated with the following equation

$$\frac{1}{k_T} = \frac{1}{2\pi r_{Pi} h_{iT}} + \frac{\ln\left(\frac{r_{Po}}{r_{Pi}}\right)}{2\pi k_P} + \frac{\ln\left(\frac{r_{So}}{r_{Po}}\right)}{2\pi k_S} + \frac{1}{2\pi r_{So} h_{cT}} \quad [94]$$

and the overall heat transfer for the steady conduction through the top and bottom plate, k_{TP} and k_{BT}, is calculated with the following equation (Kuchling (1989))

$$\frac{1}{k_{TP}} = \frac{1}{h_{iT}} + \frac{t_A}{k_A} + \frac{t_P}{k_S} + \frac{1}{h_{cTP}} \quad [95]$$

$$\frac{1}{k_{BP}} = \frac{1}{h_{iT}} + \frac{t_A}{k_A} + \frac{t_P}{k_S} + \frac{1}{h_{cBP}} \quad [96]$$

where $k_P = 0.19$ W m^{-1} K^{-1} represents the thermal conductivity at 20°C for the Perspex tube, $k_S = 0.036$ W m^{-1} K^{-1} at 20°C is the thermal conductivity for the polystyrene, and $k_A = 220$ W m^{-1} K^{-1} at 20°C the thermal conductivity for the aluminium plates. The inside radius of the Perspex cylinder is $r_{Pi} = 185$ mm and the outside $r_{Po} = 195$ mm. The inside radius of the insulation is the same as the outside radius of the cylinder and the outside radius of the insulation is $r_{So} = 201$ mm. Polystyrene sheets with a thickness of $t_P = 25$ mm are used to insulate the aluminium top and bottom plates with a thickness of $t_A = 10$ mm. The convection heat transfer coefficient for inside the cylinder is given by $h_{iT} = 70.0$ W m^{-2} K^{-1} and the outside of the tube is $h_{cT} = 10$W m^{-2} K^{-1}. The convection heat transfer coefficient for top and bottom pate is $h_{cTP} = h_{cBP} = 10$ W m^{-2} K^{-1}. Kuchling (1989) reports these standard values for convection heat transfer coefficients. The radiation in all cases is neglected because it is insignificantly small and has virtually no influence on the measured data.

The result of the heat loss for the inside temperature of 80°C is $Q_{80} = 40$ W and for 150°C the heat loss is $Q_{150} = 87$ W. Both results are based on a 20°C ambient air temperature. The heat loss can be considered as the small compared, 0.8% to 1.7%, with the droplet-gas heat transfer at the inside the cylinder.

3.3.7 Time to steady state

Some judgement was required to determine steady-state conditions. Approaching the steady-state condition from both directions (heating-up and cooling-down) verified the time to reach a steady temperature achieved in the spray chamber. To determine this time, the spray nozzle was started while the inlet air was not heated. The air heater was pre-set to heat up the inlet air to 150°C when activated. Simultaneous manual activation of the air heater and data logger gave the information of the duration needed to reach steady-state conditions when the spray chamber is heated up while the spray nozzle is operating. The error here was a maximum of 1 second. The scanning rate of the data logger was set to 1 per 30 seconds as used later in the experiments. After thirty-eight scans the temperature did not change any more for the particular nozzle configuration tested (27b25) and was therefore considered to be the steady state temperature. The temperature at this point was 28.1°C. The injection of spray droplets into the spray chamber was stopped and the recording of the data logger stopped. The spray chamber was heated up to about 80°C before the same water flow rate to the spray nozzle and the data logger were simultaneously activated. The air heater was not altered. The reason to start the injection of water droplets at 80°C was that the Perspex tube of the spray chamber started to deform at higher temperatures. Thirty-eight scans were made to find out that the steady state temperature was 28.3°C. The difference between cooling down and heating up the spray chamber is therefore 0.2°C and is within the uncertainty limits of the used thermocouples reported in Table 3-4.

This test showed that the maximum time to reach a steady state temperature from extreme conditions is 19 minutes and that the difference of the steady state air temperature leaving the spray chamber is not influenced from which direction the steady state temperature was approached. The result of the test is shown in Figure 3-5. This preliminary test does not influence the later results, but it was essential for of the experimental programme planning.

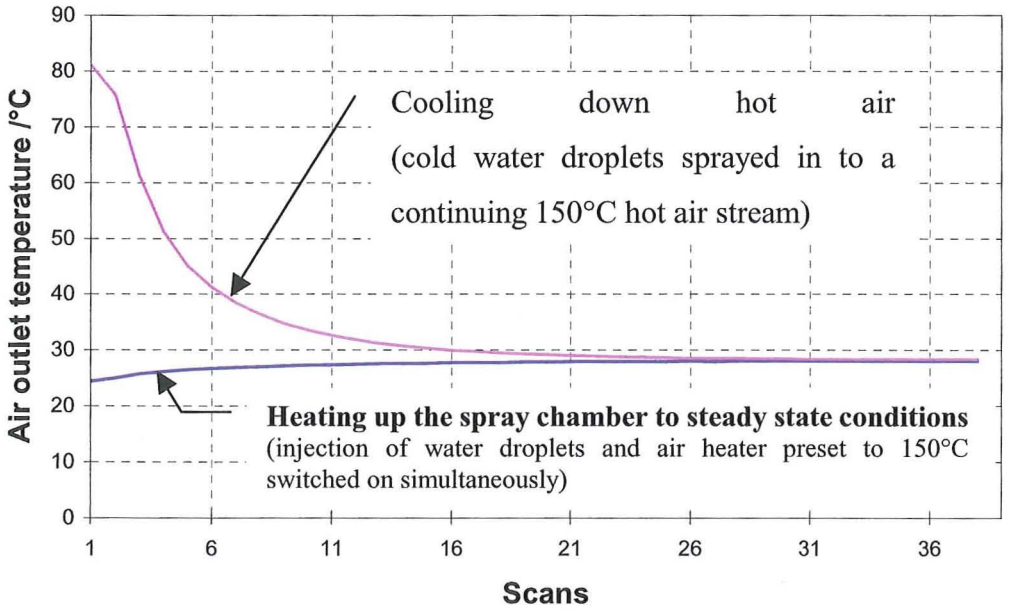

Figure 3-5: Heating up and cooling down curve vs. scans at 30 seconds intervals

3.4 Droplet Size Measurement

3.4.1 Introduction

Spray quality can be assessed using information about droplet size, velocity, and distribution. Different measurement techniques are available. The employed technique must:

- Not disturb the atomisation process.
- Be able to measure diameters in a dynamic range size of 30:1.
- Measure the spatial and temporal distributions of the spray.
- Use a high sample rate. At least 5000 droplets (build in function of the LPDA software) should be sampled to determine a representative statistical mean diameter.
- Be independent of the liquid, gas, and ambient conditions.
- Be able to provide a fast analysis of the collected data, as repeating of measurements may not be possible

None of the existing techniques listed below are able to fulfil all of the above mentioned points. The spatial sampling involves the measurement of droplets within a constant volume for a given time. The temporal sampling describes the measurement of drops that passed through a fixed area in a certain plane. It is not possible to use techniques where the droplets are collected for a spray with high density, because the overlapping of the droplets leads to a false measurement. This also happens if a technique is used where the droplets can coalesce.

Lefebvre (1989) described various techniques that have been developed for this purpose. These can be grouped into three categories:

- Mechanical Methods
  - Collection of Drops on Slide
  - Cascade Impactors
  - Collection of Droplets on Cells
  - Molten Wax Technique
  - Drop Freezing Technology
- Electrical Methods
  - Wicks-Dukler Technique
  - Wire Techniques
- Optical Methods
  - High Speed Photography
  - TV Image Scanning Spray Analyser
  - Holography
  - Single-Particle Counter Methods
  - Light-scattering interferometry
  - Large Off-Axis Light Scattering Technique
  - Phase/Doppler Particle Analyser (PDPA)
  - Intensity Deconvolution Technique

Phase/Doppler Particle Analyser (PDPA)

The use of lasers opened new possibilities for measurement techniques. Instead of using short-pulsed laser beams to take pictures of droplets, a continuous laser beam is used to determine droplet size and velocity. The intersection of two laser beams is the measurement volume. A sphere that is passing through this volume reflects the light in other directions and lowers the intensity of the laser beam according to the Lorenz-Mie theory.

A beam-splitter splits a laser beam into two coherent beams of equal intensity and parallel polarisation. A lens is used to cross the beams at a predefined distance. The crossover of these beams is the measurement region called the interference fringe region. Droplets passing through this region change the intensity of the laser beams. The Gaussian intensity profile of each laser beam is measured and a correlation is used to determine the droplet size and velocity of the sampled particle. The limitation of this technique described by Bachalo and Houser (1984) is the on-axis forward light detection which set limits to the measured spray density. Another limit is reported by Uhlenwinkel et al. (1990), who mentioned that this technique is limited to a dynamic range size of 10:1 at droplet size measurements.

Instead of measuring the intensity of the laser beam, Bachalo (1984) measured the intensity of the scattered light of the control volume. This scattered light results from the refection of the laser beams on the transparent surface of droplets after the Lorenz-Mie theory. If a droplet crosses a beam, the beam is scattered within the droplet and part of the light is redirected. This redirected light is measured and its intensity describes the size and velocity of the droplet. A collection lens mounted at a 30° off-axis angle is used to focus the scattered light on the photomultimeter, which registered the droplets signals (see Figure 3-6). The velocity of the particle is then determined by the Doppler frequency and the droplet size is obtained from of the intensity of the scattered laser beam.

For the PDPA, the instrumentation measuring the light scatter to determine the droplet size and velocity is a similar arrangement to the Large Off-Axis Light Scattering Technique. The difference of this technique is the receiver instrumentation, which is placed at a 30° off-axis angle in relation to the main angle of the two crossing beams. The receiver consists of a collecting lens that focuses the scattered fringe pattern to an opening called an aperture. The focused fringe pattern expands after the aperture and

three detectors record the phase shift of the Doppler burst signal. The spatial and temporal frequencies of the scattered light are measured. Each detector records and filters the signal to remove the pedestal components and now has the Doppler burst signal. The phase shift for each of the three provides the information on the droplet size and velocity of the droplet.

This technique is able to measure droplet sizes in the range of 5 μm to 3000 μm, with different optical lenses. One lens setting for measuring droplets has a dynamic range size of 35:1. Hence, droplet diameters ranging from 10 μm to 350 μm can be measured with one optical arrangement. The accuracy of this technique is ±1% for the droplet size and ±0.2% for the mean droplet velocity. The size of the Doppler burst signal depends on the diameter of the laser beam. In our case the diameter of the laser beams was 1.1 mm and crossed at an angle of 3.2° and resulted in a 19.7 mm long oval-shaped fringe region. The height of the fringe region needs always be larger then the droplets measured.

Summary points of the PDPA technique:

- It does not disturb the atomisation process
- A continuous laser beam is used to measure droplet size and velocity
- The Gaussian intensity correlation is used to determine the droplet size and velocity of sampled particles
- Different volume locations can be accurately specified for measurement
- Three detectors are used for recording and filtering the signal to remove the pedestal components

The same technique was use by Wan et al. (1995), Lefebvre (1991), Richter and Walzel (1990), and Uhlenwinkel et al. (1990) and many others.

3.5 Supplementary Test Equipment

At a later stage of this work a Phase Doppler Particle Analyser (PDPA) became available. The PDPA was used to measure the droplet size of 4 different pressure swirl nozzle configurations, which were used for the numerical model. The reason for measuring these four configurations was that the results of the numerical model did

not agree the experimental results for lower water injection pressure. The analysis of these measurements leads to the conclusion that Leferbvre's equation [20] to calculate the droplet size gave results that are on average 30% too high. To confirm this conclusion it was necessary to measure the droplet size of the four configurations at each water pressure differential across the nozzle used in the experiments and simulations. The results of the measurement are then used for the Inlet-Data-File for the computational model. The results are also compared with the empirical equation [20] developed by Lefebvre.

3.5.1 Phase doppler particle analyser

A HeNe PDPA from Aerometrics was used for this part of the experimental program. A PDPA 2100 with a XMT145-2 10 mA Transmitter and a RCV2100 Receiver was used. A 500 mm focus lens was used that allowed a 30° forward scatter to measure the droplet size range of 7.5 to 374 μm. Particle velocity up to 194 m/s can be measured and the standard deviation of the measured velocity is given. The software for the Real-Time Signal Analyser System is a DataVIEW package and permits a user screen set-up. The software provides for four different mean diameters, which are the D_{10}, D_{20}, D_{30}, and D_{32}. These mean diameters are displayed Probe Volume Corrected (PVC) and Non-PVC. Probe Volume Corrected means that particles that pass the probe volume near the edges are not counted as a valid sample.

The optical components are situated on an L-shaped bench, which has a height of approximately 1 metre. The water collection system was designed so that air leaves to the side of the water collection system (see Figure 3-7) and does not influence the measurement. Hence, re-circulation of small water droplets into the probe volume is prevented and does not influence the measurements. The nozzle was held in a constant position relative to the probe volume. Figure 3-6 shows the top view of a principal set-up of a PDPA and the instrumentation. On the left hand side of the hollow cone spray pattern is the transmitter. The transmitter houses the laser, beam splitter and lens. The experimental measurement point of the droplets of the hollow cone spray pattern is indicated in Figure 3-6. Figure 3-7 shows the side view of the experimental arrangements of the PDPA and the water collection system.

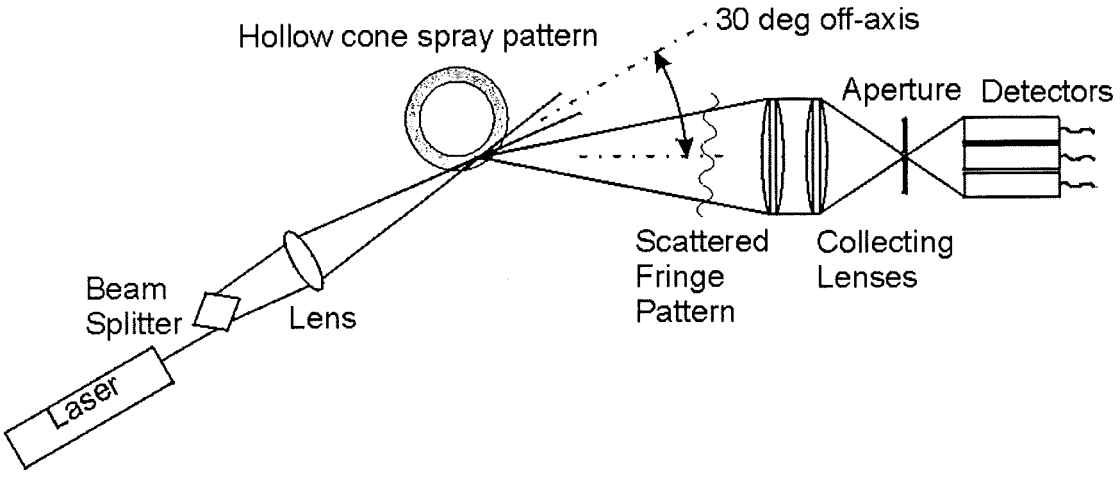

Figure 3-6: Top view of PDPA assembly and outlining the measurement point of the hollow cone spray pattern

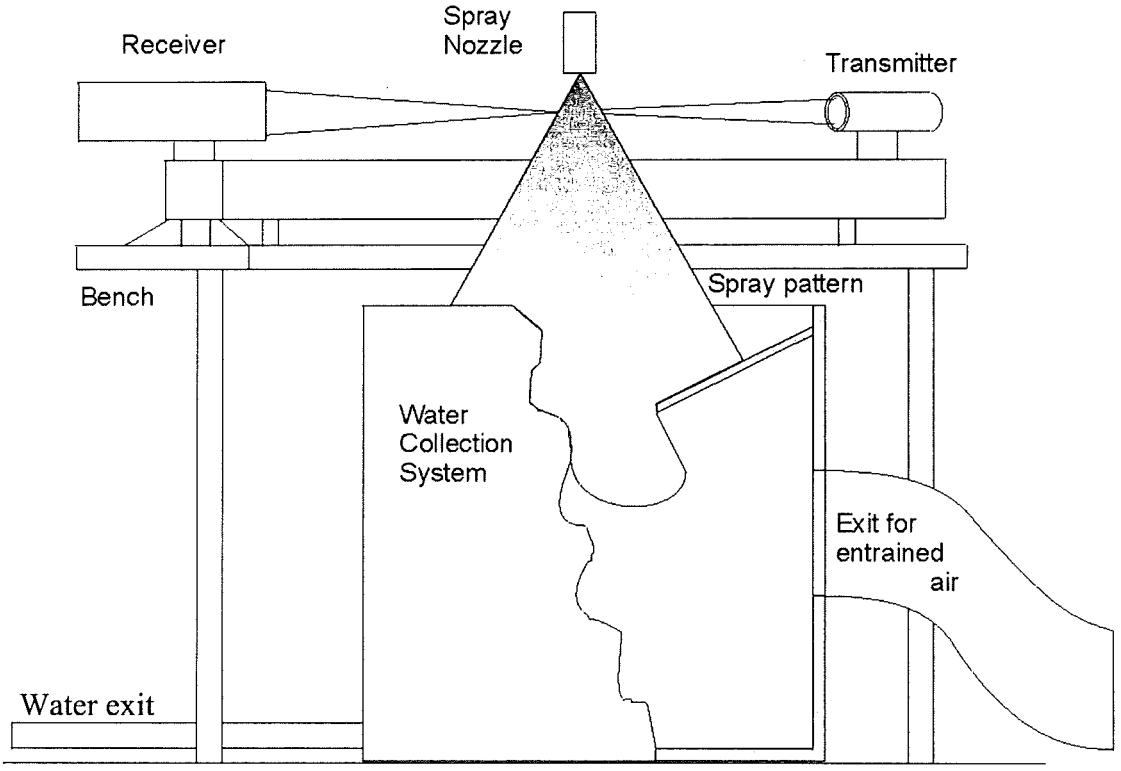

Figure 3-7: Side view of the PDPA and the assembly of the water collection system

After aligning the optical components and software settings the following nozzle configurations were tested:

9a20	27a20
9a26	27a26

The droplet size was measured in a free stream 40 mm below the exit orifice. Every configuration was tested at 200 to 600 kPa absolute pressure in steps of 100 kPa. Every pressure point was measured a minimum of 5 times and if the change was larger than 2% then up to 13 times. The uncorrected results of SMD and the mean velocity of each measurement were transferred to an EXCEL spreadsheet and an average calculated.

3.5.2 Spray cone angle measurement

The spray angle was measured from a digital photograph, which was then transferred onto a PC. The software Paint Shop was used to determine for each pressure setting and configuration the x-y position of the spray angle. The spray angle is measured at its outer boundaries as shown in Figure 3-8. To overcome problems of the vertical alignment of the pressure swirl nozzle a software package that gives X and Y co-ordinates of the mouse pointer was used. The mouse pointer was placed on the edge of the visible spray cone and the co-ordinates were notified. This procedure was repeated four times. With these co-ordinates it was possible to calculate the outer mean spray angle and detect its variation with the water injection pressure.

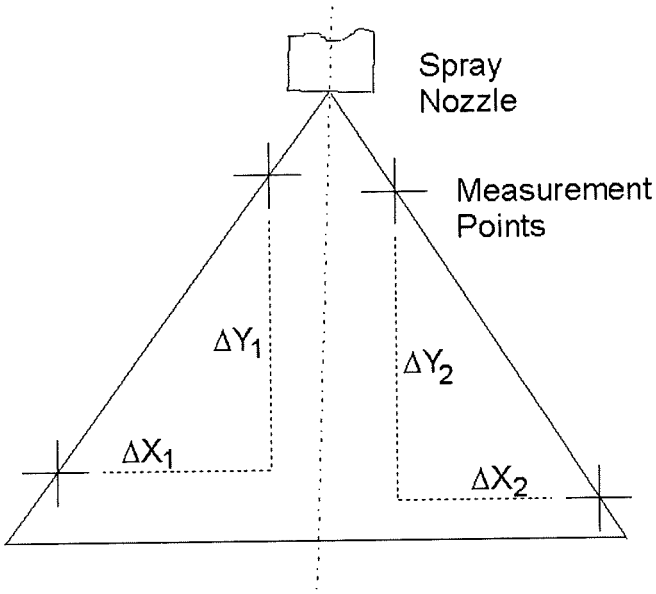

Figure 3-8: Principal of spray angle measurement

3.6 Experimental program

A preliminary investigation allowed testing of the most important nozzle configurations. Therefore, not all the nozzles built were tested. Preliminary tests have shown that the results of the swirl chamber of the pressure swirl nozzle with four tangential inlet slots is in-between the swirl chamber with two and six tangential inlet slots. The same observation was made for the exit orifice with the diameter of 3.4 mm.

Table 3-5: Experimental program of the pressure swirl nozzle

Spray chamber No.			Exit orifice D_e = 2.5 mm & L_e/D_e ratio			Exit orifice D_e = 4.7 mm & L_e/D_e ratio		
			0.7	0.5	0.3	0.7	0.5	0.3
			No. 19	No. 20	No. 21	No. 25	No. 26	No. 27
9	NTS=2	**a** (L_s=6 mm)	**80°C** **150°C**	**80°C** **120°C** **150°C**	**80°C** **150°C**		**80°C** **120°C** **150°C**	
9	NTS=2	**b** (L_s=4.5 mm)	**80°C** **150°C**	**80°C** **150°C**	**80°C** **150°C**			
9	NTS=2	**c** (L_s=3 mm)	**80°C** **150°C**	**80°C** **120°C** **150°C**	**80°C** **150°C**		**80°C** **120°C** **150°C**	
27	NTS=6	**a** (L_s=6 mm)		**80°C** **120°C** **150°C**		**150°C**	**80°C** **120°C** **150°C**	**150°C**
27	NTS=6	**b** (L_s=4.5 mm)				**150°C**	**150°C**	**150°C**
27	NTS=6	**c** (L_s=3 mm)		**80°C** **120°C** **150°C**		**150°C**	**80°C** **120°C** **150°C**	**150°C**
28	NTS=3	**c** (L_s=3 mm)		**150°C**			**80°C** **150°C**	**150°C**
29	NTS=3	**c** (L_s=3 mm)		**150°C**			**80°C** **150°C**	**150°C**

The experimental program for the pressure swirl nozzle is shown in Table 3-5. Not all configuration possibilities for the pressure swirl nozzle are shown. At the top of the columns is the diameter of the exit orifice, the ratio of L_e/D_e and their number. On the left side of the rows is the number and the length of the spray chamber (indicated by a, b or c). The numbers (80, 120, 150) indicate at which inlet air temperature the configuration was tested. The swirl chamber configuration 28c and 29c were modified at a later stage to investigate the effect of shorter tangential inlet slots and a change of the tangential inlet area.

Each configuration at constant air inlet temperature is tested for five different absolute water pressure settings. Mao (1991) reported that an increase above 500 kPa water pressure does not reduce the droplet size significantly and it only leads to a smaller droplet distribution. Therefore, the absolute water pressure setting are from 100 kPa up to 500 kPa in steps of 100 kPa. These configuration possibilities lead to 300 different test runs, which were performed.

There was also a preliminary test carried out for the effervescent atomiser, which resulted in the conclusion that only the exit orifice with the diameter of 4.7 mm and the inner tube with the diameter of 0.5 mm and 1.3 mm were chosen. All other configurations between these two did not show a significant difference of the results compared to the next closest configuration. The exit orifices with the length to diameter ratio of 0.7 and 0 have been chosen.

The chosen configurations are tested at three different air/liquid ratios, which are 0.025, 0.050 and 0.100. The water pressure is varied from 100kPa up to 250kPa in steps of 50kPa. The air inlet temperature was held constant at 150°C throughout the tests.

The variations of the settings on the test rig for pressure swirl and effervescent atomisers can be seen in Table 3-6.

Table 3-6: Variations of the settings for pressure swirl and effervescent atomiser

Test rig settings at the pressure swirl nozzle

Name	Symbol	Value	Units
Water pressure	p_w	1.0 - 5.0	10^5 Pa
Water mass flow rate	$\dot{m}_w$	0.033 – 0.218	kg/s
Air inlet temperature	T_{al}	80 – 150	°C
Hot air mass flow rate	$\dot{m}_a$	0.044	kg/s

Variation of the internal geometry of the pressure swirl nozzle

Swirl chamber diameter	D_s	7.5	mm
Swirl chamber length	L_s	3 – 6	mm
No. of tangential inlets	NTS	2 – 6	-
Exit orifice diameter	D_e	2.5 – 4.7	mm
Exit orifice length	L_e	0.75 – 3.29	mm

Test rig settings at the effervescent atomiser

Name	Symbol	Value	Units
Water pressure	p_w	1.0 - 5.0	10^5 Pa
Water mass flow rate	$\dot{m}_w$	0.033 – 0.218	kg/s
Air inlet temperature	t_{al}	80 – 150	°C
Hot air mass flow rate	$\dot{m}_a$	0.044	kg/s
Atomising air pressure	P_{aw}	1 – 2.5	10^5 Pa
Atomising air flow rate	$\dot{m}_{aw}$	0.018 – 0.094	kg/s
Atomising air temperature	T_{aw}	app. 24	°C

Variation of the internal geometry of the effervescent atomiser

Air inlet holes	D_{ai}	0.5 – 1.3	mm
Exit orifice diameter	D_e	4.7	mm
Exit orifice length	L_e	0.0 – 3.29	mm

Chapter 4 Experimental Results and Analysis

4.1 Introduction

This chapter presents the experimental data, derived results and their analysis for the pressure swirl nozzle and the effervescent atomiser. Furthermore, the results of the droplet size and the spray angle measurements are shown.

Firstly, the experimental data and the derived results for the pressure swirl nozzle are presented and analysed. Secondly, the experimental data and the derived results for the effervescent atomiser nozzle are presented and analysed. Thirdly, the results of the droplet size measurement are shown and compared with an empirical equation for four different pressure swirl nozzle configurations that are later used for the CFD model. Finally, the measured spray angle of these four configurations is presented and compared with an empirical equation. The experimental data are taken from the experimental apparatus described in Chapter 3. An EXCEL spreadsheet was used to analyse the data. A description of the spreadsheet structure and a list of the equations used are presented in the appendix C.

The decrease of the air temperature is the result of evaporation and heat transfer into the liquid medium. The heat transfer process takes place partly at the surface of the droplets and the falling water film. The rate of the heat transfer and evaporation of the droplets and the falling water film is not discussed in this chapter. The main emphasis is the total heat and mass transfer within the spray chamber. Experimental data and derived results of the hot air measurements are presented here. The test rig was designed and the instrumentation chosen and calibrated to measure the properties of:

- Hot air
  - temperature difference
  - humidity difference
  - mass flow rate
- Water
  - flow rate
  - temperature difference
  - pressure difference across nozzle

- Atomising air - flow rate
  - pressure
  - temperature
- Ambient air - ambient air pressure
  - humidity
  - temperature

The range covered by the experimental data is as follows:

Medium	Temperature / °C		Mass flow rate / kg/s		Differential pressure / MPa	
	min.	max.	min.	max.	min.	max.
Water	12	20	0.033	0.210	0.1	0.5
Hot Air	80	150	Const. 0.044		none	
Effervescent air	≅ 24		0.018	0.094	0.1	0.25

The results for each nozzle configuration were calculated on an EXCEL-spreadsheet consisting out of the following four worksheets:

CODE: Scanned values from the data logger are pasted. Graphics for each channel allows a first overview of the results to check for conspicuous measurement errors. All five different water pressures tested at one nozzle configuration are included.

VALUES: Main worksheet where all the averages are calculated and imported results are shown. The start and the end of a constant pressure stage were updated. Data collected manually during the test, e.g. mass flow rate of water and nozzle configuration, are inserted at the top. The results on the worksheet values show temperature and temperature differences of air and water as well as the mass transfer rate of water vapour and mass flow rates of all media. This data was used to calculate the energy transfer rates for each medium and the total from air to water.

CONFIGURATION: Relevant data and the configuration of the test rig are implemented in this worksheet. All internal dimensions of the nozzle configuration are stated here and can be changed on demand. Important dimensional and non-dimensional nozzle parameters are calculated here to complete the information of the current configuration.

CALCULATION: The mass and volume flow rate of air calculated following BS1042 Section 1.1 as well as the calculation of necessary values, e.g. vapour pressure, specific humidity, and saturation temperature, of air and water for the energy balance is calculated on this worksheet.

4.2 Pressure swirl nozzle

The most important measurement of these tests was the temperature difference of the air between inlet and outlet and the mass flow rate of injected water. The mass flow rate of injected water was dependent on the nozzle configuration and water pressure.

First tests for pressure swirl nozzles were performed at air inlet temperature of 80°C and 150°C. Figure 4-1 shows the nozzle configuration, e.g. 9a20, followed by the tested temperature separated by a slash. These temperatures were chosen to investigate the influence of air inlet temperature on the result. Figure 4-1 presents the air temperature difference achieved with the configuration 9a20 and 27a26 for varing mass flow rate of injected water at two different inlet temperatures.

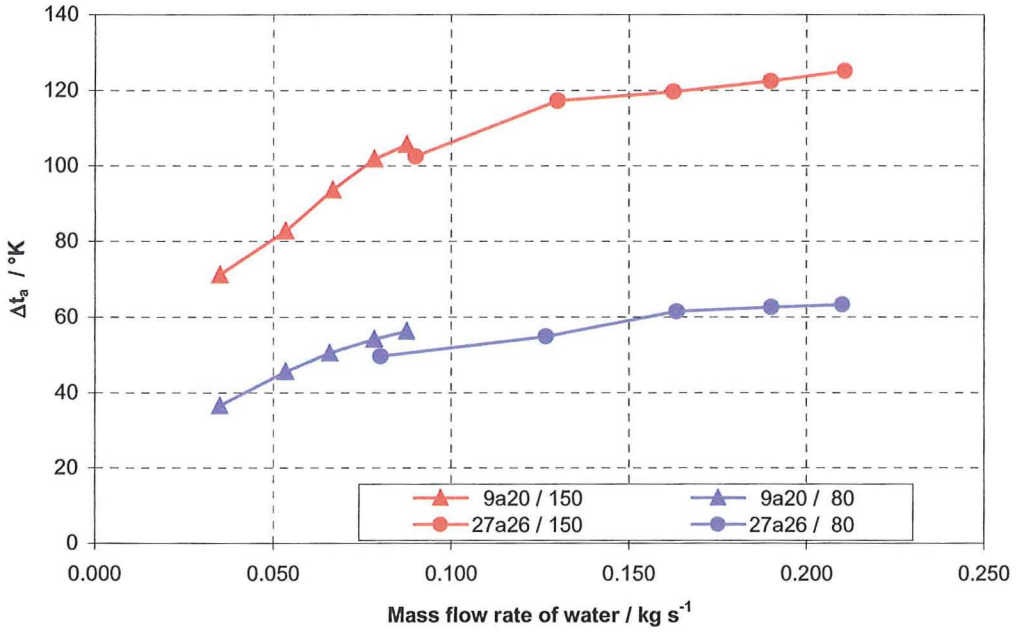

Figure 4-1: Influence of different air inlet temperatures

Each configuration was tested at the same pressure drop range across the nozzle ranging from $1x10^5$ Pa to $5x10^5$ Pa in steps of $1x10^5$ Pa. The nozzle configuration

with the orifice number 26 (27a26) had a higher transfer rate at the same water pressure. All tests performed with 150°C have approximately twice the temperature difference as at 80°C. A higher temperature difference between the surrounding gas and water droplets causes larger energy transfer. The error of the instrumentation, in relation to the measured temperature difference is smaller.

Measuring the humidity difference between in and outlet conditions of the air determined the evaporation rate of the water. Two humidity sensors, described in Chapter 3, were used to determine the evaporation of the water. The analysis is focussed on the evaporation across the spray chamber and not the evaporation in the boundary layer of the droplet. The heat and mass transfer between water droplets and air depends on the temperature and the saturation of the surrounding air. Different mass and heat transfer regions are known and can be found in the literature (Incropera and De Witt, 1990).

If the air temperature is above the saturation temperature and below the saturation point, see Figure 4-2, part of the water droplet can evaporate until the saturation point is reached.

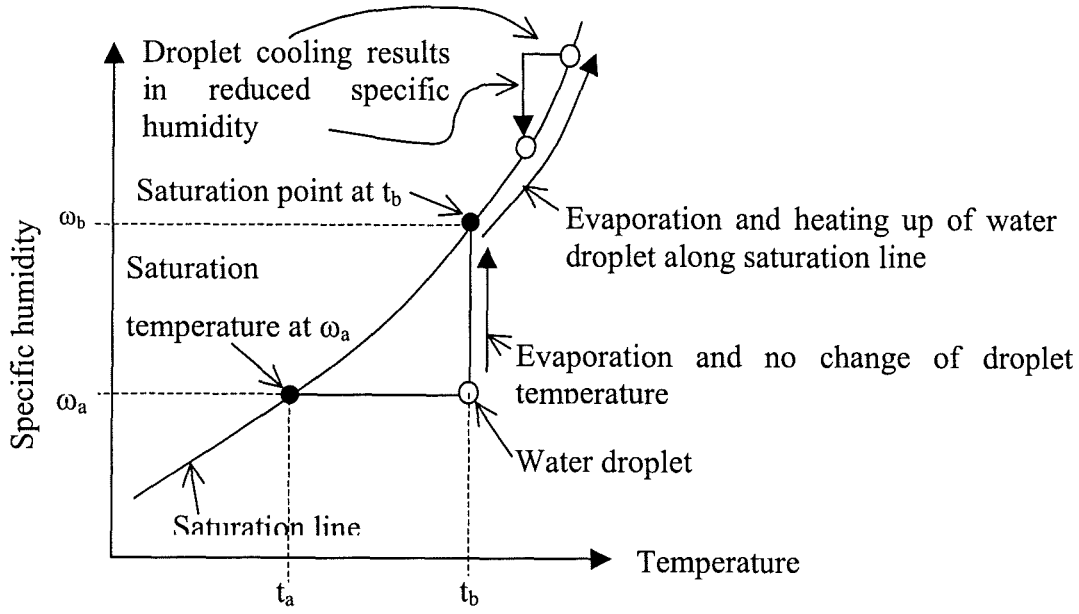

Figure 4-2: Change of the specific humidity depending on the droplet temperature

If the liquid continues to evaporate and the saturation point is reached, the latent heat, which is used to evaporate the liquid, is now used to increase the water droplet

temperature and evaporate the droplet until energy equilibrium is reached. The droplet is now "moving" on the saturation line as it is shown in Figure 4-2.

The decrease of temperature of saturated air results in condensation. Below its saturation temperature the vapour condenses out onto the cold water droplets and cold surrounding objects. This is also shown in Figure 4-2.
If the pressure of the saturated vapour is decreased a homogeneous condensation or fog formation is the result. Small water droplets are formed and suspended in the air. With an increase in mass, the droplets are dominated by the gravity rather then the flow field suspended in.

During the experiments, it was found that some of these conditions, evaporation and condensation of droplets, existed simultaneously inside the spray chamber. At first, the hot air enters, see Figure 4-3, at the bottom of the spray chamber. The airflow was perpendicular to the spray chamber axis and the air was flowing towards the Perspex wall. Droplets with a larger spray angle were hitting the wall; others travelled the distance to the bottom plate. Therefore a continuous falling water film created by the water droplets covered the Perspex wall. The liquid was relatively cold compared to the hot air. At a temperature difference of approximately 120°K and a specific humidity far below the point of saturation, evaporation of the liquid occurred. At this location evaporation of liquid from the falling water film and the droplets took place.

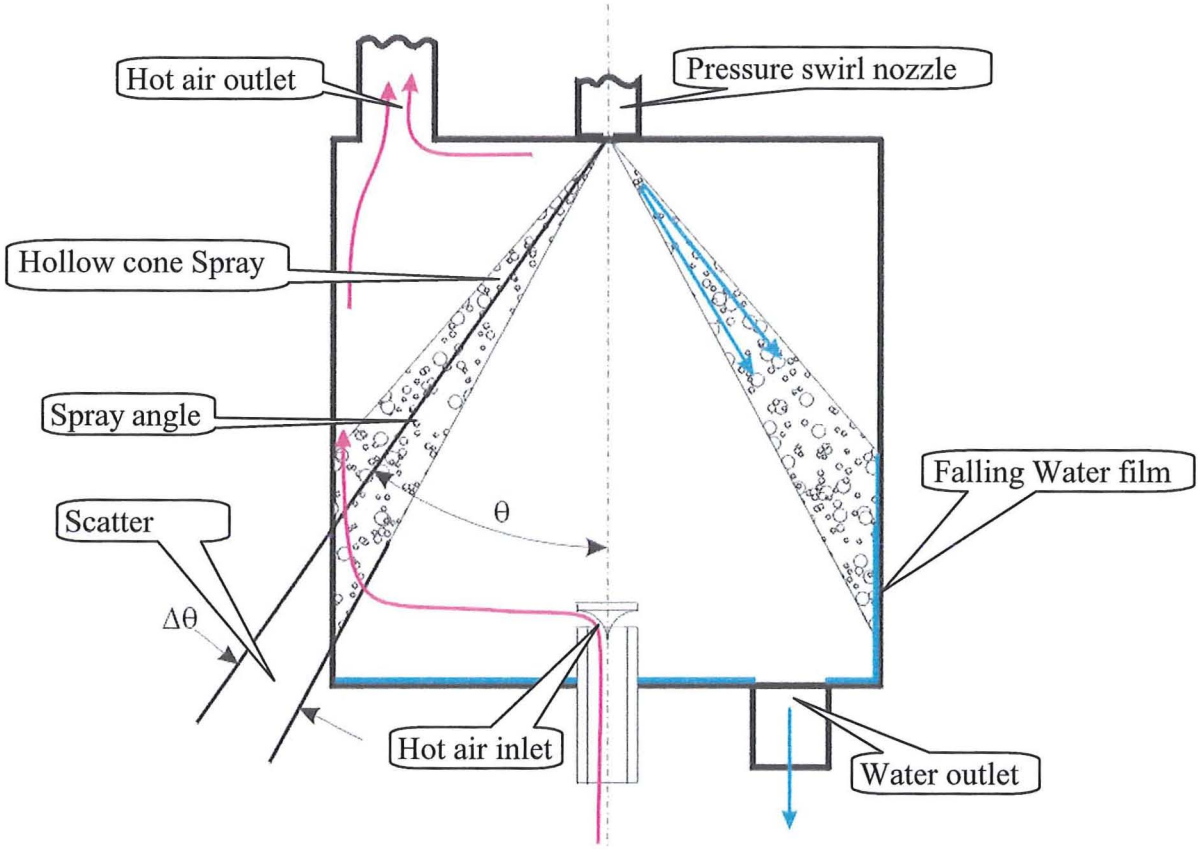

Figure 4-3: Diagram of the air and water flow in the spray chamber including the description of the Spray angle and the scatter of the spray angle

Inside the spray chamber with an operating nozzle the pressure was approximately 200 Pa above ambient air pressure. At certain conditions, high water flow rates and small droplet sizes, the air leaving the spray chamber is fully saturated because of the effective cooling of the air. A pressure drop of 200 Pa after the outlet of the spray chamber caused a homogeneous condensation of the vapour inside the down stream section where the humidity sensor was located. The humidity sensor took these small water droplets as vapour and measured humidity above 100%. Understanding the physics described above explains why the reading is incorrect and should be treated as 100%.

At low water flow rates, the cooling of the air is not so high that the saturation point is reached. The relative humidity at exit increases with the water pressure. Two effects taking place by increasing the water pressure are: a) the amount of water flow rate is increased, b) smaller droplets with a higher velocity are produced. This results in an increased water surface area because of the smaller droplets and the higher

mass flow rate of water. Also, due to the higher mass flow rate of water the droplet velocity is increased. The change of the spray angle is relatively small compared with the difference between various nozzle configurations.

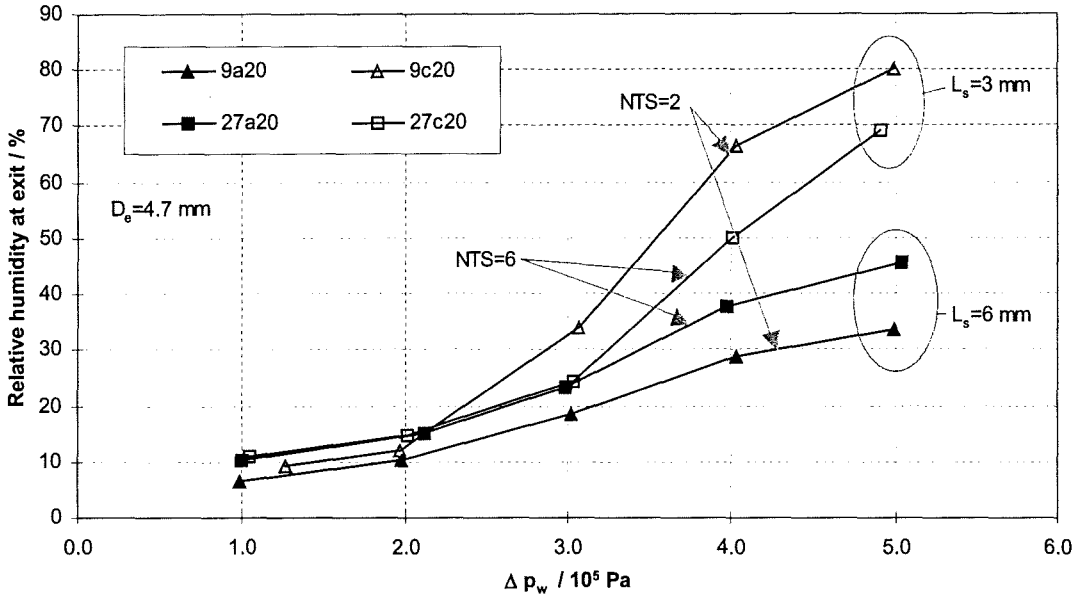

Figure 4-4: Relative humidity vs. pressure drop across nozzle for the configurations 9a/c20 and 27a/c20

The number of tangential slots at the swirl chamber has an influence on the evaporation. In Figure 4-4 it can be seen that the air at the spray chamber exit with the nozzle configuration 9c20, two tangential slots and a spray chamber length of 3 mm, has a higher relative humidity than the configuration 27c20, six tangential slots and a spray chamber length of 3 mm. After deriving the specific humidity and plotting it against the mass flow rate of water, in Figure 4-5, is it clear that the configuration with six tangential slots has an advantage. The spray emerging from the nozzle with six tangential slots provides a higher rate of evaporation. The reason for this is that the spray is more evenly distributed. The droplet velocity at both nozzles configuration, with two and six tangential slots, is identical because of the same cross sectional area. Figure 4-5 shows that similar configurations have similar specific evaporation rates.

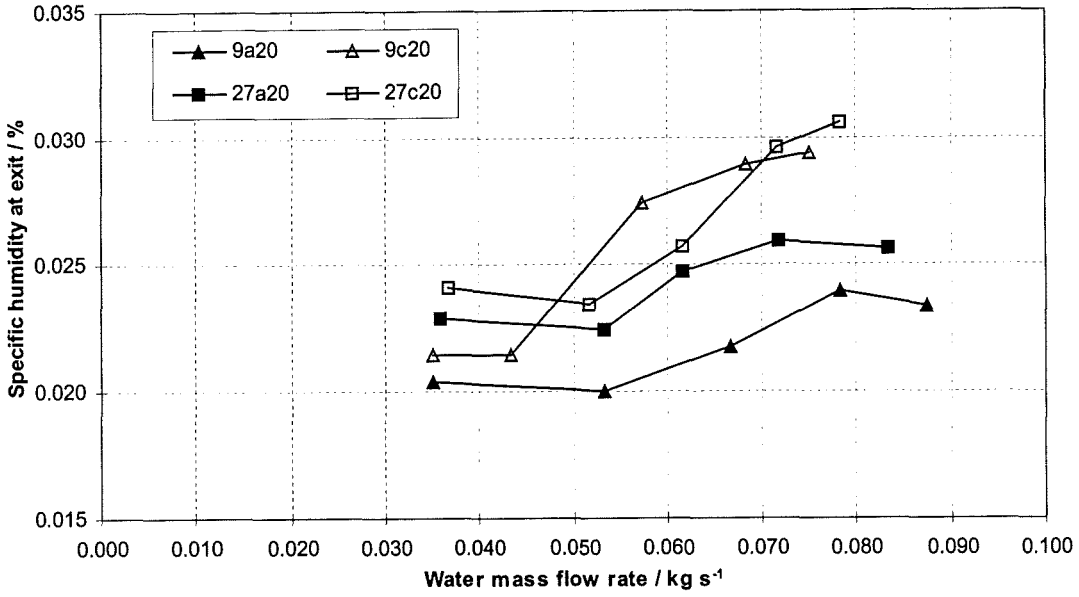

Figure 4-5: Specific humidity vs. water mass flow rate for the configuration 9a/c20 and 27a/c20

The reason for the different relative humidity is due to air outlet temperatures from the spray chamber. The relative humidity depends on the air outlet temperature, especially at high specific vapour contents. Figure 4-6 shows the saturation lines vs. air temperature from 100% down to 20% in steps of 20%.

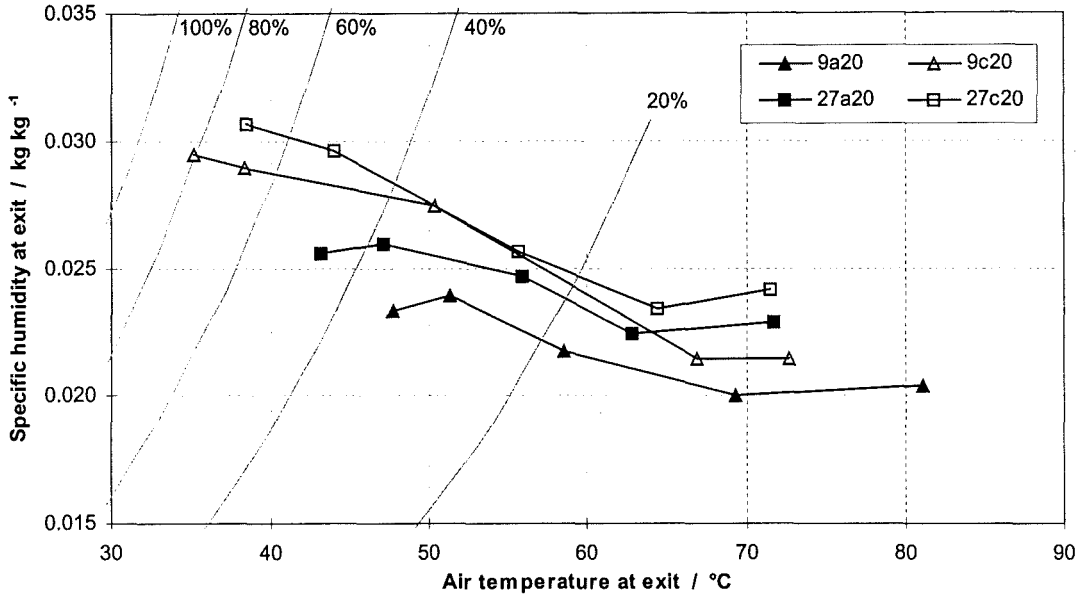

Figure 4-6: Specific humidity vs. air outlet temperature for the configurations 9a/c20 and 27a/c20 with saturation lines from 100% to 20% in steps of 20%

At the lowest temperatures the configuration 9c20 and 27c20 have a humidity difference of 0.002 kg H_2O/kg dry air and a temperature difference of 3°C. This is

enough for the 9c20 configuration to give a 10% higher relative humidity even if the specific humidity is less. Following the examples given before, the air does not leave the spray chamber fully saturated and droplets can evaporate until the air has left the spray chamber. The pressure drop of the air did not lead to homogeneous condensation.

Two exit orifice diameters with three different lengths to diameter ratios were tested on different swirl chambers. The exit orifice diameters were 2.5mm (19, 20, 21) and 4.7mm (25, 26, 27). The length to diameter ratio range is from 0.3 (19/25), 0.5 (20/26) to 0.7 (21, 27). The length to diameter ratio has an influence at a low-pressure drop across the nozzle. The experimental data for configuration 27b25/26/27 are presented in Figure 4-7.

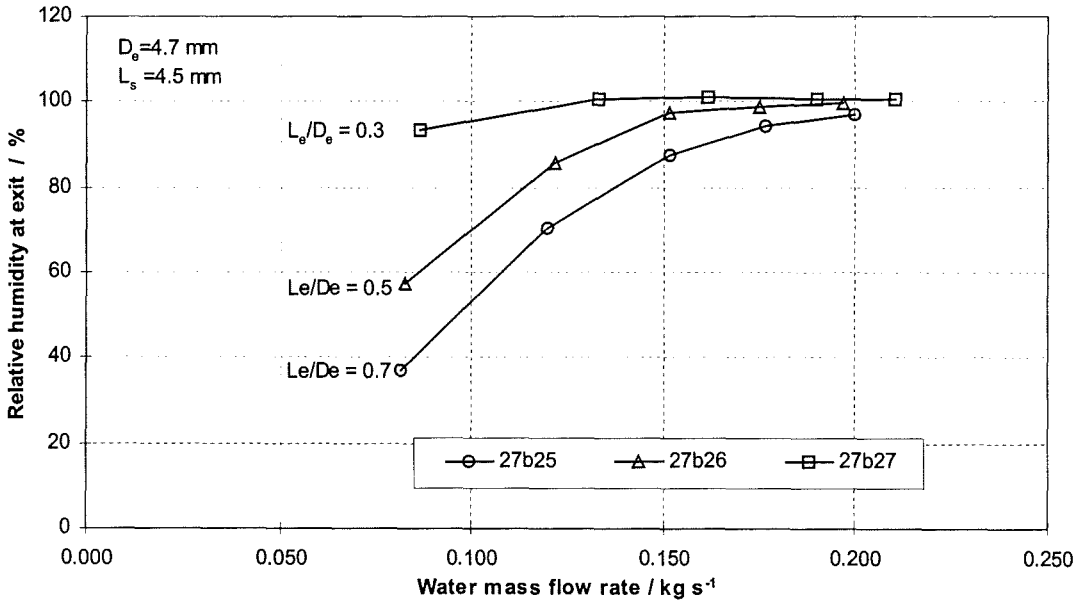

Figure 4-7: Relative humidity vs. water mass flow rate for configuration 27b25/26/27

There is a clear indication of a difference in relative humidity at low mass flow rates of water. At a water mass flow rate of approximately 0.2 kg/s, which is between 4 to 5 bar water pressure across the nozzle, the relative humidity values are close to each other. At low water flow rates, the air outlet temperature causes the difference in relative humidity. As Figure 4-8 shows, the specific vapour contents for all 27b nozzle configurations at low water flow rates, which are at the highest temperature,

are within ±0.002 kgH_2O/kg dry air. The specific humidity is limited by the saturation point of the air. This saturation point depends on the air temperature and the pressure. The air exit temperatures at configuration 27b25 and 27b26 are above the saturation point.

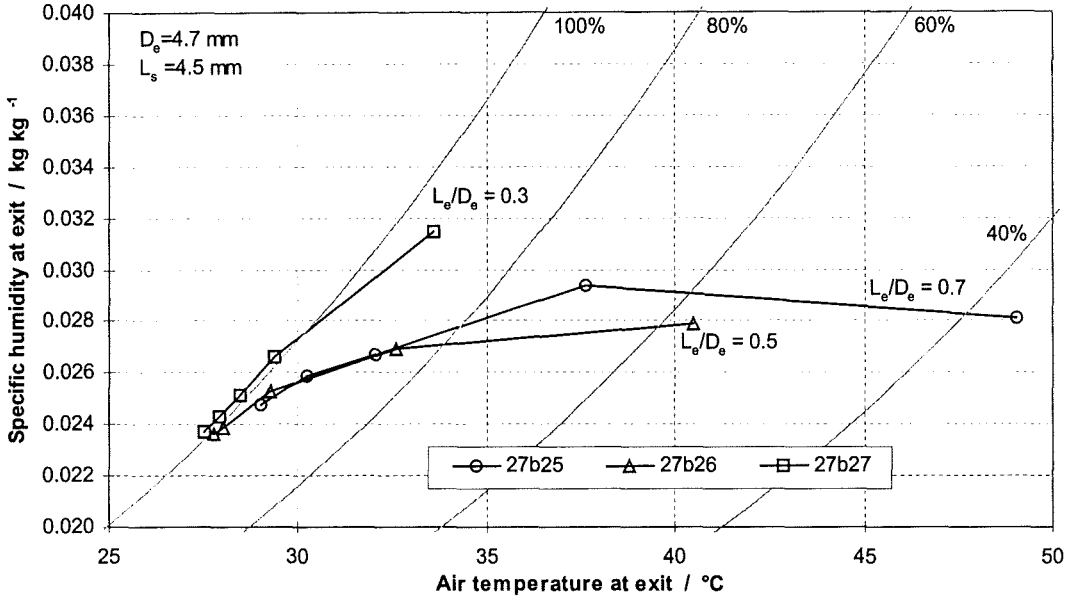

Figure 4-8: Specific humidity vs. water mass flow rate for configuration 27b25/26/27 with saturation lines

The air outlet temperature at configuration 27b27 is cooled down so much that the saturation point is reached before the air leaves the spray chamber. It is impossible to determine where inside the spray chamber the air reaches this point. The pressure drop at the spray chamber exit produces homogeneous condensation. The small water droplets carried within the air causing a false reading of the humidity sensor. The size of the droplets could not be determined because at this time the LPDA system was not available. A shield placed perpendicular to the airflow at the exit was used to collect the water droplets and stop their distribution in the lab. The transparency was located approximately 10 cm behind the air exit at ambient conditions. The shield got wet after being placed in the air stream and the collected water was drained.

From observations of how the rig performed the following improvements were made. Modifications of the swirl chamber geometry led to the manufacturing of the

configuration 28c and 29c since the preliminary analysis indicated that a nozzle with 6 tangential slots operated more satisfactorily than one with 2 tangential slots.
A swirl chamber 27c, which had 6 tangential slots, was modified. Instead of the 6 tangential slots only 3 tangential slots are inserted. This configuration was then called 28c. The reason was to half the tangential inlet area because to have the same kinetic energy at a smaller mass flow rate of liquid. This forms a thinner water film leaving the exit orifice and results in smaller droplets.

The swirl chamber 29c has the same three tangential slots as the configuration 28c and additionally a centred hole. With this centred hole the inlet area is the same as for the configuration 27c. The nozzle configuration 29c produces due to the centred hole, independent of the exit orifice, a full cone spray pattern.

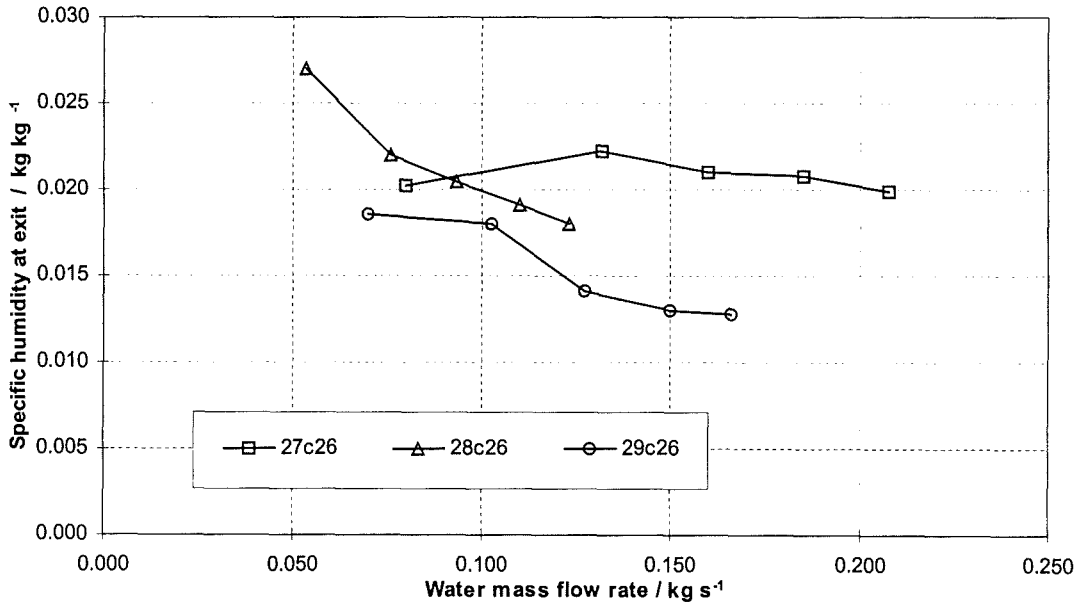

Figure 4-9: Specific humidity vs. water mass flow rate for configuration 27/28/29c26 at air inlet temperature of 150°C

Figure 4-9 shows the specific humidity of the air at the spray chamber exit versus the mass flow rate of water. The differences between these three nozzle configurations are the inlet area and number of tangential slots. In nozzle configuration 28c26 the tangential inlet area is halved compared with the nozzle 27c26. The reduction of the inlet area does not reduce the mass flow rate by the same amount. The mass flow rate of water is 33% higher than the half of the flow rate of the configuration 27c26. This

leads to an increase of the velocity through the tangential slots. Due to the higher velocity and the smaller amount of water, the liquid sheet emerging from the exit orifice is thinner compared with the configuration 27c26. The thinner liquid sheet disintegrates into smaller droplets that produce a larger surface area for the heat and mass transfer. The smaller droplets have a higher initial velocity that affects the Reynolds number. Due to the change of the Reynolds number and the droplet size the heat transfer coefficient is increased. The increased Nusselt number and the larger droplet surface area leads to a higher heat and mass transfer between the water droplets and the surrounding air. In a hollow cone spray these droplets are relatively close together, because all droplets have the same initial spray angle. For these test runs, there is approximately an 8% deviation from the initial spray angle. This is a relatively small volume compared with the rest of the spray chamber. The configuration 29c26 has, due to the axial centre hole in the swirl chamber, a full cone nozzle and means that all the volume of the spray cone is used for heat and mass transfer.

The comparison of the full cone nozzle (29c26) with the hollow cone nozzle (28c26) with a fitted exit orifice of 4.7 mm and a length to diameter ratio of 0.5 in Figure 4-10 indicates that the full cone nozzle has better cooling results. One reason for that is the 32% higher mass flow rate of water passes through the centre hole and causes a full cone spray. The ratio of spray droplet per unit volume is increased and results in a higher heat and mass transfer for the droplets.

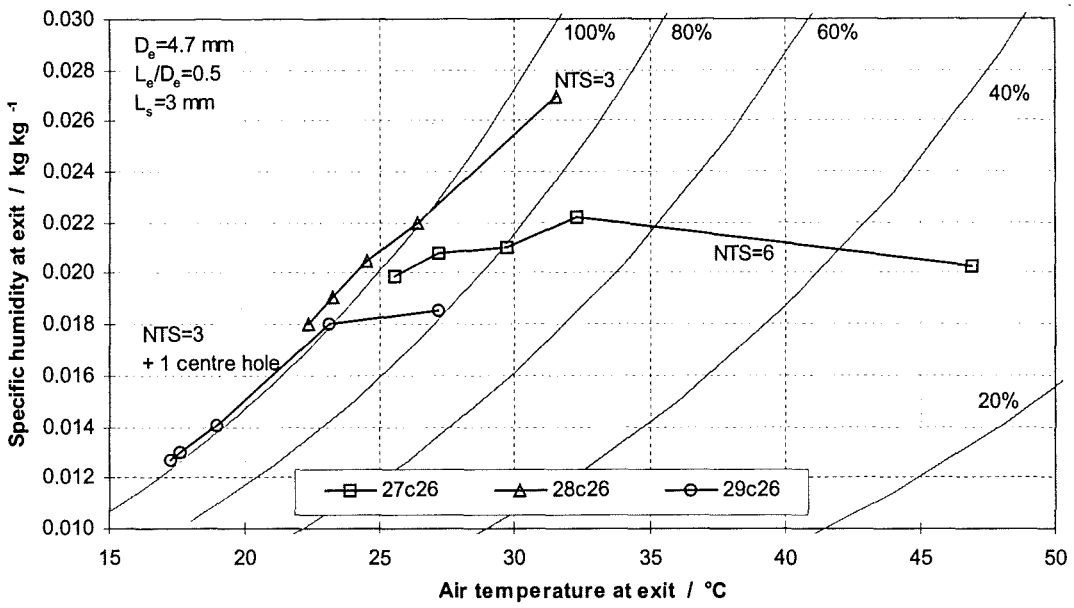

Figure 4-10: Specific humidity vs. air temperature at exit for configuration 27/28/29c26

An error of ±3°C for the air inlet temperature during the test runs can lead to false conclusions by just observing the air outlet temperature. The air temperature difference is used to determine the correct cooling caused by the nozzle and is therefore the basis of further calculations. The best nozzle configuration derived from the experimental data is shown in Figure 4-11. As mentioned before, a short length at the swirl chamber with six tangential inlets and the exit orifice with a short length to diameter ratio shows an advantage compared with the other configurations. The reason is a reduction of the friction loss. The friction loss is reduced due to a smaller internal wetted surface of the pressure swirl nozzle.

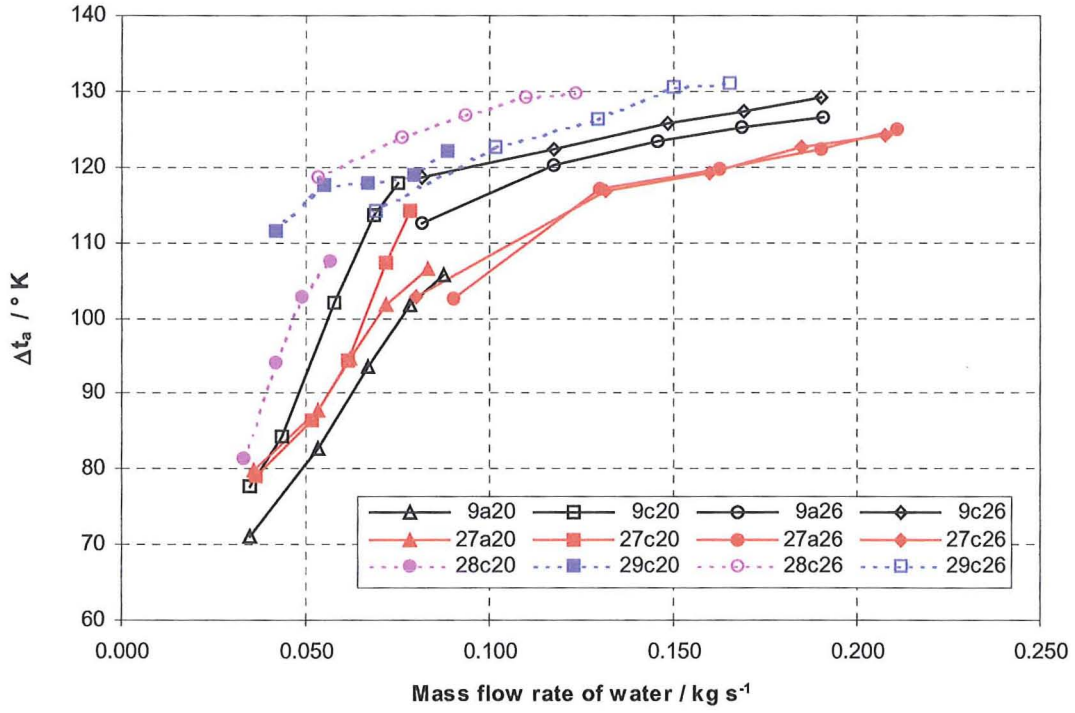

Figure 4-11: Comparison of best pressure swirl nozzle configuration

The specific energy transfer rates for one kilogram of water was calculated by dividing the steady state energy transfer by the used mass flow rate of water.

Figure 4-12 indicates the specific energy transfer rates for one kilogram of water at a certain mass flow rate per nozzle. The power requirements to increase the pressure drop across the nozzle grow more rapidly than the heat transfer rates to the spray droplets. From this it is possible to calculate how many nozzles are needed to achieve this energy transfer. The reduction here is from 29 down to 5 nozzles.

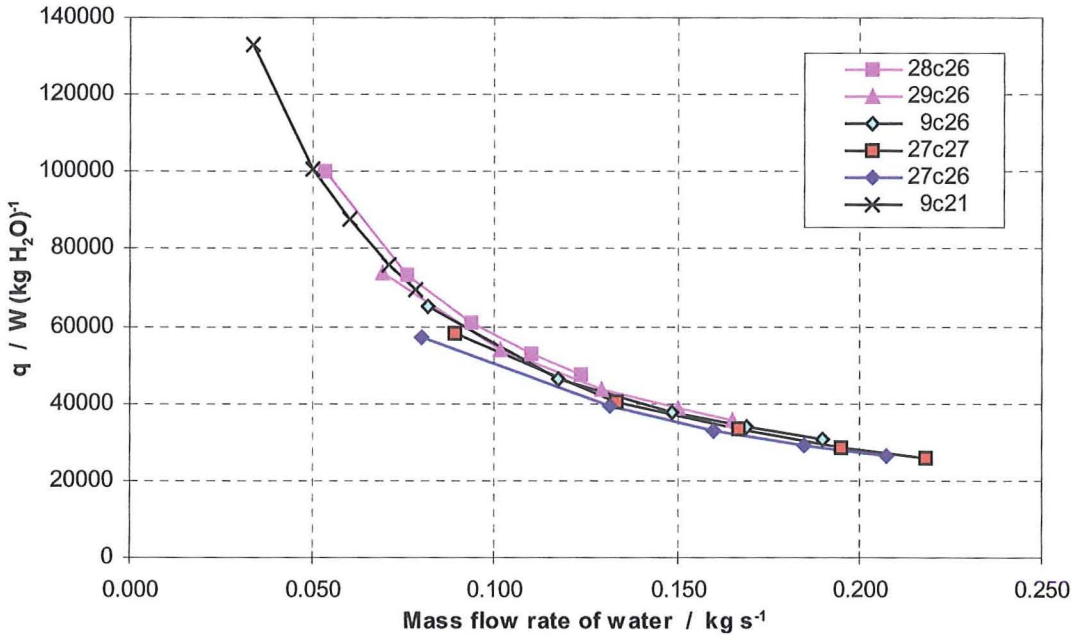

Figure 4-12: Specific heat transfer rate per kilogram/s water vs. the mass flow rate of injected water

The effectiveness of the direct contact counter-flow heat exchanger based on the energy loss of the hot fluid over the injected mass flow rate of water is shown in Figure 4-13 which was calculated with the following equation.

$$\eta = \frac{T_{ai} - T_{ao}}{T_{ai} - T_{wi}} \qquad [97]$$

The effectiveness strongly depends on the air inlet temperature, t_{ai}. It shows that the best results for the standard nozzle are achieved with the configuration of the shortest length of the swirl chamber and exit orifice with the smallest length to diameter ratio. It is obvious that the nozzle with six tangential inlets obtains a higher effectiveness than the nozzle with two tangential inlets. The special configuration 29c27, which produces a full cone spray pattern, is better than 29c26 and is the best tested configuration. The result of the configuration 28c27 is better than the standard configuration and has, due to a lower mass flow rate of injected water, a lower effectiveness than the 29c27 at the same water injection pressure. Both cases confirm the conclusion that a short length of the exit orifice is the best configuration.

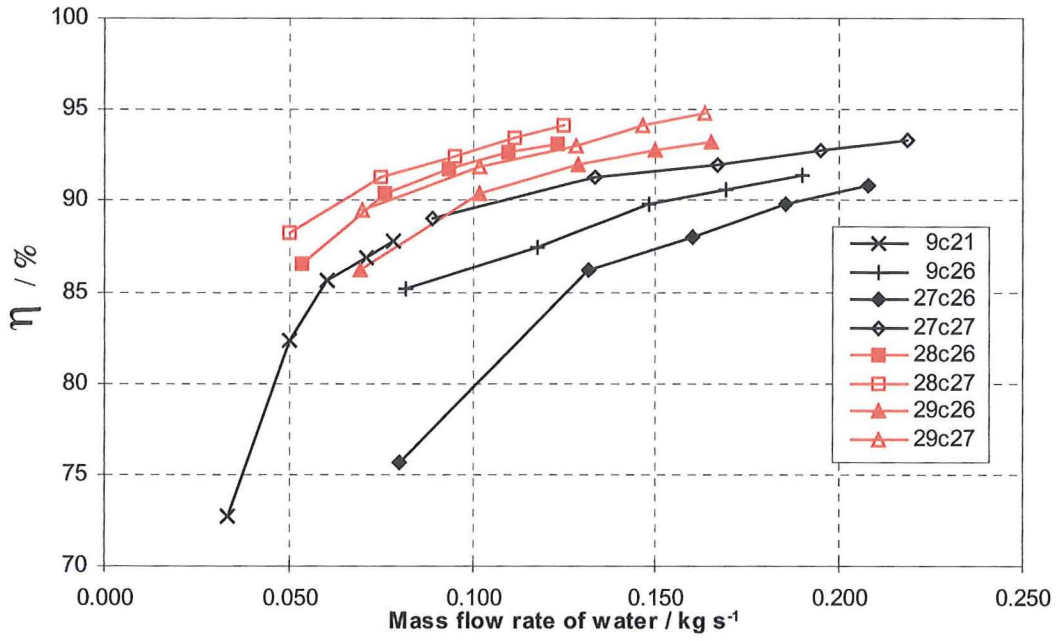

Figure 4-13: Effectiveness at various injected mass flow rate of water

The maximum effectiveness of about 95%, which was measured in the present series of experiments, is determined by the geometrical configuration of the system.

To consider also the energy that was required to produce these droplets, a new equation, index of energy performance was defined. The index of energy performance is defined as the ratio of the rate of heat transfer between the spray droplets and the surrounding gas and the power requirements needed to produce the spray droplets. The index of performance is calculated by the following equation.

$$\psi = \frac{\dot{m}_a (c_{pa_i} t_{ai} - c_{pa_o} t_{ao})}{(T_{ai} - T_{wi}) P_w} \qquad [98]$$

where P_w is the result of

$$P_w = \Delta p_w \frac{\dot{m}_w}{\rho_w} \qquad [99]$$

The results presented in Figure 4-14 show that the index of performance depends appreciably on both, the nozzle design and the mass flow rate of the injected liquid throughout the range of flow rates investigated.

Firstly, the index of performance decreases very strongly with the mass flow rate of the injected liquid. The reason for this is that the pressure drop through the nozzle

and hence the power requirements to produce the spray droplets increase much more rapidly than the heat transfer rate to the spray droplets. Secondly, for a given mass flow rate of the injected liquid, the nozzle design parameter is significantly influenced by the diameter of the exit orifice, D_e. The index of performance is for a given mass flow rate of the injected liquid about five times higher for the nozzles with the larger exit orifice diameter. The reason is that the exit orifice provides the controlling flow resistance, with the most significant influence on the pressure drop across the nozzle and hence the power requirements needed to produce the spray droplets.

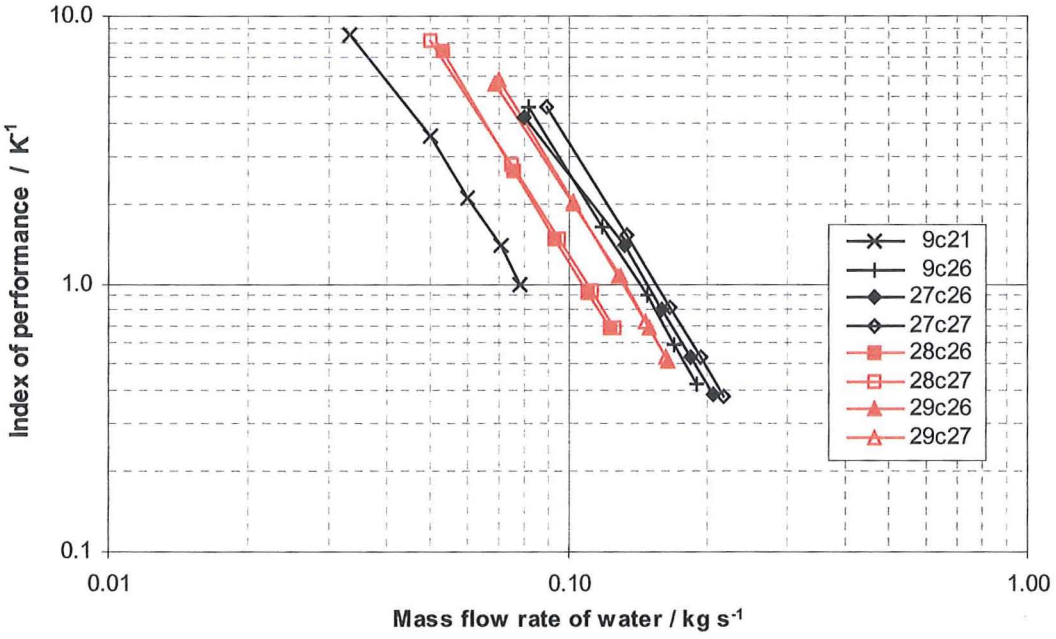

Figure 4-14: Index of energy performance over water flow rate

This implies that in order to achieve high heat transfer rates without the penalty of excessive power requirements large nozzles should be used and the mass flow rate of the injected water should not be increased significantly above the value for which the effectiveness has reached its effective maximum of 95% for this specific spray chamber. Whether the effectiveness can be increased by using different spray chambers has to be determined by further research.

4.3 Effervescent nozzle

The tests of the effervescent atomiser were performed at an air inlet temperature of 150°C. The configurations chosen are described in the chapter on experimental procedure. Four different configurations were tested:

470500	471300
470507	471307

The notation for the configuration code is as follows. For example: **470507**

Code	Description		Dimension
47	Gives the diameter of the exit orifice	D_e	4.7 mm
05	Gives the size of the air inlet hole of the inner pipe	D_{ai}	0.5 to 1.3 mm
07	Indicates the ratio of the length to diameter of the exit orifice	$\frac{L_e}{D_e}$	0 & 0.7

The above listed configuration where tested for different air liquid mass flow ratios (ALR) which ranged from 0.025 to 0.100.

The effervescent atomiser has two different fluids that need to be pressurised. In our case is it water and air. The amount of power needed to pressurise the water, P_w, is calculated by

$$P_w = \Delta p_w \frac{\dot{m}_w}{\rho_w} \qquad [100]$$

The air is a compressible fluid and the temperature changes with the change in density and the air pressure energy E_a and therefore is calculated by

$$P_{aw} = \frac{p_\infty^{1/\kappa} \dot{m}_{aw}}{\rho_\infty} \frac{p_{aw}^{1-\frac{1}{\kappa}} - p_\infty^{1-\frac{1}{\kappa}}}{1-\frac{1}{\kappa}} \qquad [101]$$

where the p_∞ is the ambient air pressure outside the spray chamber and p_{aw} is the air pressure in the atomiser. The term $\dot{m}_a$ is the mass of air per second used to atomiser the liquid and κ is the ratio of specific heat capacities. The energy required for the production of spray droplets, $P=P_{aw}+P_w$ is high compared with the pressure swirl nozzles.

According to the literature the frothy flow regime starts above an ALR of 0.2. The aim was not to exceed an ALR of 0.1 in order to operate the nozzle in an affordable region.

Figure 4-15 shows the influence of the ALR on the relative humidity at the spray chamber exit of the air. The relative humidity for different ALR's of configuration 470507 is plotted against differential pressure across the nozzle. The greatest relative humidity is achieved in the experiments with an ALR of 0.100. The increase of air bubbles inside the liquid water jet decreases the thickness of water separating the bubbles. If the liquid water jet is emerging from the exit orifice, the sudden expansion of the compressed air bubble can shred the water into smaller droplets with a higher initial velocity. The smaller droplets with a higher initial velocity cause better heat transfer rates. The limit of ALR is reached when the bubbles inside the liquid jet coalesce. The flow regime is then changed from a bubbly flow to a frothy flow. However, the best results are achieved by using an ALR of 0.1.

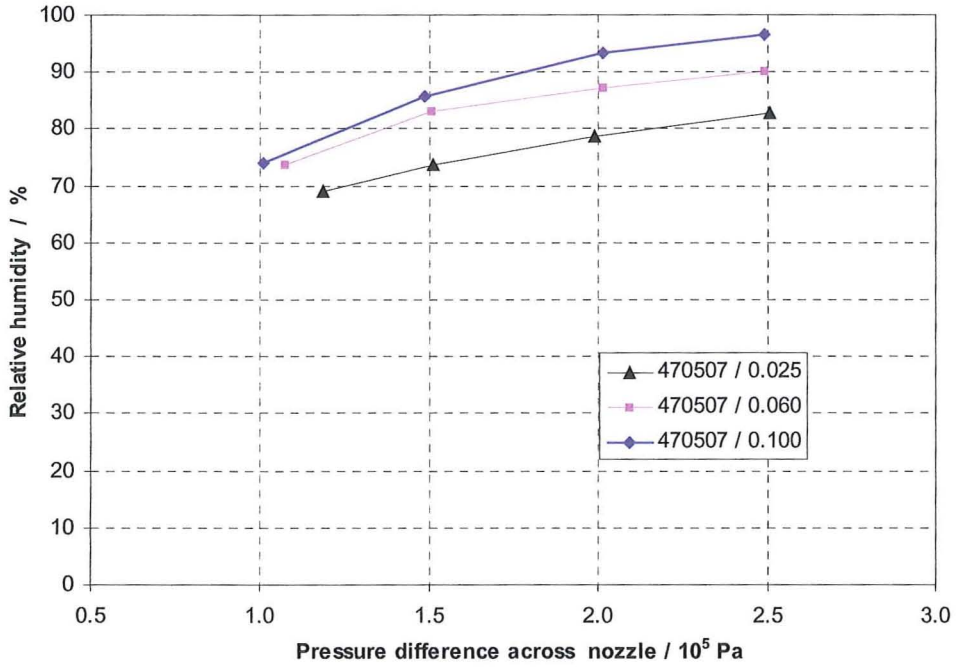

Figure 4-15: Relative humidity vs. pressure difference across the nozzle for the configuration 470507 at varying air/liquid ratios

The size of the air bubbles that enter the liquid jet depends on the air inlet holes in the inner pipe. Preliminary tests, which are not shown, indicated that the differences between the intermediate sizes of the air inlet holes ranging between 0.5 mm and

1.3 mm is insignificant. The two diameters of 0.5 and 1.3 mm were chosen and tested with different length to diameter ratios of the exit orifice, which are 0 and 0.7. Preliminary tests have indicated that the same applies for exit orifice ratios that are within this range.

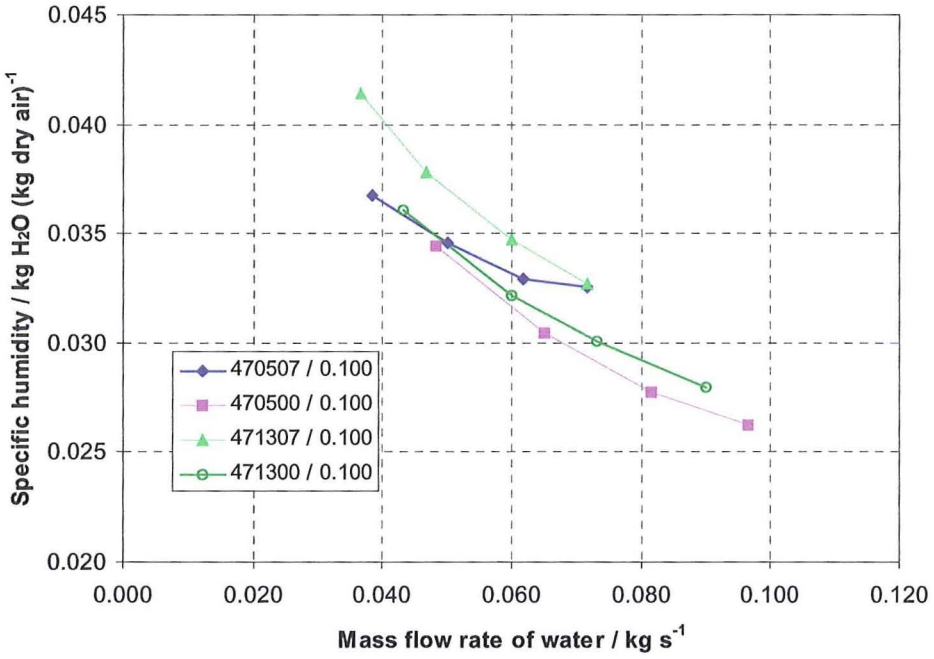

Figure 4-16: Specific humidity vs. mass flow rate of water for all tested effervescent configurations at ALR 0.100

The specific humidity achieved with all tested configuration over the mass flow rate at an ALR of 0.100 are presented in Figure 4-16. The largest specific humidity was measured for the 471307 configuration. Plotting the result against the air exit temperature, Figure 4-17, shows that the lowest air temperature is achieved with the 470500 configuration. The nozzles with the length to diameter ratio 0 have a higher mass flow rate of water at the same pressure difference across the nozzle, which is independent from the air inlet holes. This is caused by the reduction of the discharge coefficient and the reduction of friction. The measurement of the humidity sensor must be wrong, because a 106% cannot be achieved by homogeneous condensation at this test rig. Tests with the humidity sensor have shown that if liquid is in contact with the sensor the measured output is 106%. Most probable explanation is, that many droplets are carried with the airflow through the spray chamber exit and must have wetted the humidity sensor. This test run could not be repeated, because the test rig had been already converted for other tests.

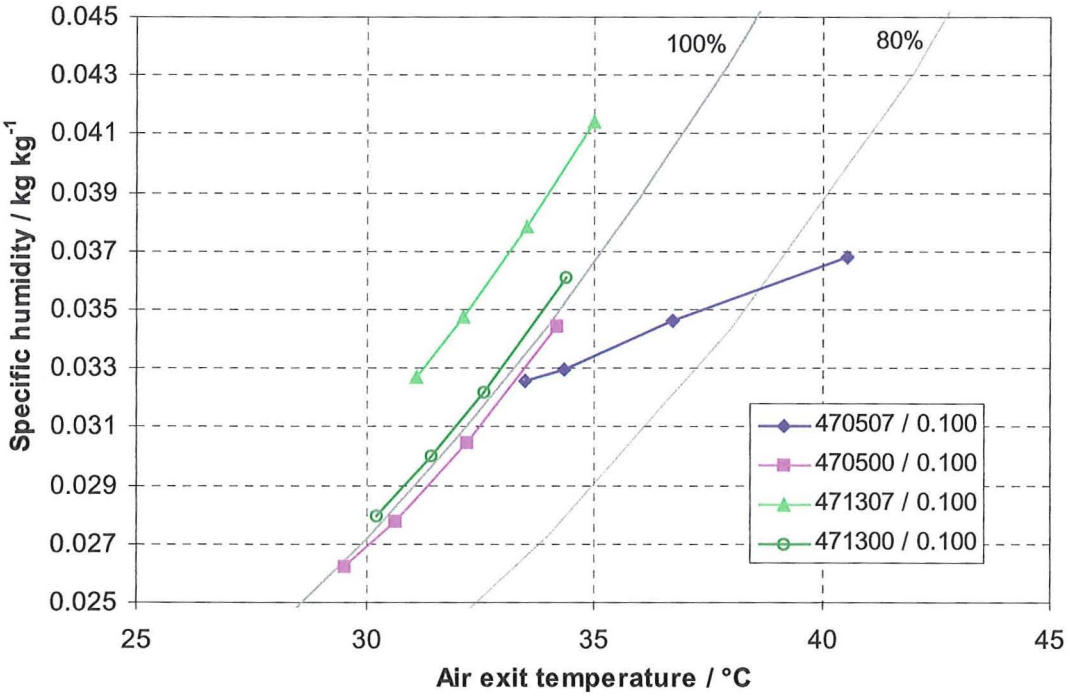

Figure 4-17: Specific humidity vs. air exit temperature for all tested effervescent configurations at ALR 0.100

The air energy requirement depends primarily on the ALR and increases with the increase of the ALR. Figure 4-18 shows three ALR's, 0.025, 0.060, and 0.100. Each ALR was tested with two different air inlet holes at the inner pipe. The diameter of the air inlet holes of the inner pipe has the followings effects on the energy requirement. An increase of the ALR increases the energy requirement difference between the 0.5 mm and 1.3 mm air inlet holes. The 1.3 mm air inlet hole requires approximately a maximum of 35% less air pressure energy to achieve the same mass flow rate. A 6.76 times larger interface area at the inner tube cause this. The energy requirement for a given ALR is proportional to the mass flow rate of water. Figure 4-19 shows the energy required for the water pressure across the atomiser.

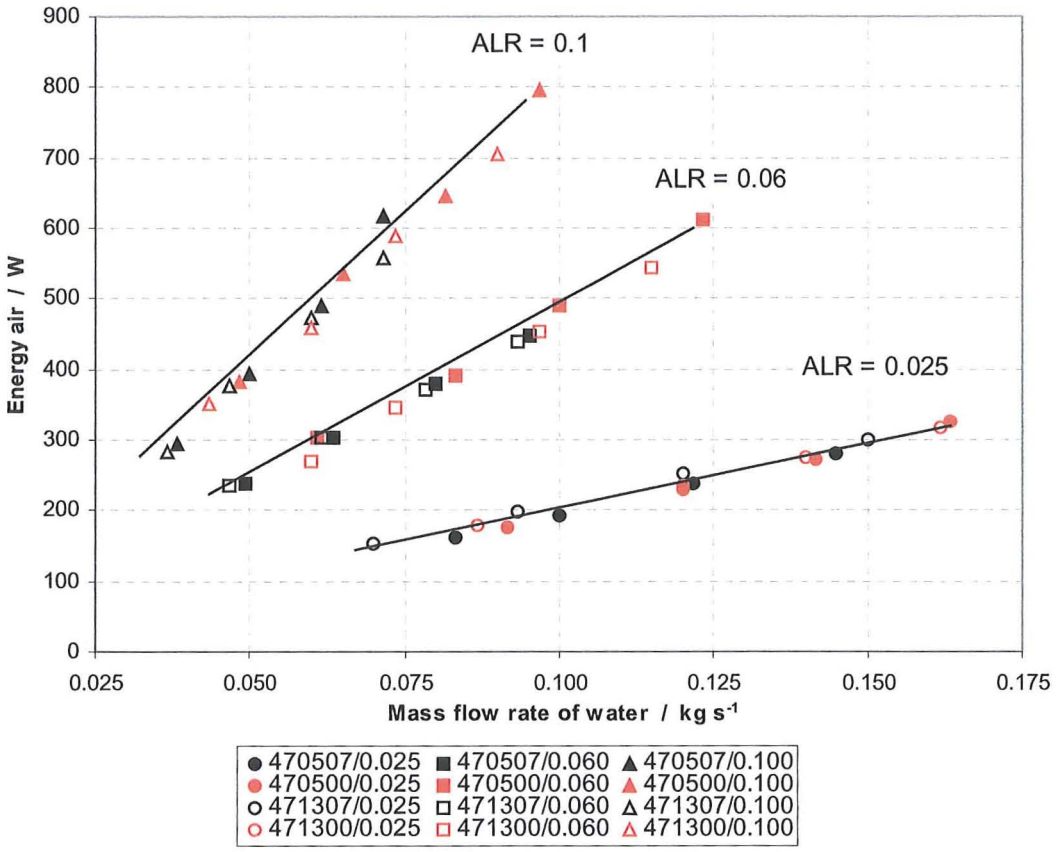

Figure 4-18: Demand on air energy to maintain the ALR

The energy requirement of water in Figure 4-19 compared to the energy requirement of air, shown in Figure 4-18, is approximately 5%. For a constant water pressure the energy requirement decreases as the ALR increases. With an increase of the ALR the atomiser discharges more air than water. This reduces therefore the available cross section area for the water and hence, automatically the flow rate of the water. The power requirement, for a constant water pressure, depends on the ALR and increases with the mass flow rate.

At constant water pressure the mass flow rate for the exit orifice, with the length to diameter ratio of 0, is higher than for the exit orifice with the 0.7 ratio. Figure 4-18 shows that the diameter of the air inlet holes in the inner pipe have only a very minor influence on the energy requirement for the water.

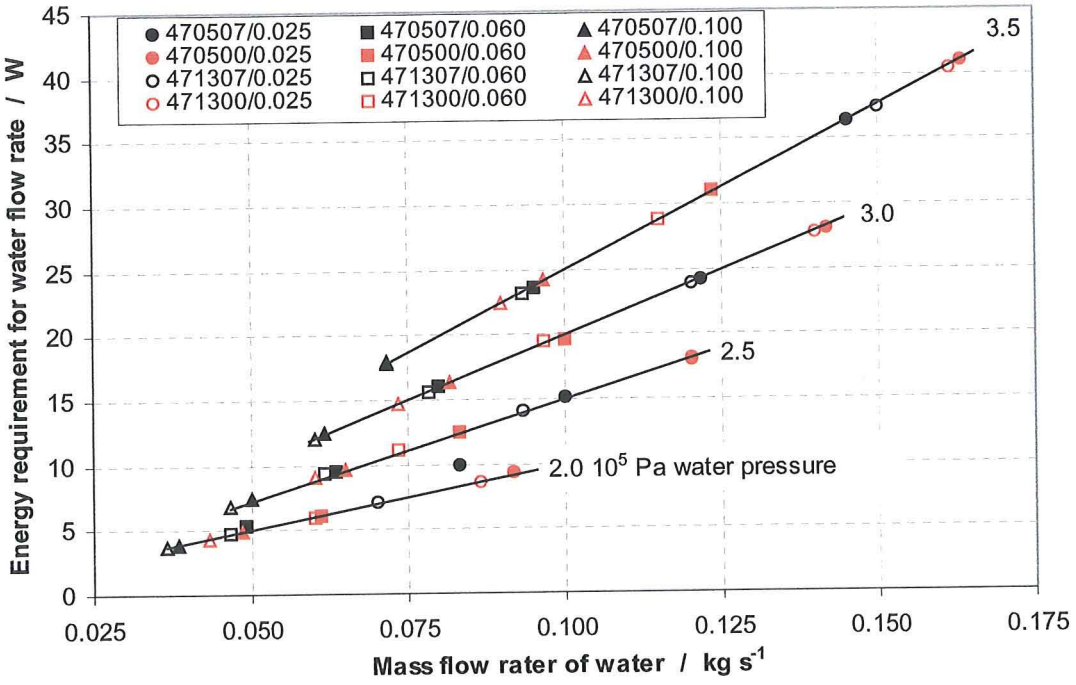

Figure 4-19: Energy requirement for the water

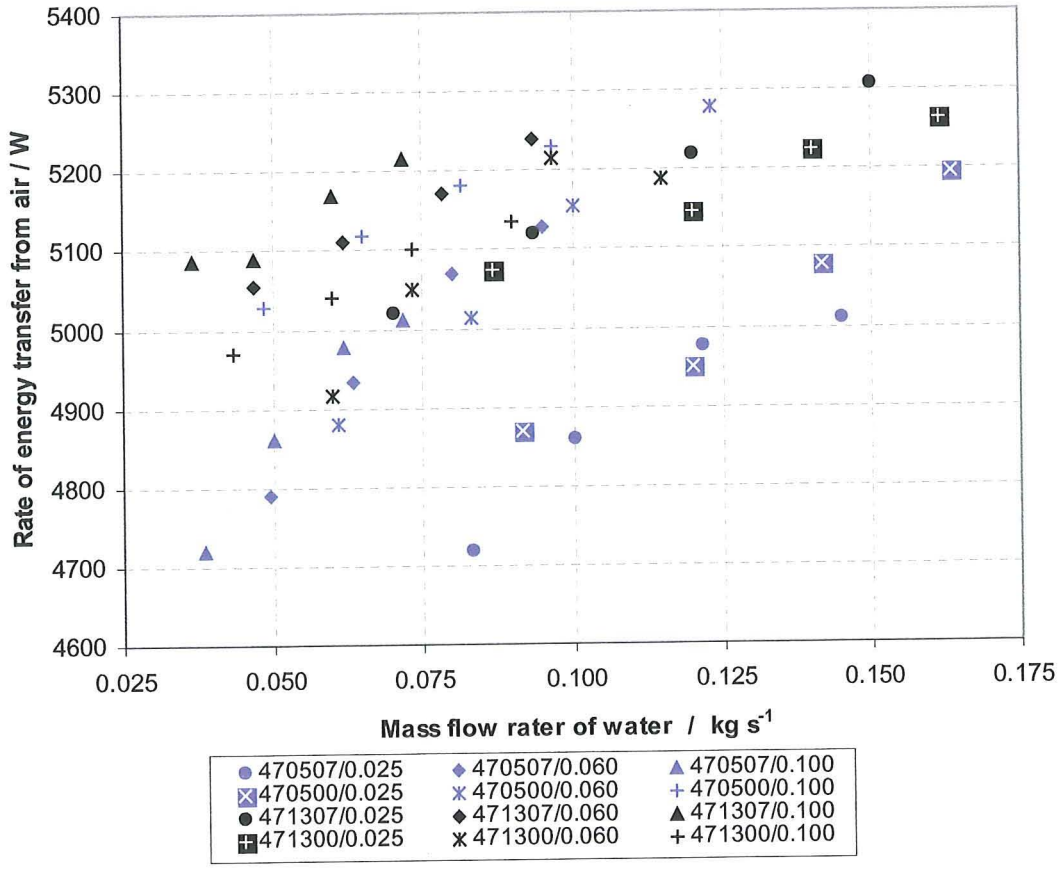

Figure 4-20: Energy transferred from the air to the water

The energy transfer was calculated from the inlet and outlet conditions of the hot air (h_{ai} = hot air inlet, h_{ao} = hot air outlet) with the following equation.

$$\Delta\dot{Q}_a = \dot{m}_{am}(h_{ai} - h_{ao}) \quad [102]$$

The energy transfer from air to water droplets is between 4700 and 5400 W and is, as shown in Figure 4-20, increasing with the ALR. This pattern is within a bandwidth of 600W. All configurations cause a maximum change of within 12.7%. Considering that the effervescent atomiser is operating with two fluids, where one is decreased if the other one is increased, made it necessary to find out how good the atomiser operates if only one fluid is considered, so as to give a comparison of the droplet quality to the pressure swirl nozzle.

The analysis of the effervescent nozzle is very complex due to the fact that two media emerge from the nozzle. The atomising gas, in our case air, after leaving the orifice mixes instantaneously with the hot air and reduces the initial temperature of the hot air, in which the droplets are suspended. Hence, the temperature difference of the hot air and water droplets is reduced. Due to this reduced temperature difference the energy transfer to the water droplet is not as high as for the pressure swirl nozzle. Because of the interest in the effectiveness of the spray droplets from the effervescent atomiser the results were recalculated. It is assumed that the atomising air mixes the temperature and the humidity evenly within the spray chamber. The temperature and humidity of the hot air that the droplet was exposed to was obtained from:

$$\dot{m}_{am} = \dot{m}_a + \dot{m}_{aw} \quad [103]$$

$$\omega_{am} = \frac{\dot{m}_a\omega_a + \dot{m}_{aw}\omega_{aw}}{\dot{m}_a + \dot{m}_{aw}} \quad [104]$$

$$t_{am} = \frac{\dot{m}_a T_a + \dot{m}_{aw} T_{aw}}{\dot{m}_a + \dot{m}_{aw}} \quad [105]$$

The specific heat transfer coefficient, c_p, for the mixing temperature is determined for the property tables of Rogers and Mayhew (1996), so that the enthalpy of the air and of the vapour could then be calculated.

With the given information it is possible to re-work the experimental data and distinguish between the droplet performance and the nozzle performance. The droplet performance indicates the transfer performance between the mixed

surrounding gas and the water droplets. The temperature of the mixed surrounding gas depends on the air inlet temperature and ALR of the nozzle. The nozzle performance does not consider the cooling down of the hot air by the atomising gas. The results of the re-calculated data are presented in Figure 4-21 and make clear that the temperature difference achieved by the droplets is smaller as the temperature difference of the nozzle were both mediums are considered. The configuration 471307 with an ALR of 0.025 achieves a temperature difference of 122°C whereby the droplets reduced the temperature by 112°C, hence the atomising air reduced the hot air temperature by 10°C. It obviously that at higher ALR the temperature difference produced by the droplets is smaller due to a lower temperature difference between the mixed air and the droplet temperature. This is caused by a larger amount of atomising air introduced into the spray chamber.

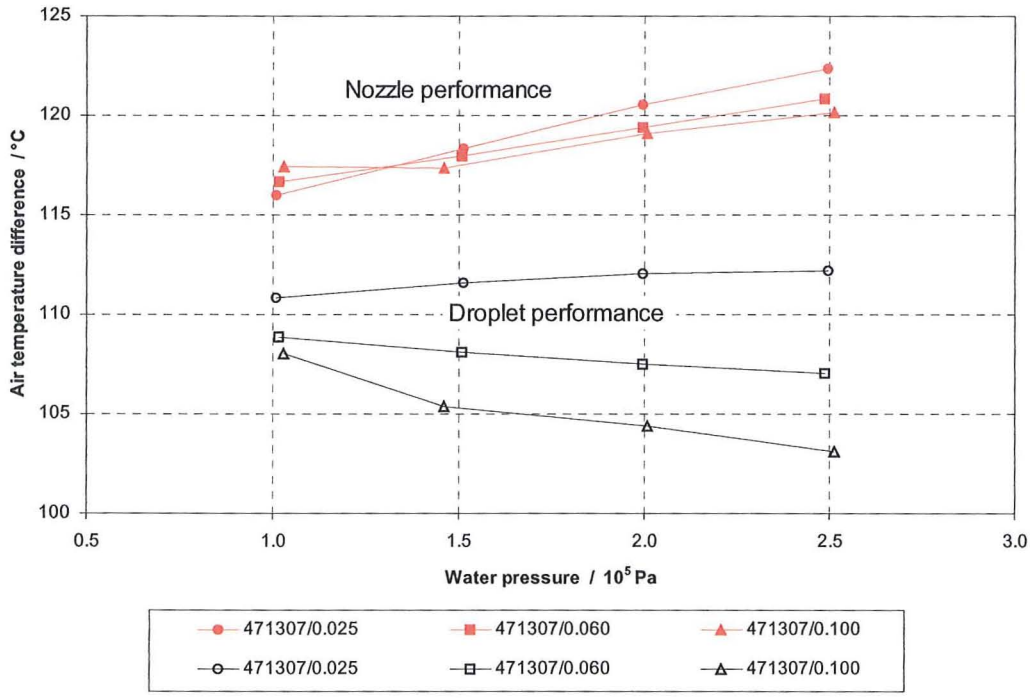

Figure 4-21: Difference of nozzle and droplet performance of the energy transfer

Figure 4-22 and Figure 4-23 compare the air temperature difference for the droplet performance only in respect to the influence of the air inlet holes. Figure 4-22 shows the air outlet temperature at a constant L_e/D_e ratio of 0.7 and Figure 4-23 of 0. The increase of the ALR decreases the droplet cooling performance at all tested configurations. The cooling caused by the droplets is for high ALR's lower because

of the larger amount of atomising air induced into the spray chamber. The larger amount of atomising air inside the spray chamber reduces the hot air temperature. A reduction of the hot air temperature leads to a smaller air temperature difference between the water droplet and the surrounding air. Hence, the energy transfer is reduced.

There is no significant air temperature difference because of the Le/De ratio. A more significant difference is the size of the air inlet holes at the inner pipe. Air inlet holes with a diameter of 1.3 mm cause a higher air temperature difference than for the 0.5 mm holes. The 1.3 mm air inlet holes produce less but bigger bubbles that have a higher internal energy per bubble. The connection between the air bubble size and the exit orifice diameter could not be tested but considering the physics of the atomisation process there must be one.

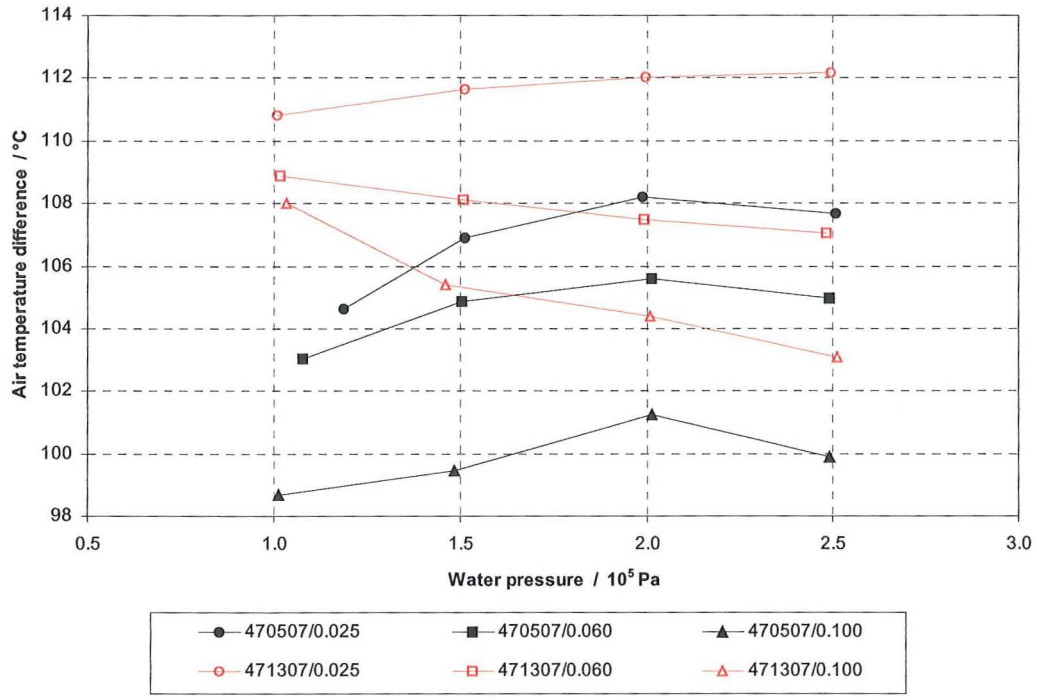

Figure 4-22: Comparison of the 0.5 and 1.3 mm air inlet holes at the inner pipe at L_e=0.7 D_e

The droplet cooling performance of the effervescent atomiser is less influenced by the water pressure then for the pressure swirl nozzle. The air temperature difference varies over the tested water pressure up to 7°C. The same pressure difference caused an air temperature difference of 20°C for the pressure swirl nozzle. The effervescent atomiser has at low water pressures a higher air-cooling. An air temperature

difference of up to 112°C at $1x10^5$ Pa is approximately 40°C more than pressure swirl nozzle.

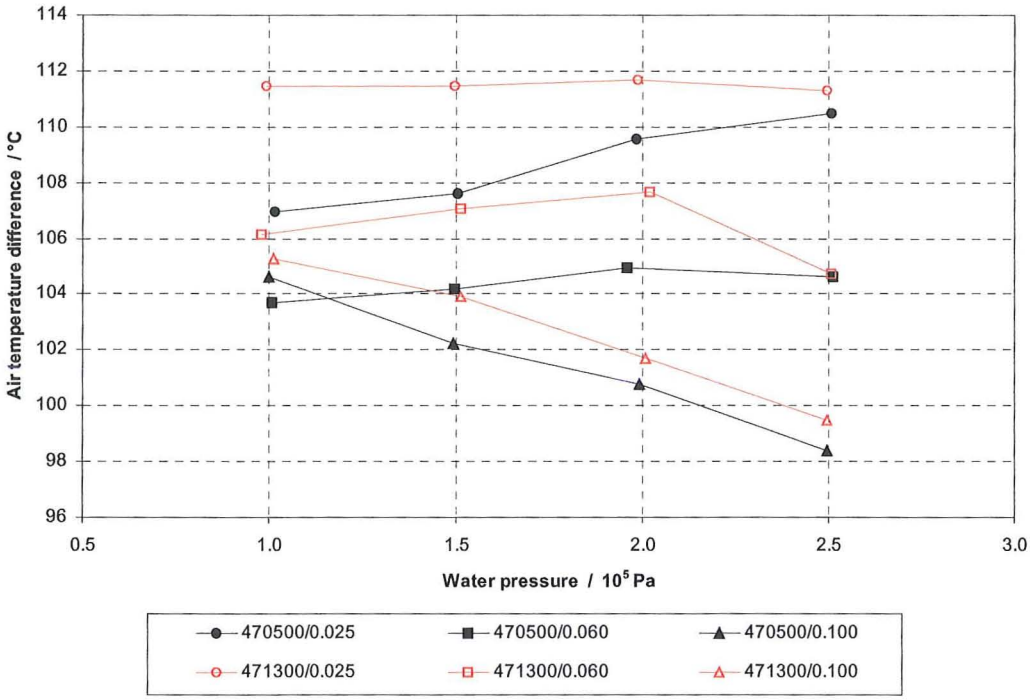

Figure 4-23: Comparison of the 0.5 and 1.3 mm air inlet holes at the inner pipe at L_e=0 D_e

The comparison of the inner pipe with 1.3 mm holes and the exit orifice with a ratio of 0.7 and 0 D_e in Figure 4-24 indicates the influence of the air temperature difference. The air temperature difference in cooling for both configurations is relatively small. It seems that the length to diameter ratio has a very small influence on the nozzle performance. Especially at ALR 0.0025 is the difference insignificant. At ALR of 0.1 the length to diameter ratio of 0.7 is an advantage.

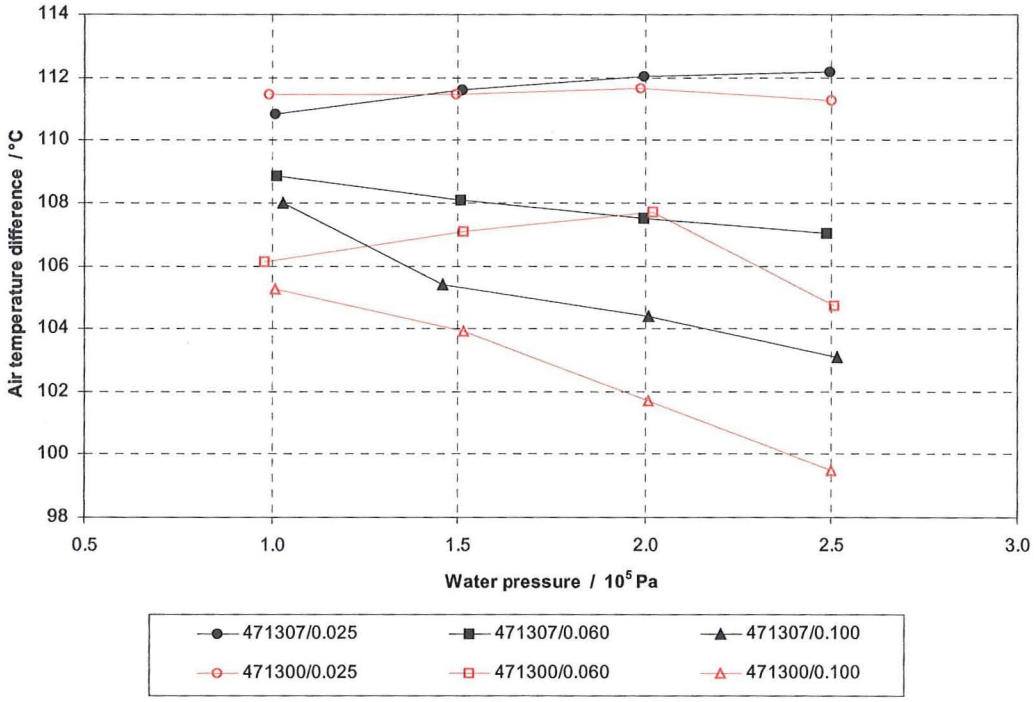

Figure 4-24: Comparison of the influence of the exit orifice length ratio at the inner pipe with 1.3 mm air inlet holes and different ALR's

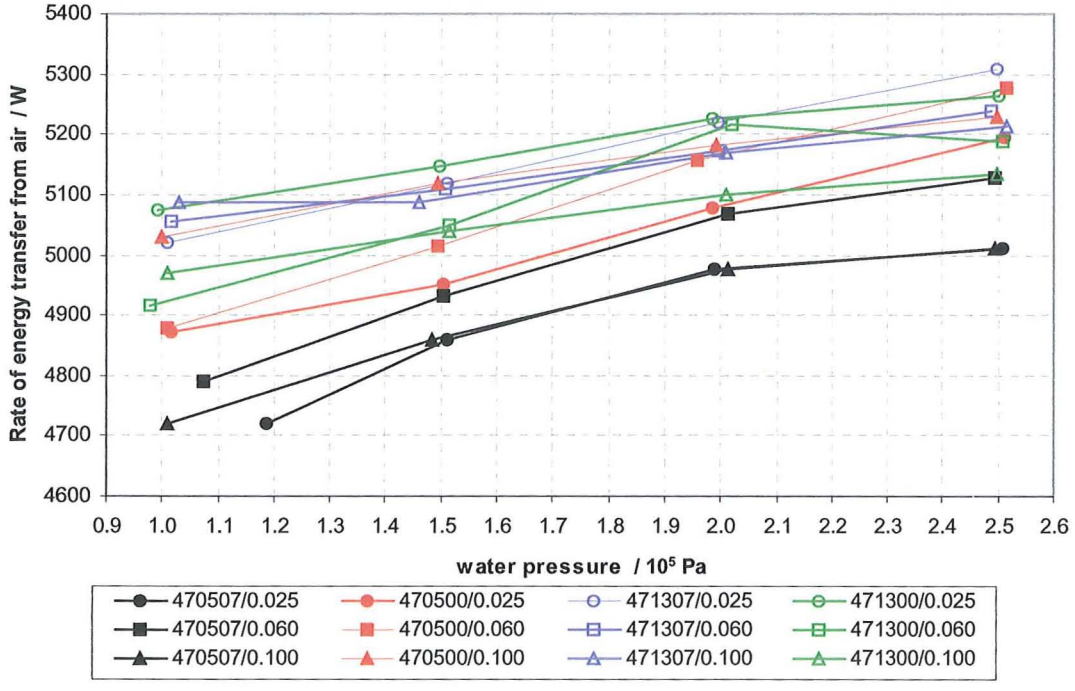

Figure 4-25: Rate of energy transfer from air to water vs. water pressure

The variation of the rate of energy transfer from air over the water pressure for all nozzle configurations is shown Figure 4-25. The energy transfer is between 4700 W and 5300 W. The large scale shows that the difference in energy transfer for every configuration increases approximately 300 W. The specific heat transfer, defined as,

$$\dot{q} = \frac{\dot{m}_{am}(h_{am} - h_{ao})}{\dot{m}_{wi}} \qquad [106]$$

and is shown in Figure 4-26.

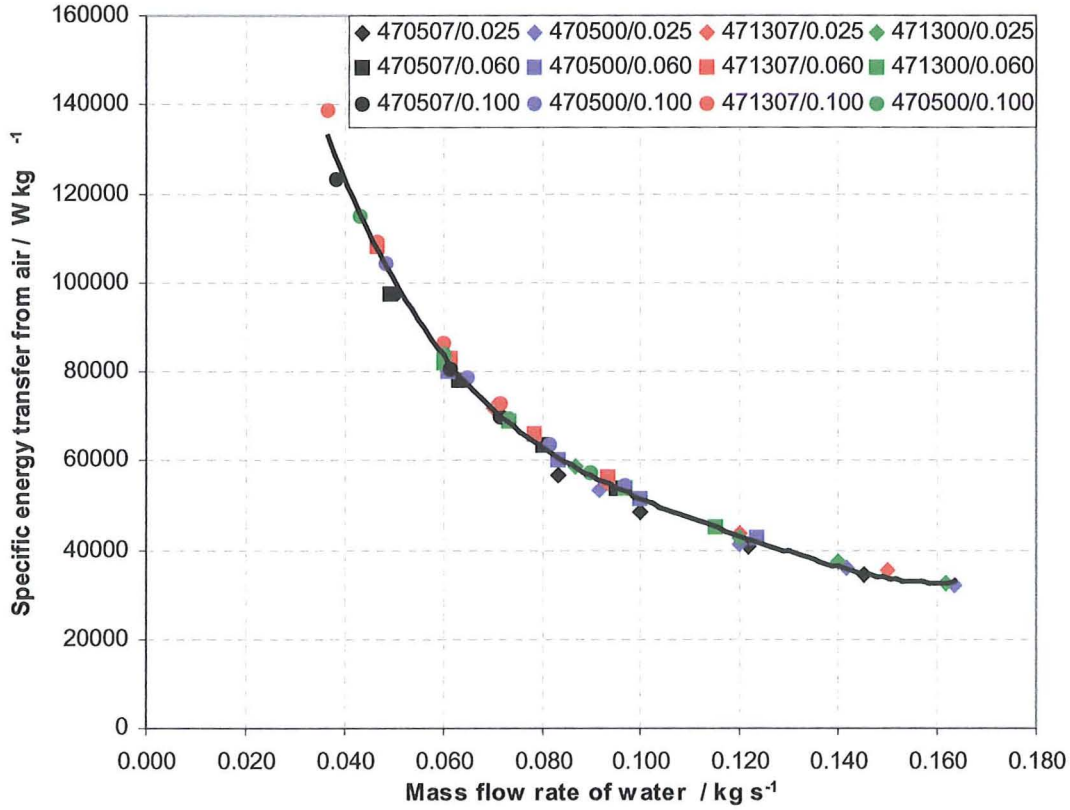

Figure 4-26: Specific energy transfer over the mass flow rate of water

The heat transfer effectiveness, shown in Figure 4-27, is between 87% and 93% for all configurations. The heat transfer effectiveness is defined as the ratio of the air temperature difference divided by the maximum temperature difference. Equation [107] calculates the effectiveness given by considering only the droplets performance at mixed air conditions.

$$\eta = \frac{T_{am} - T_{ao}}{T_{am} - T_{wi}} \qquad [107]$$

The dashed line indicates the effectiveness driven by both media, atomising air and water droplets, emerging from the nozzle, consequently, this is the effectiveness of the nozzle. The solid line describes the effectiveness of the droplet only. The gap between these two lines is the cooling of the air mixture, which is increasing with the decrease of the mass flow rate of water.

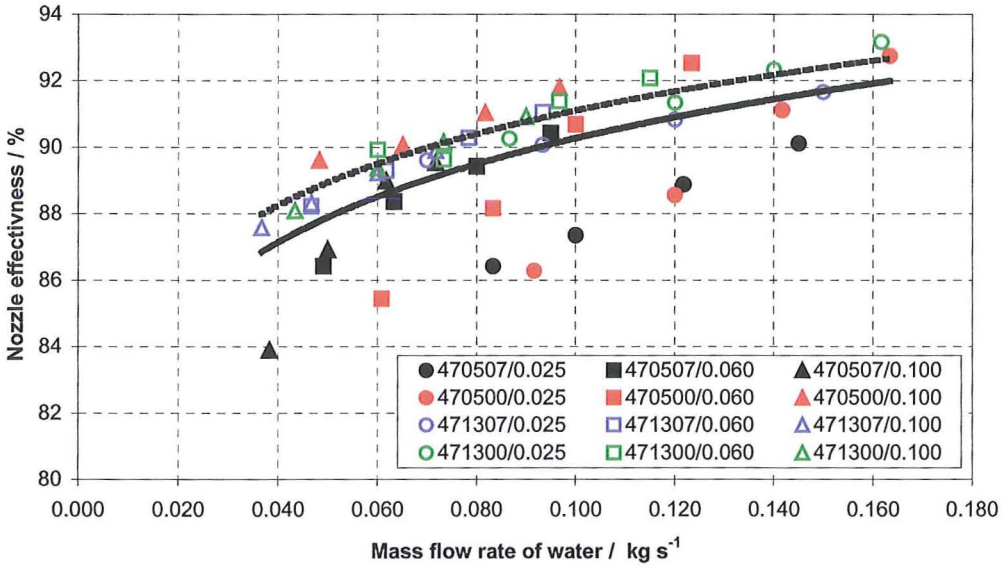

Figure 4-27: Nozzle effectiveness of all configurations vs. the mass flow rate

It is obvious that the ALR has influence on the effectiveness due to the instantaneous air mixing in the spray chamber. All calculations are based on the achieved temperature difference by the nozzle including the air mixing and the droplet heat mass transfer.

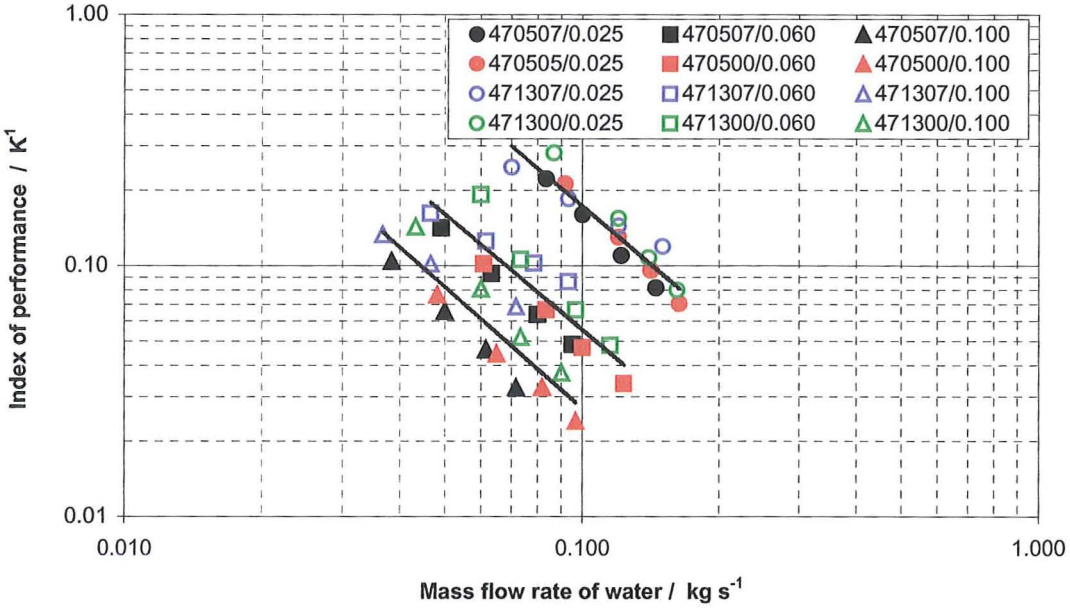

Figure 4-28: Index of performance vs. mass flow rate of injected water

The Index of Performance for the effervescent atomiser in Figure 4-28 is calculated considering the incoming air temperature. The change of the ALR has a great influence of the Index of Performance. The index of performance for the effervescent atomiser is defined as

$$\psi = \frac{\dot{m}_a (h_{ai} - h_{ao})}{(T_{ai} - T_{wi})(P_w + P_{aw})} \qquad [108]$$

where the power for the air is calculated as

$$P_{aw} = \frac{p_\infty^{1/\kappa} \dot{m}_{aw}}{\rho_\infty} \frac{p_{aw}^{1-\frac{1}{\kappa}} - p_\infty^{1-\frac{1}{\kappa}}}{1-\frac{1}{\kappa}} \qquad [109]$$

As shown in Figure 4-28 a tendency for each ALR becomes visible, independent of the configuration. As ALR increases the Index of Performance reduces. This is a result of the increasing energy needed for the generation of a high ALR.

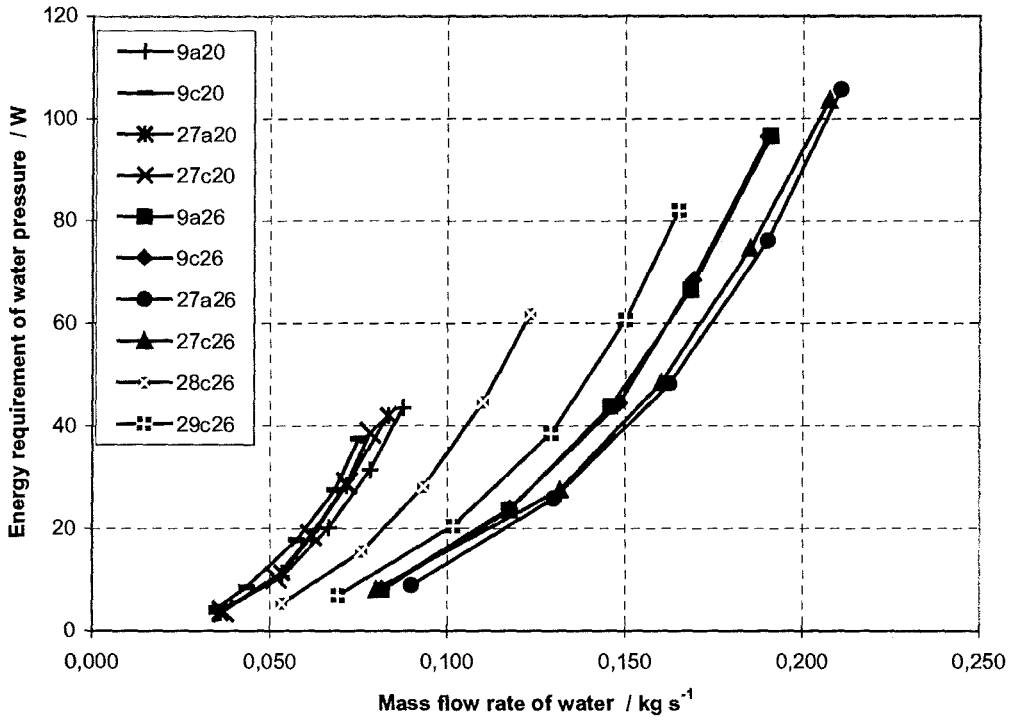

Figure 4-29: Energy requirement vs. the mass flow rate for various pressure swirl nozzle configurations

The energy required to produce a liquid spray at a certain mass flow rate is shown in Figure 4-29. The equation to calculate the required energy is

$$P_w = \Delta p_w \frac{\dot{m}_w}{\rho_w} \qquad [110]$$

Figure 4-29 shows the energy requirement for the pressure swirl nozzle with different internal geometries. The following internal geometries were varied:

- the exit orifice diameter, De,
- the number of tangential inlet slots, NTS.

As well as the nozzles described in section 3.2 the later modified 28c26 and the 29c26 nozzles are included in Figure 4-29. This is done to show the influence of the tangential inlet area into the swirl chamber.

The influence in the internal geometry of the nozzles described in section 3.2 is mainly influenced due to the change of the exit orifice diameter. Comparison of the nozzle configurations 27c20 and 27c26 shows the influence of the exit orifice diameter. The increase of the diameter from 2.5 mm to 4.7 mm results in a higher

D_e=4.7mm 0.208 kg s^{-1}) at the same pressure difference across the nozzle (0.5 MPa). The reason for this is a combination of an increase of the outlet area of the exit orifice, A_e, by 250% and results in a 120% higher Flow number, *FN*. Another point is the reduction of the discharge coefficient, C_D, by 38%. The conclusion of this is, that an increase of the exit orifice diameter results in a 56% increased mass flow rate at the same energy requirement.

The influence of the number of tangential slots is seen in Figure 4-29 by comparing 9c26 and 27c26. The difference of these two configurations is only the number of tangential slots, *NTS*, which led the liquid flow into the swirl chamber. The configuration with three tangential slots has a 5% smaller liquid mass flow rate than the one with 6 tangential slots and needs 18.4% more energy. The higher pressure at the same liquid mass flow rate results in a higher internal velocity of the liquid and consequently a higher droplet velocity and a smaller Sauter mean diameter. This is seen in section 4.4. This conclusion seems to be only valid for the larger exit orifice diameter.

The difference of the 27c26 and the 28c26 is the reduction of the tangential inlet area by 50%. Three tangential slots of a swirl chamber with 6 tangential slots were blocked to achieve this. The rest of the internal geometry was kept constant. The reduction of 40% mass flow rate reveals that the "bottleneck" is not the exit orifice anymore, it is now the tangential inlet slots. The fact that the tangential inlet area is halved and that the liquid flow rate is only decreased by 40% means that the liquid inlet velocity, U_i, (see section 2.3) is increased by 20%. A higher internal velocity of the liquid and consequently a higher droplet velocity and a smaller Sauter mean diameter.

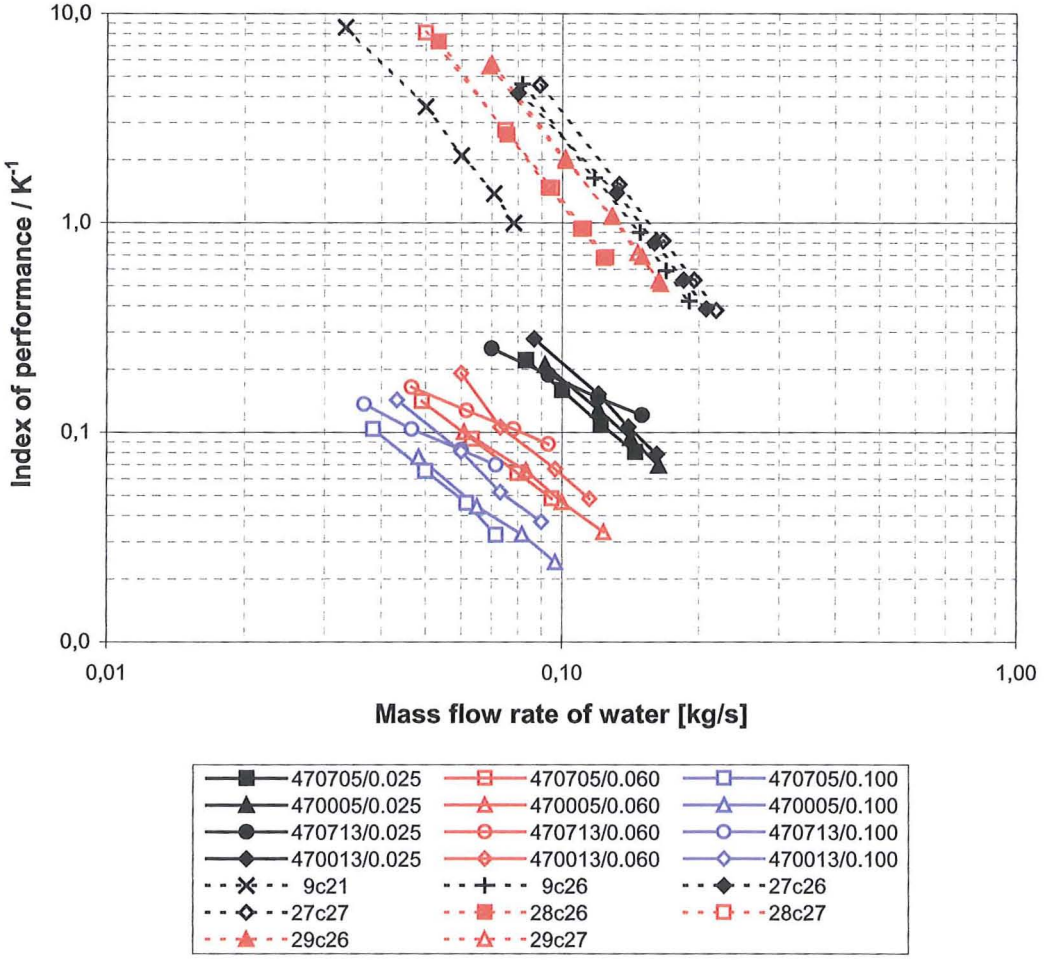

Figure 4-30: Comparison of the index of performance between pressure swirl nozzle and effervescent atomiser

The comparison of the index of performance in Figure 4-30 between pressure swirl nozzle and effervescent atomiser shows that the pressure swirl nozzle has about 100 times higher performance. The effervescent atomizer performance is low due to the air used for the production of the droplet spray.

4.4 Results of the droplet size and spray angle measurement

Measurements with the PDPA for the nozzle configuration 9a20, 9a26, 27a20, and 27a26 are made to determine the Sauter Mean Diameter and the droplet velocity for each pressure value. These measurements are made after the numerical simulation gave result that deviate from the experimental results. The measured Sauter Mean Diameter and the measured droplet velocity were then used to generate the droplet inlet file for the numerical simulation. The laser was not powerful enough to measure the droplet size across the spray region as Zhang and Ziada (2000) did. Therefore it was not possible to establish a 3-D spray pattern.

The droplet size was mainly influenced by the size of the exit orifice. The configuration with the orifice of 2.5 mm (9a20 & 27a20) had a smaller mass flow rate of water and produced (at the same pressure drop across the nozzle) droplets that are 75 μm smaller than the nozzle with the 4.7 mm exit orifice diameter. This is shown in Figure 4-31. It can also be seen that the influence of the number of tangential inlets has a minor effect on the droplet size and that the droplet sizes are close to each other.

The PDPA was only measuring the vertical droplet velocity. The spray angle is used to calculate the true droplet velocity at the control volume. This is necessary, because the PDPA just measuring the X component of the droplet velocity. The mean velocity of the droplets was measured 40 mm downstream of the exit orifice. A measurement closer to the exit orifice could not be made because of the high spray density and a lack of laser intensity. An attempt to measure the droplet size across the nozzle was not possible for the same reason. The laser used has an output of 10 mW, which is not enough to make measurements in a highly dense spray.

Figure 4-33 and Figure 4-34 are printed screen plots of the real time analysis software for the droplet diameter acquisition. These plots show the evaluated data of a droplet Figure 4-34 presents the '1D Diameter Acquisition' screen, which contains the diameter and velocity information in graphical and numerical output. The screen can be divided into the following parts:

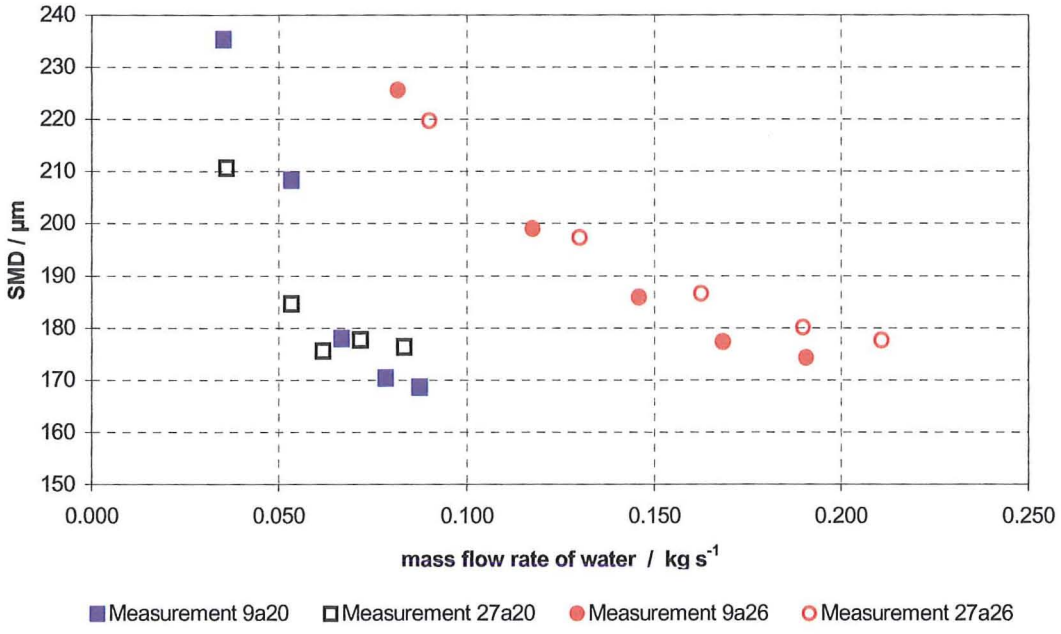

Figure 4-31: Result of the droplet measurement of the configuration used at the numerical simulation

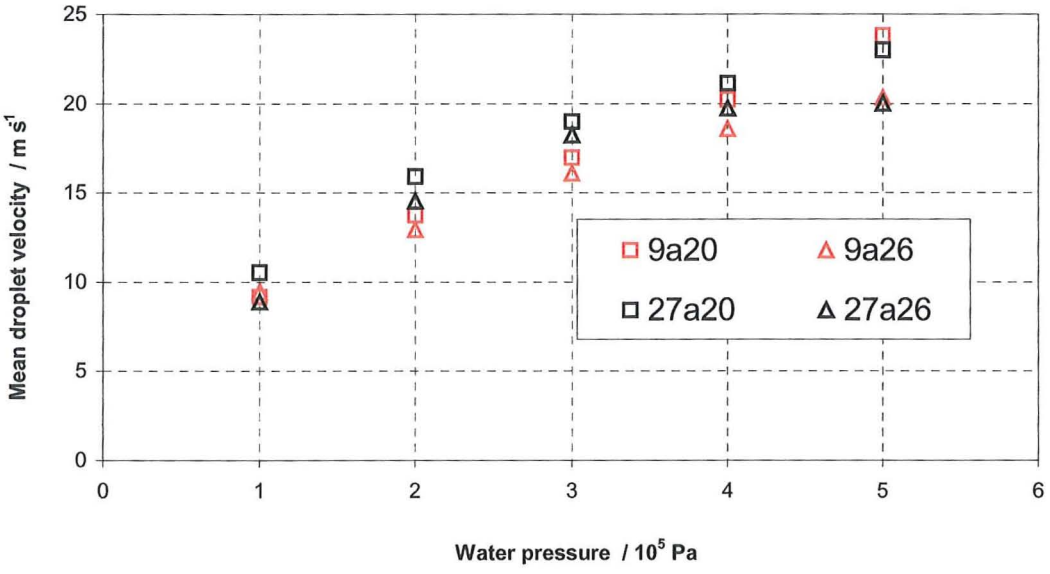

Figure 4-32: Comparison of the calculated mean droplet velocity of the configuration used at the numerical simulation

One the left hand side is the graphical display of the diameter and velocity of each measured droplet. The scale for the droplet size is up to 374.1 µm. All droplets above that size are not measured because of the existing optical arrangement.

The first graph presents the number of droplets measured over the droplet size.
The graph below displays the result of the number of droplets measured over the droplet velocity.
The third graph plots the velocity of the droplets vs. the droplet diameter. It can be seen that the droplets below 100 μm have a reduced velocity compared to the bigger droplets above 100 μm which reach a maximum velocity of about 20 [m/s]. Due to the high number of small droplets the mean droplet velocity for this example is 14.16 [m/s].

- The top half of the right panel contains the information of the LPDA settings and the mean droplet velocity, 'Vel. Mean', in m/s.

Below that are different diameters, calculated form the data, listed for the corrected and non-corrected PVC. PVC means Particle Volume Corrected and deducts the droplets that have not fully passed through the measurement volume.
Because of the wide droplet distribution that the nozzles produce, for the later numerical model the non-corrected D32 (also known as Sauter Mean Diameter) droplet diameters were used. At this droplet distribution some droplets are so big that they do not necessarily pass through the control volume.
Figure 4-34 shows the 'Volume Distribution' screen that displays information about the droplet distribution and calculates the parameters needed for the Rosin-Rammler distribution. The screen can be divided into graphical and numerical output data and described as follows:

- On the left hand side is the graphical output. At the top graph is the percentage of a size range printed over the droplet diameter and at the bottom graph over the volume distribution. Different size fitted equations are plotted across the distribution range and indicate their best fit of the droplet diameter distribution for the existing data.

The top half of the right panel contains the information of the LPDA settings and the mean droplet velocity, 'Vel. Mean', in m/s.
At the right hand bottom are numerous droplet diameters and the parameters for the Rosin-Rammler equation presented.

- This software made it possible to gain all data that are needed for the numerical modeling and the comparison of the droplet diameter with the literature.

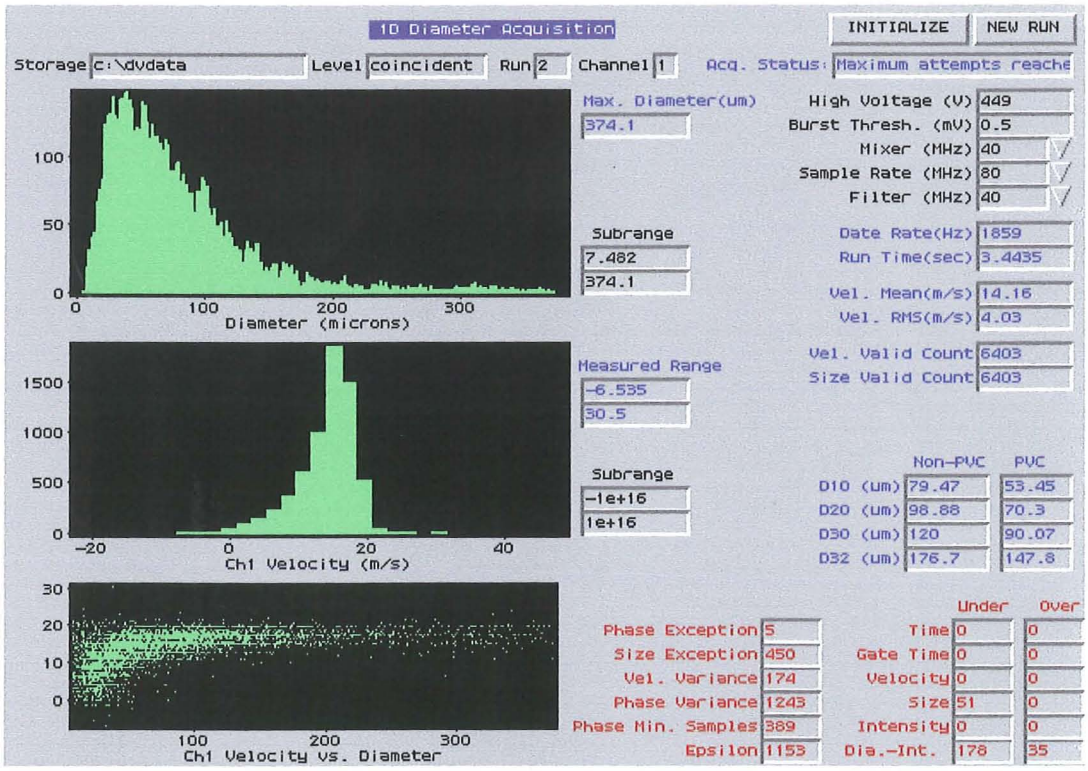

Figure 4-33: Output of the real time analyser of the PDPA showing the droplet distribution

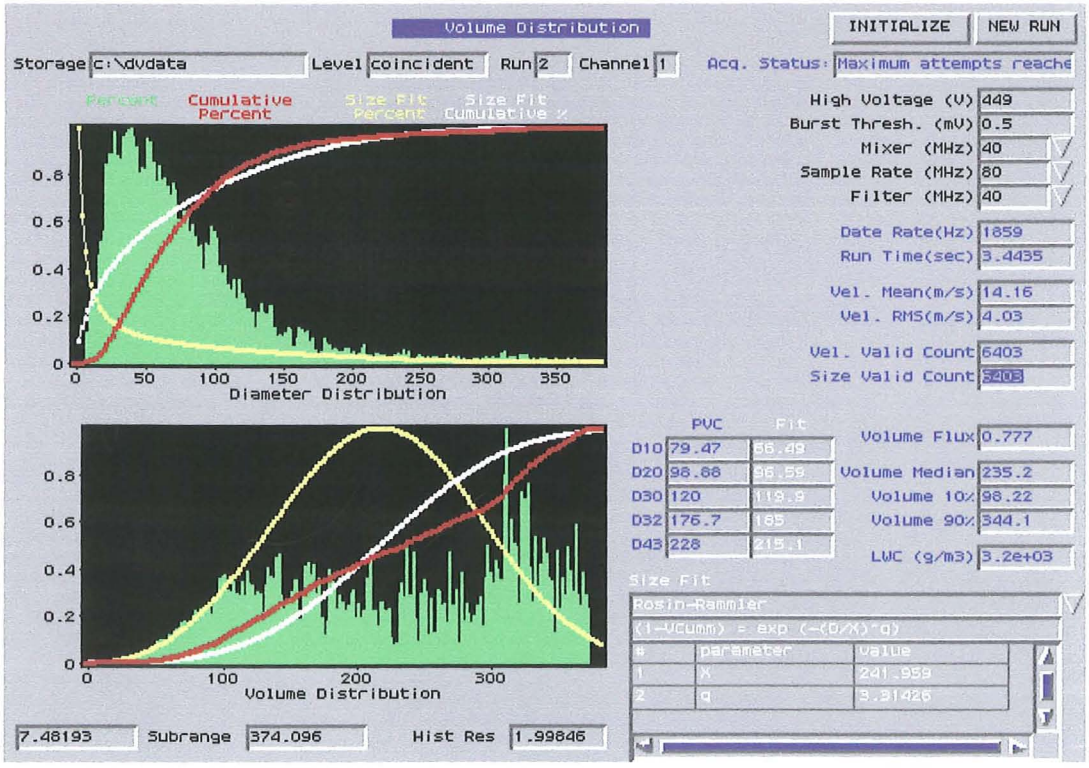

Figure 4-34: Diameter and Volume Distribution result from PDPA

The measurement of the spray angle for the configuration 9a20, 9a26, 27a20 and 27a26 are made at the same water pressure as for the droplet size measurement and experiments. The results of these similar configurations are not shown to avoid confusion. The spray angle in Figure 4-35 is presented over the water pressure to emphasise what effect the difference in the internal geometry has on the spray angle. The line indicates the calculated spray angle after the literature. The empirical equation does not allow for the number of tangential slots and therefore the 9/27a26 and the 9/27a20 nozzles have the same results. It is easy to see that the measured spray angle for the configuration 9/27a26 is in a reasonable agreement with the calculated results. The results for the 9/27a20 configuration are always lower and have a difference of approximately 5° over the whole pressure range from the calculated spray angle. There is no impact on the spray angle due to the hot air flow.

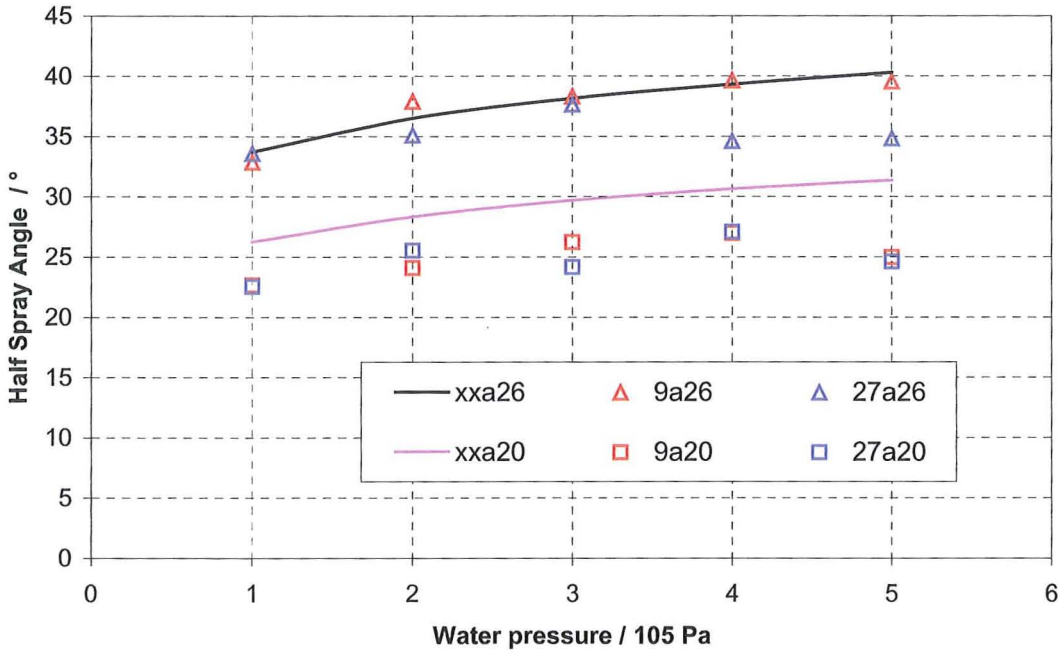

Figure 4-35: Comparison of measured to theoretical spray angle over the water pressure

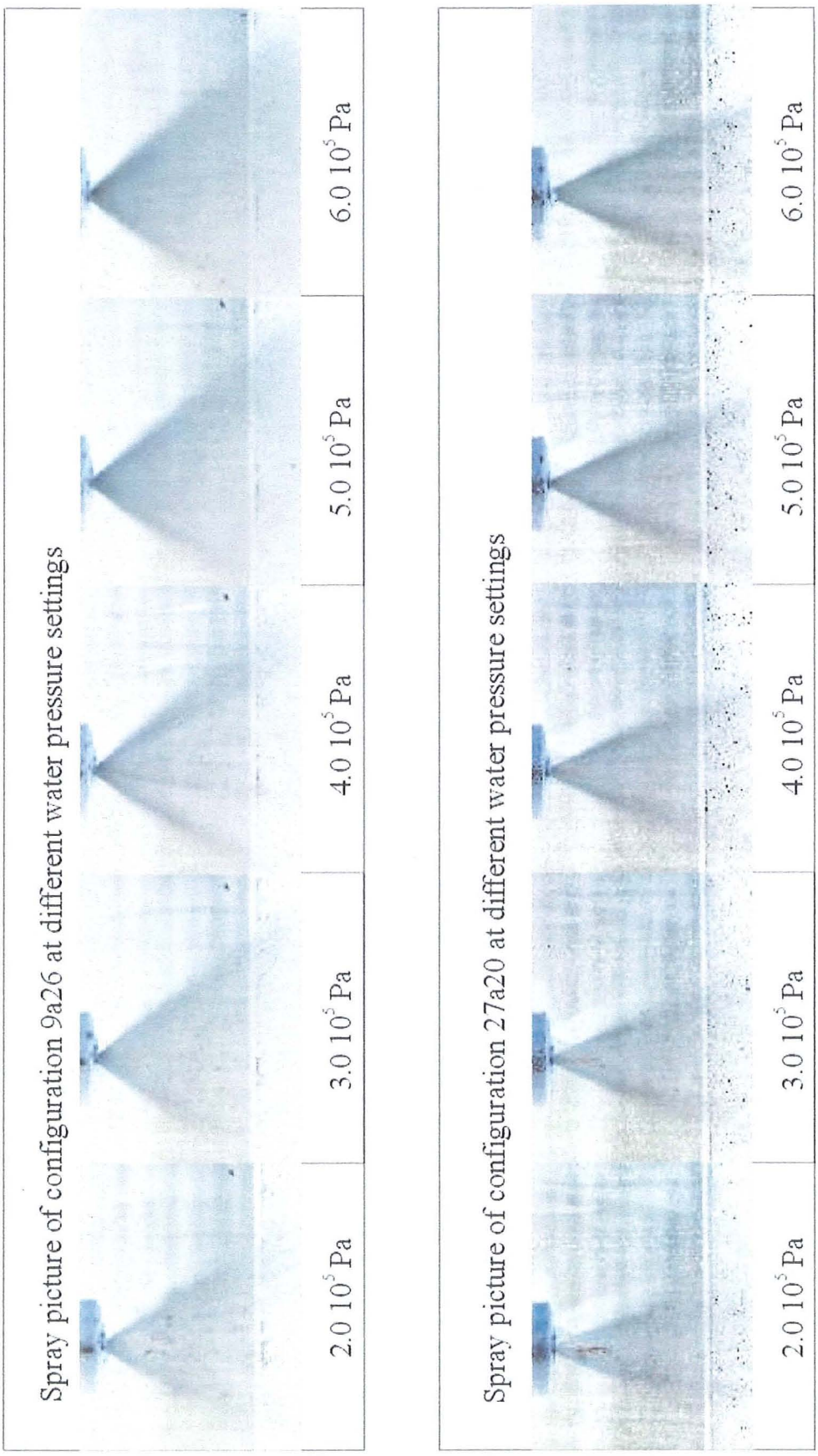

Figure 4-36: Spray pictures of the configuration 9a26 and 27a20 for different absolute water pressure settings

4.5 Summary of experimental results

The work described in this chapter has been undertaken to understand the mechanisms of heat and mass transfer between liquid sprays produced by pressure swirl nozzles and effervescent atomisers and gases. The transfer rates are calculated from measurements of the inlet and outlet conditions of both mediums. The pressure swirl nozzles and effervescent atomisers were designed to allow for change of internal configuration. Tests with different gas inlet temperatures, nominally 80°C and 150°C, have shown that the heat transfer is proportional to the driving temperature difference. An air inlet temperature of 150°C was chosen to minimise random errors of the intrumentation. An important factor to use high temperature difference is, that the error rate of the instrumentation, in relation to the measured temperature difference is smaller. This reduction of errors is important because the experimental data are the basic elements for further calculation and therefore a minimisation of the deviation is essential. The maximum temperature was limited by the capabilities of the perspex chamber. Water inlet pressure of $1x10^5$ to $5x10^5$ Pa was used with the pressure swirl nozzle. The water flow rate ranged from 30 to 220 g s^{-1}. Water inlet pressure of $1x10^5$ to $2.5x10^5$ Pa was used with the effervescent nozzles, which operated with the same water flow rate range as the pressure swirl nozzles.

- The heat transfer rates depend on the droplet size and the droplet velocity. For injected water pressure of $1x10^5$ Pa the pressure swirl nozzle's spray droplets are of approximately 240 μm diameter and a velocity of 10 m/s. Specific heat transfer rates for pressure swirl and effervescent nozzles are compared in Figure 4-37.

- The effectiveness of the effervescent atomiser is constant at about 90% over the whole water flow rate. The effectiveness of the pressure swirl nozzle ranges from approximately 60% at 35 g/s to 90% at 100 g/s and it eventually increases to about 94%. The change of geometrical dimensions has a greater influence on the performance of a pressure swirl nozzle than for the effervescent atomiser.

- The energy requirement to produce spray droplets for a given rate of heat transfer are considerably lower for pressure swirl nozzles than for

effervescent nozzles. The reason is that in the pressure swirl nozzle the water pressure energy is transformed into kinetic energy, which is needed for the production of the droplets (see Chapter 2).

- The high energy requirement of the effervescent atomiser results from the second medium, in this case air. The ALR has a major influence as described in section 4.3. For higher ALR, more energy is needed. The high ALR reduces the air temperature by mixing the water with the atomising air. The droplet cooling performance is reduced in these conditions. In Figure 4-18 it is shown that at higher ALR's more energy is needed. It is also seen that at higher ALRs less water is used. This result is more visible in Figure 4-38 where the transferred energy is divided by the total energy needed to produce the droplets.

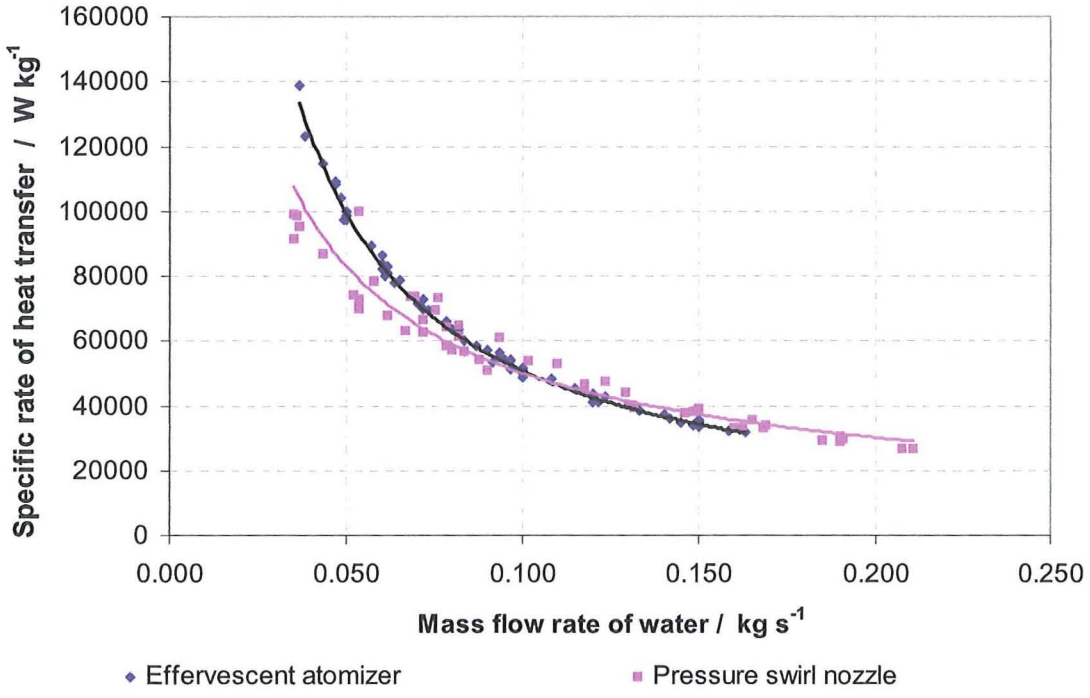

Figure 4-37: Comparison of the specific energy transfer from pressure swirl and effervescent atomiser

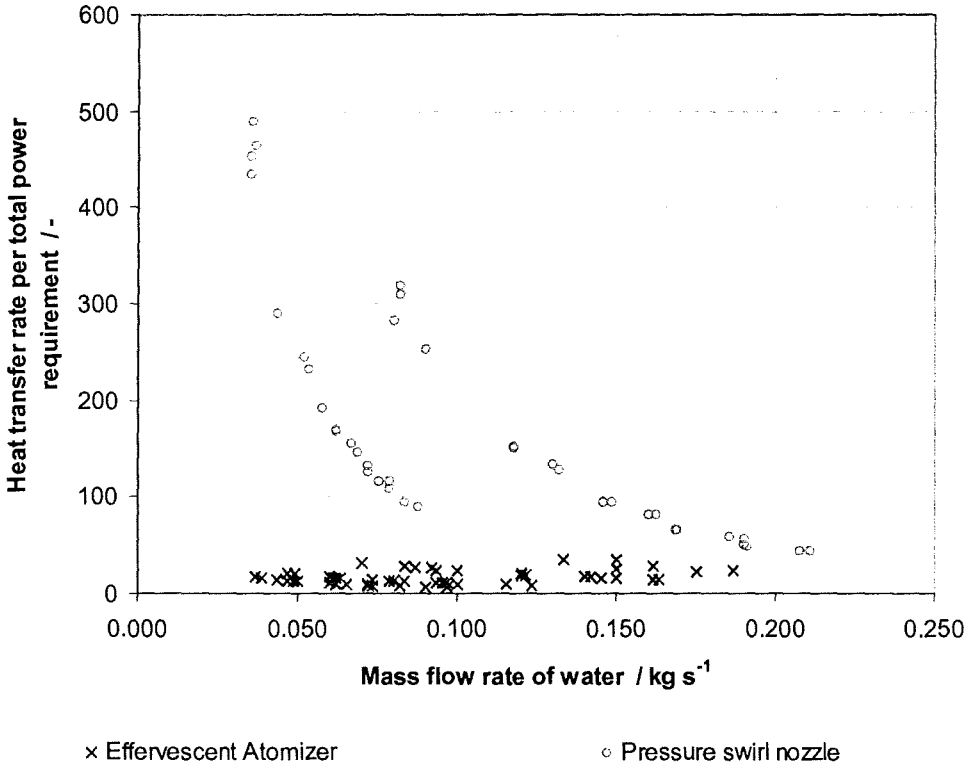

Figure 4-38: Comparison of the energy transferred per unit energy required to produce the mass flow rate of water

- From the point of view of energy requirement for the production of the spray droplets the pressure swirl nozzle is the better nozzle. The best configuration with the highest heat transfer rate and effectiveness is a nozzle with the atomiser constant, K = 0.267, which differs from the result found by Jones (1982). Jones research was designed to find the best spray quality and his result for the atomiser constant is 0.53. The result of the ratio of the spray chamber to exit orifice diameter is 1.6 whereby Jones obtained 2.7. The ratio of the length to diameter of the exit orifice was determined at 0.489. Investigation of the ratio of the length to diameter of the swirl chamber for the pressure swirl nozzle was not performed. These ratios were determined under consideration of the best heat transfer performance and not considering the spray quality produced by the nozzle.

An energy balance for the direct contact heat exchange was calculated for the configurations that have been considered in the numerical simulations. For the configuration 9a20/26, 9c20/29, 27a20/26, 27c20/29 the heat transfer through the spray chamber was based on the experimental results of the inlet and outlet conditions calculated. The calculation was made by using equations shown below from Bird et al, 1960, Incropera and De Witt, 1990, Holman, 1992, Eastop and McConkey, 1986, Rogers and Mayhew,1995. Radiation, the heat loss of the spray chamber, and the momentum transfer are neglected because of its insignificant effect on the results. The reason for the calculation was to find out how much the error rate of the instrumentation influences the result of the energy balance and if this simple calculation can give an estimated result within ±20% accuracy.

Inside the spray chamber the air was cooled by the water droplets. The surface area of the droplets mainly influenced the cooling. The hot air entered the spray chamber at the bottom with a temperature of approximately 150°C. The energy was divided into that of the dry air and the energy carried within the specific humidity. The air left at the top of the spray chamber with a lower temperature than the inlet temperature. The water droplets entered the spray chamber at the top and left through the water trap at the bottom. The trajectories of the water droplets are in a counter current radial flow outward to the spray chamber wall. Some of the droplets bounced back into the spray chamber after hitting the wall, some coalesced and formed a falling water film. Heat transfer from the air to the water droplet increased the water temperature. The saturation temperature of the vapour contents in the air was not reached and therefore some of the energy was used to vaporise parts of the water droplet. The latent heat to vaporise water came from the air and caused a temperature drop. Hence, a non-vaporising fluid would not have achieved the same rate of heat transfer (if the rest of the physical properties are the same). This is the reason to distinguish the calculation of the energy balance into energy transfer caused by the water and by the air.

The calculation was divided into two sections: a) Energy transfer of water between inlet and outlet conditions, b) Energy transfer of air between inlet and outlet conditions.

The energy transfer of the water at inlet and outlet conditions was calculated from

$$Q_{w_{in}} = \dot{m}_{w_1} h_{w_1} \quad [111]$$

$$Q_{w_{out}} = \dot{m}_{w_2} h_{w_2} + \dot{m}_a(\omega_2 - \omega_1)h_{v_2} \quad [112]$$

$$\Delta Q_w = Q_{w_{out}} - Q_{w_{in}} \quad [113]$$

whereby the heat transfer coefficient was calculated as a function of the water temperature. The energy absorbed by the water includes the latent heat of vaporisation of the liquid. This is measured as the increase of the specific humidity of the air.

The energy transfer of the water at inlet and outlet conditions was calculated from

$$Q_{a_{in}} = \dot{m}_a\left(c_{p_1} t_{a_1} + \omega_1 h_{v_1}\right) \quad [114]$$

$$Q_{a_{out}} = \dot{m}_a\left(c_{p_2} t_{a_2} + \omega_1 h_{v_2}\right) \quad [115]$$

$$\Delta Q_a = Q_{a_{out}} - Q_{a_{in}} \quad [116]$$

whereby the specific humidity at inlet conditions was taken as the reference for the change of the vaporised phase. The temperature of the specific humidity changed and causes an energy loss of the vapour phase. The temperature drop of the air resulted in an energy loss.

The energy balance was calculated by adding the change of energy of the two properties (air and water). The change of energy between in let and outlet conditions at the water was positive and at the air negative.

$$\Delta Q = \Delta Q_w + \Delta Q_a \quad [117]$$

The error rate was calculated based on the change of energy of water, because the transfer is cause by the water and is its main variable and was therefore taken to be the basis of the error rate. The resulting difference of the energy balance was divided by the change of energy of the water.

$$Error = \frac{\Delta Q}{\Delta Q_w} \quad [118]$$

This calculation was made for five different pressure points for all eight above mentioned configurations. A total of forty energy balance errors were calculated and shown in Figure 4-39 over the mass flow rate of water.

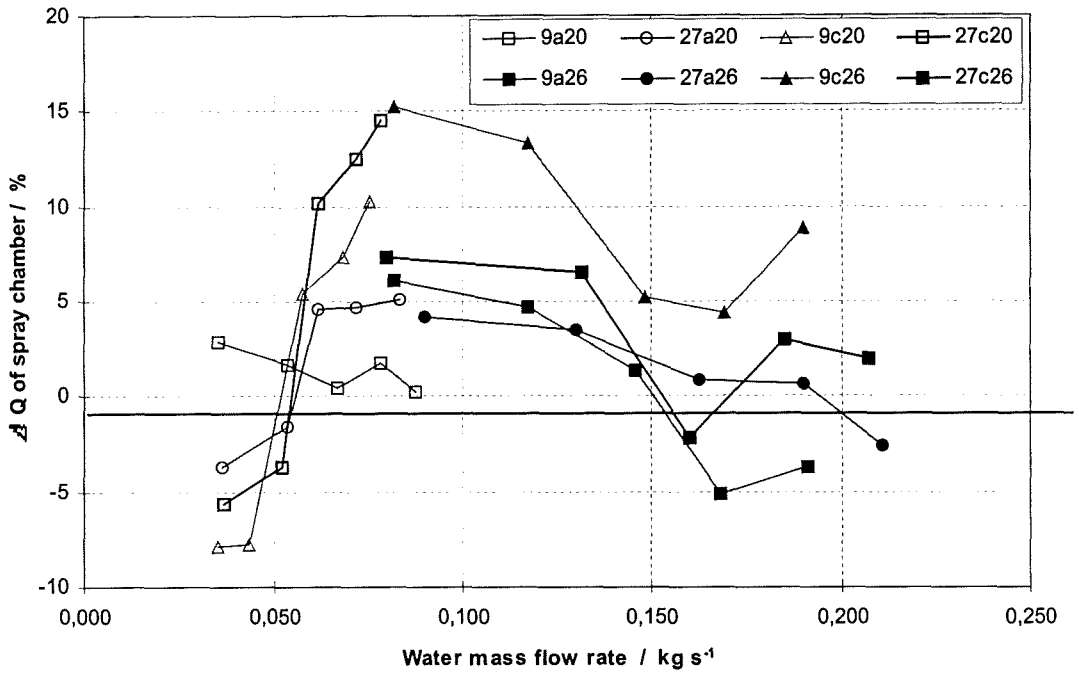

Figure 4-39: Percentage difference of the energy balance from the experimental results

The energy balance errors vary between –8% and +15%. The reason for the relative high error is the measurement of the water temperature. It was not possible to keep a constant supply water temperature. The incoming water temperature varied up to 2°C, because it came from a storage tank outside the university, which was refilled during the experiments. The second uncertainties are the K-type thermocouples that were used to measure the water temperature at inlet and outlet conditions. An error of 0.1°C in the water temperature results in a 4.8% error of the energy balance. The smallest errors were found for the configuration 9a20, 9a26, 27a20, and 27a26. The experimental results of these four configurations are used for comparison with the results of the simulation. The simulation does not calculate the error of the energy balance. The result will be the outlet temperature of the air, which has due to the high temperature difference with the same uncertainty a smaller error rate.

The result of the energy balance error shows that it is possible to determine the approximate mass flow rate of water to achieve a certain air temperature. The energy balance errors for some of the effervescent atomisers are not calculated for two reasons. Firstly the energy balance error for the effervescent is of secondary interest. Secondly the uncertainty of the experimental results for the effervescent atomiser are higher than for the pressure swirl atomiser due to the use of atomising air.

Chapter 5 Computational Fluid Dynamics Model and Results

5.1 Introduction

This chapter describes the essential features of the computational fluid dynamics (CFD) model developed to numerically simulate the spray chamber test conditions. The immediate purpose of the model in this work is to provide numerical predictions of the overall temperature and moisture content changes of the gas flowing through the spray chamber for comparison with the experimental test results.

The model was developed using a commercially available CFD software package that employs the finite volume method. Computation of the three-dimensional recirculating gas flow and associated spray droplet motion, including droplet-wall interaction, gas-droplet heat transfer and droplet evaporation are all accommodated by the model. In addition to the overall gas property changes, e.g. vector velocity, pressure, and density, the model provides information about the velocity components, flow patterns, temperature and moisture content of the gas throughout the spray chamber. Detailed histories of droplet diameter and velocity changes and droplet trajectories can be obtained.

The numerical modelling considers only the case of a single centrally mounted pressure swirl nozzle providing a downward spray of cold water droplets into a hot unsaturated air flow in overall upward counter flow through a cylindrical chamber. The model allows results to be obtained for different gas and spray liquid mass flow rates, and spray characteristics (initial spray droplet angles and velocity, spray droplet size distribution) by simply changing the input data. The model developed could be easily adapted to deal with changes to the spray chamber dimensions, the number and positions of the spray nozzles, and the positions and sizes of the inlet and exit gas ducts. Simulation of the spray chamber conditions for the case of an effervescent spray nozzle has not been attempted, because of the high power requirement.

Results obtained using the model are presented below. These include results demonstrating grid independence and convergence of iterations of the numerical model, as well as predicted gas temperature and humidity changes for typical spray

chamber conditions. The main comparison of numerical predictions with the experimental test data is presented in chapter 6.

5.2 Simulation software

5.2.1 Introduction

The physical aspects of any fluid flow are governed by three fundamental principles: mass conservation, conservation of momentum (Newton's second law of motion), and energy. These fundamental principles can be expressed in terms of mathematical equations, which in their most general form are usually partial differential equations. Computational Fluid Dynamics (CFD) is the technology of determining a numerical solution for the governing equations of fluid flow whilst advancing the solution through space or time to obtain a numerical description of the complete flow field of interest.

The governing equations for Newtonian fluids, and the unsteady Navier-Stokes equations, have been known for over a century. However, the analytical investigation of reduced forms of these equations is still an active area of research (Young (1995) and Park et al. (1996)). Experimental fluid dynamics has played an important role in validating and delineating the limits of the various approximations to the governing equations (Coleman and Stern (1997)).

Johnson (1996) reported that the steady improvement in the speed of computers and the available memory size since the 1950s has led to the emergence of CFD. CFD complements experimental and theoretical fluid dynamics by providing an alternative cost effective means of simulating real flows. It offers the means of testing theoretical advances for conditions unavailable on an experimental basis (Fritsching and Bauckhage (1994) and Fritsching et al. (1995)).

5.2.2 Mathematics used by Computational Fluid Dynamics

A number of articles and books are available that report and explain the used theory including Versteeg and Malalasekera, "An Introduction to Computational Fluid Dynamics", and SV Patankar, "Numerical Heat Transfer and Fluid Flow". Useful information is also provided in the articles of Crowe et al. (1977), Nam (1993), and Jicha et al. (1994).

A domain volume is divided into small cells. CFD considers a small cell to one element of the domain that has to be solved. The domain is the geometry of the flow problem that is investigated. This domain can have obstacles inside and represents the true geometrical reconstruction of the body of interest where the fluid flow appears as shown by Risk et al. (1997) and Crocker and Fuller (1997). A grid is used to define cells for the calculation for a 3D problem. Each cell, placed in a co-ordinate axes system, has six surfaces, which are labelled North (N), South (S), East (E), West (W), Top (T) and Bottom (B) with the lengths of δx, δy, and δz. Fluid flux through these surfaces changes the properties of the cell, which is represented by the small element in the centre of the cell. The numerical calculation is based on the assumption that all fluid properties are in thermodynamic equilibrium.

The net rate of flow of mass into a fluid element that crosses the boundaries of the cell is given by

$$\left.\begin{aligned}&\left(\rho u-\frac{\partial(\rho u)}{\partial x}\tfrac{1}{2}\delta x\right)\delta y\delta z-\left(\rho u+\frac{\partial(\rho u)}{\partial x}\tfrac{1}{2}\delta x\right)\delta y\delta z\\&+\left(\rho v-\frac{\partial(\rho v)}{\partial y}\tfrac{1}{2}\delta y\right)\delta x\delta z-\left(\rho v+\frac{\partial(\rho v)}{\partial y}\tfrac{1}{2}\delta y\right)\delta x\delta z\\&+\left(\rho w-\frac{\partial(\rho w)}{\partial z}\tfrac{1}{2}\delta z\right)\delta x\delta y-\left(\rho w+\frac{\partial(\rho w)}{\partial z}\tfrac{1}{2}\delta z\right)\delta x\delta y\end{aligned}\right\} \quad [119]$$

Figure 5-1 shows the cell with its boundaries and the general description of mass flow and heat flow components crossing its boundaries.

The following substitutions should be made on the general mathematical description:

Symbol	Mass flow	Heat flux
K_X	ρu	q_x
K_Y	ρv	q_y
K_Z	ρw	q_z

Flow that is flowing into the cell, increases the mass of the element and therefore has a positive sign whereby flow leaving the cell decreases the mass of the element hence has a negative sign.

To use the conservation equations for solving flow and fluid properties in the domain they need to be discretised. A grid divides the domain into cells. The centrelines of

the cells are called nodes. Assuming a three dimensional grid created in the domain, a line of nodes is created for every axial direction. A control volume is defined with its boundaries halfway between the nodes. Hence, a control volume with the size of δx by δy by δz, as illustrated on a two dimensional grid in Figure 5-3, is created.

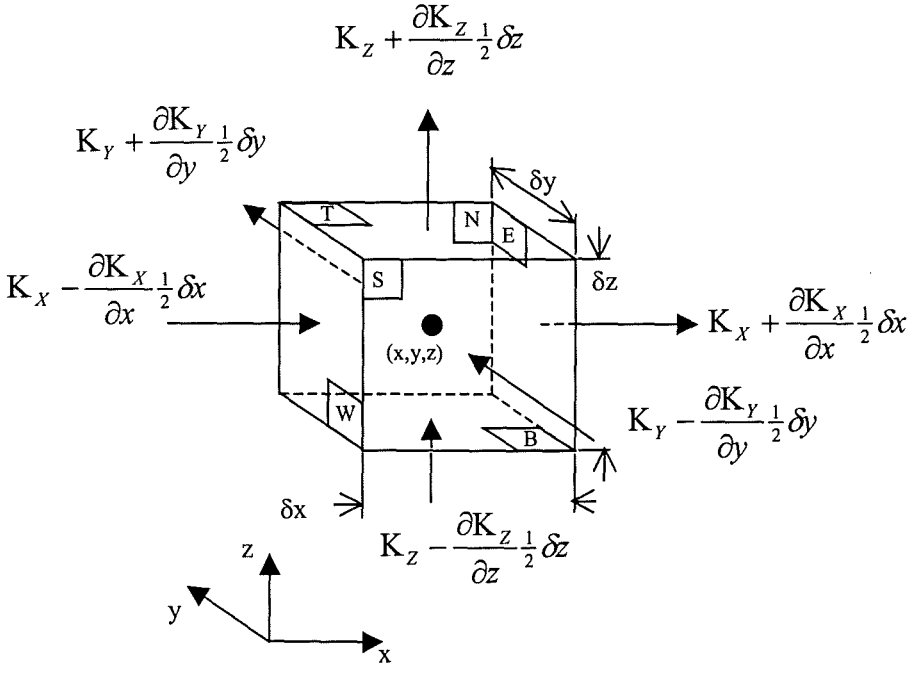

Figure 5-1: Flow across cell boundaries and components used for mass flow and heat flux

The discretised conservation equation is then used to solve for the fluid flow and properties for a specific point by taking into account the values at the neighbouring cells. The node, at the centre of the cell, holds the value of the pressure and temperature or enthalpy for the control volume. The velocities are calculated at the vertices surfaces of the control volume.

The most complex two-phase flow problem is that for which there is non-negligible transfer of momentum, heat, and mass between the phases. For such problems, the literature provides two distinct modeling methods:

- Eulerian
- Lagrangian

Eulerian Method

In the Eulerian method, each phase is treated as a continuum. This treatment is based on the assumption that there exists a set of continuum equations (such as the Navier-Stokes and energy equations) for each phase at every point in the computational domain. To account for the fact that, in theory, both fluids are present at every point, the notion of volume fraction is introduced—which allows the concept of averaging over arbitrarily small volumes. The two sets of equations are coupled through the volume fraction as well as through interfacial forces and heat- and mass-transfer relations.

Lagrangian Method

In the Lagrangian method, only the carrier phase is treated as a continuum, subject to the equations of continuum fluid mechanics. The dispersed phase is treated as if it were com-posed of particles that are subject to the Lagrangian equations described below. However, this model assumes a two-way transfer of momentum, mass, and heat between the phases. In particular, the dynamics of the dispersed phase influences the dynamics of the carrier phase.

The solution procedure used in the Lagrangian two-phase flow model is iterative in nature. It involves the following steps.

1. Obtain a solution to the governing continuum equations for the carrier phase.
2. Solve the Lagrangian (ordinary differential) equations, using the fields from the continuum solution, for a number of particles of different sizes and different starting locations.
3. Take into account the effect of the presence of the particulate phase on the continuum phase by transfer of mass, momentum, and heat. In GENTRA, this step employs the Particle Source in Cell (PSIC) method. In the PSIC method, the computed trajectories, temperatures, and masses of the particles are combined into source terms for mass, momentum, and heat, which are inserted into the right-hand sides of the respective continuum equations. Specifically, the equations of motion for the particle trajectories provide the

source term for the momentum equations, the heat transfer equations for the particles provide the source term for the continuum energy equation, and the mass transfer equations for the particles provide the source terms for the continuity and species equations.

4. Solve the continuum equations again, this time including the source terms from Step 3 in place.
5. Use the output of the computation to specify a new set of field quantities for the Lagrangian equations, which are then re-integrated.

The process of iteration is continued until an equilibrium is attained between the solution of the two phases. These coupling phenomena comprises a very complex interaction that affects both the gas and droplet phase as illustrated in Figure 5-2

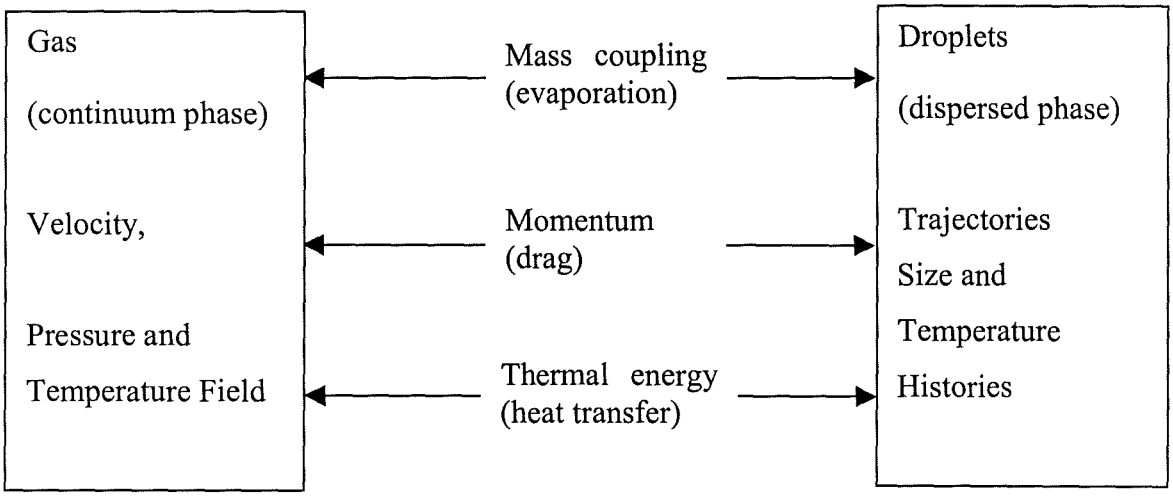

Figure 5-2: Coupling phenomena between continuum and dispersed phase

5.2.3 Governing Equations

The following sections describe the equations that GENTRA uses to model the dispersed and carrier phases for two-phase flow problems.

5.2.4 Dispersed Phase

Mass Conservation

The mass conservation equation for each particle in the dispersed phase is as follows:

$$\frac{dm_p}{dt} = Sh(\pi\rho\alpha D_p)(c - c_s) + f_m \qquad [120]$$

where

c = concentration (mass fraction) of any particular component in the carrier phase that is increasing or decreasing due to interaction with the particle

c_s = surface concentration of the component on the surface of the particle

f_m = an arbitrary source term

α = species diffusivity

Sh = Sherwood number, a dimensionless parameter that serves as a measure of the mass transfer between the phases

The Sherwood number is obtained from the correlation

$$\mathrm{Sh} = 2 + 0.6\mathrm{Re}^{0.5}\,\mathrm{Sc}^{0.33} \qquad [121]$$

where Sc is the Schmidt number.

Meaning of Terms

The first term on the right hand side of [120] is a model of diffusion dominated mass transfer at a wet surface. It expresses the fact that the rate of change of the particle mass is proportional to the difference between the component concentration in the carrier phase and in an infinitesimally thin layer on the surface of the particle. As such, the term is appropriate for modelling of phenomena such as evaporation and condensation.

The surface concentration, c_s, is related to the saturation (vapour) pressure of the component in the carrier phase by the equation

$$c_s = \frac{M_k p_s}{\rho R T_p} \qquad [122]$$

where

M_k= molecular weight of the species (k) undergoing phase change

R = universal gas constant

ρ = density of the carrier phase

T_p= temperature of the particle

p_s = saturation pressure

Typically, the saturation pressure, p_s, is defined by the Clausius-Clapeyron equation that is,

$$p_s = p_{ref} \exp\left[-\frac{LM_k}{RT_{ref}} \left(\frac{T_{ref}}{T_p} - 1 \right) \right] \qquad [123]$$

where L is the latent heat, and p_{ref} and T_{ref} are, respectively, reference values of pressure and temperature associated with the Clausius-Clapeyron curve.

The second term on the right hand side of [120] is an arbitrary source term. In modeling combustion, for example, this term takes the form of a chemical reaction that describes how a particle reacts with its environment to lose mass and produce a gaseous component of the mixture that is the carrier phase.

Momentum Conservation

The motion of each particle of the dispersed phase is governed by an equation that balances the mass acceleration of the particle with the forces acting upon it. The GENTRA model assumes that all particles are spherical and that they remain spherical even if they gain or lose mass.

For a particle of density ρ_p and diameter D_p, the relevant governing equation is

$$\frac{du_i^p}{dt} = \frac{1}{\tau}\left(u_i - u_i^p\right) + \left(\frac{\rho_p - \rho}{\rho_p} \right) g_i + f_i^p \qquad [124]$$

where

u_i^p = particle velocity, which is related to x_i^p, the position coordinate of the particle at time t, by the kinematic equation $\frac{dx_i^p}{dt} = u_i^p$

u_i = velocity of the fluid (that is, the carrier phase)

f_i^p = combination of forces acting on the particle

τ = particle relaxation time

The particle relaxation time, τ, is defined by

$$\tau = \frac{4\rho_p D_p^2}{3\mu C_D \mathrm{Re}^p} \quad [125]$$

where

μ = viscosity of the fluid

Re^p = particle Reynolds number

C_D = drag coefficient

The particle Reynolds number, Re^p, in [125] is defined by

$$\mathrm{Re}^p = \frac{D_p \left| u_i - u_i^p \right| \rho_a}{\mu_a} \quad [126]$$

Calculating the Drag Coefficient

The general form of the drag coefficient, C_D, can be written as follows

$$C_D = \frac{24}{\mathrm{Re}^p} F(\mathrm{Re}^p) \quad [127]$$

where F is an empirical function.

Energy Conservation

The equation for the rate of change of thermal energy for a particle has the form

$$m_p c_p^p \frac{dT_p}{dt} = Nu(\pi k D_p)(T - T_p) + L\frac{dm_p}{dt} + m_p c_p^p f_T \quad [128]$$

where

m_p = mass of the particle

c_p^p = specific heat of the particle

k = thermal conductivity of the bulk fluid phase

f_T = general heat source term

Nu = Nusselt number

The Nusselt number, *Nu*, is a dimensionless measure of the heat transfer between the particulate phase and the carrier phase. In general, it is a function of the particle Reynolds number, Re^p, [126] and the Prandtl number, Pr. That is,

$$Nu = F\left(\mathrm{Re}^p, \mathrm{Pr}\right) \qquad [129]$$

As is true of the drag coefficient, there are several empirically based model expressions for the Nusselt number. For particles that do not undergo the loss or gain of mass in the flow, one commonly used representation is

$$Nu = 2 + 0.6\left(\mathrm{Re}^p\right)^{0.5} \mathrm{Pr}^{0.33} \qquad [130]$$

For a particle that undergoes a phase change, [128] can be generalized to the form

$$Nu = F(\mathrm{Re}^p, \mathrm{Pr}, T, T_p) \qquad [131]$$

a specific form of which, for evaporating particles, is

$$Nu = \frac{2 + 0.6\left(\mathrm{Re}^p\right)^{0.5} \mathrm{Pr}^{0.33}}{1 + B} \qquad [132]$$

Meaning of Terms

The first term in equation [128] is the exchange of energy due to the difference in temperature between the particle and the carrier phase. The second term on the right-hand side of [128] is only relevant if phase change is occurring. The general source term, f_T, allows the definition of problem-specific heat transfer between the phases.

5.2.5 Carrier Phase

The equations that pertain to the carrier phase are the Eulerian equations. Each of which is modified to allow for the interaction between the phases. The modifications consist of the addition of a source term on the right-hand side of each equation. Each source term describes the effect of the dispersed phase on the conservation equation in question.

Conservation Equations

For two-phase flow, the Eulerian equations take the following forms.

Mass Conservation

For global mass conservation,

$$\frac{\partial}{\partial x_j}\left(\rho u_j\right)=\Phi^m \qquad [133]$$

where Φ^m is the global mass transfer source term.

For mass conservation of the individual species that are present when the fluid is a mixture

$$\frac{\partial}{\partial x_j}\left(\rho u_j c_k\right)=\frac{\partial}{\partial x_j}\left(\rho\alpha_k\frac{\partial c_k}{\partial x_j}\right)+\Phi_k^c \qquad [134]$$

where Φ_k^c is the source term for species k, and the subscript k refers to the k'th species.

Momentum Conservation

For conservation of momentum,

$$\frac{\partial}{\partial x_j}\left(\rho u_i u_j\right)=-\frac{\partial p}{\partial x_i}+\frac{\partial \tau_{ij}}{\partial x_j}+\Phi_i^M \qquad [135]$$

where Φ_i^M is the source term representing momentum transfer between the carrier phase and the dispersed phase.

Energy Conservation

For the conservation of thermal energy, in the case of an ideal gas,

$$\rho c_v u_j\frac{\partial T}{\partial x_j}=\frac{\partial}{\partial x_j}\left(k\frac{\partial T}{\partial x_j}\right)-p\frac{\partial u_j}{\partial x_j}+\tau_{ij}\frac{\partial u_i}{\partial x_i}+\Phi^T+\left(0.5u_i u_j-c_v T\right)\Phi^m-u_i\Phi_i^M \qquad [136]$$

where Φ^T is the source term representing thermal energy exchange between the carrier phase and the dispersed phase.

In the case of a fluid the density of which depends on temperature and species concentration, but not on pressure, equation [136] is replaced by

$$\rho c_v u_j\frac{\partial T}{\partial x_j}=\frac{\partial}{\partial x_j}\left(k\frac{\partial T}{\partial x_j}\right)+\tau_{ij}\frac{\partial u_i}{\partial x_i}+\Phi^T+\left(0.5u_i u_j-c_v T\right)\Phi^m-u_i\Phi_i^M \qquad [137]$$

The equations described above do not include terms involving body forces, heat sources, or chemical reactions.

Specification of Source Terms

Each of the continuum phase equations described above contains a source term which needs to be defined. The underlying principle of the PSIC method described above (see Crowe, 1977) is that such source terms are defined on an element level rather than globally for the entire computational domain. The procedure for calculating such terms is as follows.

Let N be the total number of elements in the mesh and let n be the total number of particle trajectories passing through the computational domain. A particle trajectory is defined by the solution of the particle momentum equation [124] coupled with the kinematic equation for particle trajectories (equation [125]). Each distinct solution of the pair of equations [124] and [125] (each set of initial conditions, each different size of particle), defines a distinct trajectory.

For any element, E, let n_E be the total number of particle trajectories, see Figure 5-3, passing through E. In general, n_E is less than n, and may even be zero. Each trajectory represents multiple particles the number of which depends on the injection rate or release rate of particles in the computational domain.

Let η_j be the number of particles per unit time traversing the j'th trajectory. Furthermore, let δt_j^E be the time that a particle on the j'th trajectory takes to pass through element E (that is δt_j^E is the residence time of a particle on the j'th trajectory with respect to element E).

Mass Transfer

For mass transfer between the particle and the k'th species of the fluid mixture, we define

$$\Phi_k^c(E) = \frac{1}{V_E}\sum_{j=1}^{n_E}\eta_j \int_{\delta_j}\frac{dm_p^k}{dt}dt = \frac{1}{V_E}\sum_{j=1}^{n_E}\eta_j\left(m_{out}^k - m_{in}^k\right) \qquad [138]$$

for each element, where the integrand is the left hand side of equation [120] referred to the k'th species. The global mass transfer source term is then given by

$$\Phi^m(E) = \sum_k \Phi_k^c(E) \qquad [139]$$

where the summation is made over those species that experience phase change. In many problems there is only one such species, in which case

$$\Phi^m(E)=\Phi^c(E) \qquad [140]$$

Momentum Transfer

As noted above, the transfer of momentum between the carrier phase and the particulate phase is accounted for in the source term Φ_i^M. This momentum transfer is due to the relative drag between the phases. Thus, for each element E, we define

$$\Phi_i^M(E)=\frac{1}{V_E}\sum_{j=1}^{n_E}\eta_i\int\frac{3\mu C_D\,\mathrm{Re}^p V_p}{4D_p^2}\left(u_i-u_i^p\right)dt \qquad [141]$$

where V_E is the volume of the element, and V_P is the volume of the particle. This integral is numerically evaluated using the trapezoidal rule. The accuracy of the computation depends on the number of time steps that a particle takes within an element. In the case where the only forces applied to the particles are the momentum drag and gravity, a more accurate integration is obtained by evaluating the net efflux of momentum from the element adjusted for gravity. That is,

$$\varphi_i^M=\eta_j\left[\left(mu_i^p\right)_{out}-\left(mu_i^p\right)_{in}\right]-\eta_j\left(m-\rho V_p\right)g_i\delta t_j \qquad [142]$$

Heat Transfer

Finally, for the heat transfer between the phases, we define

$$\begin{aligned}\Phi^T(E)&=\frac{1}{V_E}\sum_{j=E}^{n_E}\eta_j\int_{\delta t_j}\left(m_pc_p^p\frac{dT_p}{dt}-L\frac{dm_p}{dt}\right)dt\\&=\frac{1}{V_E}\sum_{j=E}^{n_E}\eta_j\left\{\left[\left(m_pc_p^pT\right)_{out}-\left(m_pc_p^pT\right)_{in}\right]-\left[(mL)_{out}-(mL)_{in}\right]\right\}\end{aligned} \qquad [143]$$

As noted above, the solution procedure used in GENTRA is iterative. The general procedure is as follows:

1. Solve equations [135] – [137] with all source terms set equal to zero.
2. Insert the solution (u_i, T, c) of these equations into the Lagrangian equations
3. [124], [128], and [120].
4. Integrate the Lagrangian equations together with the trajectory equations [125].

5. From these solutions, compile the source terms from the formulas [141] – [143].
6. Substitute the values from Step 4 into [135] – [137].
7. Repeat the procedure until convergence is attained.

Impermeable Boundaries

When a particle reaches an impermeable boundary, the distribution of source terms between the carrier phase and the environment (or wall) depends on the resulting condition of the particle. With respect to striking an impermeable boundary, there are three such possible conditions for the particle:

- Escape
- Rebound
- Trap

Our model was set to use a rebound condition, where the particle exchanges momentum with the carrier phase and the wall. That exchange of momentum is determined by the value of the restitution coefficient. A restitution coefficient less than one indicate that the particle loses some momentum to the wall. Conversely, a restitution coefficient greater than one implies that the particle gains some momentum from the wall.

The conservation equations used are able to solve for laminar flow in the domain. If the flow becomes turbulent, the conservation equations are not able to come to a converged result, because of the interia and viscosity forces which are related to convective effects. Various turbulence models exist to build the system of mean flow equations, e.g. Mixing Length, Reynolds Stress Equation Model, Algebraic Stress equation models, and k-ε model. The k-ε model is the most general turbulence model for mixing and allows the effect of transport of turbulent properties, to be taken into account.

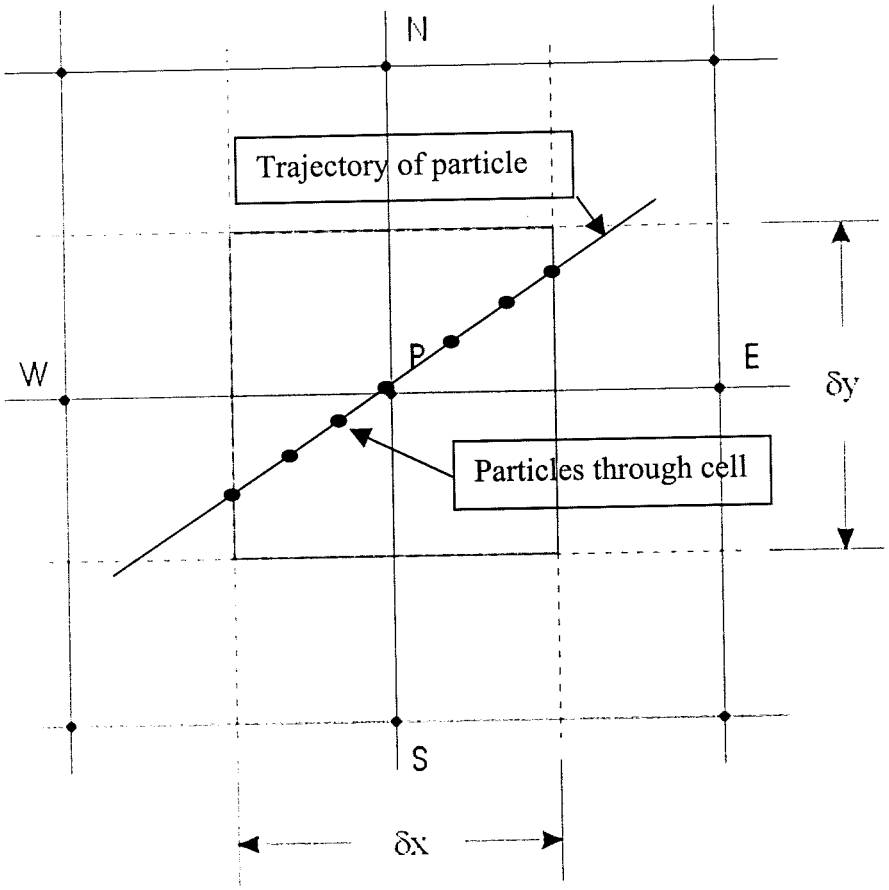

Figure 5-3: Two dimensional grid with control volume

Two additional partial differential transport equations needed to be solved when using the *k-ε* model. First one to calculate the turbulent kinetic energy, k, and the second one to obtain the rate of dissipation of turbulence kinetic energy, ε. To obtain the effective turbulence viscosity the following equation is used

$$\mu_t = \rho C_\mu \frac{k^2}{\varepsilon} \qquad [144]$$

where k is described by

$$\frac{\partial(\rho k)}{\partial t} + div(\rho k U) = div\left[\frac{\mu_t}{\sigma_k} grad\, k\right] + 2\mu_t E_{ij} \cdot E_{ij} - \rho\varepsilon \qquad [145]$$

and ε is calculated by

$$\frac{\partial(\rho \varepsilon)}{\partial t} + div(\rho \varepsilon U) = div\left[\frac{\mu_t}{\sigma_\varepsilon} grad\, \varepsilon\right] + C_{1\varepsilon} 2\mu_t E_{ij} \cdot E_{ij} - C_{2\varepsilon}\rho\varepsilon \qquad [146]$$

The adjustable constants for the general k-ε model are

$$C_\mu=0.09 \qquad \sigma_k=1.00 \qquad \sigma_\varepsilon=1.30 \qquad C_{1\varepsilon}=1.44 \qquad C_{1\varepsilon}=1.92$$

Theses numbers are derived by other researchers from a comprehensive data fitting for a wide range of turbulent flow. A large number of CFD users choose the k-ε model to predict a flow field , e.g. Crow et al. (1977), Nam (1993), Jicha et al. (1994).

The revised Semi-Implicit Methods for Pressure-Linked Equations (SIMPLER) algorithm is used in PHOENICS to calculate pressure, velocities, and the properties of the fluid. SIMPLER is an iterative method to solve the discretised transports equations until they converge. The range of convergence is set to be 0.001, which means that the equation must be solved within 0.1% accuracy. Any higher accuracy is not necessary due to the error of the instrumentation at the test rig. Starting with an initial guess of velocities, pressure, and other transport properties, it solves the discrete momentum and pressure correction equation for the control volume and the vertices surfaces of the cell. After correcting pressure and velocities, it calculated all other properties, e.g. temperature, and humidity with the Navier-Stokes equation based on the corrected pressure and velocities. If the results are converging, it stops. Otherwise the calculation starts from the beginning where the initial guess is replaced by the corrected and calculated results (Figure 5-4).

If other scalars are coupled to the momentum equation, the calculation is performed sequentially (Creismeas (1995)). This happens for example when particles in the flow influence the flow field and properties of the fluid as shown by Edson and Fairell (1994) and Rogers and Katman (1989).

The Lagrangian-Eulerian approach is used to yield the droplet trajectories and the diameter and temperature of the droplet along each trajectory. Each trajectory has a specific mass flow rate, $\dot{m}_p$, and droplets with an initial diameter, d_i, with an initial droplet mass friction, Y_i. From the initial velocity, v_i it is possible to determined the number of droplets, and therefore mass, X_j, entering the cell through the boundaries. Hence, the total mass of droplets entering a cell per unit time is given by

$$\dot{m}_{pj}(D_i)=\dot{m}_p X_i Y_i \qquad [147]$$

where D_i is the droplet diameter entering the cell.

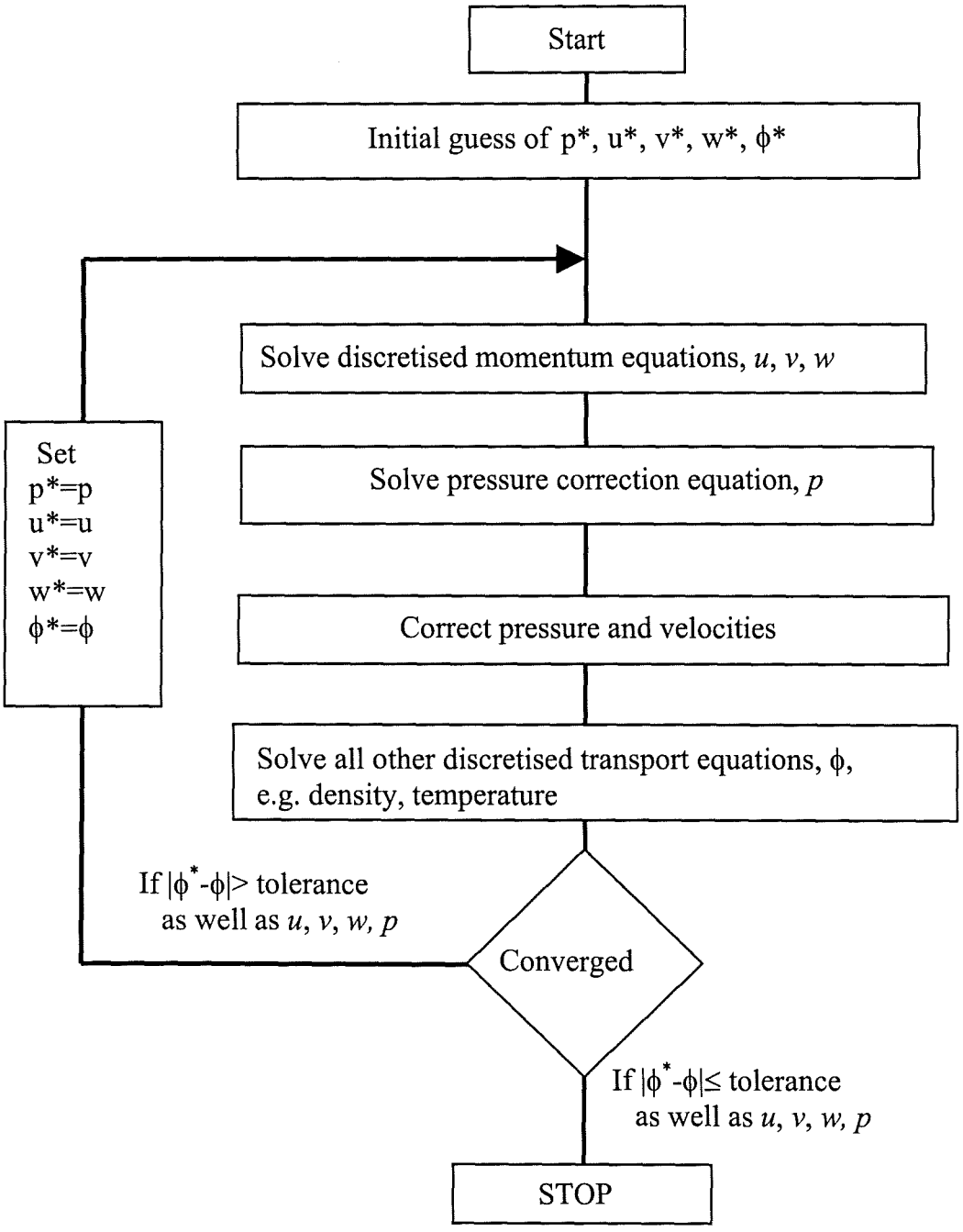

Figure 5-4: The SIMPLER algorithm

The efflux rate of a droplet momentum due to the droplet trajectory is given by

$$\Delta M_{di} = \pi \rho_d \dot{\eta}_i \left(\frac{v_{i,out} D_{i,out}^3 - v_{i,in} D_{i,in}^3}{6} \right) \qquad [148]$$

where ρ_d is the density of the liquid, and $\dot{\eta}_i$ the flow rate of droplets of initial diameter D_i along a given trajectory.

The net efflux rate of droplet enthalpy, ΔE_{di}, for a trajectory in a cell is calculated with the following equation

$$\Delta E_{di} = \pi \rho_d \dot{\eta}_i \left(\frac{h_{i,out} D_{i,out}^3 - h_{i,in} D_{i,in}^3}{6} \right) \quad [149]$$

5.3 Description of the computational fluid dynamics model

5.3.1 PHOENICS code

The PHOENICS version 2.2.1 was used to create the model. This version is a DOS based program and runs on a PC Pentium I 160 MHz with 32 MB Ram and a 1.7 GB hard drive. The software includes a pre- and post-processor (SATELLITE and PHOTON) and a solver (EARTH).

The pre-processor SATELLITE is used to define the model and establish an input file for the solver. The solver uses the particle-in-cell type approach by adopting a combined Lagrangian - Eulerian approach. In this method the dispensed liquid phase, represented by a discrete particle distribution whose motion is calculated in the chosen coordinate system, is integrated with the continuous gas phase, whose motion is solved in the standard Eulerian framework. This is made possible in PHOENICS, by the application of the GENTRA particle tracking software, which is an optional add-on to PHOENICS installations. GENTRA handles different types of particles, including ones for which heat and mass transfer takes place with the gas. GENTRA also allows the investigation of the interaction of particles with the chamber wall, providing for particle removal, 'stick', bounce and flash vaporisation.

5.3.2 General assumption of model

The simulation solves for the velocity, pressure, humidity and temperature field of the gas flow considering the size, trajectory, temperature and history of the droplets. With the mass coupling, momentum and thermal energy transfer between the two phases is calculated and the software provides an overall balance between the inlets

and outlets. The transfer regions, GENMAS and GENPAT, are the areas inside the domain. The boundaries of the transfer regions are the walls, blockages, and the inlet and outlet patches. The dry hot gas enters at the bottom of the domain perpendicular to the spray chamber axis. The average gas flow is upstream and leaves through the coaxial outlet patch at the top of the domain. The coaxial outlet patch made it necessary to model a 3D-problem.

The droplet inlet location is 10 mm from the centre line axis at the top of the spray chamber to avoid numerical clashes. The droplets have an initial velocity, spray angle, temperature, and droplet size. The change of direction and velocity caused by the air is considered. Wall conditions, except for the bottom of the domain, and blockages are set to cause particles bounce. The bottom wall condition of the domain is set to remove any droplets from the domain touching this surface. The coaxial air outlet patch is only for a two-phase gas, dry air and vapour, but not for particles. If a particle tries to pass through this air outlet, it is bounced back into the domain.

The software limits what could be done, especially in the droplet simulation. One limit is the assumption that droplets only leave through the bottom plate of the spray chamber and not through the air outlet patch. The injection point of the droplets has to be moved from the centre line of the domain because it caused numerical clashes, because the south face, see Figure 5-8, is missing of the cell nearest to the centre at the polar grid. The east and the west face are connected. The distance between these faces are treated as zero. If a particle crosses this volume it causes a pressure difference that results in a numerical clash.

In the experiments, some of the droplets are hitting the chamber wall. Some droplets bounced, the rest was forming a falling water film. A falling water film with an average temperature of the droplets that hit the wall could not be defined. The wall restitution coefficient was set to compensate these limits. The water exit is defined as the whole bottom plate and not as a coaxial located opening. This is a compromise and is necessary because the software is unable to move droplets over a surface. The round, coaxially located air outlet patch is defined as a wedge shaped opening, but it has the same opening area.

5.3.3 Choice of grid and grid independency

The first task is to define the size of a domain. Knowing that the heat loss of the spray chamber is negligibly small, the inside, which was set up in the units metres and radians, of the spray chamber forms the domain. A cylindrical co-ordinate system was used to design the spray chamber. In this co-ordinate system, the X-axis represents the angle of the cylinder, which was set to 2π to have a full cylinder. The Y-axis becomes the radius, which was defined to be 0.186 m. The Z-axis is the height of the cylinder, and was defined as 0.372 m.

A grid size for all three axes was defined. Different grid sizes were tested to assure the grid independence. Grid independence means that the results of simulations with different grid sizes are similar. Therefore, a model with constant inlet condition was tested with seven different grid sizes. The number of tested cells was in the range of 2500 to 20000 cells. The table below shows the different tested grid sizes in detail.

Table 5-1: Summary of the different tested grid sizes

Grid size			Number of	Number of iteration	
X-axes	Y-axes	Z-axes	Cells	Total	First Lagrangian
15	13	13	2535	1000	100
20	16	16	5120	1000	100
22	20	19	8360	1000	100
25	20	20	10000	1000	100
25	20	25	12500	1000	100
30	20	25	15000	1000	100
30	25	27	20250	1000	100

All simulations were carried out for a constant number of iterations before they were stopped. The total number of iterations was 1000, whereby after 100 iterations the first Lagrangian step was solved. The convergence rate was set so that when the next computed value was within 0.05% of the previous value then the system was set to have converged. All test runs were performed twice to determine the repeatability. The results for the air humidity varied within ±5% and the air temperature difference was within ±0.7%. This forms evidence that the same result is not reached after the same number of iterations and that every simulation is unique until converged. The

results of the air temperature difference and air humidity difference from the simulations with different grid sizes are compared in Figure 5-5 and Figure 5-6. The air temperature difference is slightly decreasing and the air humidity is increasing. This trend is in agreement with the assumption, where the latent heat to evaporate the water is coming from the air and therefore decreases the temperature of the air. The model with the higher number of cells is reaching the final numerical solution quicker than the one with a coarse grid structure. The reason for that is the smaller distance of the nodal points at finer grid structure. A smaller distance between the nodal points results in a smaller volume and therefore every iteration is more accurate. The maximum inconsistency of the air humidity difference for the tests with different grid sizes is 16% and for the air temperature difference 2%.

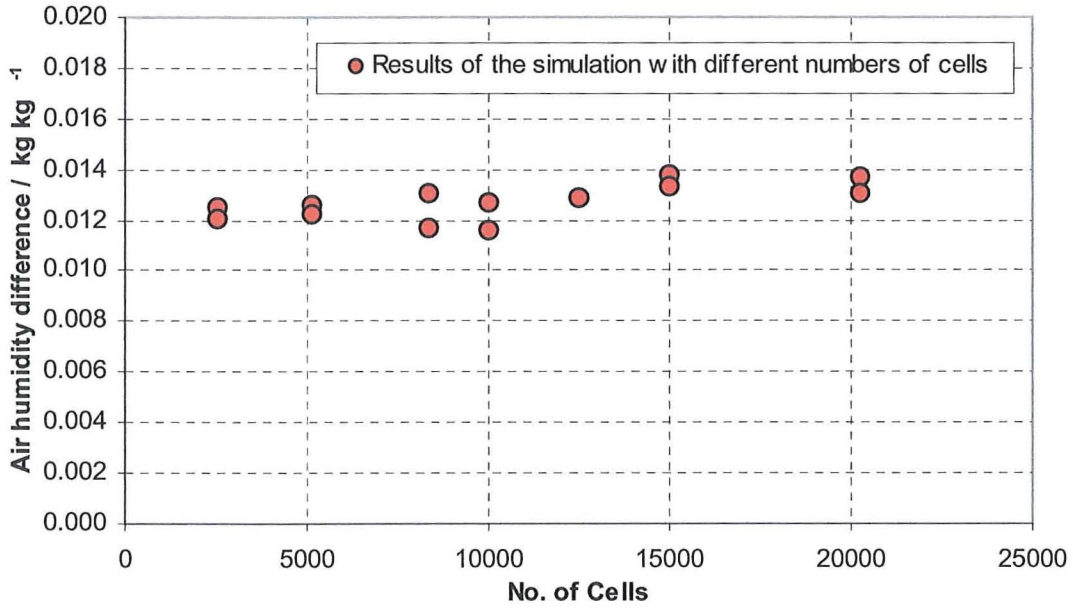

Figure 5-5: Results of air inlet and air outlet humidity difference for models with different grid sizes

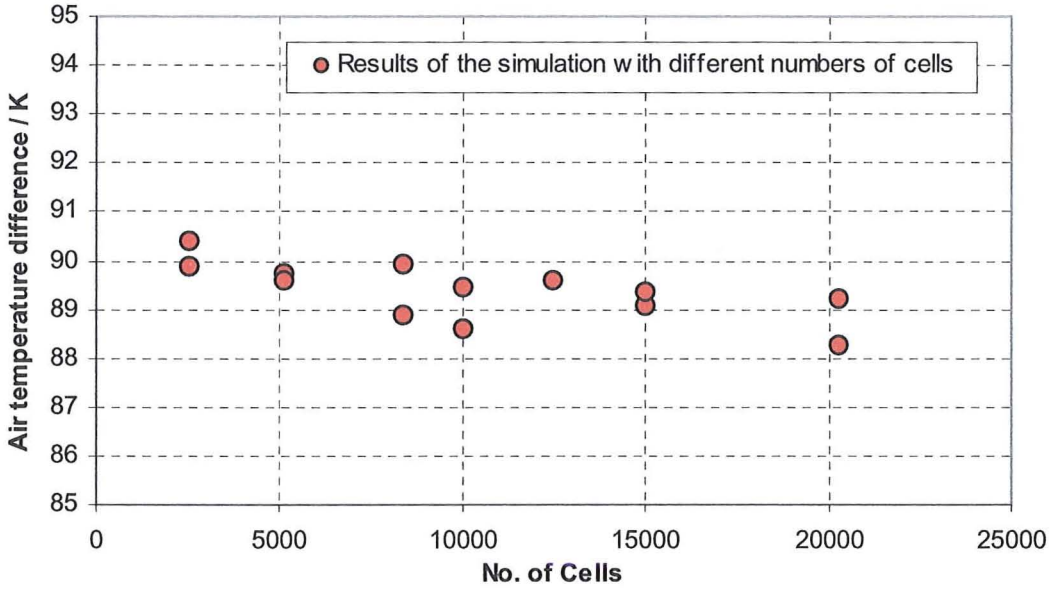

Figure 5-6: Results of air inlet and air outlet temperature difference for models with different grid sizes

As a result of these tests the model with the grid size of X=25 Y=20 Z=25 was chosen. The finer grid ensures that with the setting of the iteration a suitable result is achieved. This leads to 12500 cells and is a good compromise between the results and the computing time of 24 hours. Figure 5-7 shows a three dimensional picture of the cylinder and parts of the grid. The influence of total number of iterations for a model with constant grid size is another point of interest and is discussed later.

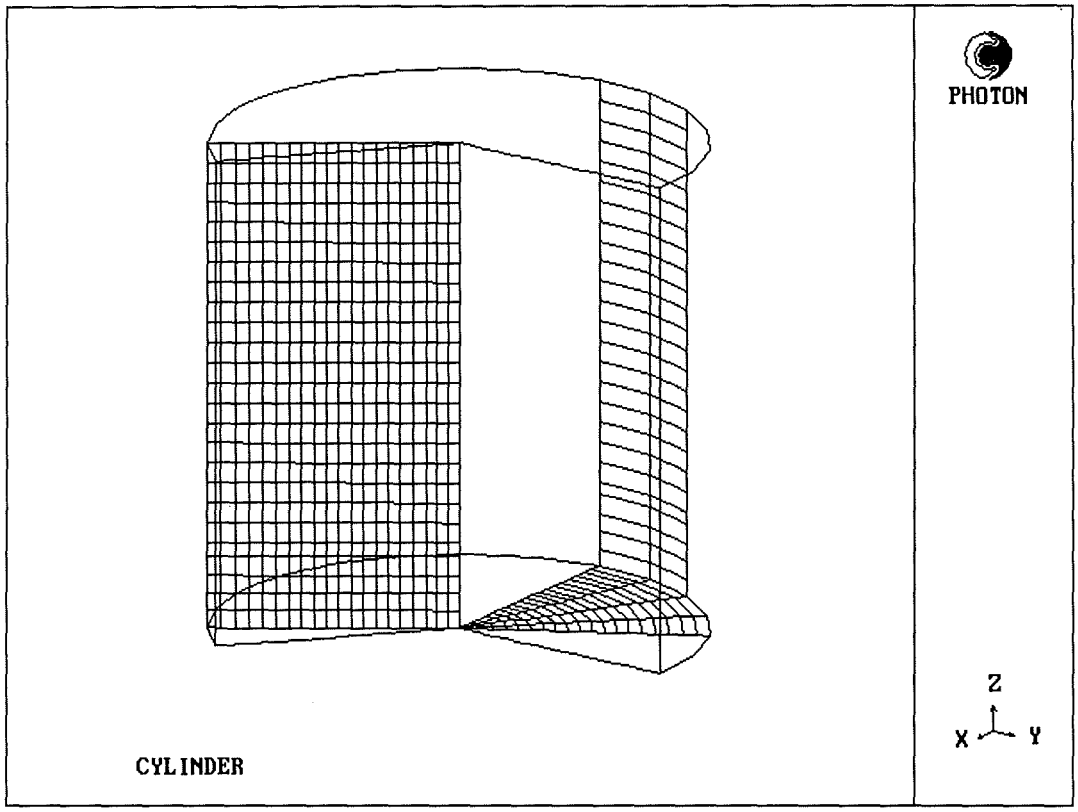

Figure 5-7: Three-dimensional view of the cylinder with a cutout and some grid components

5.3.4 Chamber wall boundary conditions

Each cell surface was named to identify its location from the cell centre and is shown in Figure 5-8. A coordinate system was used to determine the axis. Along the x-axis is the 'East' (positive) and 'West' (negative) face, along the y-axis is the 'North' (positive) and the 'South' (negative) face, and at the z-axis is the 'Low' (negative) and 'High' (positive) face.

Knowing that the heat loss of the spray chamber was insignificantly small, all walls are defined as an adiabatic plate type wall with surface friction applied to them. The program iterates the temperature locally until the heat transfer is zero through the wall. Different materials have different friction factors and the software supported this feature. Therefore the cylindrical wall of the domain is defined as adiabatic Perspex. The top and bottom of the Cylinder are set to adiabatic aluminium for the air. Settings made here apply only to the air phase. The boundaries of the liquid phase, in our case droplets, have to be specified separately.

The cylindrical wall is attached to the 'North' face of all the last cells in the radial direction. Hence, the wall has a length of 2π radian and a height of 372 mm.

The bottom plate wall is located at the 'Low' face of all cells at the bottom row in the x-y plane.

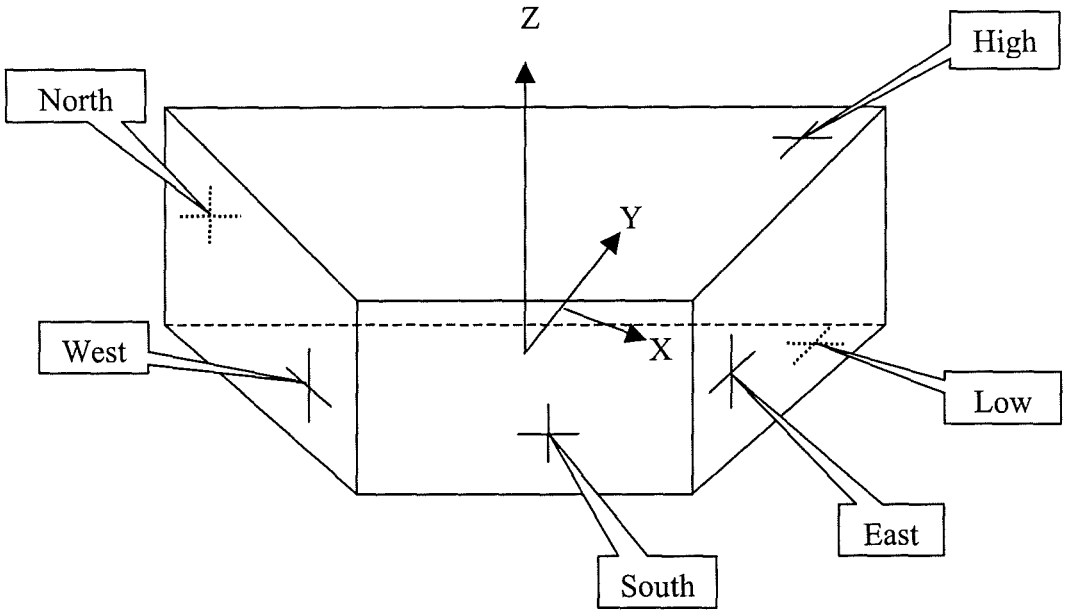

Figure 5-8: Wedge shaped cell with names of the faces and coordinate system

A coaxial air outlet patch of the top of the spray chamber made it necessary to define four plate types on the 'North' face of the top row cells in the x-y plane, as can be seen in Figure 5-9.

The surface settings of the circular wall and for the top walls were set to 'bounding'. The bottom plate wall was set to 'remove'. That means that particles that hit this surface are removed from the domain and have no further influence on the results.

5.3.5 Internal blockages

The internal geometry, the air inlet distributor and the extended pipe of the air inlet, of the spray chamber were defined according to the size of the experimental set-up. The air inlet distributor, the extended pipe, and the gap through which the air was flowing, were defined together as a cylinder. The gap between the air inlet distributor and the extended pipe was set to a height of 0.0125 m and the north face of the cells were later used as air inlet patch. By building a feature, a region was created and was

subdivided by cells. The grid was self-adjusting, so that cells were uniform within the region. Boundary feature, e.g. blockage or fluid, were adapted to the cells.

The internal geometry is shown in Figure 5-10, which is a cut through the cylinder as indicated in Figure 5-9 at A-A. The black filled cells are the blockages and the cell in between with the air inlet conditions at Y direction.

The internal geometry was defined as adiabatic steel. All boundaries had surface friction applied to it. The gravity force was applied to the particles moving in the cylinder along the Z-axis. The Z-axis was pointing upwards and the gravity therefore needed to be set to –9.81 m s^{-1}. The droplet injection is accommodated at the top face of the cylinder at the Y-co-ordinate 0.001 m. It takes the distance of the water film into account when it leaves the exit orifice, because the pressure swirl nozzle is mounted along the Z-axis.

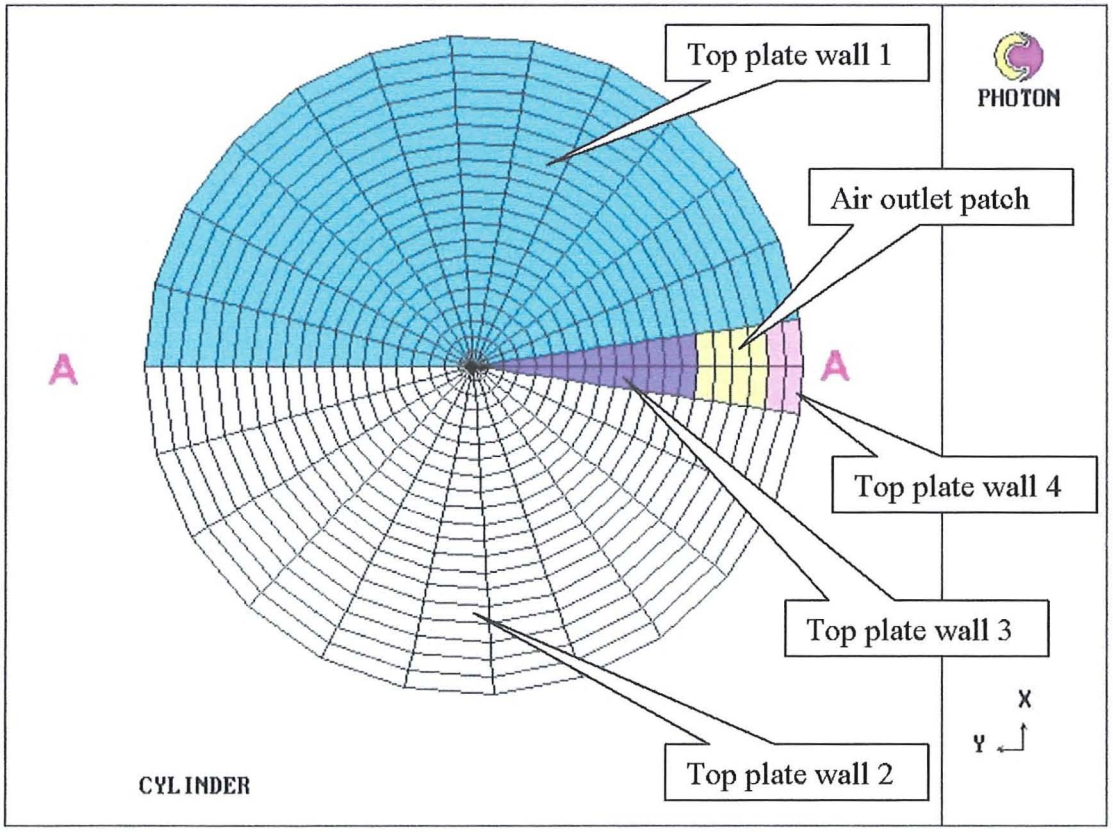

Figure 5-9: View from the top of the domain showing the X-Y grid and the air outlet

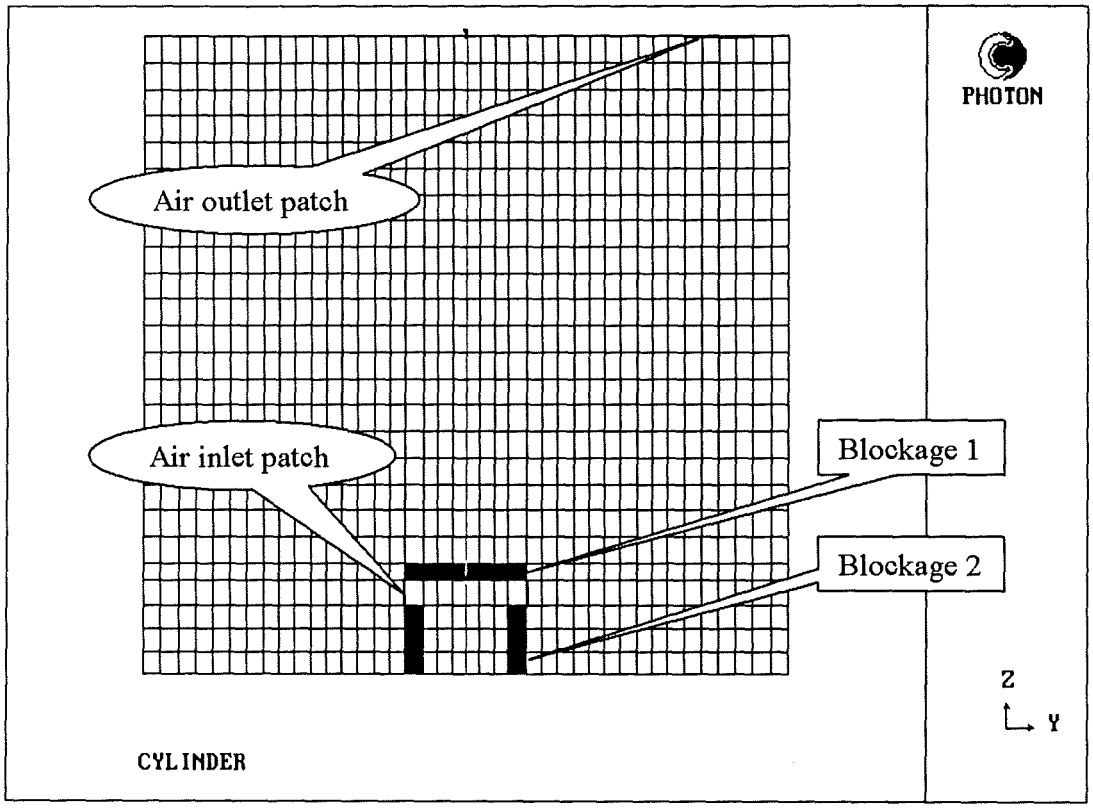

Figure 5-10: Cut through cylinder showing the grid in X-Y plane, the internal geometry (black) and the air inlet and outlet patches

5.3.6 Gas inlet and outlet conditions

The air inlet was placed between the gap of the pipe and air distributor. The inlet air velocity along the Y-axis was calculated by using the defined mass flow rate, inlet area and the inlet temperature according to the experimental data.

The air outlet patch was placed at the top of the cylinder in a rhombus shape. The area of this rhombus was equal to the area of the circular air outlet of the experimental spray chamber that can be seen in Figure 5-10.

5.3.7 Turbulence model and relaxation settings

The air flow field is solved with the Eulerian equation using the k-ε model. The k-ε model has a general description of the turbulence that allows for the effects of transport of turbulence properties by the mean flow and diffusion for the production of turbulence. The turbulence intensity of the flow at entry for the k-ε model was set

to 2%. The intensity lies between 1% - 5%. A setting of 2% has shown the best combination in connection with the relaxation (0.001) and inlet velocity. The relaxation needed to be set to 0.001 because the software became unstable. With a higher relaxation the oscillation of the program was increasing instead of decreasing. The program diverged and reached the limits set to the software, which terminated the simulation process.

5.3.8 Spray droplet modelling

The GENTRA Menu is used to define particles that enter the domain. Water droplets that partly evaporate are used during the experiments and therefore, the option 'Vaporising Droplets' was selected. The combined Lagrangian – Eulerian approach solves a set of non-linear equations of gas-droplet equations. Initially the presence of droplets is neglected so that two independent solutions can be determined for the conservation equations applied to the gas phase and the droplet spray. Once the first solution for the gas phase is known, it is used to solve the droplet equations from which the energy and mass contribution terms can be estimated. Newton's law thus following the Lagrangian approach governs the particle motion. Momentum exchange from the particle to fluid is modeled in the fluid phase momentum equation. This procedure continues until convergence is reached for both sets of equations. Physical properties, e.g. the temperature, viscosity, velocities, and humidity, are used to determine the degree of convergence.

The Inlet-Data-File contains the initial droplet size, velocity, spray angle, and droplet temperature. This is different to Petr and Kolovratnik (2000), who used predefined streamlines. The 3 D trajectory for each droplet is calculated by the CFD software GENTRA, which is included in PHOENIX software. The trajectory of the droplet is influenced by the airflow in which the droplet is suspended. The energy, mass and momentum transfer for the droplets is calculated using the Lagrangian approach. The maximum Lagrangian time step per cell was 0.001 sec and a minimum of 5 and a maximum of 20 calculations per cell were carried out. The time out value, when the droplet is removed after it entered the domain, was set to 0.5 of a second. This time out control applies to droplets that are captured in a re-circulating flow. The bottom plate was defined as the droplet exit patch. The droplet data are defined by an Inlet-

Data-File, which contains the initial conditions of the droplet. The initial conditions are defined following the measurement of droplet properties 40 mm below the exit orifice. The droplet velocity, size and spray angle are measured with a PDPA and visual systems as reported in chapter 4. The Inlet-Data-File and the droplet mass fraction distribution are discussed later in section 5.3. There was no turbulence model available to calculate the droplet currency. The PHOENICS software does not have the feature to calculate the droplet internal currency. The droplet currency is the internal flow of the droplet as studied by Antar (2000). The coalescing and the break-up of droplets are also not considered.

The impingement model in PHOENICS 2.2.2 is a simple momentum and velocity conservation, which can be influenced by a wall restitution coefficient. The wall restitution coefficient is a setting that allows one to give particles a different velocity after hitting a boundary wall. New impingement codes have been developed, but they (Kawashima (1999), Lee & Ryou (2000), Bourgault et. al. (2000)) are not yet integrated in the software. The droplets in the experiments formed a falling water film and only a small amount bounced off the Perspex cylinder wall. The CFD software PHOENICS does not allow the user to define a falling water film. Therefore, a wall restitution factor between 0 and 1 has to be applied. Knowing from visual observation that small droplets are carried with the air flow and that with a wall restitution coefficient of 1 none of the droplets are carried with the flow, hence the wall restitution coefficient must be below 1. Knowing the experimental data of an average test run, a series of tests with 72 droplet trajectories was carried out with different wall restitution coefficients, ranging from 0.05 to 1. The restitution coefficient that came closest to the experimental data was chosen. Figure 5-11 shows the results of the test where the air humidity and temperature difference are presented for the different wall restitution coefficients. The best result closest to the experimental result, displayed here as dashed lines, was achieved with a coefficient of wall restitution of 0.3 and is therefore used for the numerical simulation of the experiments. For testing the different coefficients and settings that gives the closest result between the numerical and experimental result the configuration 9a20-1 was chosen. The inlet data are:

	Temperature °C	Mass flow rate kg s^{-1}	Density kg m^3
Air	152.14	0.044	0.831
Droplets	9.6	0.035	999.8

The differences of air in- and outlet conditions are used in Figure 5-7 to 5-12 as reference values, e.g. temperature difference.

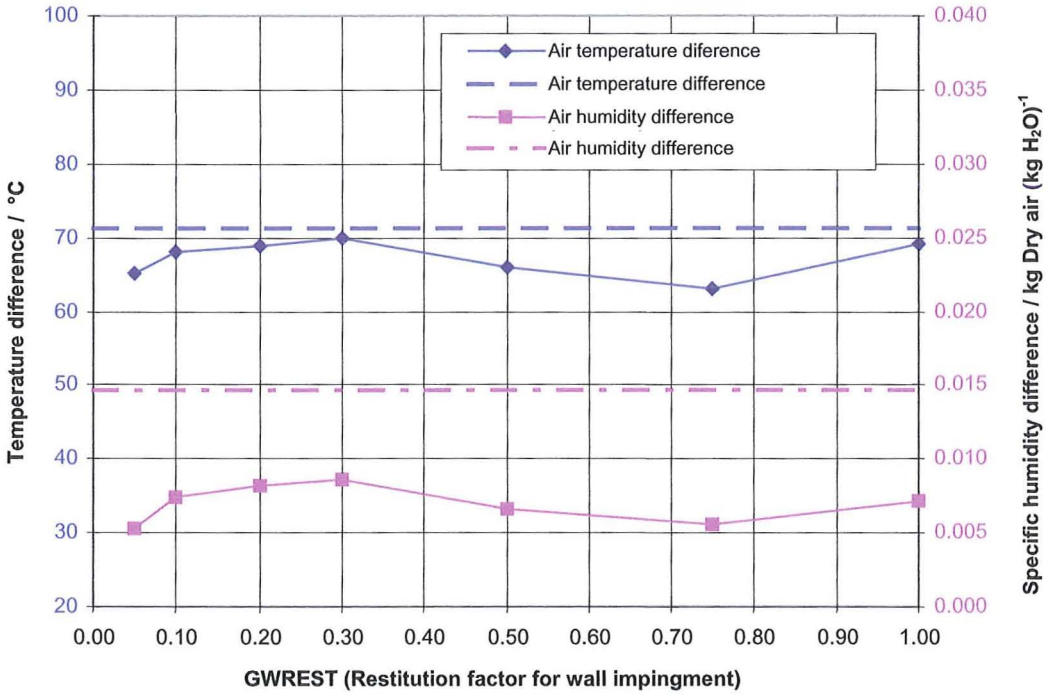

Figure 5-11: Air humidity and temperature difference of in and outlet over different wall restitution coefficients for the configuration 9a20-1

Due to the adiabatic walls and internal geometry only the heat, mass and energy transfer equation for the domain were solved. The inlet conditions for the air and droplets for every simulation were set according to the experimental data. The total number of sweeps is set to 1000 with a relaxation of 0.001.

The GENTRA menu gives the option to specify a file that contains all of the necessary information about the droplets. Ten different values for each droplet trajectory and size were needed to be given for the option 'Vaporising Droplets'. The first three values are the X, Y, Z-coordinates of the starting position, where the droplet enters the domain. The second three values are the X, Y, Z-velocity

components of the droplet. The seventh value is the droplet diameter followed by the liquid density. The ninth value is the mass flow rate for the particular trajectory and is followed by the temperature of the droplet. Theoretically it is possible to define an infinitely large number of trajectories, but this would also require an infinitely large time to finish the simulation. A number of simulations carried out with different droplet sizes and mass distributions for the same simulation showed the importance of selecting the correct droplet size and mass distribution. The droplet size distributions that were tested are shown in Table 5-2. Five different droplet distributions were initially tested to find the appropriate droplet distribution. The tested droplet distributions ranged from single sized droplets up to four different droplets sizes. The diameter and mass flow rates were chosen after the measured droplet distribution with the PDPA. The numbers in the table represent the percentage of the SMD followed by a number in brackets, which is the percentage of the total mass flow rate. For example, case five represents a single droplet size distribution, which is the measured SMD and is therefore written as 100 (100).

Table 5-2: Droplet size and mass distribution tested

Case No.	Droplet 1 Ø % (m_w%)	Droplet 2 Ø % (m_w%)	Droplet 3 Ø % (m_w%)	Droplet 4 Ø % (m_w%)	**No. of droplets** $(kg\ s)^{-1}$
1	30 (10)	100 (45)	187 (45)	--	23.00E+9
2	33 (3)	66 (18)	100 (30)	145 (49)	10.60E+9
3	65 (25)	100 (50)	150 (25)	--	7.14E+9
4	90 (25)	100 (50)	112 (25)	--	5.62E+9
5	100 (100)	--	--	--	5.51E+9

Results of this simulation are shown in Figure 5-12. The droplet distribution case number two has the best fit to the experimental data, shown here as dashed-dotted line, and is therefore chosen for the all Inlet-Data-Files. The optimum was found by using 18 different trajectories containing 4 different droplet sizes, which leads to a total of 72 trajectories. The sum of the four different droplet sizes and their assigned mass flow rate results in the Sauter Mean Diameter as shown at equation [150].

$$D_{32} = \frac{N_1 D_1^3 + N_2 D_2^3 + N_3 D_3^3 + N_4 D_4^3}{N_1 D_1^2 + N_2 D_2^2 + N_3 D_3^2 + N_4 D_4^2} = \frac{\sum N_i D_i^3}{\sum N_i D_i^2} \quad [150]$$

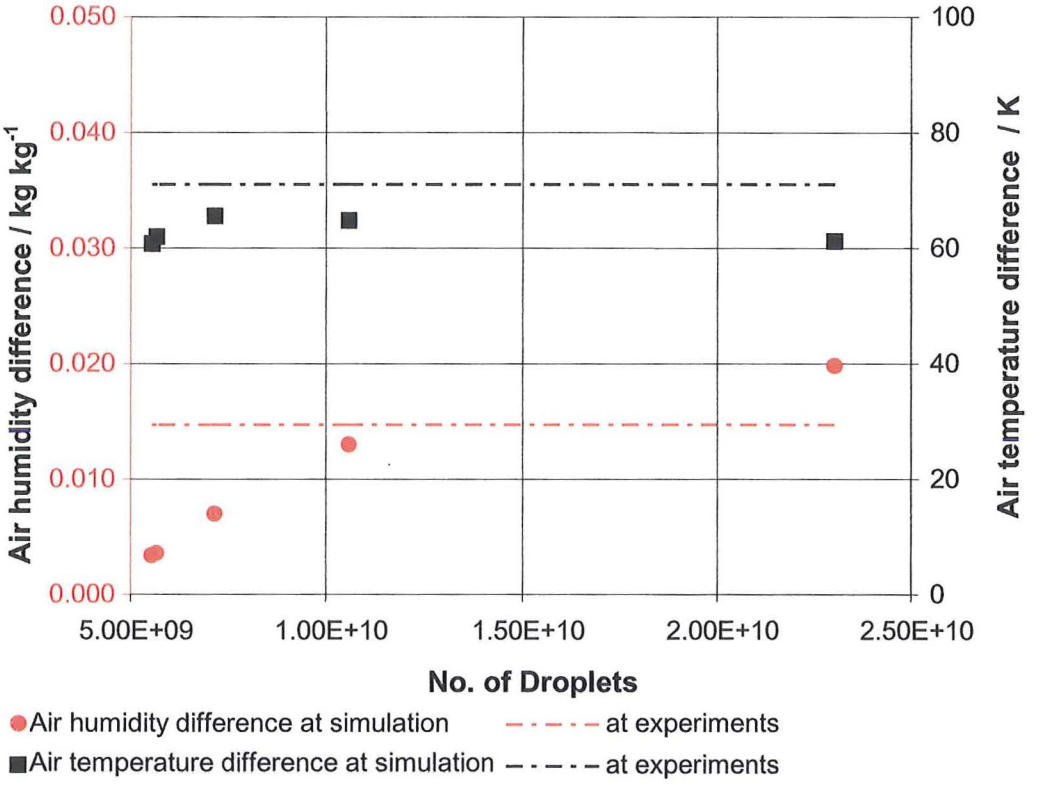

Figure 5-12: Results of the simulation for temperature and evaporation with different droplet size distribution

The assigned mass flow rate for a specific droplet size results in the number of droplets. The approximate droplet distribution and constants for the distributions, defined in Table 5-2, are used to generate the Inlet-Data-File. For this purpose a FORTRAN program was written, shown in the appendix, which allows the specification of the droplet properties.

Four different nozzle configuration, listed below, which showed an average performance, were chosen to be simulated.

- 9a20
- 9a26
- 27a20
- 27a26

These are the nozzles for which the droplet size was measured so that all the important parameters of the spray are known. The experimental tests performed with these nozzles gave the results that are necessary to compare the computation model

with the experimental results. The main interest was the airflow leaving the cylinder. In the computational model this opening was defined as a patch, named GXOUT, so that all variables can be calculated very accurately from the RESULT file.

5.3.9 Interaction settings and convergence

An investigation was carried out focusing on how the results are influenced by the total number of sweeps and the first iteration with droplets. The problem was separated in two main investigations:

a) The influence on the results of a constant number of iterations to solve the flow field and a varying number of iteration with droplets

b) The result of a simulation with a constant number of iterations with droplets and a varying number of iterations when solving the flow field

A model with the grid size X=20, Y=16, and Z=16 is chosen. The inlet conditions for air and Water droplets are held constant as well as all other conditions.

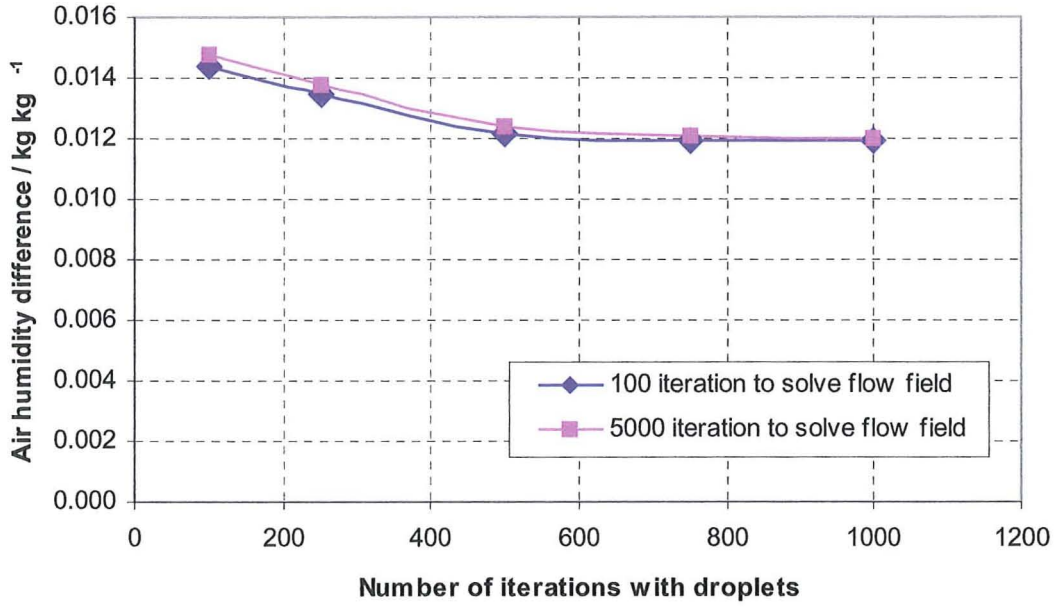

Figure 5-13: Air humidity difference depending on the number of iterations with droplets

The problem a) is solved by the comparison of the results with two simulations where one has only 100 iteration and the second set of simulation has 5000 iterations to solve the flow field before the first iteration with droplets starts. Different numbers of iterations with droplets, which are 100, 250, 500, 750, and 1000, are then tested.

The influence of the air humidity difference and air temperature is presented in Figure 5-13 and Figure 5-14.

The result of these simulations show that the influence of the number of iterations to solve the flow field is not very significant. The main difference of the result is influenced by the number of iterations with droplets. Up to 500 iterations the result for the air humidity difference is strongly influenced by the iterations. Above 500 the variation of the results is insignificantly small. Consequently 500 iterations with droplets are sufficient to gain a satisfying solution.

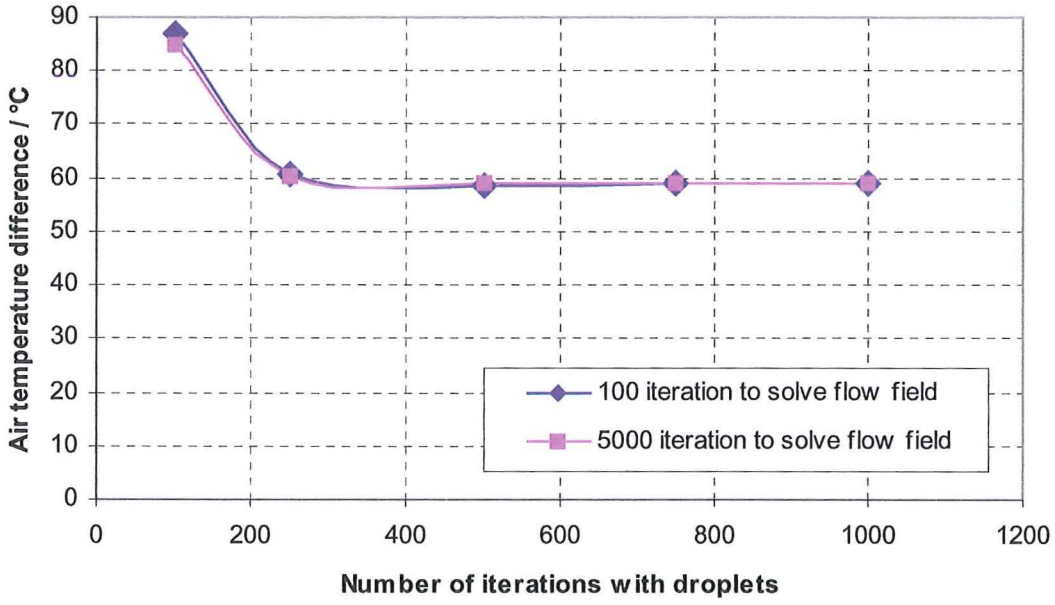

Figure 5-14: Air temperature difference depending on the number of iterations with droplets

The number of iterations with droplets at problem b) are set to 100 and 500 iterations whereby the number of iteration to solve the flow field was varied, 100, 500, 1000, 2500, and 5000. The same variables for the simulations as for problem a) are used to display the results and are shown in Figure 5-15 and Figure 5-16.

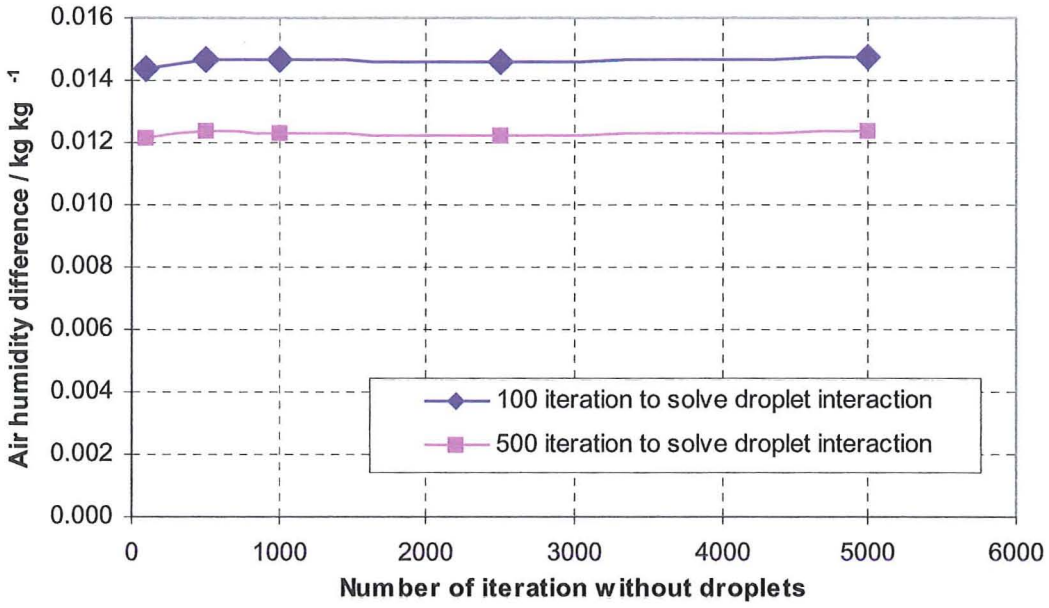

Figure 5-15: Air humidity difference depending on the number of iterations to solve the flow field

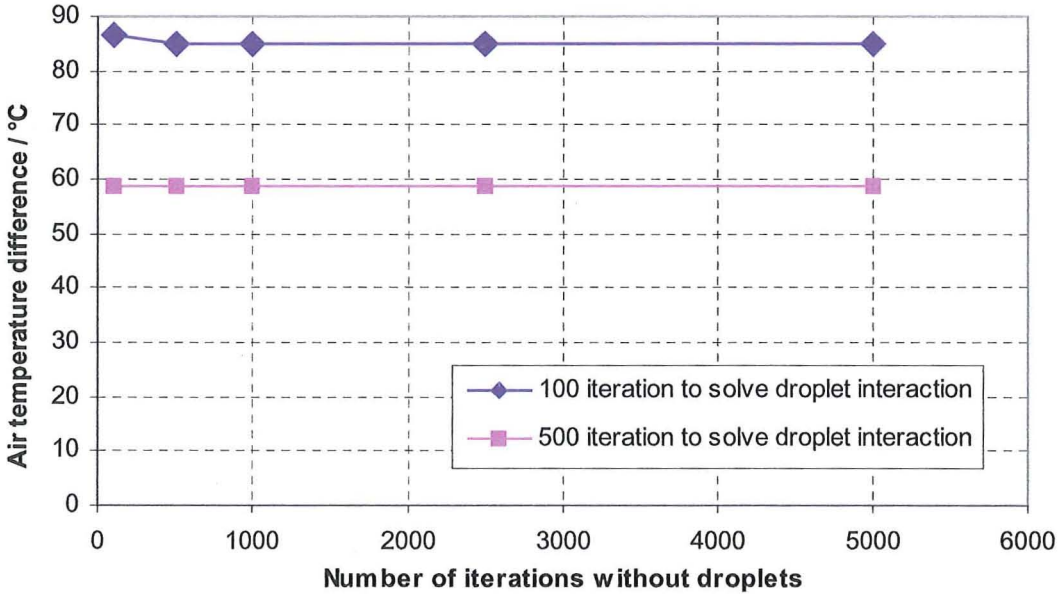

Figure 5-16: Air temperature difference depending on the number of iterations to solve the flow field

The result shows that the number of iterations to solve the flow field has only a very small influence on the result. The number of iterations with droplets mainly influences the result. The result above 500 iterations with and without droplets remains nearly constant.

To reduce the time of the simulation process, a batch file was written and used to control the computer. Because of the similar air inlet condition the flow field with 500 sweeps was solved only for the first simulation. From 500 sweeps onward the flow field solved in turns between Eulerian and Lagrangian approach. All other simulations used this solved flow field and all variables were restarted of it for another 100 iterations to solve the flow field incorporating the small changes of the inlet conditions. The changes of the inlet conditions for the flow field where adjusted in-between the GENTRA sweeps.

Parts of the commands inside the batch file are executing the copy of the Inlet-Data-File for the specific simulation and the PIL file. Earth produced, a numerical result file, called RESULT, and the PHI file containing the graphical solution, are copied with different names, which enables a later analysis of the data. The data were analysed with an EXCEL-spreadsheet and compared with the experimental data.

5.4 The analysis of the RESULT files

5.4.1 Graphical results

The software PHOENICS gave an option to perform a cut through the centre of the cells along the z-y plane at x=1 and x=13. This allowed for vertical cross section colour plots through the spray chamber to be obtained. Five different results are compared for the configuration 9a26 and 27a20. Each configuration is compared at $1x10^5$ Pa and $5x10^5$ Pa. The results for each liquid pressure are:

Variable	Description	Output	Units
P1	The pressure inside the spray chamber	Contour plot	Pa
Vector	Direction and velocity of the gas phase	Vector plot	$m\ s^{-1}$
H1	Enthalpy of gas phase	Contour plot	$J\ kg^{-1}$
Den1	Density of gas phase	Contour plot	$kg\ m^3$
VAPO	Specific humidity of the gas phase	Contour plot	$\frac{kg\ H_2O}{kg\ dry\ air}$

The black frame in the plotted results is the border of the outer cells. The results are plotted only between the centres of the cells. This is the reason for the gap between the frame and the coloured contour plot. The air outlet opening is always on the left

hand side of all the plots. The cut through the cylinder gives us the two most divergent flow patterns inside the spray chamber.

An air pressure with linear increase up to 200 Pa gauge was measured at the bottom of the spray chamber during the experiments. The numerical model was calculating the pressure distribution inside the spray chamber. Figure 5-17 shows the result of the configuration 9a26 at $1x10^5$ Pa and verifies the increase of air pressure at the experiments. An overpressure at the bottom corner of the spray chamber is caused by the airflow distribution. The airflow direction perpendicular towards the spray chamber wall causes slight over pressure at the spray chamber wall between the perpendicular airflow direction and the bottom plate.

The software calculated at a liquid pressure of $5x10^5$ Pa, an air pressure difference to the ambient pressure of –487 Pa inside the spray chamber. This pressure is at the cell borders of the air outlet patch not be visually detected, because it is on the cell centre, which cannot be plotted. Figure 5-18 proves this assumption with the velocity profile comparison between the two different liquid pressures. At a liquid pressure of $5x10^5$ Pa at the spray inlet location the air velocity was calculated with a maximum of 15.3 m/s. These local accelerations causing a localised low-pressure zone near the boundaries of the droplet inlet area.

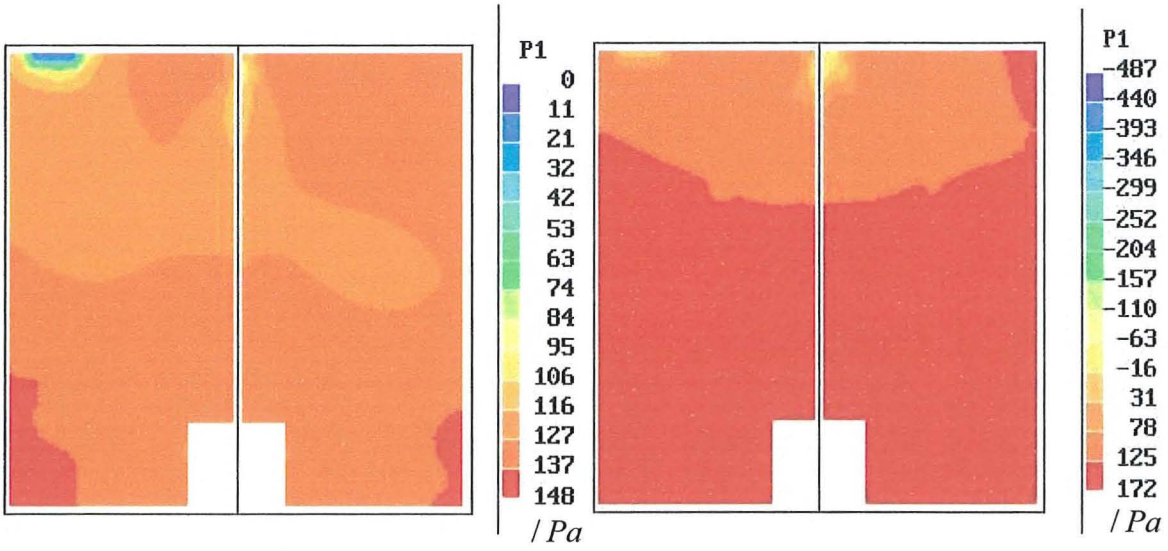

Figure 5-17: Pressure distribution for the 9a29 configuration

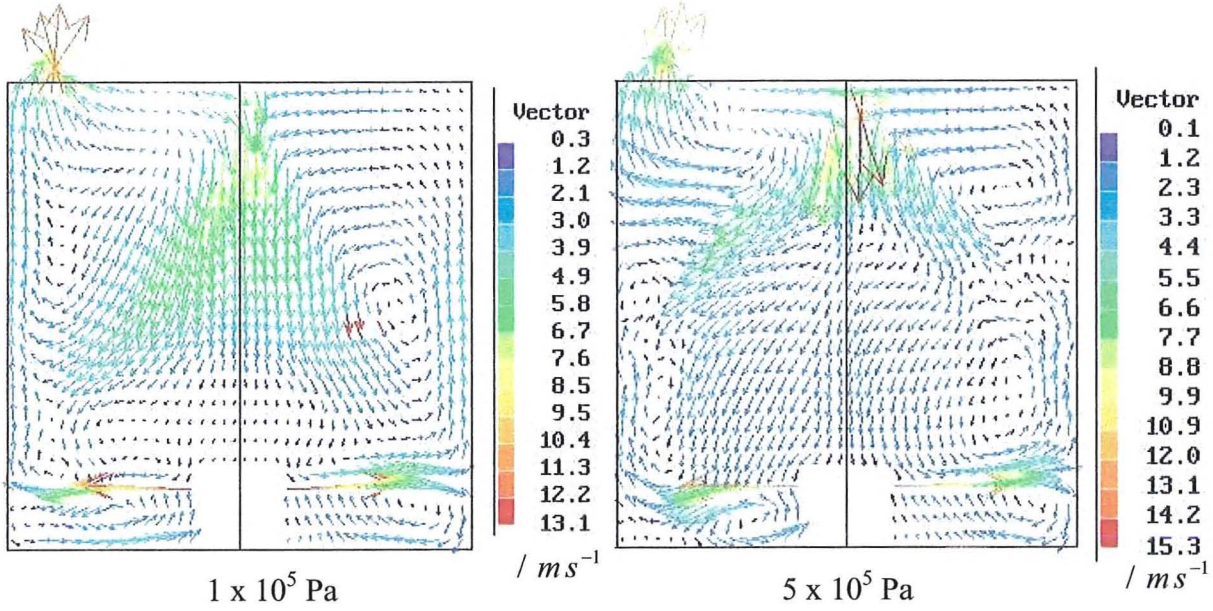

Figure 5-18: Comparison of airflow velocity & directions for the configuration 9a26

Figure 5-18 compares the air velocity and flow direction at two different liquid pressures for the configuration 9a26. The airflow for a liquid pressure of $5x10^5$ Pa is much more disturbed than for $1x10^5$ Pa. This is due to the higher droplet velocity and increased number of droplets. This makes the spray denser and increases the resistance to the airflow. The widening of the spray angle, approximately 7°, at $5x10^5$ Pa liquid pressure causes a higher amount of re-circulating air flow.

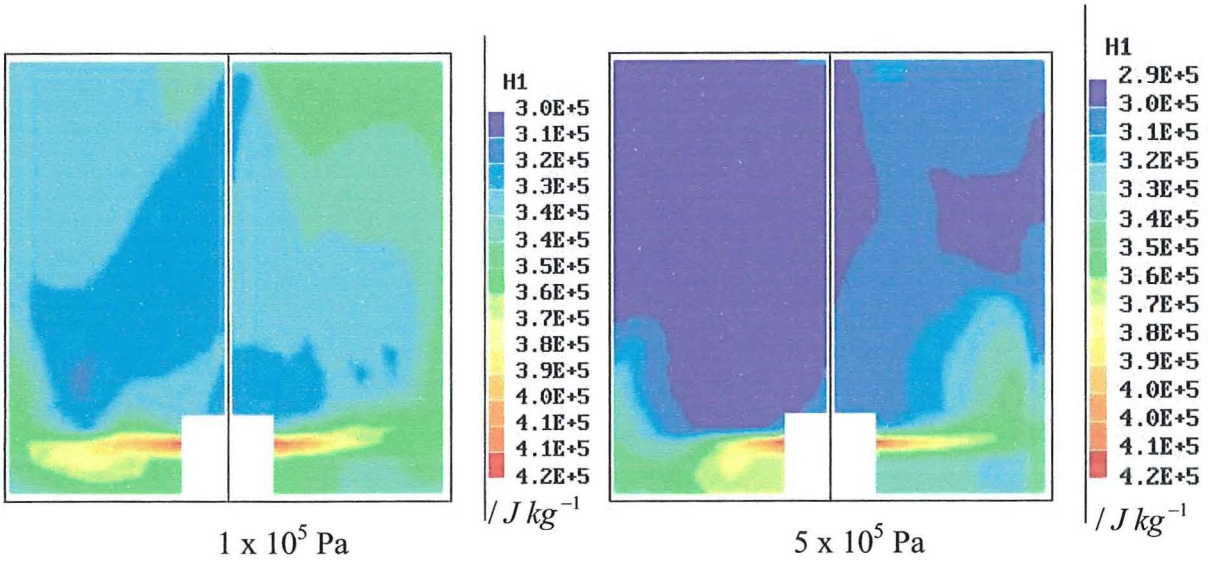

Figure 5-19: Comparison of the air enthalpy at configuration 9a26

The droplets that bounce off the spray chamber wall disturb the up-streaming air flow above the air outlet. 75 % of the airflow below the hollow cone spray pattern moves towards the side of the air outlet opening, here seen at the left hand side. This is deflecting the incoming air stream on that side, which causes more distorted airflow and hence a pressure change.

Figure 5-19 shows the effect of the coaxial air outlet geometry on the air enthalpy. As mentioned before, the air outlet opening is always on the top left hand side of all the plots. Figure 5-19 proves the assumption made before that the airflow is moving to the left side. The air enthalpy of the spray entrained at the top on the right hand side is higher that on the left hand side. At the liquid pressure of $1x10^5$ Pa this is due to the influence of the spray pattern. Air with different enthalpies intersects and mixes close to the spray chamber wall. At the liquid pressure of $5x10^5$ Pa the influence of the previous described deflection on the right hand side of the incoming air stream can be seen. The wider spray angle has a positive effect on the right hand side of the spray chamber. Less air compared to the liquid pressure of $1x10^5$ Pa is passing the spray droplets. This is because of the re-circulating flow pattern caused by the wider spray angle.

One factor that influences the enthalpy is the temperature. The temperature also influences the dry air density shown in Figure 5-20. The colour contour plot is very similar to the contour plot of the enthalpy. Contour difference between the enthalpy and density arise where the relative vapour content is high and the air temperature low. The differences are very small and can only be seen by studying the vapour contents distribution in Figure 5-21.

At a liquid pressure $1x10^5$ Pa the vapour is relatively evenly distributed compared with the liquid pressure of $5x10^5$ Pa. Figure 5-21 indicates that the air flow at low liquid pressure has a higher mixing of the vapour compared to that of the higher liquid pressure. The vapour content at the air outlet is similar for both liquid pressures. At a liquid pressure of $5x10^5$ Pa the amount of smaller droplets is higher and produces a larger surface area, which enhances the evaporation of liquid.

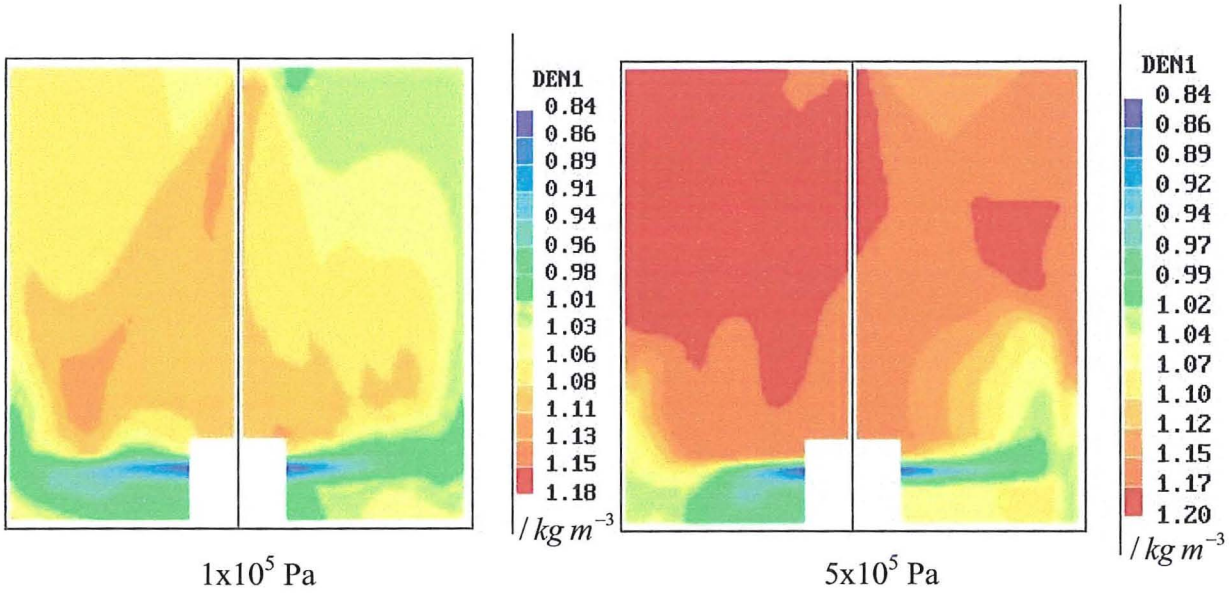

Figure 5-20: Comparison of the density of the dry air gas phase at configuration 9a26

At the same time, since it has a larger surface area higher heat transfer occurs and this cools down the air faster. This enhanced cooling of the air lowers the dew point of the air and limits the amount of specific vapour content in the dry air. Hence, at the same specific vapour content the relative humidity of the air is higher at lower temperatures. The specific vapour contents at low pressure achieve a maximum of 0.024 kg/kg somewhere at the outside boundaries of the cells. The averaged vapour contents leaving through the air outlet opening is calculated as 0.012 kg/kg. This is 37% lower than the experimentally determined value. At higher liquid pressure the difference decreases to 15%. The simulations of the 9a20 configuration, for which the results are presented here, have the highest deviation from the experimental data. Even so it can be seen that the tendency of the numerical solution is similar to the experimental measurement.

For configuration 27a20 the spray angle is little influenced by the liquid pressure. The widening of the spray angle between a liquid pressure of $1x10^5$ Pa and $5x10^5$ Pa is just 2°. The mass flow rate at the same liquid pressure is for the 2.5 mm exit orifice less than the 4.7 mm exit orifice but produces smaller droplets. The smaller droplets are not small enough to replace the missing surface area of the missing liquid mass flow. Hence, the cooling of the hot air is less. The higher temperature

increases the dew point. Because of this the specific humidity is much higher and increases by approximately 33% from $1x10^5$ Pa to $5x10^5$ Pa. Due to the relatively constant spray angle the air flow has changed insignificantly.

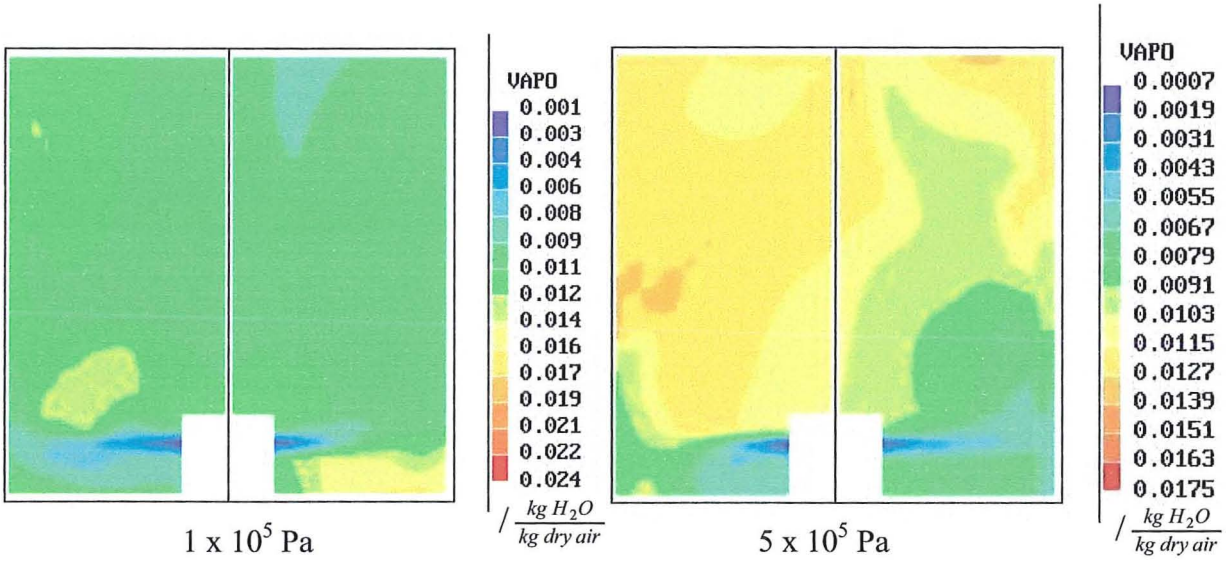

1 x 10^5 Pa 5 x 10^5 Pa

Figure 5-21: Comparison of the specific vapour content of the dry air gas phase at configuration 9a26

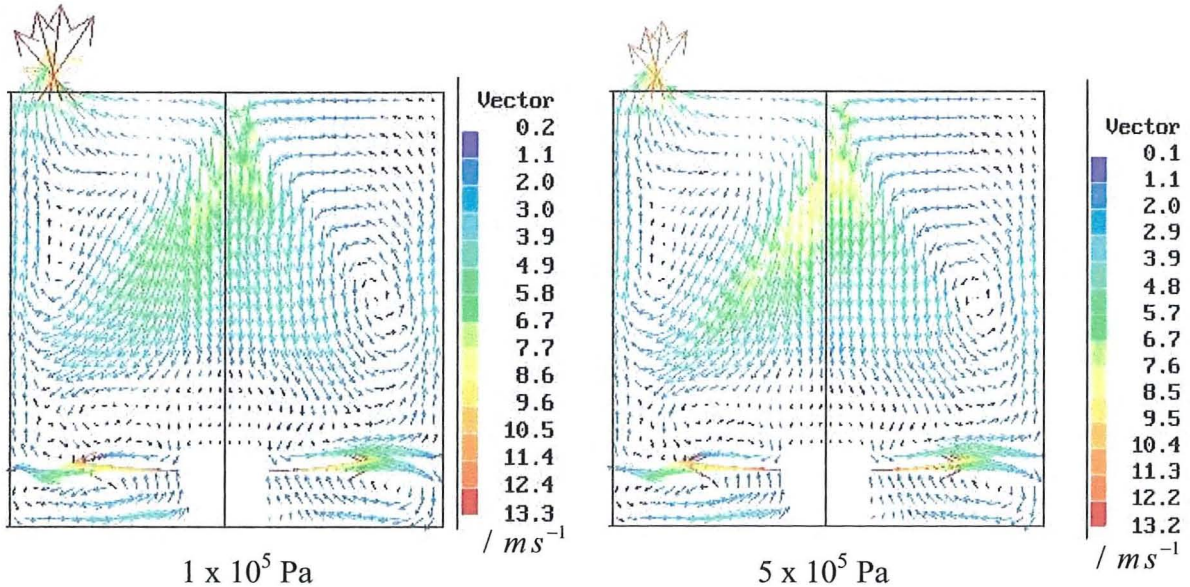

1 x 10^5 Pa 5 x 10^5 Pa

Figure 5-22: Comparison of the air flow velocity and directions at configuration 27a20

Figure 5-22 displays the vector result of the simulation between a liquid pressure of $1x10^5$ Pa and $5x10^5$ Pa. No significant difference of the air flow inside the spray chamber is observed.

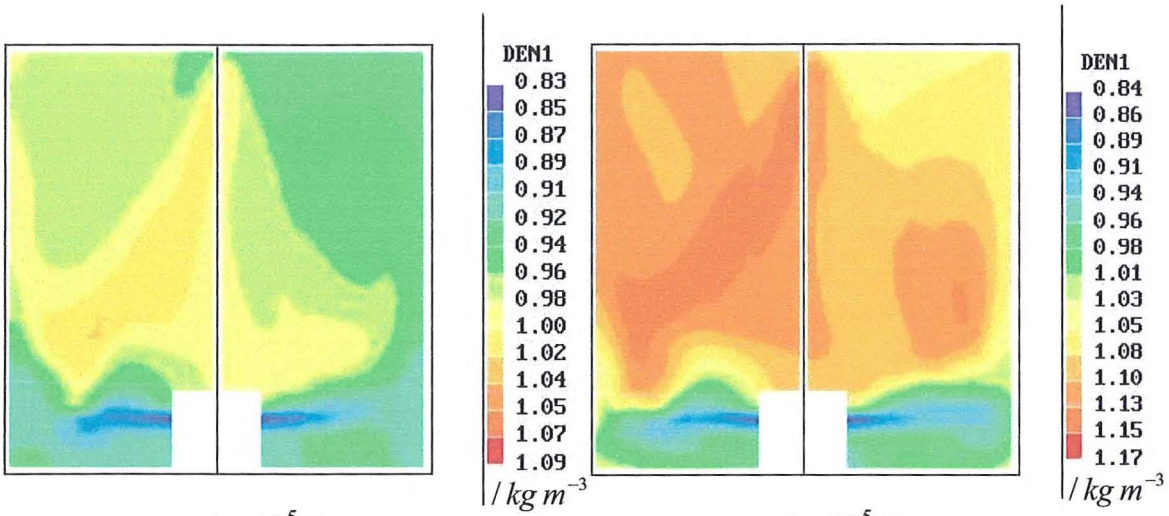

1 x 10^5 Pa 5 x 10^5 Pa

Figure 5-23: Comparison of the gas phase density for configuration 27a20

The only difference is the cooling of the hot air due to the increased mass flow rate of liquid. The air outlet temperature difference is approximately 35°C higher at a pressure of $5x10^5$ Pa. The gas phase density results, shown in Figure 5-23 of the simulation confirm this and visualises the cooling inside the spray chamber.

5.4.2 Numerical analysis

The temperature and the humidity were calculated using the RESULT file. The average temperature of the outlet air at GXOUT was determined by the equation

$$t_{a2} = \frac{H1TMP1B}{R1} - 273 \qquad [151]$$

and the specific humidity was calculated with

$$\omega = \frac{VAPO}{R1} \qquad [152]$$

were the source H1 represents the enthalpy at GXOUT and has the unit [J/s], TMP1B is a constant related to the fluid properties with the unit [kg K/J], R1 is the mass flow rate of air [kg/s] and VAPO is the average humidity at GXOUT. Every measurement point has its own RESULT file. An example of the RESULT file is shown below. The "nett sum" represents the unsolved amount of the variable.

```
Nett source of R1  at patch named: INLET   = 4.145E-02
Nett source of R1  at patch named: GXOUT   =-4.152E-02
Nett source of R1  at patch named: GENMAS  = 6.908E-05
nett sum=-1.341E-07 pos. sum= 4.152E-02 neg. sum=-4.152E-02

Nett source of H1  at patch named: INLET   = 1.792E+04
Nett source of H1  at patch named: GXOUT   =-1.540E+04
Nett source of H1  at patch named: GENMAS  =-1.078E+02
Nett source of H1  at patch named: GENPAT  =-2.405E+03
nett sum= 2.383E-05 pos. sum= 1.792E+04 neg. sum=-1.792E+04

Nett source of VAPO at patch named: GXOUT  =-4.015E-04
Nett source of VAPO at patch named: GENMAS =-2.198E-06
Nett source of VAPO at patch named: GENPAT = 4.026E-04
nett sum=-1.136E-06 pos. sum= 4.026E-04 neg. sum=-4.037E-04
```

Table 5-3: Results of the simulation for all configurations tested

Nozzle Configuration	Water pressure Average [bar]	Air temperature diff. Average [°C]	Humidity diff. Average [kg/kg]
9a20-1	2.015	64.68	1.30E-02
9a20-2	3.005	87.44	1.53E-02
9a20-3	4.046	100.49	1.62E-02
9a20-4	5.040	109.53	1.61E-02
9a20-5	6.005	115.07	1.59E-02
9a26-1	1.987	97.12	1.19E-02
9a26-2	3.016	116.67	1.24E-02
9a26-3	4.012	124.67	1.17E-02
9a26-4	4.960	129.75	1.14E-02
9a26-5	5.946	133.02	1.12E-02
27a20-1	2.009	67.33	1.51E-02
27a20-2	3.134	85.38	1.65E-02
27a20-3	3.996	91.78	1.85E-02
27a20-4	4.979	98.22	1.79E-02
27a20-5	6.047	106.88	1.98E-02
27a26-1	2.005	102.32	1.20E-02
27a26-2	3.007	119.15	1.24E-02
27a26-3	3.988	125.98	1.23E-02
27a26-4	5.021	129.72	1.27E-02
27a26-5	6.030	132.35	1.22E-02

The air outlet temperature was calculated and deducted from the inlet temperature and resulted in the temperature difference. The humidity was calculated and represents the amount of droplet evaporation. The results of these calculations are shown in Table 5-3.

Chapter 6 Comparison of the experimental and theoretical results and discussion

6.1 Introduction

In this chapter the experimental results of four different pressure swirl nozzle configurations are compared with the results of the relevant simulations. The air inlet condition for the simulations is the same as for the experimental test runs. The air outlet conditions will be compared with each other and analysed. An uncertainty calculation is carried out for both sets of results. For the experimental data, the errors in the instrumentation are considered. For the simulation results, the numerical RESULT file is used for the calculation.

6.2 Comparison of the experimental measurements and numerical results

The results of the numerical simulation at each pressure value are listed and compared for each nozzle configuration. The four tested configurations are

	NTS -	L_s mm	D_e mm	L_e mm
9a20	2	6.0	2.5	1.25
9a26	2	6.0	4.7	2.35
27a20	6	6.0	2.5	1.25
27a26	6	6.0	4.7	2.35

The numerical results that are compared with the experimental measurement are the

- differences in specific humidity
- air temperature differences

between inlet and outlet of the spray chamber

The results of every simulation and for each configuration are graphically displayed and discussed. Each pressure value that was simulated is compared with the associated experimental result (temperature and humidity). The accuracy is of the simulations is expressed in percentage.

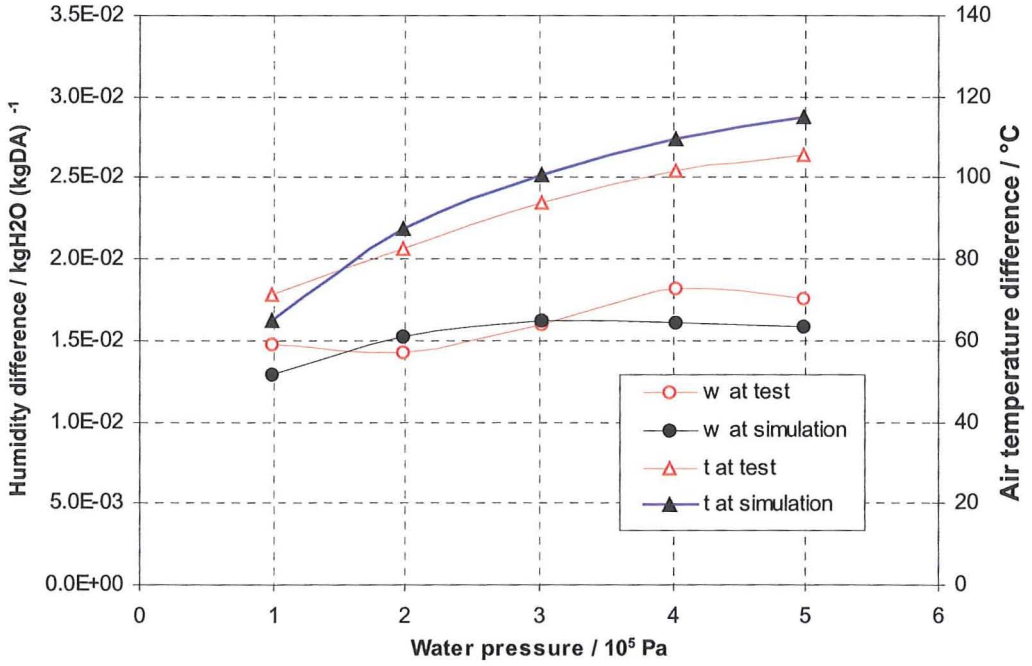

Figure 6-1: Results of temperature (t) and humidity (ω) from the simulation of the 9a20 configuration in comparison with experimental results

The results of the 9a20 nozzle configuration for the case 1 to 5, which is the water pressure from 2 to 6 bar, follow the trend of the experimental data. The result of the temperature, see Table 6-1, is within ±9%. The result for the evaporation is within –6.9% to 11.9%, in good agreement with the experimental data.

Table 6-1: Results of temperature and humidity from the simulation of the 9a20 configuration in comparison with experimental results and their differences

Configuration	Δt (simulation)	Δt (test)	Difference of temperature simulation	$\Delta\omega$ (simulation)	$\Delta\omega$ (test)	Difference of vapour simulation
	°C		%	kgH2O / (kgDA)		%
9a20-1	64.68	71.1	-9.0	1.295E-02	1.471E-02	11.9
9a20-2	87.44	82.6	5.8	1.528E-02	1.430E-02	-6.9
9a20-3	100.49	93.6	7.4	1.620E-02	1.600E-02	-1.2
9a20-4	109.53	101.7	7.7	1.613E-02	1.822E-02	11.5
9a20-5	115.07	105.6	9.0	1.585E-02	1.762E-02	10.0

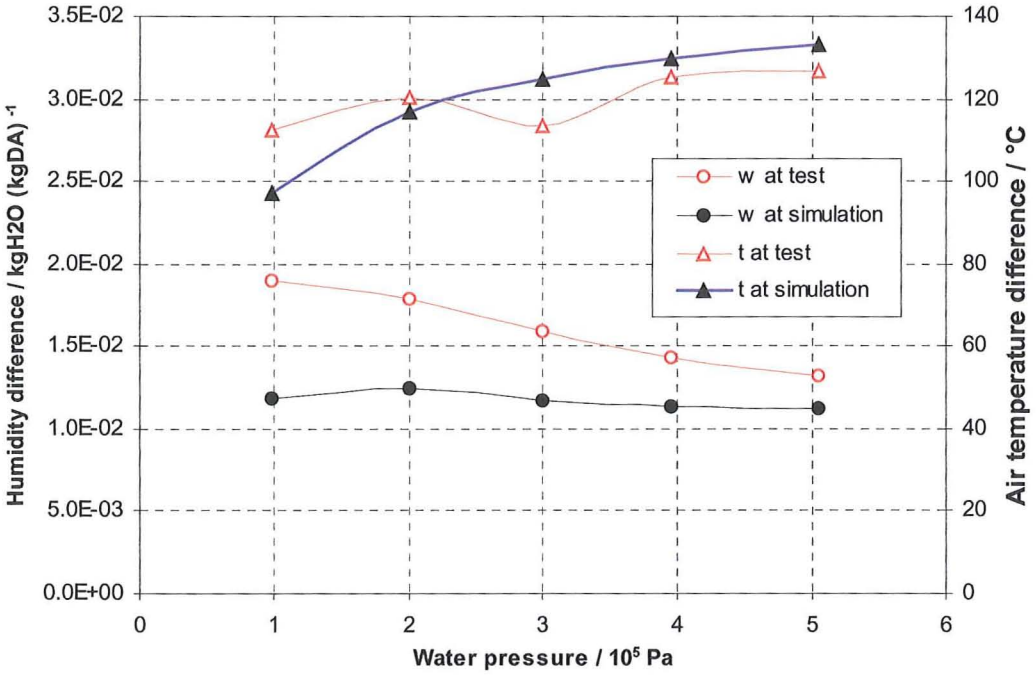

Figure 6-2: Results of temperature (t) and humidity (ω) from the simulation of the 9a26 configuration in comparison with experimental results

The results for the 9a26 simulation is not as close to the experimental data as the 9a20 simulation, but it verifies the temperature difference achieved with higher water flow rates. The difference between experimental results and computational evaporation results for a water pressure difference of $1*10^5$ Pa is of 37.6%. With the increase in water pressure the difference in evaporation between experimental and simulation decreases. The final value for the measured evaporation is then 14.9% from the simulation, which is equivalent to 0.002 kg H_2O (kg Dry Air)$^{-1}$.

Table 6-2: Results of temperature and humidity from the simulation of the 9a26 configuration in comparison with experimental results and their differences

Configuration	Δt (simulation)	Δt (test)	Difference of temperature simulation	$\Delta\omega$ (simulation)	$\Delta\omega$ (test)	Difference of vapour simulation
	°C		%	kgH2O (kgDA)		%
9a26-1	97.12	112.6	-13.7	1.185E-02	1.901E-02	37.6
9a26-2	116.67	120.2	-2.9	1.242E-02	1.786E-02	30.4
9a26-3	124.67	113.4	9.9	1.166E-02	1.587E-02	26.5
9a26-4	129.75	125.2	3.7	1.139E-02	1.428E-02	20.3
9a26-5	133.02	126.6	5.1	1.125E-02	1.322E-02	14.9

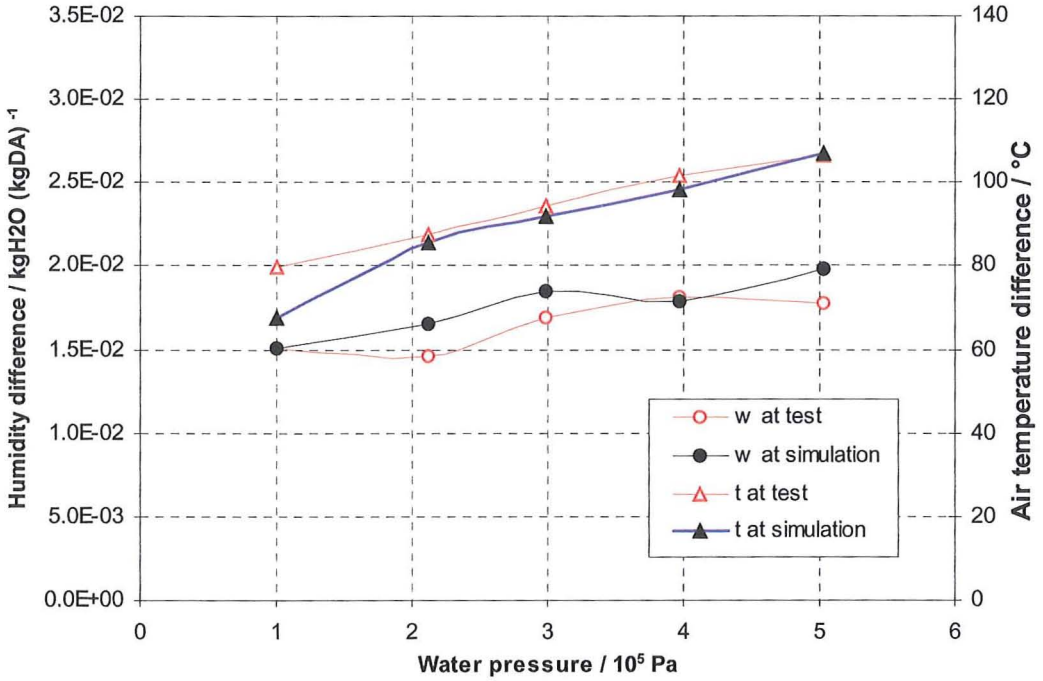

Figure 6-3: Results of temperature and humidity from the simulation of the 27a20 configuration in comparison with experimental results

The results for the temperature for case 2 to 5 are in very good agreement with the experimental data and show a steady increase in the temperature difference with a increase in evaporation.

Table 6-3: Results of temperature and humidity from the simulation of the 27a20 configuration in comparison with experimental results and their differences

Configuration	Δt (simulation)	Δt (test)	Difference of temperature simulation	$\Delta\omega$ (simulation)	$\Delta\omega$ (test)	Difference of vapour simulation
	°C		%	kgH2O (kgDA)		%
27a20-1	67.33	79.7	-15.6	1.505E-02	1.510E-02	0.3
27a20-2	85.38	87.7	-2.6	1.651E-02	1.459E-02	-13.2
27a20-3	91.78	94.5	-2.8	1.853E-02	1.688E-02	-9.8
27a20-4	98.22	101.7	-3.4	1.786E-02	1.814E-02	1.6
27a20-5	106.88	106.4	0.4	1.979E-02	1.777E-02	-11.3

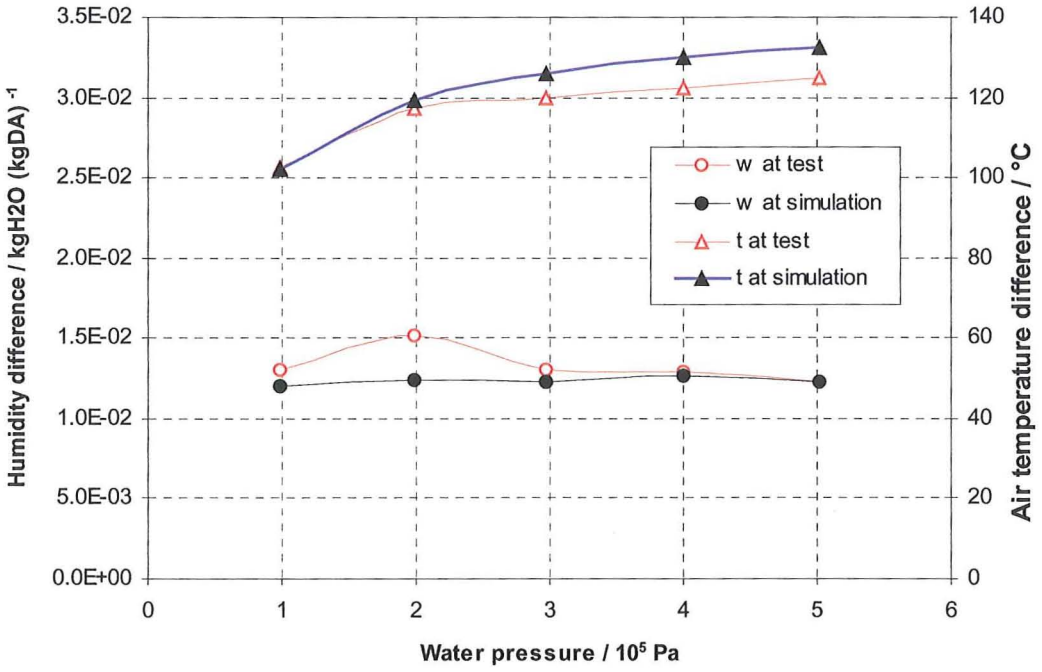

Figure 6-4: Results of temperature and humidity from the simulation of the 27a26 configuration in comparison with experimental results

The results for the simulation 27a26 show a good agreement with the experimental data. The evaporation is stable at approximately 1.25 10^{-2} kg H_2O/kg dry air for the experimental data except for case number two, where the experimental data shows a difference of 18.7% from the simulation.

Table 6-4: Results of temperature and humidity from the simulation of the 27a26 configuration in comparison with experimental results and their differences

Configuration	Δt (simulation)	Δt (test)	Difference of temperature simulation	$\Delta\omega$ (simulation)	$\Delta\omega$ (test)	Difference of vapor simulation
	°C		%	kgH2O (kgDA)		%
27a26-1	102.32	102.5	-0.1	1.199E-02	1.295E-02	7.4
27a26-2	119.15	117.1	1.7	1.244E-02	1.518E-02	18.1
27a26-3	125.98	119.6	5.4	1.232E-02	1.303E-02	5.5
27a26-4	129.72	122.4	6.0	1.269E-02	1.292E-02	1.8
27a26-5	132.35	125.0	5.8	1.223E-02	1.224E-02	0.1

6.3 Uncertainty calculation for experimental data

Single-sample uncertainty analysis for the instrumentation was used to calculate the uncertainty of the experimental data. The ambient conditions were recorded before each measurement. Preliminary measurements showed that a change in ambient relative humidity at the input had a very small effect on the results. A single measurement of the ambient wet and dry bulb temperature was taken before the measurements. The location to define these bulb temperatures was 10 cm before the inlet of the blower, so that a constant draft was guaranteed.

All bought in instrumentation used was pre-calibrated by the manufacturers and were used within their calibration intervals. Single point measurements were made before and after the experiments to find out if there was drift in the measurement. In all cases was no drift detected. Systematic errors were not detected. The orifice plate was designed to BS1042. Errors in its performances were dominated by the errors in pressure measurement and density values.

The volume flow rate is calculated by

$$\dot{V} = \frac{C_D A_2}{\sqrt{1-\left(\frac{A_2}{A_1}\right)^2}} \sqrt{2\frac{\Delta p}{\rho_{air}}} \qquad [153]$$

Where $\Delta p = g\,\rho_w \Delta h$ and $A = \frac{\pi}{4} D^2$. The volume flow rate can be rewritten as

$$\dot{V} = \frac{C_D \frac{\pi}{2} D_2^2}{\sqrt{1-\frac{D_2^4}{D_1^4}}} \sqrt{2\frac{g\,\rho_w \Delta h}{\rho_{air}}} \qquad [154]$$

The combined uncertainty is calculated from

$$\frac{E_o}{\dot{V}} = \sqrt{\left(\frac{\delta(\Delta h)}{\dot{V}}\frac{\partial \dot{V}}{\partial \Delta h}\right)^2 + \left(\frac{\delta D_1}{\dot{V}}\frac{\partial \dot{V}}{\partial D_1}\right)^2 + +\left(\frac{\delta D_2}{\dot{V}}\frac{\partial \dot{V}}{\partial D_2}\right)^2 + \left(\frac{\delta \rho_{air}}{\dot{V}}\frac{\partial \dot{V}}{\partial \rho_{air}}\right)^2 + \left(\frac{\delta \rho_w}{\dot{V}}\frac{\partial \dot{V}}{\partial \rho_w}\right)^2} \qquad [155]$$

where

$$\frac{\partial \dot{V}}{\partial \Delta h} = k_1\, 0.5 \Delta h^{-0.5} \qquad [156]$$

$$\frac{\partial \dot{V}}{\partial D_1} = k_4 (-0.5) D_2^2 \left[1-\left(\frac{D_2}{D_1}\right)^4\right]^{-0.5} (-D_2^4)(-4D_1^{-5}) \qquad [157]$$

$$\frac{\partial \dot{V}}{\partial D_2} = k_4 D_2^2 \left[1-\left(\frac{D_2}{D_1}\right)^4\right]^{-0.5} + k_4 D_2^2 \left[1-\left(\frac{D_2}{D_1}\right)^4\right]^{-1.5} (-D_1^{-4}) 4 D_2^3 \quad [158]$$

$$\frac{\partial \dot{V}}{\partial \rho_{air}} = k_2 0.5 \rho_w^{-0.5} \quad [159]$$

$$\frac{\partial \dot{V}}{\partial \rho_{air}} = k3(-0.5)\rho_{air}^{-1.5} \quad [160]$$

where $k_1 - k_4$ are defined as follows

$$k_1 = C_D 0.25\pi(2g)^{0.5} \rho_w^{0.5} \rho_{air}^{-0.5} \left[1-\left(\frac{D_2}{D_1}\right)^4\right]^{-0.5} \quad [161]$$

$$k_2 = C_D 0.25\pi(2g)^{0.5} \rho_{air}^{-0.5} \left[1-\left(\frac{D_2}{D_1}\right)^4\right]^{-0.5} \Delta h^{0.5} \quad [162]$$

$$k_3 = C_D 0.25\pi(2g)^{0.5} \rho_w^{0.5} \left[1-\left(\frac{D_2}{D_1}\right)^4\right]^{-0.5} \Delta h^{0.5} \quad [163]$$

$$k_4 = C_D 0.25\pi(2g)^{0.5} \rho_w^{0.5} \rho_{air}^{-0.5} \Delta h^{0.5} \quad [164]$$

The accuracy of the measurements are:

	D_1	D_2	ρ_{air}	ρ_w	h	C_D	$\dot{V}$
Unit	m	m	kg m^{-3}	kg m^{-3}	m	-	m^3 s^{-1}
Values	0.05	0.025	1.298	998	0.9	0.747923	0.0251548
Error	0.0001	0.00001	0.005	0.005	0.0005		

The diameter D_1 and D_2 are determined by a Truth co-ordinate measuring machine. The accuracy of the diameter D_1 is not as good as for the diameter D_2 due to the surface roughness. For the calculation of the air and water density was an ASME program used that has an accuracy of 0.005 kg m^{-3}.

The error of the orifice plate measurement is calculated to $\frac{E_0}{\dot{V}} = 0.009549817$ or around 1%.

The uncertainty of other calculated values was determined in the same way and the maximum error is stated below.

The error for the thermal effectiveness derived with the equation

$$\eta = \frac{T_{ai} - T_{ao}}{T_{ai} - T_{wi}} \qquad [165]$$

is calculated to $\frac{E_0}{\dot{V}} = 0.0445$ or around 4.5% based on the following values and errors

Variable	t_{a1}	t_{a2}	t_{w1}
Units	°C	°C	°C
Value	156.4	29	19.9
Error	3%	3%	3%
Error value	4.692	0.87	0.597

The error for the index of performance derived with the equation

$$\psi = \frac{\dot{m}_a (c_{pa_i} t_{ai} - c_{pa_o} t_{ao})}{(T_{ai} - T_{wi}) P_w} \qquad [166]$$

is calculated to $\frac{E_0}{\dot{V}} = 0.01546$ or around 1.5% based on the following values and errors

Variable	$\dot{m}_a$	$\dot{m}_w$	t_{a1}	t_{a2}	t_{w1}	Δp_w	ρ_w	c_{pai}	c_{pao}
Units	kg s^{-1}	kg s^{-1}	°K	°K	°K	Pa	kg m^{-3}	J kg K^{-1}	J kg K^{-1}
Value	0.042	0.218	156.1	29	19.9	499780	998	1016	1005
Error	2%	2%	3%	3%	3%	1%	0,005	none	none
Error value	0.00084	0.00436	4.683	0.87	0.597	2498.9	0.005		

The error in c_{pa} is insignificantly small and was neglected.

The error for the flow number derived with the equation

$$FN = \frac{\dot{m}_L}{(p_L)^{0.5} (\rho_L)^{0.5}} \qquad [167]$$

is calculated to $\frac{E_0}{\dot{V}} = 0.020184$ or around 2% based on the following values and errors

Variable	$\dot{m}_w$	Δp_w	ρ_w
Units	kg s^{-1}	Pa	kg m^{-3}
Value	0.218	499780	999.2
Error	2%	1%	0,005
Error value	0.00436	2498.9	0.005

The error for the discharge coefficient derived with the equation

$$C_D = \frac{\dot{m}_L}{A_e \sqrt{2 \Delta p_L \rho_L}} \qquad [168]$$

is calculated to $\frac{E_0}{\dot{V}} = 0.128796$ or around 12.9% based on the following values and errors

Variable	$\dot{m}_w$	Δp_w	ρ_w	De
Units	kg s^{-1}	Pa	kg m^{-3}	m
Value	0.218	499780	999.2	0.0047
Error	2.0%	0.5%	0.005	0.00005
Error value	0.00436	2498.9	0.005	0.00005

At least forty measurements were taken for each sensor at steady state conditions. The evaporation rate and the temperature difference between inlet and outlet of the air were compared. The root-sum-square (RSS) combination was used to calculate the uncertainty of the measurements.

Temperature and its uncertainty can be represented by

$$t = \bar{t}_{measured} \pm \Delta t \qquad [169]$$

The value Δt represents 2 σ for a single-sample analysis as described by Moffat (1988), where σ is the standard deviation of the temperature measurements taken and $\bar{t}_{measured}$ is the average of the measurements. The standard deviation is calculated with the following equation:

$$\sigma = \sqrt{\frac{n\sum t^2 - \left(\sum t\right)^2}{n(n-1)}} \qquad [170]$$

The standard deviation for each data series is calculated for each point and nozzle configuration and is compared with the results of the simulation. The results for the 9a20/26 and 27a20/26 configurations are shown in Table 6-1.

Table 6-5: Standard deviation of the experimental data from 9a20/26 & 27a20/26 nozzle configuration

9a20	$\bar{t}_{a1}$	Δt_{a1}	$\bar{t}_{a2}$	Δt_{a2}	$\bar{\varphi}_2$	$\Delta\varphi_2$	$\bar{p}_w$	Δp_w
Liquid pressure MPa	[°C]	[°C]	[°C]	[°C]	[%]	[%]	[MPa]	[MPa]
0.1	152.1	0.49	81.0	1.47	6.0	0.74	1.015	0.028
0.2	151.9	0.59	69.3	2.39	9.9	1.36	2.005	0.043
0.3	152.1	0.63	58.5	0.81	17.9	1.40	3.046	0.039
0.4	153.0	0.40	51.3	0.58	28.2	1.52	4.040	0.050
0.5	153.3	0.58	47.7	0.23	33.1	1.42	5.005	0.058

9a26	$\bar{t}_{a1}$	Δt_{a1}	$\bar{t}_{a2}$	Δt_{a2}	$\bar{\varphi}_2$	$\Delta\varphi_2$	$\bar{p}_w$	Δp_w
Liquid pressure MPa	[°C]	[°C]	[°C]	[°C]	[%]	[%]	[MPa]	[MPa]
0.1	150.3	0.36	37.8	1.89	61.0	5.63	0.987	0.024
0.2	150.9	0.57	30.7	0.31	86.9	1.63	2.016	0.054
0.3	150.7	0.47	27.3	0.05	97.5	0.78	3.012	0.056
0.4	151.0	0.52	25.9	0.14	98.9	0.69	3.960	0.089
0.5	151.5	0.54	24.9	0.59	99.4	0.77	4.946	0.720

27a20	$\bar{t}_{a1}$	Δt_{a1}	$\bar{t}_{a2}$	Δt_{a2}	$\bar{\varphi}_2$	$\Delta\varphi_2$	$\bar{p}_w$	Δp_w
Liquid pressure MPa	[°C]	[°C]	[°C]	[°C]	[%]	[%]	[MPa]	[MPa]
0.1	151.5	0.45	71.7	0.63	9.9	0.79	1.009	0.029
0.2	150.5	0.34	62.8	0.57	14.7	0.66	2.134	0.026
0.3	150.4	1.99	55.9	0.78	22.6	2.01	2.996	0.028
0.4	148.8	0.34	47.1	0.56	37.2	1.90	3.979	0.031
0.5	149.5	0.85	43.1	0.26	45.3	2.18	5.047	0.032

27a26	$\bar{t}_{a1}$	Δt_{a1}	$\bar{t}_{a2}$	Δt_{a2}	$\bar{\varphi}_2$	$\Delta\varphi_2$	$\bar{p}_w$	Δp_w
Liquid pressure MPa	[°C]	[°C]	[°C]	[°C]	[%]	[%]	[MPa]	[MPa]
0.1	149.2	0.56	46.7	0.15	31.6	1.12	1.005	0.013
0.2	150.2	0.39	33.0	0.36	73.4	2.14	2.007	0.015
0.3	149.7	1.00	30.2	0.17	79.0	1.31	2.988	0.026
0.4	149.4	0.46	27.0	0.12	94.4	1.78	4.021	0.030
0.5	150.7	0.78	25.6	0.10	99.2	1.52	5.030	0.035

The specific humidity at the outlet of the spray chamber was calculated from the relative humidity. The measured relative humidity was temperature corrected as advised by the manufacturer of the instrument. The uncertainty for the specific humidity has to be traced through two equations that are a function of temperature and relative humidity. The equation for the temperature correction is

$$\varphi_{2c} = \varphi_2\left(1.041 - 0.0036\, t_2 + 8.3\, 10^{-5} t_2^2 - 3.5\, 10^{-7} t_2^3\right) \quad [171]$$

and the partial differential equation with respect to φ_2 is

$$\frac{\partial \varphi_{2c}}{\partial \varphi_2} = 1.041 - 0.0036 t_2 + 8.310^{-5} t_2^2 - 3.5110^{-7} t_2^3 \quad [172]$$

and with respect to t_2

$$\frac{\partial \varphi_{2c}}{\partial t_2} = \varphi_2\left(-0.0036 + 16.610^{-5} t_2 - 10.5310^{-7} t_2^3\right) \quad [173]$$

The overall uncertainty for the corrected relative humidity is then determined with the equation

$$\Delta\varphi_{2c} = \sqrt{\left(\frac{\partial \varphi_{2c}}{\partial \varphi_2}\Delta\varphi_2\right)^2 + \left(\frac{\partial \varphi_{2c}}{\partial t_2}\Delta t_2\right)^2} \Rightarrow \varphi_{2c} = \overline{\varphi}_{2c} \pm \Delta\varphi_{2c} \quad [174]$$

The specific humidity is determined with the following equation

$$\omega_2 = 0.622 \frac{p_{v2}\varphi_{2c}}{p_{amb} - p_{v2}\varphi_{2c}} \quad [175]$$

were the uncertainty of p_{amb} and p_{v2} is negligible small. Therefore, the partial differential equation in respect of φ_{2c} is

$$\frac{\partial \omega_2}{\partial \varphi_{2c}} = 0.622 \frac{p_{v2} p_{amb}}{\left(p_{amb} - p_{v2}\varphi_{2c}\right)^2} \quad [176]$$

and the final uncertainty is calculated by

$$\Delta\omega_2 = \frac{\partial \omega_2}{\partial \varphi_{2c}}\Delta\varphi_{2c} \quad [177]$$

Hence, the uncertainty for the humidity difference turn out to be the following

$$\omega_2 = \overline{\omega}_2 \pm \Delta\omega_2 \quad [178]$$

Calculated uncertainties for the nozzle configuration 9a20/26 and 27a20/26 are shown at the table below

Table 6-6: Uncertainties of the specific air outlet humidity from the spray chamber for configuration 9a20/26 & 27a20/26

Measurement 9a20 (pressure difference across nozzle)	$\partial\varphi_{2c}/\partial\varphi_2$	$\partial\varphi_{2c}/\partial t_2$	$\Delta\varphi_{2c}$	$\Delta\omega_2$
1. (0.1 MPa)	1.108	0.018	0.826	0.00264
2. (0.2 MPa)	1.074	0.028	1.466	0.00286
3. (0.3 MPa)	1.044	0.045	1.463	0.00176
4. (0.4 MPa)	1.027	0.061	1.564	0.00134
5. (0.5 MPa)	1.020	0.064	1.450	0.00104

Measurement 9a26 (pressure difference across nozzle)	$\partial\varphi_{2c}/\partial\varphi_2$	$\partial\varphi_{2c}/\partial t_2$	$\Delta\varphi_{2c}$	$\Delta\omega_2$
1. (0.1 MPa)	1.005	0.071	5.658	0.01808
2. (0.2 MPa)	0.999	0.044	1.627	0.00317
3. (0.3 MPa)	0.997	0.015	0.780	0.00094
4. (0.4 MPa)	0.997	0.001	0.684	0.00059
5. (0.5 MPa)	0.997	0.011	0.771	0.00055

Measurement 27a20 (pressure difference across nozzle)	$\partial\varphi_{2c}/\partial\varphi_2$	$\partial\varphi_{2c}/\partial t_2$	$\Delta\varphi_{2c}$	$\Delta\omega_2$
1. (0.1 MPa)	1.081	0.029	0.857	0.00274
2. (0.2 MPa)	1.056	0.039	0.698	0.00136
3. (0.3 MPa)	1.038	0.054	2.087	0.00251
4. (0.4 MPa)	1.019	0.070	1.935	0.00166
5. (0.5 MPa)	1.012	0.073	2.206	0.00158

Measurement 27a26 (pressure difference across nozzle)	$\partial\varphi_{2c}/\partial\varphi_2$	$\partial\varphi_{2c}/\partial t_2$	$\Delta\varphi_{2c}$	$\Delta\omega_2$
1. (0.1 MPa)	1.018	0.059	1.139	0.00364
2. (0.2 MPa)	1.000	0.054	2.139	0.00417
3. (0.3 MPa)	0.998	0.036	1.307	0.00157
4. (0.4 MPa)	0.997	0.011	1.778	0.00153
5. (0.5 MPa)	0.997	0.003	1.517	0.00109

6.4 Result and uncertainty calculation for CFD simulation

The residual errors are an indication of the convergence of the simulation and were used to calculate the uncertainty of the computational model. The results of the simulations are within an average of ±5.9% for the temperature and ±12% for the humidity from the averaged experimental result. The highest temperature difference was obtained for the 27a20 configuration at a water pressure of 0.2 MPa with a difference of 15.6%. The maximum difference for humidity is 37.6% at the 9a26 configuration for a water pressure of 0.2 MPa.

The uncertainty for the temperature at the simulation is calculated from the residual errors

$$t_{a2} = \frac{H1\ TMP1B}{R1} - 273 \qquad [179]$$

and the partial differential in respect to $H1$ is

$$\frac{\partial t_{a2}}{\partial H1} = \frac{TMP1B}{R1} \qquad [180]$$

and in respect to $R1$

$$\frac{\partial t_{a2}}{\partial R1} = -\frac{H1TMP1B}{R1^2} \qquad [181]$$

The temperature uncertainty in °C is calculated with the equation

$$\Delta t_{a2} = \sqrt{\left(\frac{\partial t_{a2}}{\partial H1}\Delta H1\right)^2 + \left(\frac{\partial t_{a2}}{\partial R1}\Delta R1\right)^2} \qquad [182]$$

and the percent of temperature uncertainty is calculated by

$$\frac{\Delta t_{a2}}{t_{a2}} = \sqrt{\left(\frac{\Delta H1}{\partial H1}\right)^2 + \left(\frac{\Delta R1}{\partial R1}\right)^2} \quad 100 \qquad [183]$$

The uncertainty for the specific humidity is derived in the same procedure. The specific humidity is calculated with the equation

$$\omega = \frac{VAPO}{R1} \qquad [184]$$

Therefore is the partial differential equation in respect to $VAPO$

$$\frac{\partial \omega}{\partial VAPO} = \frac{1}{R1} \qquad [185]$$

and in respect to $R1$

$$\frac{\partial \omega}{\partial R1} = \frac{VAPO}{R1^2} \qquad [186]$$

The uncertainty is then calculated by

$$\Delta\omega = \sqrt{\left(\frac{\partial \omega}{\partial R1}\Delta R1\right)^2 + \left(\frac{\partial \omega}{\partial VAPO}\Delta VAPO\right)^2} \qquad [187]$$

and in percent uncertainty

$$\frac{\Delta\omega}{\omega} = \sqrt{\left(\frac{\Delta R1}{\partial R1}\right)^2 + \left(\frac{\Delta VAPO}{\partial VAPO}\right)^2}\ 100 \qquad [188]$$

Table 6-7: Uncertainties of air temperature difference and air humidity difference of the simulation for the cases 1 to 5 at configuration 9a20/26 and 27a 20/26

Nozzle	Air temperature		Humidity	
Configuration	Average	Δt	Average	Δω
	[°C]		[kg_{H2O}/kg_{DA}]	
9a20-1	64.7	0.08	1.30E-02	2.45E-04
9a20-2	87.4	0.03	1.53E-02	2.07E-04
9a20-3	100.5	0.51	1.62E-02	8.88E-04
9a20-4	109.5	0.15	1.61E-02	4.42E-04
9a20-5	115.1	0.06	1.59E-02	3.25E-04

Nozzle	Air temperature		Humidity	
Configuration	Average	Δt	Average	Δω
	[°C]		[kg_{H2O}/kg_{DA}]	
9a26-1	97.1	0.04	1.19E-02	1.05E-04
9a26-2	116.7	0.43	1.24E-02	1.36E-03
9a26-3	124.7	0.18	1.17E-02	5.12E-04
9a26-4	129.7	0.18	1.14E-02	5.60E-04
9a26-5	133.0	0.23	1.12E-02	7.41E-04

Nozzle	Air temperature		Humidity	
Configuration	Average	Δt	Average	Δω
	[°C]		[kg_{H2O}/kg_{DA}]	
27a20-1	67.3	0.17	1.51E-02	3.08E-04
27a20-2	85.4	0.09	1.65E-02	1.46E-04
27a20-3	91.8	0.03	1.85E-02	3.05E-04
27a20-4	98.2	1.80	1.79E-02	4.70E-04
27a20-5	106.9	0.10	1.98E-02	3.24E-04

Nozzle	Air temperature		Humidity	
Configuration	Average	Δt	Average	Δω
	[°C]		[kg_{H2O}/kg_{DA}]	
27a26-1	102.3	0.18	1.20E-02	4.14E-04
27a26-2	119.2	0.07	1.24E-02	2.52E-04
27a26-3	126.0	0.05	1.23E-02	2.62E-04
27a26-4	129.7	0.35	1.27E-02	5.60E-04
27a26-5	132.3	0.18	1.22E-02	2.30E-04

6.5 Discussion

The discussion is divided into two different themes.

- The design of nozzles for heat transfer purpose was investigated by producing nozzles with different internal geometry and then tested experimentally. A comparison is made of measurements, with other workers results.
- A numerical simulation of a gas-liquid direct heat exchanger was carried out and the computations were compared with the experimental results.

6.6 Design of low pressure nozzle for heat transfer purpose

The aim of this investigation was to find a nozzle that produced the best heat transfer. This is the nozzle configuration 28c26 (see section 4.2) which operated at a liquid pressure difference of up to $5*10^5$ Pa. Low pressure difference is an important factor for industrial applications to increase the efficiency of the apparatus. Therefore, the objective is to decrease the pressure difference and preferably increase the mass flow rate of water to achieve a higher amount of energy transfer between the mediums. A pressure swirl nozzle and an effervescent atomiser were used in this experimental program. Both nozzles were designed to have the same flow rates so that the cooling performance can be directly compared.

The effervescent atomiser showed good heat transfer rates at high ALR's and consequently low water flow rates. The heat transfer per total power requirement is approximately ten times less for the pressure swirl nozzle and depends on the ALR. The reason for this was the high ALR. Some 95% of the power is invested to produce droplets. The remaining 5% is needed to pump and pressurise the water. At higher liquid mass flow rates, above 0.1 kg s^{-1} and at a constant pressure achieved by reducing the ALR, the heat transfer for the effervescent atomiser was not as good as that for the pressure swirl nozzle. This was because of the reduction of the spray angle and an increase of droplet size. The increase of the droplet size is caused by the thicker liquid sheet passing through the exit orifice. The increase of the liquid sheet is due to the reduction of air bubbles passing through the exit orifice. Another factor for the reduction in energy transfer is the residence time of the droplets in the hot air. High liquid mass flow rates were coupled with a increase of droplet velocity. The coupling of bigger droplets with reduced velocity decreased the energy transfer. The bigger droplets reduced the area of energy transfer and the reduced velocity decreased the Nusselt number. The time where the droplet is in suspension is extended, but can not make up for the decreased Nusselt number. The attempt to overcome this problem by applying different geometrical dimensions to the exit orifice and varying the inner pipe showed no significant effect.

A pressure swirl nozzle was designed, which allowed alteration of the internal geometry. Several configurations were tested at different water mass flow rates achieved by changing the water pressure. The water pressure was varied between $1*10^5$ Pa and $5*10^5$ Pa. The kinetic energy of the water was used to produce a liquid

sheet, which disintegrated into ligaments and then finally into droplets. Droplet sizes produced at low pressure were approximately 240 μm and decreased with the increase of water pressure to approximately 150 μm. The droplet velocity was between 10 to 30 m/s. The increase of pressure changes the radial and axial velocity component unequally, which resulted in a reduction of the spray angle. A result of this was the travel distance increased, due to the geometrical shape of the spray chamber. The best heat transfer was achieved with pressure swirl nozzles that have an exit orifice of 4.7 mm and therefore the highest amount of water mass flow rate. The best nozzle configuration for heat transfer was 28c26 and is compared in dimensionless terms with those used by Jones (1982) in Table 6-8.

The spray droplet distributions produced by the pressure swirl nozzle are not as narrow as it is for the Rotary atomiser. The measurement of the droplet size gave a range from 1.2 to 372 μm. The spray has a relatively wide scatter area for the hollow cone spray, which enhances the heat transfer because of number of droplets exposed to a higher volume of air.

The measurements of the SMD for the specified nozzle configuration showed a significant difference in comparison to the calculated SMD with the empirical equation defined by Lefebvre (1983), labelled as "Theory 9/27a2x" and plotted as a solid line in Figure 6-5. Generally, there was the same tendency of decreasing droplet size with increasing water pressure but the measured droplet size at low water pressure is between 58% and 78% smaller then the empirical results. This is seen in Figure 6-5. It is also obvious that the influence of the number of tangential inlets has a minor effect on the droplet size and that the droplet sizes for each case are close to each other.

Table 6-8: Differences in non-dimensional groups covered by Jones (1982) with 28c26 nozzle

Dimensionless group	Value for nozzle with best heat transfer rate	Typical value recommended by Jones (1982)
$\frac{L_e}{D_e}$	0.3	0.15
$\frac{L_s}{D_s}$	0.4	0.7
$\frac{L_p}{D_p}$	4.5	1.2
$\frac{A_p}{D_e D_s}$	0.267	0.52
$\frac{D_s}{D_e}$	1.6	2.7
$\frac{\mu_L}{\mu_A}$	60	750
$\frac{\rho_L}{\rho_A}$	780	700

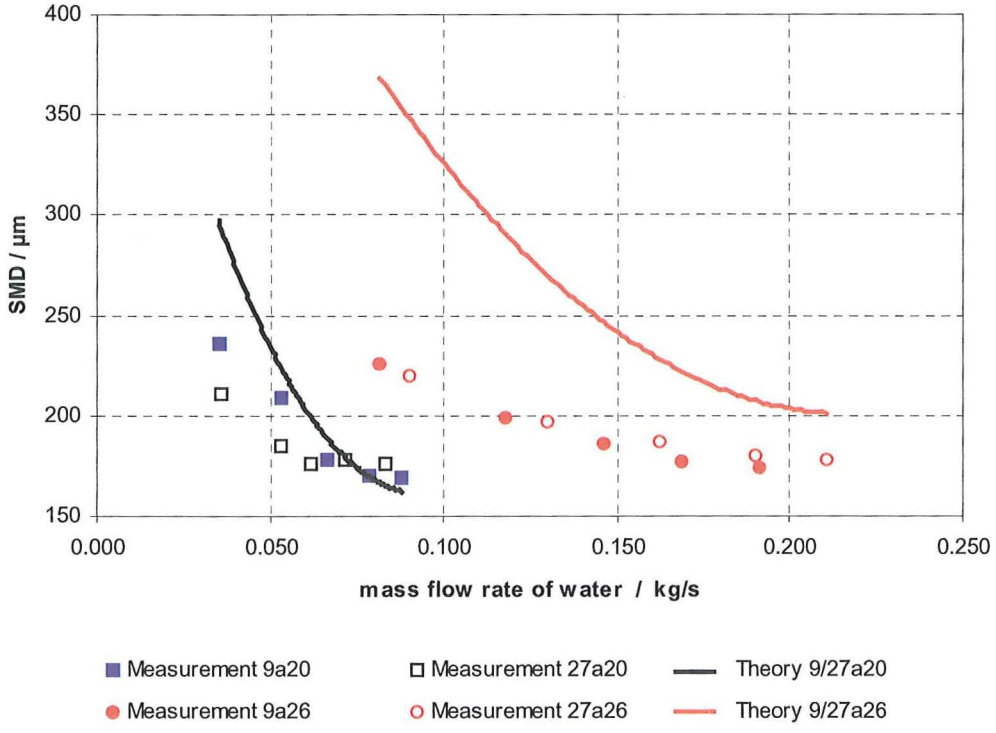

Figure 6-5: Result of the droplet measurement in comparison with the results of the empirical equation developed by Lefebvre

Three different derived equations, Babu et al (1982) [189], Lefebvre (1983) [190], and Richter and Walzel (1989) 191], are compared in Figure 6-6 and Figure 6-7 with the measured droplet sizes.

Babu et al (1982)

$$SMD = 133\frac{FN^{0.64291}}{\Delta p_L^{0.22565}\,\rho_L^{0.3215}} \qquad [189]$$

Lefbvre (1983)

$$SMD = 2.25\sigma_L^{0.25}\,\mu_L^{0.25}\,\dot{m}_L^{0.25}\,\Delta p_L^{-0.5}\,\rho_A^{-0.25} \qquad [190]$$

Richter and Walzel (1989)

$$SMD = 1.6\,D_e\,We^{-0.33}\,\chi^{0.4}(1+5\,Oh)^{1.5} \qquad 191]$$

where χ is defined as

$$\chi = \frac{2\dot{V}}{\left[D_e^2\pi^2\sin(0.5\theta)v\right]} \qquad [192]$$

For the 9/27a20 configuration with the 2.5 mm exit orifice diameter and the D_s/D_e ratio of 3 at a liquid mass flow rate of up to 0.070 kg s^{-1} the SMD is below the results of all the derived equations. At a flow rate above 0.070 kg s^{-1} Lefebvre's (1983) derived equation is the best prediction of the results as shown in Figure 6-6. The worst prediction of the measured droplet size was the equation derived by Babu (1982). The result is even worse for the measurements for the 9/27a26 configuration shown in Figure 6-7.

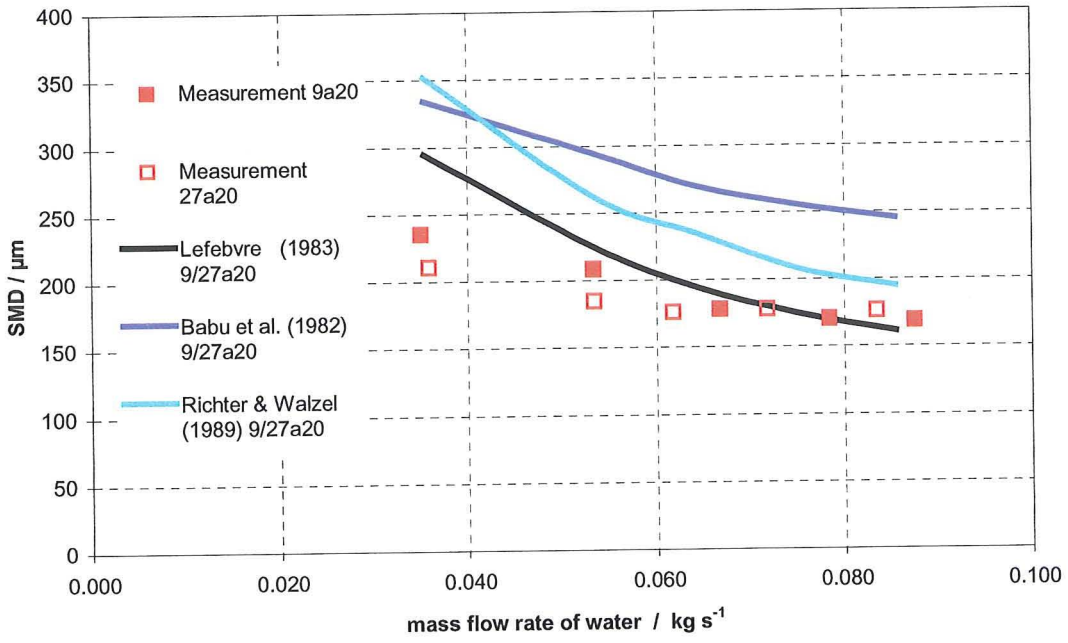

Figure 6-6: Comparison of the measured SMD at the configuration 9/27a20 with an exit orifice diameter of 2.5 mm with derived equations from the literature.

The prediction from Richter and Walzel (1989) comes closest to the measured droplet sizes for the 9/27a26 configuration at a liquid mass flow rate of 0.090 to 0.125 kg s^{-1} shown in Figure 6-7. The gap between the measured droplet size and Lefebvres prediction is at low liquid mass flow rate approximately 78%. With an increased liquid mass flow rate this gap decreases. The reason for this is that commercial pressure swirl nozzles are normally operated with a liquid pressure difference of above 1 MPa.

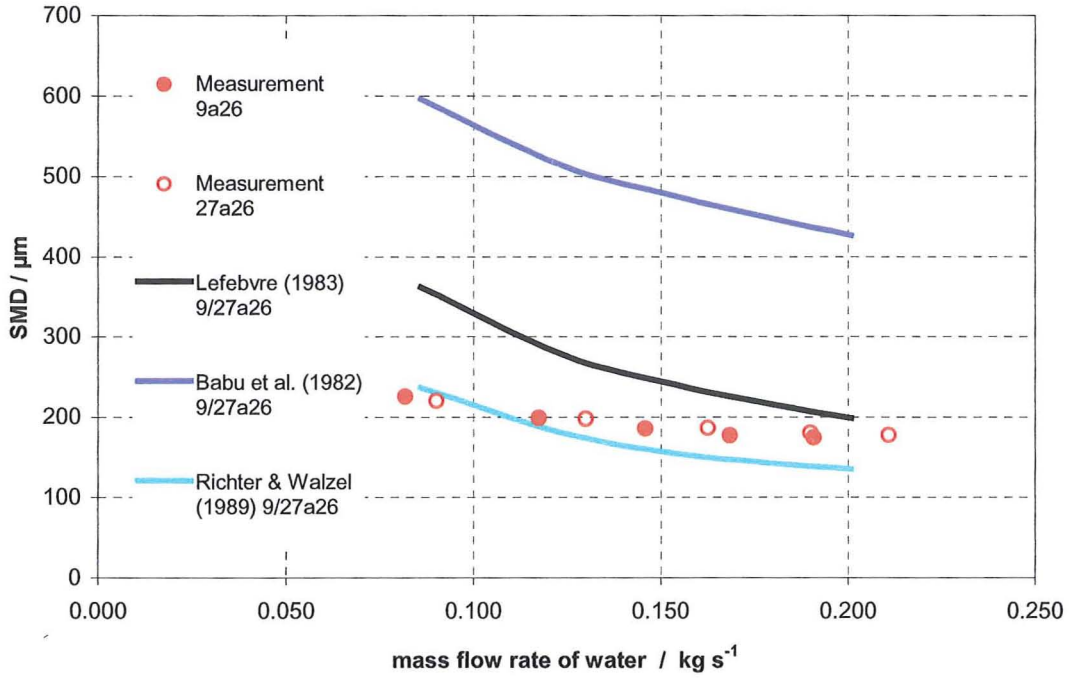

Figure 6-7: Comparison of the measured SMD at the configuration 9/27a26 with an exit orifice diameter of 4.7 mm with derived equations from the literature.

The reason for the deviation of Babu's derived equation is due to the deviation of the Lefebvre's (1985) prediction of the *FN* number, shown in Figure 6-8, which was used to calculated the SMD. The measured flow number, *FN*, as described in Chapter 2, is compared with Lefebvre's (1985) prediction of the flow number depending on the internal geometry of the pressure swirl nozzles over the exit orifice diameter, D_e. The flow number for the configuration with an exit orifice diameter of 2.5 mm is in close agreement with Lefebvre's prediction. There is for the nozzle configuration with an exit orifice diameter of 4.7 mm a difference of approximately 25% from Lefebvre's prediction. The standard nozzles are above the predicted flow number. The modified nozzle, 28c26, with half of the tangential inlet area into the swirl chamber is approximately 25% below the predicted result.

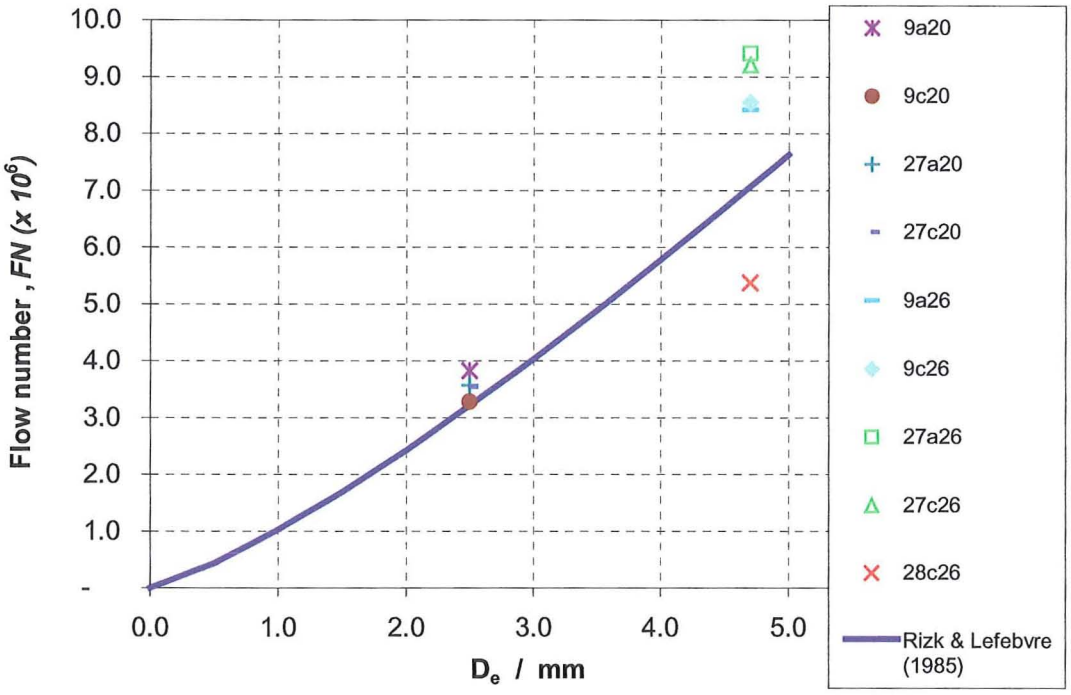

Figure 6-8: Comparison of the predicted flow number of Lefebvre's equation with the measured flow number at experiments.

This could be in part explained by the value of the discharge coefficient, C_D. Figure 6-9 compares the measured discharge coefficient with three derived equations from the literature that predict the discharge coefficient. The discharge coefficient is calculated with the equation (Jones, 1982, Chin and Lefebvre, 1993, Crocker et al., 1997)

$$C_D = \frac{\dot{m}_L}{A_e \sqrt{2\,\Delta p_L\,\rho_L}} \qquad [193]$$

where A_e is the outlet area of the exit orifice, Δp_L the pressure drop across the nozzle, and ρ_L the density of the liquid is. The mass flow rate of liquid, $\dot{m}_L$ is defined as

$$\dot{m}_L = A_r\, u\, \rho_L \qquad [194]$$

where A_r is the area of the exit orifice, A_e, occupied by the water. The remaining area is then used for the air core. u is the velocity along the centre line of the pressure swirl nozzle. The velocity component v is not present inside the exit orifice. This radial component arises due to the swirling motion after the liquid has left the exit orifice.

The derived equations used to compare the measured discharge coefficient are from Taylor (1950), Carlisle (1955), and Rizk & Lefebvre (1985).

Taylor (1950)

$$C_D = 1.17\left[\frac{(1-X)^3}{1+X}\right]^{0.5} \qquad [195]$$

where X is defined as the ratio of A_a/A_e

Carlisle (1955)

$$C_D = \sqrt{0.0616\frac{D_s}{D_e}\frac{A_p}{D_s D_e}} \qquad [196]$$

Rizk and Lefebvre (1985)

$$C_D = 0.35\left(\frac{A_p}{D_s D_e}\right)^{0.5}\left(\frac{D_s}{D_e}\right)^{0.25} \qquad [197]$$

The measured discharge coefficient varies with the liquid pressure. All measured points are displayed in Figure 6-9. The highest point in each measured configuration is the pressure point of $1*10^5$ Pa. The liquid pressure is not included in the derived equations from the literature. The discharge coefficient for the standard nozzles is in reasonable agreement with the derived equation [195] - [197] from the literature by other workers. The 28c26 configuration however is above the predicted discharge coefficient of all the derived equations. At the same time the measured discharge coefficient of the configuration 28c26 is below the nozzles with the same exit orifice diameter. This explains why the flow number is so low.

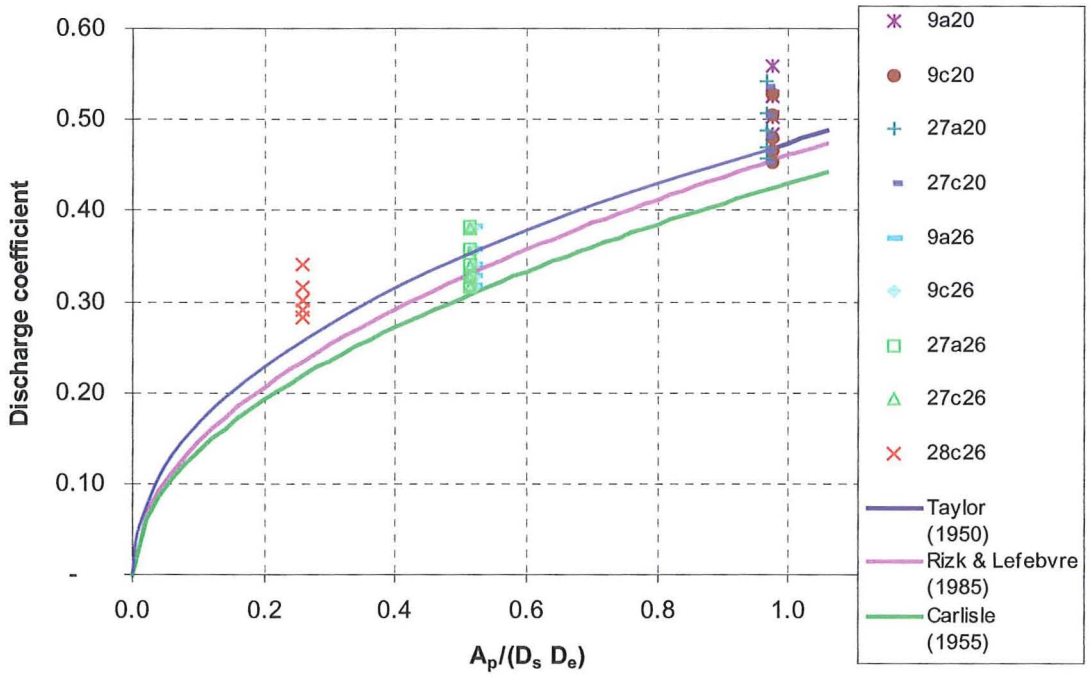

Figure 6-9: Comparison of the measured discharge coefficient, C_D, with the literature

The measured mean droplet velocity with the PDPA was calculated considering the spray angle. This is necessary, because the PDPA just measures the X-component of the droplet velocity. The mean velocity of the droplets was measured 40 mm down stream of the exit orifice. A measurement closer to the exit orifice could not be made because of the high spray density and a lack of laser intensity. The initial droplet velocity was calculated by using the equation of motion, which was also used by Crowe et al. (1977). An attempt to measure the droplet size distribution across the nozzle was not possible for the same reason. The laser used has an output of 10 mW, which is not powerfull enough to make measurements in a highly dense spray.

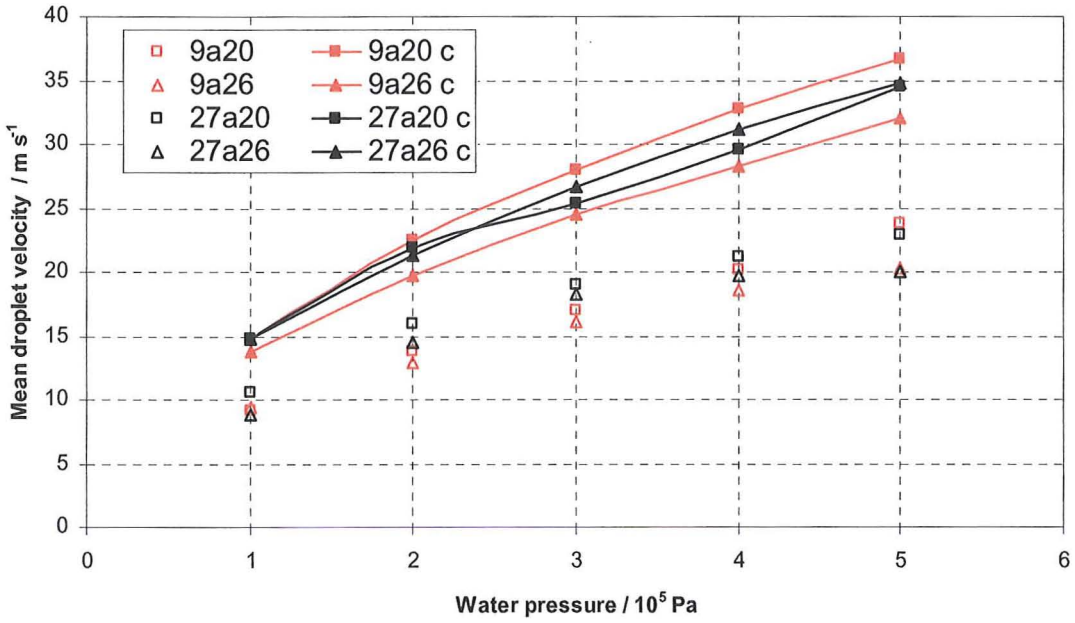

Figure 6-10: Comparison of the calculated mean droplet velocity with the measured mean droplet velocity over the water pressure

The calculated mean droplet velocity, displayed in the graph as lines with solid markers, from the literature, are approximately 60% higher then the measured mean droplet velocity, shown as hollow markers. The general tendency of the calculated and the measured result show an increase with rising water pressure. The significant difference of approximately 60% over the whole range of tested water pressure possible results from the unusual internal geometry and the wide droplet distribution. The wide droplet distribution results from the surface finish, which is not as smooth as commercially available nozzles. Commercially available nozzles have polished surfaces to reduce the friction loss and the disturbances in the liquid flow. The workshop did not have the machinery to polish the manufactured nozzles.

The spray angle for the configuration 9a20, 9a26, 27a20 and 27a26 were measured at the same water pressure as for the droplet size measurement and experiments. The result of the measured spray angle was verified, because similar configurations had similar values of the spray angle. The results of these similar configurations are not shown to avoid confusion. The spray angle in Figure 6-11 is presented over the range of water pressures to emphasise what effect the difference in the internal geometry

and water pressure has on the spray angle. The solid line in Figure 6-11 indicates the calculated spray angle from equation [14], which was derived by Rizk and Lefebvre (1985). The empirical equation does not consider the number of tangential slots and therefore 9/27a26 and 9/27a20 have the same results.

The measured spray angle for the configuration 9/27a26, which has a D_s/D_e ratio of 1.6, is in a reasonable agreement with the calculated results. The maximum difference is about 14.2% at a water pressure difference of $5*10^5$ Pa for the 27a26 configuration. The 9a26 configuration has a maximum difference of 5.2% and is over the whole pressure range close to the theoretical results.

The results for the 9/27a20 configuration, which has a D_s/D_e ratio of 3.0, are always lower and have a difference of approximately 5° over the whole pressure range from the calculated spray angle. The highest difference is at the water pressure of $5*10^5$ Pa and is 20% from the theoretical results.

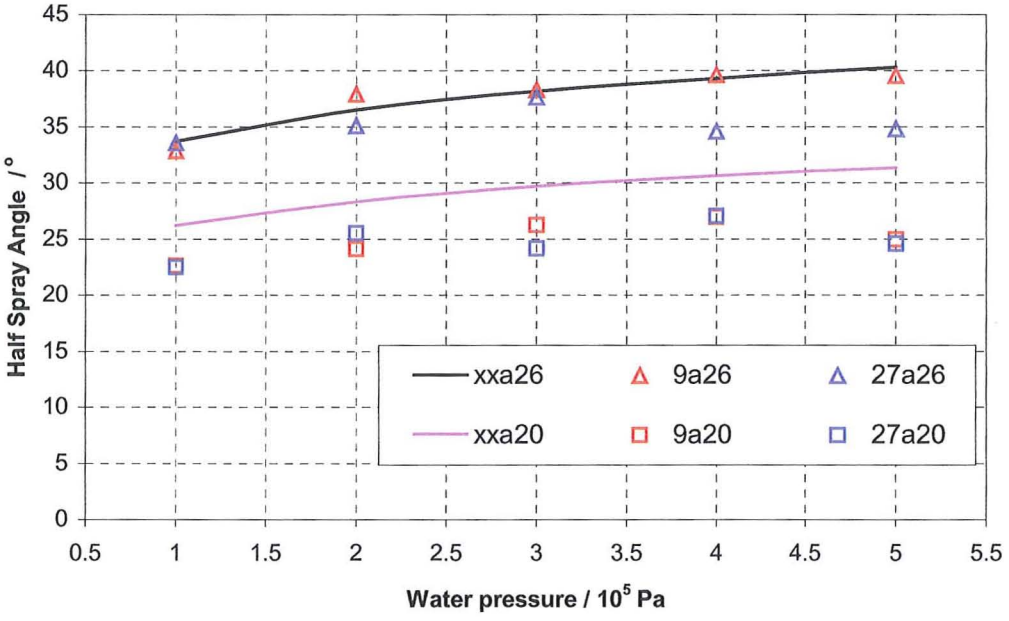

Figure 6-11: Comparison of measured to theoretical spray angle by Rizk and Lefebvre over the water pressure for 9/27a20 and 9/27a26

Droplets with the size of 225µm, produced by a pressure swirl nozzle with an exit orifice diameter of 4.7 mm, and 175µm, produced by a pressure swirl nozzle with an exit orifice diameter of 2.5 mm, have at the same liquid mass flow rate the same cooling performance. In Table 6-9 a calculation is performed to give information

about the surface area produced by the droplets. Values used for these calculations are taken from the measurements and listed in the first six rows. The area for the droplets per second is larger for the xx20 configuration because of the smaller droplets size. However, the instant area of the droplet size is 38% larger for the xx26 compared with the xx20. This is caused by the reduced velocity of the droplets, which increases the suspension time of the droplets with the surrounding gas.

If the droplets hit the Perspex spray chamber a falling water film is created by the droplets that do not bounce off. The wider spray angle of the xx26 configurations produces a larger falling water film area. The area is increased by approximately 340% and but has a small influence on the heat transfer performance.

The increase in wetted surface is large enough to counter the reduction of the Nusselt number caused by the lower droplet velocity.

Table 6-9: Comparison of the total instant area at different exit orifice diameters at the same liquid mass flow rate

Description		Results	
Configuration	Units	xx20	xx26
Mass flow rate	kg s^{-1}	0.085	0.085
Spray angle	deg	25	33
Scatter	deg	4	4
Droplet velocity	m s^{-1}	23	10
Sauter mean diameter	m	1.75E-04	2.25E-04
Area of droplets per second $\dot{A}_D = \frac{6\dot{m}_w}{\rho_w D_{32}}$	m^2 s^{-1}	2.920	2.271
Instant area of droplets $A_D = \frac{R_{ch}\dot{A}_D}{U_D \sin(\theta)}$	m^2	0.055	0.076
Area of falling water film $A_{fwf} = D_{ch}\pi\left(H_{ch} - R_{ch}\tan(90-\theta-\Delta\theta)\right)$	m^2	0.043	0.146
Total instant area	m^2	0.097	0.222

6.7 Simulation of heat transfer in a direct contact heat exchanger

The temperature and humidity data obtained from the computational simulation and experimental data are compared including their uncertainties.

The following graphs in this chapter have two lines that indicate the minimum and the maximum uncertainties for the experimental and computational results. The separation of these lines indicates for the experimental data the uncertainty of the instrumentation, for the computational model the residual errors. The small variation in the air temperature difference, Figure 6-12 to Figure 6-15, is an indication of a convergence from the simulations. It can be assumed that, when the model has fully converged, the result is within these limits. The results of the computational simulations compared with the experimental data are within acceptable agreement. The results of the air temperature difference from the simulation are at lower pressure in most cases smaller than the experimental data, except for the configuration 27a26. The computational air temperature difference exceeds the experimental air temperature difference at the increase of water pressure, except for the simulation 27a20. The uncertainty for the air temperature difference of the experimental data does not exceeding 3.6% and is therefore in an acceptable region for predicting the air temperature difference and the air outlet humidity.

For the configurations with lower water flow rate, 9a20 and 27a20, the air temperature difference follows a trend, which is increasing with the rise in water pressure. This leads for the 9a26 configuration to a 6.4°C average air temperature difference, which is equivalent to 9%. The simulation of the 27a20 configuration, Figure 6-14, follows this trend line very well and has therefore a maximum difference of 3.4% except for the 2 bar water pressure where the difference is 15.57%, which is also the maximum difference between all experimental data and the simulation results.

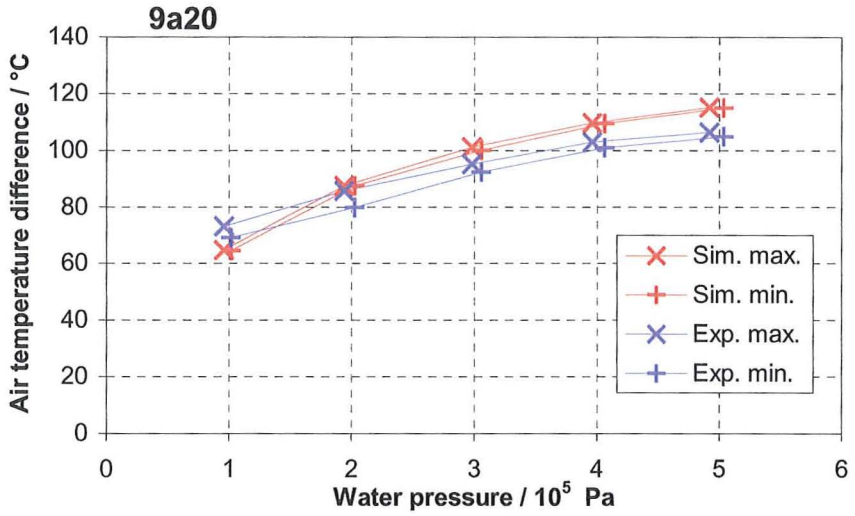

Figure 6-12: Comparison of the air temperature difference for experimental data and simulation results for configuration 9a20

The air temperature difference for the configurations 9a26 and 27a26 following a curve. These curves indicate that there will be settling points where no further temperature difference can be achieved. The experimental data indicates that this point will be at approximately 130°C. Whereas the result of the simulation indicates that this point will be at approximately 135°C. The results of the experimental data follow a curve that is not as steep as the curve for the simulation.

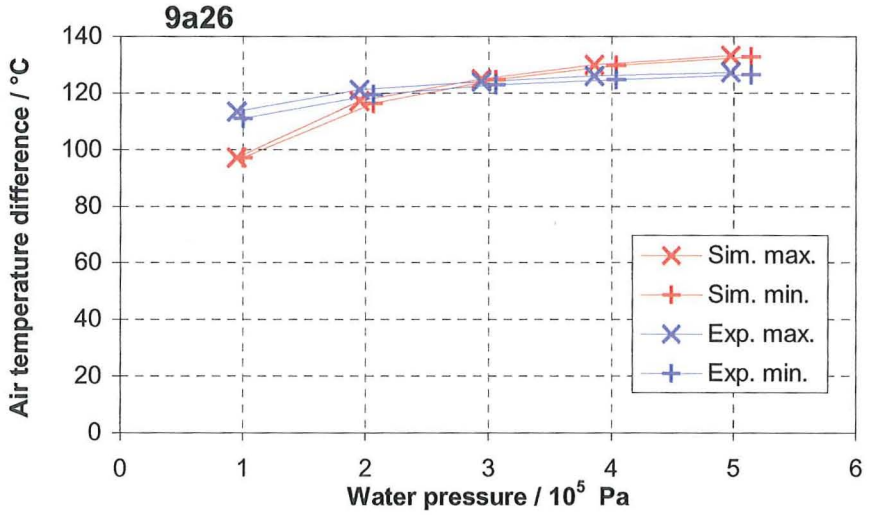

Figure 6-13: Comparison of the air temperature difference for experimental data and simulation results for configuration 9a26

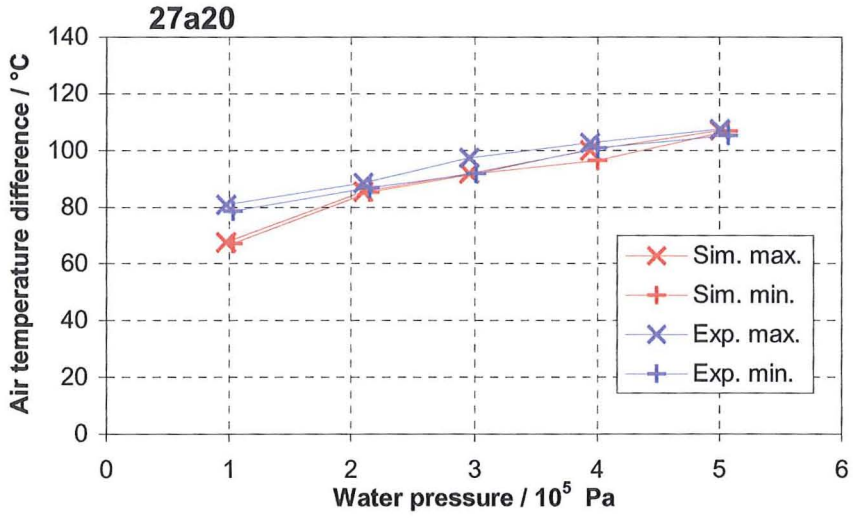

Figure 6-14: Comparison of the air temperature difference for experimental data and simulation results for configuration 27a20

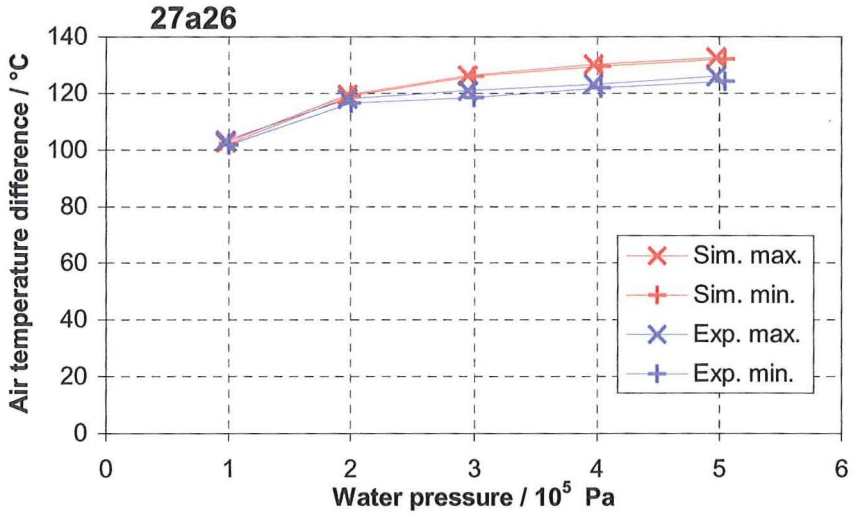

Figure 6-15: Comparison of the air temperature difference for experimental data and simulation results for configuration 27a26

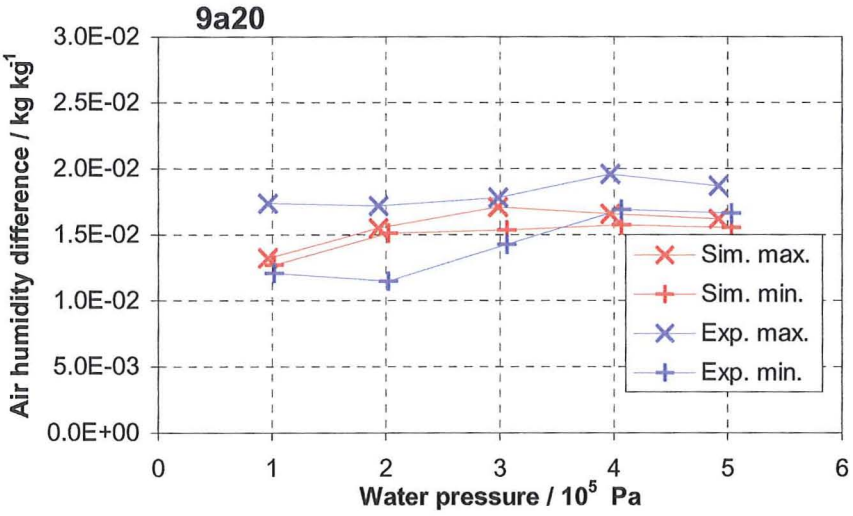

Figure 6-16: Comparison of the air humidity difference for experimental data and simulation results for configuration 9a20

The results from the experimental data for the configurations with a higher mass flow rate, 9a26 and 27a26, show a constant evaporation over the pressure range. The experimental data shows a high uncertainty of 37.6% maximum at the lower water pressure. This is caused by a standard deviation of $\Delta\varphi_2$=5.65%, which could be caused by a water droplet hitting the humidity sensor. Especially for the 9a26 configuration were the experimental data shows a declining amount of specific humidity with the increase of the water pressure. At this configuration the result of the simulation is not in the region of specific humidity but shows also a declining evaporation. This high uncertainty for the experimental data can only come from very small droplets carried with the air flow leaving the spray chamber and impinging on the humidity sensor were they finally evaporate. This leads to a higher uncertainty for the evaporation especially for lower pressure were the droplets produced by the nozzle are bigger.

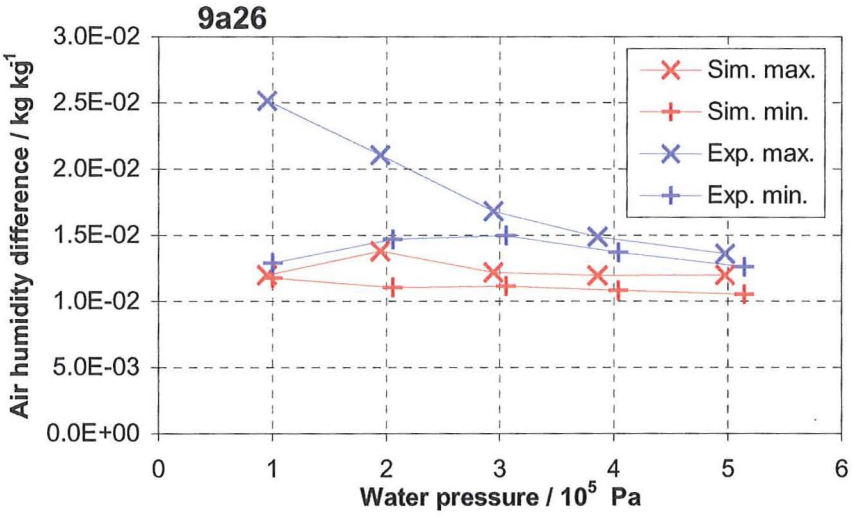

Figure 6-17: Comparison of the air humidity difference for experimental data and simulation results for configuration 9a26

The results of the simulation do not match exactly the result of the experimental data but they are in close agreement. This model gives an indication of the expecting results. The accuracy of the model depends on the Inlet-Data-File. This file contains the droplet information of the spray. The more accurate the droplet size, spray angle, and droplet velocity is, the closer is the result of the simulation to the experimental data. The developed model is as close to the existing spray chamber as PHOENICS is capable of defining it. Some simplifying assumptions have had to be made because it was not possible to define certain features. For example, the CFD software used had no option to define a falling water film on the wall of the cylinder coupled with heat and mass transfer. To overcome this problem the 'bouncing-off' function was activated with a coefficient of restitution of 0.3. This factor was determined by a series of tests with different restitution values. To minimise calculation time and errors the complete bottom plate was defined as the outlet area for droplets. The heat loss from the spray chamber was negligible and was assumed adiabatic.

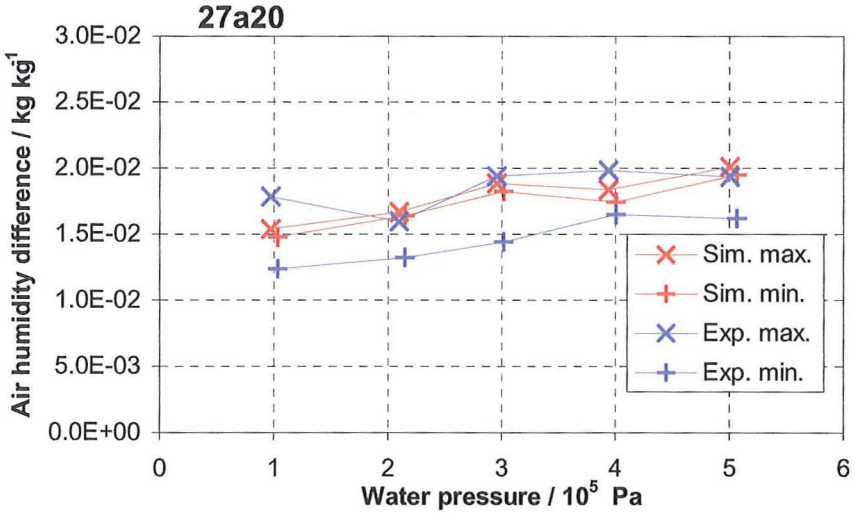

Figure 6-18: Comparison of the air humidity difference of experimental data and simulation results for configuration 27a20

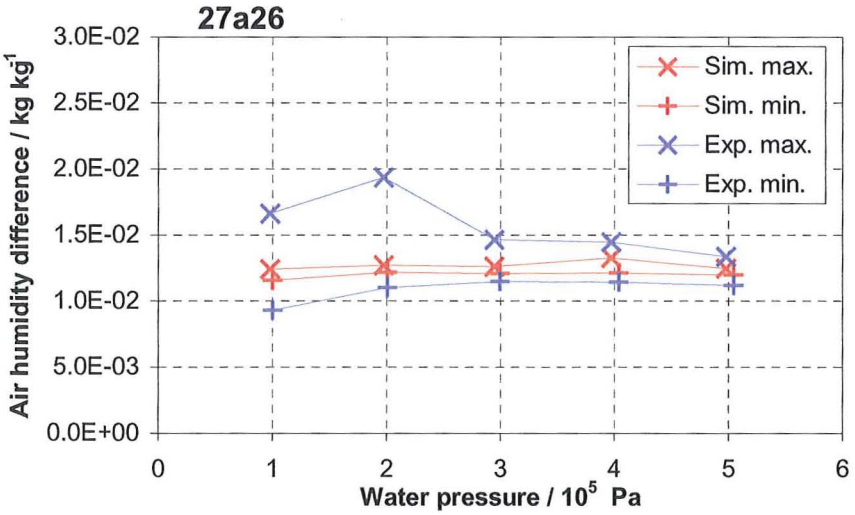

Figure 6-19: Comparison of the air humidity difference of experimental data and simulation results for configuration 27a26

The over all results of this model show that it is possible to simulate a heat transfer process in a direct heat exchanger and to obtain results which are close to the real process.

A further result of this study was that the geometrical design of the spray chamber is very important and has a significant influence in the efficiency. The result of the solved flow presented in vectors of the simulation is shown in Figure 6-20.

The area above the hollow cone spray pattern has none or only small droplets in suspension. This volume area is a 'dead zone' because it is unused for the heat and mass transfer. The options to minimise this area are:

a) two or more nozzles
b) redesign of the spray chamber

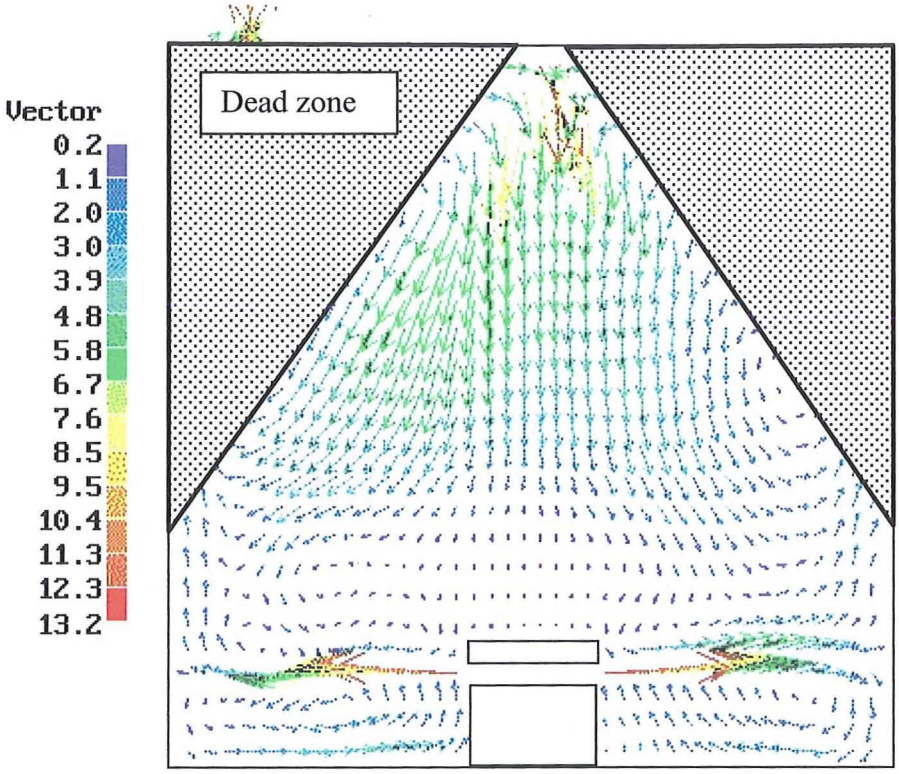

Figure 6-20: Solved flow in the spray chamber presented in vector form

Chapter 7 Conclusions and Recommendations

Heat transfer in a direct contact heat exchanger is a relative new technology, which can be used for many of applications as described in chapter 1. The advantage of this technique is that it has a small volume and can operate everywhere. The problem of blocked nozzles and high-energy consumption in producing the spray droplets has been solved by the use of a relatively large exit orifice and tangential slots. With this internal geometry, pressure swirl nozzles designed in this research, have reached an efficiency for heat transfer of 90%. The following conclusions are obtained from this work:

- The internal geometry of effervescent atomiser has only a minor influence on the heat transfer rates.
- The heat transfer of effervescent atomiser performance is influenced by the ALR.
- The highest heat transfer rates from air are for the effervescent atomiser with ALR of 0.1, which operates in the bubbly flow regime.
- The temperature of the atomising air for the effervescent atomiser has a strong influence on the nozzle performance. For lower gas inlet temperatures the nozzle effectiveness improved.
- The effectiveness of the effervescent atomiser tested starts at 88% for a liquid mass flow rate of 0.040 kg s^{-1} and reaches 93% at 0.160 kg s^{-1}.
- Pressure swirl nozzle needs 20 times less energy than effervescent atomisers to produce droplets having the same heat transfer rates
- Less pressure is needed for a pressure swirl nozzle with a bigger exit orifice diameter having the same mass flow rate as one with a smaller exit orifice diameter.
- The internal geometry, e.g. number of tangential slots (*NTS*), exit orifice diameter (D_e), length of swirl chamber (L_s) and exit orifice (L_e) of the pressure swirl nozzle have a strong influence on the water mass flow rate.

- An increase from $1*10^5$ to $5*10^5$ Pa in liquid pressure decreases the Sauter mean diameter, e.g. from 240 to 170 μm, for a given internal geometry of a pressure swirl nozzle.
- The use of pressure swirl nozzles with a 3 mm swirl chamber length has a better cooling performance and a higher specific humidity content than the same configuration with a 6 mm swirl chamber length at a smaller liquid mass flow rate. This is caused by less friction loss at the swirl chamber with a length of 3 mm.
- Pressure swirl nozzles with a 4.7 mm exit orifice diameter have a higher mass flow rate than one with a 2.5 mm exit orifice at the same tangential inlet slot area. This is due to the higher flow number, *FN*, and a reduction of the discharge coefficient, C_D, which is caused by the change of the exit orifice diameter.
- The numbers of tangential inlets of the pressure swirl nozzle have a minor effect on the droplet size. The maximum difference between 2 to 6 tangential slots is 5%. The 2.5 mm exit orifice has no distinguishable advantage, but the 4.7 mm exit orifice the swirl chamber with 2 tangential slots has a higher cooling performance.
- The L_e/D_e ratio of 0.3 showed the best cooling performance for the pressure swirl nozzle.
- The effectiveness of the pressure swirl nozzle starts at 85% for a liquid mass flow rate of 0.050 kg s^{-1} and reaches 95% at 0.160 kg s^{-1}.
- The Index of performance is about 20 times higher for the pressure swirl nozzle than for the effervescent atomiser. The higher the index of performance, the more cost effective the nozzle operation is.
- The numerical model is able to simulate the heat and mass transfer in 3 dimensional spray chamber. The average deviation of the results is about 6% for the temperature and 12% for the humidity.
- The droplet inlet file of the numerical simulation should have different droplet sizes, which are related to the droplet distribution. If different droplet sizes are used to describe the droplet distribution then the result is more accurate.

7.1 Further work

This work can be used as a basis for further research on direct contact heat exchangers. The influence of the spray chamber geometry, as mentioned in chapter 6, should be investigated.

A further interesting investigation would be to examine the heat transfer process in a pressurised spray chamber and an enclosed water and air system. Another point of interest would be the reversed process (cooling of hot water droplets) and its efficiency of it.

The effervescent nozzle should be used for smaller mass flow ratios in systems where the pressure inside the spray chamber is below the ambient pressure. This would result in a suction pressure for the atomising air. The energy for the air mixing would then be less. Such a process could be for example at the inlet manifold of an engine where a suction pressure is produced.

There are two options to minimise the "dead zone" area

a) two or more nozzles
b) redesign of the spray chamber

Solution a) is possible but the efficiency will not improve because the exit orifice of the nozzle has to be smaller, which means an increase in pumping energy. If nozzles with a bigger exit orifice are used, and the air mass flow rate is constant, the efficiency will go down, because as the experiments have shown, above a certain mass flow rate of water the cooling of the air is more or less constant and depends on the inlet temperature of the water.

Solution b) is to redesign the swirl chamber with the aim to minimise the 'dead zone'. The geometrical shape of the spray chamber of the direct heat exchanger should follow the shape of the spray pattern produced by the nozzle. Therefore, a spray chamber where a single hollow cone nozzle is used to produce the spray should have the shape of a cone with a smaller cone inside as shown in Figure 7-1.

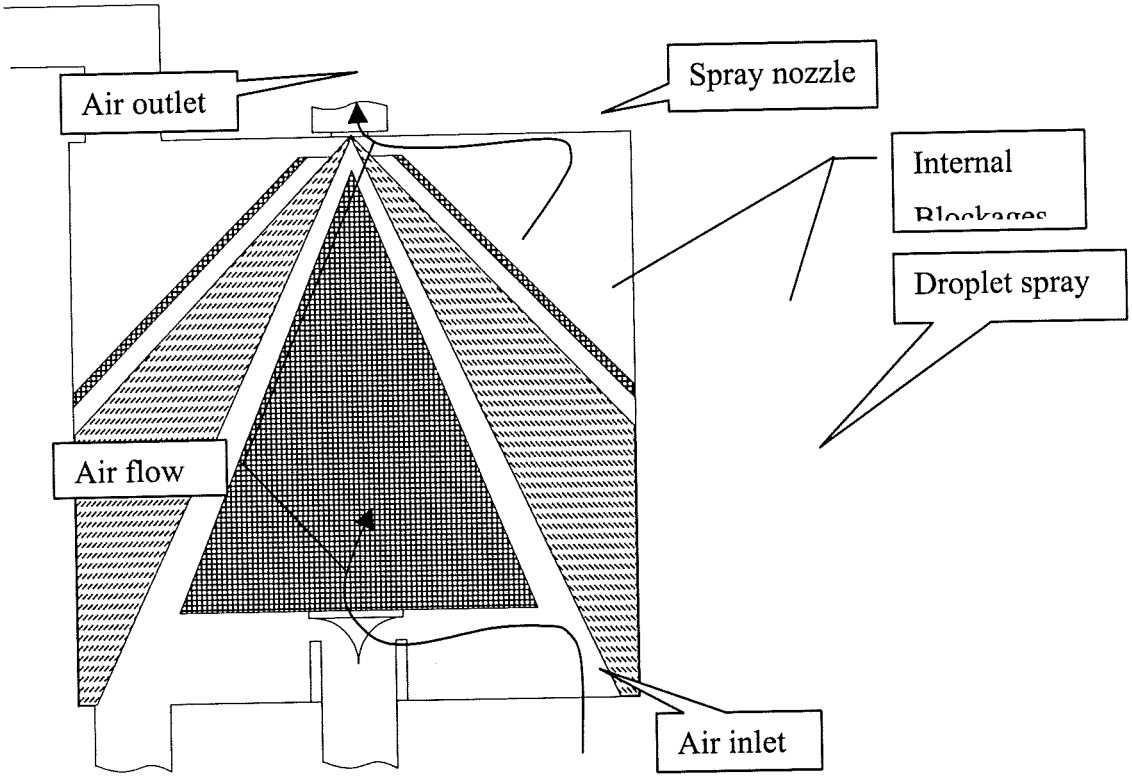

Figure 7-1: Optimised spray chamber design for hollow cone spray nozzle

The use of a full cone nozzle is possible but the efficiency is not as high as with hollow cone nozzles. The reason for this is that turbulence inside of the nozzle needs to be created and that consumes energy.

References

Antar, M. A., Al-Farayedhi, A. A., El-Shaaraiwi, M. A. I., Steady and Transient Liquid Sphere Heating in a Convective Gas Stream, Heat and Mass Transfer, **36**, 2000, 147-158

Arai, T., Hashimoto, H., Disintegration of a Thin Liquid Sheet in a Co-current Gas Stream, Proceedings of the ICLASS-85, ?, ?, 1985, VIB/1/1-VIB/1/7

Babu, K.R., Narasimham, M. V., Narayanaswamy, K., Predicting of Mean Drop Size of Fuel Sprays from Swirl Spray Atomizers, Procedings of the 2nd International Conference on Liquid Atomisation, Madison, Wis., 1982, pp. 99-106

Bachalo, W. D., Houser, M. J., Phase/Doppler Spray Analyser for Simultaneous Measurement of Droplet Size and Velocity Distributions, Journal of Optical Engineering, 1984, **23**, No. 5, 583-590

Back, G. G., 1995 Progress Report: Water Mist Fire Suppression Systems Technology, SFPE Bulletin, 1995, **23**, 1, 11-18

Bayvel, L., Orzechowski, Z., Liquid Atomisation, Taylor and Francis, 1989

BETE Fog Nozzle, Inc., Nozzles for Industry, Pollution Control and Protection – Manual No. 104L, Greenfield, MA, USA, 1995

Bhunia, S. K., Lienhard, J. H., Splattering During Turbulent Liquid Jet Impingement on Solid Targets, Journal of Fluids Engineering – Transaction of the ASME, 1994, **116**, No. 2, 338-344

Bird, R. B., Stewart, W. E., Lightfoot, E. N., Transport Phenomena, John Wiley & Son, Inc. New York, 1960

Bourgault, Y., Boutanios, Z., Habashi, W. G., Thre-Dimensional Eulerian Approach to Droplet Impingement Simulation Using FENSAP-ICE, Part 1: Model, Algorithm, and Validation, Journal of Aircraft, **37**, No. 1, 2000, 95-103

Bouse, L. F., Effect of Nozzle Type and Operation on Spray Droplet Size, Transaction of the ASAE, 1994, **37**, No. 5, 1389-1400

Buckner, H. N., Sojka, P. E., Effervescent Atomization of High-Viscosity Fluids: Part 1. Newtonian Liquids, Atomizer and Sprays, 1991, **1**, 239-252

Buglayev, V. T., Vasilyev, F. V., Strebkov, A. S., Exprimental Investigation of Heat Transfer in Evaporative Cooling of Air Flows with Fine Droplets, Heat Transfer – Soviet Research, 1985, **17**, No. 5, 97-103

Bush, S. G., Sojka, P. E., Entrainment by Effervescent Sprays at Low Mass Flow Rates, Procedings of the ICLASS-94, Rouen, France, 1994, Paper VI-3, 609-615

Bush, S. G., Sojka, P. E., Entrainment by Effervescent Sprays at Low Mass Flow Rates, Fluid Mechanics and Heat Transfer in Sprays, 1993, **178**, 117-121

Carlisle D. R., Communications on the Performance of a type of Swirl Atomiser, Proceedings of the Institution of Mechanical Engineering, 1955, **169**, 101-106

Chen, K. S., Lefebvre, A. H., Discharge Coefficients For Plain-Orifice Effervescent Atomizer, Thermal Sciences and Propulsion Center, School of Mechanical Engineering, Purdue University, West Lafayette, Indiana 47907

Chen, K. S., Lefebvre, A. H., Rollbuhler, J., Influence of Ambient Air Pressure on Effervescent Atomization, Journal of Propulsion and Power, 1993, **9**, No. 1, 10-15

Chen, S. K., Lefebvre, A. H., Spray Cone Angles of Effervescent Atomizers, Atomization and Sprays, 1994, **4**, 291-301

Chin, J. S., Lefebvre, A. H., A Design Procedure for Effervescent Atomizers, Proceedings of the International Gas Turbine and Aeroengine Congress and Exposition, Cincinnati, Ohio, 1993, Paper 93-GT-337

Chin, J. S., Lefebvre, A. H., Flow Patterns in Internal-Mixing, Twin-Fluid Atomizers, Atomisation and Sprays, 1993, **3**, 123-136

Chin, J. S., Lefebvre, A. H., The Role of the Heat-up Period in Fuel Drop Evaporation, Internation Journal of Turbo Jet Engines, 1985, **2**, 315-325

Coleman, H. W., Stern, F., Uncertainties and CFD Code Validation, Journal of Fluid Engineering, 1997, **119**, 795-803

Creismeas, P., A Eularian/Lagrangian Model to Calculate the Evolution of a Water Droplet Spray, International Journal for Numerical Methods in Fluids, 1995, **20**, 135-155

Crocker, D. S., Fuller, E. J., Fuel Nozzle Aerodynamic Design using CFD Analysis, Journal for Gas Turbines and Power, 1997,**119**, No. 7, pp. 527-534

Crowe, C. T., Sharman, M. P., Stock, D. E., The Particle-Source-In Cell (PSI-CELL)

Model for Gas-Droplet Flows, Journal of Fluids Engineering, 1977, 325-332

Dahl, H. D., Muschelknautz, E., Liquid Atomization with Hollow Cone Nozzles, Proceedings of the ICLASS-91, Gaithersburg, MD, U.S.A., 1991, 205-213

Delavan-Delta, Inc., Spray Nozzles and Accessories for Spraying Applications, Lexington, TN, USA, 1993

Dombrowski, N, Jones, W. R., The Aerodynamic Instability and Disintegration of Viscous Liquid Sheets, Chemical Engineering Sience, 1963, **18**, 203-214

Dorfner, V., Domnick, J., Durst, F., Köhler, R., Viscosity and Surface Tension Effects in Pressure Swirl Atomization, Atomization and Sprays, 1995, **5**, No. 3, 261-285

Edson, J. B., Fairall, C. W., Spray Droplet Modelling: 1. Lagrangian Model Simulation of the Turbulent Transport of Evaporating Droplets, Journal of Geophysical Research, 1994, **99**, No. C12, 25,295-25,311

Elkotb, M. M., Rafat, N. M., Hanna, M. A., The Influence of Swirl Atomizer Geometry on the Atomization Performance, Proceedings of the ICLASS-78, Tokyo, Japan, 1978, 109-115

Faeth, G. M., Current Status of Droplet and Liquid Combustion, Prog. Energy Combustion. Science, **3**, 1977, 191-244

Feng, Z.-G., Michaelides, E. E., A numerical Study on the Transient Heat Transfer from a Sphere at High Reynolds and Peclet Numbers, International Journal of Heat and Mass Transfer, **43**, 2000, 219-229

Friedman, J. A., Renksizbulut, M., Interaction of an Annular Air Jet with a Non-Evaporating Liquid Spray, Particle and Particle Systems, **11**, No. 6, 442-452

Fritsching, U., Bauckhage, K., Modelling the Spray Cone Behaviour in the Metal Spray Forming Process, PHOENICS Journal, October 1994, 68-90

Fritsching, U., Uhlenwinkel, V., Bauckhage, K., Investigation on the Atomization of Molten Metals: The Coaxial Jet and the Gas Flow in The Nozzle Vicinity, Journal of Fluid Engineering, 1995, **117**, 81-98

Geckler, S. C., Sojka, P. E., High Mass Flow Rate Effervescent Atomization of Viscoelastic Fluids, Fluid Mechanics and Heat Transfer in Sprays, 1993, **178**, 109-115

Giffen, E., Muraszew, A., Atomisation of Liquid Fuels, Chapman & Hall, London, 1953

Giles, D. K., Independent Control of Liquid Flow Rate and Spray Droplet Size from Hydraulic Atomisers, Atomization and Sprays, 1997, **7**, 161-181

Godsave, G. A. E., Studies of the Combustion of Drops in a Fuel Spray - the Burning of Single Dops of Fuel, Fourth Symposium (International) on Combustion, Williams & Wilkins, Baltimore, 1953, 847-864

Hausser, F., Strobl,G. M., Method of Catching Droplets on a Surface and Defining the Drop Size Distributions by Curves, Zeitung der Technischen Physik, 1924, **5**, No. 24, pp. 154-157

Hino, T., Shimabayashi, S., Ohnishi, N., Fujisaki, M,. Hiroyuki, M., Watanabe, O., Kawashima, K., Nagao, K., Develpoment of a New Type Nozzle and Spray-Drier for Industrial Production of Fine Powders, European Journal of Pharmaceutics and Biopharmaceutics, **49**, 2000, 79-85

Hiroyasu, H., Arai, M., Shimizu, M., Break-up Length of a Liquid Jet and Internal Flow in a Nozzle, Proceedings of the ICLASS-91, Gaithersburg, MD, U.S.A., 1991, 275-282

Holman, J. P., Heat Transfer, McGraw-Hill Book Company, New York, 1968

Inaba, H., Horibe, A., Ozaki, K., Yokohama, N., Liquid-Liquid Direct Contact Heat Exchanger Using a Perfluorocarbon Liquid for Waste Heat Recovery, JSME International Journal Series B – Fluids & Thermal Engineering, **43**, No. 1, 2000, 52-61

Incropera, F. P., DeWitt, D. P., Fundamentals of Heat and Mass Transfer, 3rd edition, John Wiley & Sons, New York, 1990

Jasuja, A. K., Atomisation of Crude and Residential Fuel Oils, ASME Journal of Engineering and Power, 1979, **101**, No. 2, pp.250-258

Jicha, M., Karki, K. C., Pantankar, S. V., Numerical Investigation of Water Spray Systems in the Entrance Region of a 2D Channel using the Langrangian Approch, Procedings of the 10th International Heat Transfer Conference, Birmingham, UK, 1994, **3**, paper 6-CD-12, 335-340

Johnson, N. L., The Legacy and Future of CFD at Los Alamos, Proceedings of the

Canadian CFD Conference, Ottawa, Canada, 1996, paper LA-UR-96-1426

Jones, A. R., Design Optimisation of a Large Pressure Jet Atomizer for Power Plant, Proceedings of the ICLASS-82, Madison, WIS, U.S.A., 1982, 181-185

Joyce, J. R., The Atomization of Liquid Fules for Combustion, Journal from Institution of Fuel, 1949, **22**, No. 124, pp. 150-156

Kachhwaha, S. S., Dhar, P. L., Kale, S. R., Experimental Studies and Numerical Simulation of Evaporative Cooling of Air with a Water Spray – I. Horizontal Parallel Flow, International Journal of Heat and Mass Transfer, 1998, **41**, No. 2, 447-464

Kachhwaha, S. S., Dhar, P. L., Kale, S. R., Experimental Studies and Numerical Simulation of Evaporative Cooling of Air with a Water Spray – II. Horizontal Counter Flow, International Journal of Heat and Mass Transfer, 1998, **41**, No. 2, 465-474

Kawashima, N., Droplets and Domain Walls in 2D Edwards-Anderson Model, International Journal of Modern Physics, **10**, No. 8, 1999, 1453-1458

Kennedy, J. B., High Weber SMD Correlations of Pressure Swirl Atomizer, ASME, 1985, Paper 85-GT-37

Kuchling, H., Taschenbuch der Physic, Verlag Harri Deutsch, Thun, G.D.R., 1989

Kutty, P. S., Narasimhan, M. V., Narayanaswamy, K., Design and Prediction of Discharge Rate, Cone Angle and Aircore Diameter of Swirl Chamber Atomisers, Proceedings of the ICLASS-78, Tokyo, Japan, 1978, 93-100

Lee, S. H., Ryou, H. S., Development of a New Spray/Wall Interaction Model, International Journal of Multiphase Flow, **26**, 2000, 1209-1234

Lee, W. Y., Sojka, P. E., The Influence of Fluid Viscoelasticity on Low Mass Flow Rate Effervescent Atomization, Fluid Mechanics and Heat Transfer in Sprays, 1993, **178**, 129-135

Lefebvre, A. H., Atomization and Sprays, Taylor and Francis, 1989

Lefebvre, A. H., Energy Consideration in Twin-Fluid Atomization, Proceedings of the International Gas Turbine and Aeroengine Congress and Exposition, Brussels, Belgium, 1990, Paper 90-GT-3

Lefebvre, A. H., Gas Turbine Combustion, Hemisphere, Washington, D.C., 1983

Lefebvre, A. H., Some Recent Developments in Twin-Fluid Atomization, Part. Part.

Syst. Charact., 1996, **13**, 205-216

Lefebvre, A. H., Twin-Fluid Atomizer: Factors Influencing Mean Drop Size, Proceedings of the ICLASS-91, Gaithersburg, MD, U.S.A., 1991, Paper D, 49-56

Lefebvre, A. H., Wang, X. F., Martin, C. A., Spray Characteristics of Aerated-Liquid Pressure Atomizer, Journal of Propulsion, 1988, **4**, No. 4, 293-298

Li, J., Lefebvre, A. H., Rollbuhler, J. R., Effervescent Atomization for Small Gas Turbines, Proceedings of the International Gas Turbine and Aeroengine Congress and Exposition, The Hague, Netherlands, 1994, Paper 94-GT-495

Lund, M. T., Jian, C. Q., Sokja, P. E., Gore, J. P., Panchagnula, M. V., The Influence of Atomizing Gas Molecular Weight on Low Mass Flow Rate Effervescent Atomizer Performance, Fluid Mechanics and Heat Transfer in Sprays, 1993, **178**, 123-128

Lund, M. T., Sokja, P. E., Lefebvre, A. H., Effervescent Atomization at Low Mass Flow Rates. Part 1: The Influence of Surface Tension, Atomization and Sprays, 1993, **3**, 77-89

Mahler, D. S., Magnus, D. E., Hot-Wire Technique for Droplet Measurements, Liquid Particle Size Measurement Techniques, American Society for Testing and Materials STP 848, 1984, pp. 153-164

Mao, C.-P., Chuech, S. G., Numerical Analysis of Pressure Swirl Atomizers, Proceedings of the ICLASS-91, Gaithersburg, MD, U.S.A., 1991, 225-232

May, K. R., The Measurement of Airborn Droplets by the Magnesium Oxide Method, Journal of Scientific Instrumentation, 1950, **27**, pp. 128-130

Moffat. R. J., Contributions to the Theory of Single-Sample Uncertainty Analysis, Journal of Fluids Engineering, 1982, **104**, 250-260

Moffat. R. J., Describing the Uncertainties in Experimental Results, Experimental Thermal and Fluid Science, 1988, **1**, 3-17

Møller, J. T., Controlling Powder Properties in the Spray Drying Process, Lecture at Powtech, F-148, Basel, Switzerland, 1980

Mundo, C., Sommerfeld, M., Tropea,C., Droplet-Wall Collisions: Experimental Studies of the Deformation and Break-up Process, International Journal of Multiphase Flow, 1995, **21**, No. 2, 151-173

Nam, S., Numerical Simulation of Actual Delivered Density of Sprinkler Spray

Through Fire Plumes, Fluid Mechanics and Heat Transfer in Sprays, 1993, **178**, 57-65

Nielsen, K. A., Glancy, C. W., Hoy, K. L., Perry, K. M., A New Atomization Mechanism for Airless Spraying: The Super critical Fluid Spray Process, Proceedings of the ICLASS-91, Gaithersburg, MD, U.S.A., 1991, 367-374

Nukiyama, S., and Tanasawa, Y., Experiments on the Atomisation of liquids in an Air stream, Report 3 on the Droplet-Size Distribution in an Atomised Jet, Defence Research Board, Department National Defence, Ottawa, Canada; translated from Trans. Soc. Mech. Eng. Jpn., **5**, No. 18, 1939, 62-67

Park, T. W., Aggarwal, S. K., Katta, V. R., A numerical Study of Droplet-Vortex Interaction in an Evaporating Spray, International Journal of Heat and Mass Transfer, 1996, **39**, No. 11, 2205-2219

Patankar, S. V., Numerical Heat Transfer and Fluid Flow, HemispherePublishing Corporation, New York, U.S.A., 1980

Petr, V., Kolovaratnik, M., Modelling of the Droplet Size Distribution in a Low Pressure Steam Turbine, Proc of the Inst of Mech Eng, **214**, A2, 2000, 145-152

Petr, V., Kolovratnik, M., Modelling of the Droplet Size Distribution in a Low-Pressure Steam Turbine, Proceedings of the Intuition of Mechanical Engineers, **214**, Part A, 145-152

Radcliffe, A., Fuel Injection, High Speed Aerodynamics and Jet Propulsion, Princeton University Press, Princeton, 1960, **11**, Sect. D

Ranz, W. E., Marshell, W. R., Evaporation of Drops, Chemical Eng. Prog., 1952, **48**, Part 1, pp.141-146, Part 2, pp.173-180

Richter, T., Walzel, P., Zerstäuben von Flüssigkeiten mit Hohlkegeldüsen, Chem.-Ing.-Tech., 1990, **61**, No. 4, 319-321

Risk, N. K., Chin, J. S., Razdan, M. K., Modelling of Gas Turbine Fuel Nozzle Spray, Journal for Gas Turbines and Power, 1997,**119**, No. 1, pp. 34-44

Rizk, N. K., Lefebrve, A. H., Internal Flow Characteristics of Simples Swirl Atomisers, Journal of Propulsion and Power, 1985, **1**, No. 3, 193-199

Rizkalla, A. A., Lefebvre, A. H., The Influence of Air and Liquid Properties on Airblast Atomization, Journal of Fluids Engineering, 1975, **97**, 316-320

Rogers, G. F. C., Mayhew, Y. R, Engineering Thermodynamics Work & Heat Transfer, Longman Group Ltd., London, UK, 1967

Rogers, G. F. C., Mayhew, Y. R, Thermodynamic and Transport Properties of Fluids, Blackwell Publisher Ltd., Oxford, UK, 1995, 5th edition

Rogers, S., Katgerman, L., Particle Tracking of Solidifying Metal Droplets During Gas Atomisation, PHOENICS Journal, October 1994, 171-182

Rosler, T. C., Lefebvre, A. H., Studies on Aerated-Liquid Atomization, International Journal of Turbo and Jet Engineers, 1989, **6**, No. 3, 221-229

Schlichting, H., Boundary–layer Theory, 7th edition, McGraw-Hill, New York, U.S.A., 1979

Schlick GmbH & Co., Schlick-Düsen Catalogue, Coburg, Germany, 1995

Schmidt, O., Lewis, J. S., Kubie, J., Index of Performance of Pressure Swirl Nozzles, Proceedings of ILASS Conference, Lund, Sweden, 1996, 13-18

Sidahmed, M. M., A Theory for Predicting the Size and Velocity of Droplets from Pressure Nozzles, Transactions of the ASAE, 1996, **39**, No. 2, 385-391

Sidahmed, M. M., Model for Predicting the Droplet Size from Liquid Sheets in Airstreams ,Transaction of the ASAE,1996, **39**, No. 5, 1651-1655

Spalding, D. B., The Combustion of Liquid Fules, Fourth Symposium (International) on Combustion, Williams & Wilkins, Baltimore, 1953, 847-864

Spraying Systems Co., Industrial Spray Products – Catalog 55M, Wheaton, Illinois, USA, 1994

Squire, H. B., Investigation of the Instability of a Moving Liquid Film, British Journal of Applied Physics, 1953, **4**, 167-169

Suzuki, K., Nakabe, K., Yamanaka, T., Heat Transfer Accompained by Evaporation to a Recirculationg Turbulent Dispersed Flow, Physico Chemical Hydrodynamics, 1985, **6**, No. 2, 311-327

Takahashi, F., Schmoll, W. Y., Dressler J. L., Characteristic of a Velocity-Modulated Pressure Swirl Atomizing Spray, Journal of Propulsion and Power, 1995, **11**, No. 5, 955-963

Tengler, A., Maschinen- und Düseneinsatz Gebiete, Funktion und Anwendungsbereiche, VCH Verlagsgesellschaft mbH, D-6940 Weinheim, 1990

Tipler, W., Wilson, A.W., Combustion in Gas Turbines, Procedings of the cong. Int. des Maschines a Combustion (CIMAC), Paper 9B, Paris, 1959, pp. 897-927

Uhlenwinkel, V., Schreckenberg, P., Bauckhage, K., Tropengrößen- und Geschwindigkeitsmessungen bei der Zerstäubung von Wasser mittles einer Hohlkegeldüse in einer Umgebung geringer Dichte, Chem.-Ing.-Tech., 1990, **62**, No. 12, 1060-1061

Versteeg, H. K., Malalasekera, W., An Introduction to Computational Fluid Dynamics, Longman Scientific & Technical, New York, U.S.A., 1995

Walzel, P., Zerstäuben von Flüssigkeiten, Chem.-Ing.-Tech., 1990, **61**, No. 12, 983-994

Wan, L. S. C., Heng, P. W. S., Liew, C. V., The Influence of Liquid Spray Rate and Atomizing Pressure on the Size of Spray Droplets and Spheroids, Interantional Journal of Pharmaceutics, 1995, **118**, 213-219

Wang, X. F., Lefebvre, A. H., Mean Drop Sizes from Pressure Swirl Nozzles, Journal of Propulsion and Power, 1987, **3**, No. 1, 11-18

Whitlow, J. D., Lefebvre, A. H., Effervescent Atomizer Operation and Spray Characteristics, Atomizer and Sprays, 1993, **3**, 137-155

Young, J. B., The Fundamental Equations of Gas-Droplet Multiphase Flow, International Journal of Multiphase Flow, 1995, **21**, No. 2, 175-191

Zhang, Z., Ziada, S., PDA Measurement of Droplet Size and Mass Flow Rate in the Three Dimensional Atomisation Region of Water Jet in Air Cross-Flow, Experimental in Fluids, **28**, 2000, 29-35

Appendix

A - Q1-file

```
TALK=f;RUN( 1, 1);VDU=VGAMOUSE
************************************************************
  Q1 created by GENTRA menu, Version 2.2.1, Date 16/04/97
□ CHAR(CPVNAM);CPVNAM=GENTRA
CHAR(CPVNAM);CPVNAM=GENTRA
************************************************************
IRUNN  =      1 ;LIBREF =      2
************************************************************
 Group 1. Run Title
TEXT(CYLINDER                        )
************************************************************
 Group 2. Transience
STEADY  =   T
************************************************************
 Groups 3, 4, 5  Grid Information
  * Overall number of cells, RSET(M,NX,NY,NZ,tolerance)
RSET(M,25,20,25)
  * Set overall domain extent:
  *       xulast  yvlast  zwlast   name
XSI= 6.283E+00;YSI= 1.860E-01;ZSI= 3.720E-01;RSET(D,CHAM    )
  * Set objects: x0     y0     z0
  *           dx     dy     dz    name
XPO= 0.000E+00;YPO= 0.000E+00;ZPO= 0.000E+00
XSI= 6.283E+00;YSI= 2.500E-02;ZSI= 0.000E+00;RSET(B,INLET   )
XPO= 3.000E+00;YPO= 1.260E-01;ZPO= 3.720E-01
XSI= 2.900E-01;YSI= 4.000E-02;ZSI= 0.000E+00;RSET(B,OUTLET  )
XPO= 0.000E+00;YPO= 2.500E-02;ZPO= 0.000E+00
XSI= 6.283E+00;YSI= 1.000E-02;ZSI= 4.000E-02;RSET(B,B3      )
XPO= 0.000E+00;YPO= 0.000E+00;ZPO= 5.500E-02
XSI= 6.283E+00;YSI= 3.500E-02;ZSI= 1.000E-02;RSET(B,B4      )
XPO= 0.000E+00;YPO= 1.860E-01;ZPO= 0.000E+00
XSI= 6.283E+00;YSI= 0.000E+00;ZSI= 3.720E-01;RSET(B,WALL    )
XPO= 0.000E+00;YPO= 3.500E-02;ZPO= 0.000E+00
XSI= 6.283E+00;YSI= 1.510E-01;ZSI= 0.000E+00;RSET(B,BP      )
XPO= 0.000E+00;YPO= 0.000E+00;ZPO= 3.720E-01
XSI= 3.000E+00;YSI= 1.860E-01;ZSI= 0.000E+00;RSET(B,TP1     )
XPO= 3.290E+00;YPO= 0.000E+00;ZPO= 3.720E-01
XSI= 2.993E+00;YSI= 1.860E-01;ZSI= 0.000E+00;RSET(B,TP2     )
XPO= 3.000E+00;YPO= 0.000E+00;ZPO= 3.720E-01
XSI= 2.900E-01;YSI= 1.260E-01;ZSI= 0.000E+00;RSET(B,B9      )
XPO= 3.000E+00;YPO= 1.660E-01;ZPO= 3.720E-01
XSI= 2.900E-01;YSI= 2.000E-02;ZSI= 0.000E+00;RSET(B,TP4     )
  * Cylindrical-polar grid
CARTES=F
************************************************************
 Group 6. Body-Fitted coordinates
BFC=T
  **********
NONORT  =   T
NCRT    =     1
  * X-cyclic boundaries switched
XCYIZ(  1, NZ, T )
************************************************************
 Group 7. Variables: STOREd,SOLVEd,NAMEd
```

```
ONEPHS =   T
  * Non-default variable names
NAME( 34) =REST ; NAME( 35) =MOMZ
NAME( 36) =MOMY ; NAME( 37) =MOMX
NAME( 38) =VPOR ; NAME( 39) =EPKE
NAME( 40) =EL1  ; NAME( 41) =ENUT
NAME( 42) =DEN1 ; NAME( 43) =PRPS
NAME( 44) =WCRT ; NAME( 45) =VCRT
NAME( 46) =UCRT ; NAME( 47) =TMP1
NAME( 48) =MASS ; NAME( 49) =HEAT
NAME( 50) =VAPO
  * Solved variables list
SOLVE(P1  ,U1  ,V1  ,W1  ,H1  ,VAPO)
  * Stored variables list
STORE(HEAT,MASS,TMP1,UCRT,VCRT,WCRT,PRPS,DEN1)
STORE(ENUT,EL1 ,EPKE,VPOR,MOMX,MOMY,MOMZ,REST)
SOLUTN(P1  ,Y,Y,Y,N,N,Y)
SOLUTN(H1  ,Y,Y,Y,N,N,Y)

**************************************************************
 Group 8. Terms & Devices
NEWRH1 =   T
**************************************************************
 Group 9. Properties
RHO1   = GRND5
RHO1A  = 0.000E+00 ;RHO1B  = 3.472E-03 ;RHO1C  = 7.179E-01
PRESS0 = 1.000E+05
TMP1   = GRND2
TMP1A  = 0.000E+00 ;TMP1B  = 9.794E-04 ;TMP1C  = 0.000E+00
CP1    = 1.017E+03
ENUL   = 2.839E-05 ;ENUT   = 5.678E-03
DRH1DP = GRND5
**************************************************************
 Group 10.Inter-Phase Transfer Processes
**************************************************************
 Group 11.Initialise Var/Porosity Fields
        RESTRT(all)

CONPOR(B3      ,  0.00,CELL  ,-#1,-#3,-#1,-#2,-#1,-#3)


INIADD =   F
**************************************************************
 Group 12. Convection and diffusion adjustments
  No PATCHes used for this Group
**************************************************************
 Group 13. Boundary & Special Sources

INLET (INLET   ,SOUTH ,#1,#3,#3,#3,#2,#2,#1,#1)
VALUE (INLET   ,P1  , 1.260E+01)
VALUE (INLET   ,V1  , 1.607E+01)
VALUE (INLET   ,H1  , 4.323E+05)

PATCH (GXOUT   ,HIGH  ,#2,#2,#4,#4,#4,#4,#1,#1)
COVAL (GXOUT   ,P1  , 1.000E+02, 0.000E+00)

PATCH (GXOUT2  ,LOW   ,#1,#3,#3,#5,#1,#1,1,1)

PATCH (WALL    ,NWALL ,#1,#3,#5,#5,#1,#4,#1,#1)
COVAL (WALL    ,U1  , GRND2    , 0.000E+00)
```

```
COVAL (WALL   ,W1  , GRND2   , 0.000E+00)

PATCH (BUOYANCY,PHASEM,#1,#NREGX,#1,#NREGY,#1,#NREGZ,#1,#NREGT)
COVAL (BUOYANCY,U1  , FIXFLU  , GRND2   )
COVAL (BUOYANCY,V1  , FIXFLU  , GRND2   )
COVAL (BUOYANCY,W1  , FIXFLU  , GRND2   )

PATCH (BP     ,LWALL ,#1,#3,#3,#5,#1,#1,#1,#1)
COVAL (BP     ,U1  , GRND2   , 0.000E+00)
COVAL (BP     ,V1  , GRND2   , 0.000E+00)

PATCH (TP1    ,HWALL ,#1,#1,#1,#5,#4,#4,#1,#1)
COVAL (TP1    ,U1  , GRND2   , 0.000E+00)
COVAL (TP1    ,V1  , GRND2   , 0.000E+00)

PATCH (TP2    ,HWALL ,#3,#3,#1,#5,#4,#4,#1,#1)
COVAL (TP2    ,U1  , GRND2   , 0.000E+00)
COVAL (TP2    ,V1  , GRND2   , 0.000E+00)

PATCH (B9     ,HWALL ,#2,#2,#1,#3,#4,#4,#1,#1)
COVAL (B9     ,U1  , GRND2   , 0.000E+00)
COVAL (B9     ,V1  , GRND2   , 0.000E+00)

PATCH (TP4    ,HWALL ,#2,#2,#5,#5,#4,#4,#1,#1)
COVAL (TP4    ,U1  , GRND2   , 0.000E+00)
COVAL (TP4    ,V1  , GRND2   , 0.000E+00)

PATCH (GENPAT  ,CELL  ,1,NX,1,NY,1,NZ,1,1)
COVAL (GENPAT  ,U1  , FIXFLU  , GRND    )
COVAL (GENPAT  ,V1  , FIXFLU  , GRND    )
COVAL (GENPAT  ,W1  , FIXFLU  , GRND    )
COVAL (GENPAT  ,H1  , FIXFLU  , GRND    )
COVAL (GENPAT  ,TMP1, FIXFLU  , GRND    )
COVAL (GENPAT  ,VAPO, FIXFLU  , GRND    )

PATCH (GENMAS  ,CELL  ,1,NX,1,NY,1,NZ,1,1)
COVAL (GENMAS  ,P1  , FIXFLU  , GRND    )

BUOYA  = 0.000E+00 ; BUOYB = 0.000E+00 ; BUOYC =-9.810E+00
BUOYD  = 8.210E-01
BFCA   = 8.373E-01
XCYCLE =  T
EGWF   =  T
************************************************************
 Group 14. Downstream Pressure For PARAB
************************************************************
 Group 15. Terminate Sweeps
LSWEEP =  1000
SELREF =  T
RESFAC = 1.000E-03
************************************************************
 Group 16. Terminate Iterations
************************************************************
 Group 17. Relaxation
RELAX(P1  ,LINRLX, 7.000000E-01)
RELAX(U1  ,FALSDT, 3.444444E-06)
RELAX(V1  ,FALSDT, 3.444444E-06)
RELAX(W1  ,FALSDT, 3.444444E-06)
RELAX(H1  ,FALSDT, 3.444444E+01)
RELAX(MOMZ,LINRLX, 1.000000E-01)
```

```
RELAX(MOMY,LINRLX, 1.000000E-01)
RELAX(MOMX,LINRLX, 1.000000E-01)
RELAX(MASS,LINRLX, 1.000000E-01)
RELAX(HEAT,LINRLX, 1.000000E-01)
RELAX(VAPO,FALSDT, 3.444444E+01)
************************************************************
 Group 18. Limits
VARMAX(U1  ) = 1.000000E+06 ;VARMIN(U1  ) =-1.000000E+06
VARMAX(V1  ) = 1.000000E+06 ;VARMIN(V1  ) =-1.000000E+06
VARMAX(W1  ) = 1.000000E+06 ;VARMIN(W1  ) =-1.000000E+06
VARMAX(VAPO) = 1.000000E+00 ;VARMIN(VAPO) = 0.000000E+00
************************************************************
 Group 19. EARTH Calls To GROUND Station
GENK   =   T
RG( 51) = 5.000E+00
RG( 52) = 5.000E+03
RG( 53) = 8.000E-03
RG( 54) = 4.520E+00
RG( 55) = 5.200E+00
RG( 56) = 4.000E+00
RG( 57) = 3.020E+00
L($G001
GENTR  =   T
 *----------------------------------------------------
 * GENTRA GROUP 1: Particle physics
 *----------------------------------------------------
 * Particle type -  60 VAPORISING_DROPLETS
GPTYPE =     60
 * Gravity components in GENTRA Cartesian system
GGRAX  = 0.000E+00  ;GGRAY = 0.000E+00  ;GGRAZ =-9.810E+00
 * Buoyancy forces
GBUOYA =   F  ;GSURPR =   F
 * Stochastic model of turbulence
GSTOCH =   F
 * Data for vaporising particles
 * Data for melting/solidifying particles
GDRAG  = GRND1    ;GKONC  = 2.630E-02 ;GNUSS  = GRND1
GKONV  = GRND1    ;GCPCON = 1.007E+03 ;GCPVAP = GRND1
GMWCON  = 2.890E+01 ;GMWVAP = 1.800E+01 ;GLIQST = 2.731E+02
GCPLIQ  = 4.132E+03 ;GHLIQD = GRND1    ;GVAPST = GRND1
GLATVP  = GRND1    ;GSTPRE = GRND1    ;GDTRCT = 0.000E+00
 *----------------------------------------------------
 * GENTRA GROUP 2: Boundary conditions for particles
 *----------------------------------------------------
 * Inlet-data file-name
GINFIL ='drop'
 * Wall treatment, and rest coefficient if appropriate
GWALLC =     3
GWREST  = 3.0E-1
 * Porosity threshold
GPOROS  = 0.000E+00
 *----------------------------------------------------
 * GENTRA GROUP 3: Numerical controls
 *----------------------------------------------------
 * 1st GENTRA sweep; frequency of calls
GSWEP1 =    500 ;GSWEPF =     1
 * Maximum Lagrangian time-step; time step size multplier
GDTMAX  = 1.000E-03 ;GRTFRC = 1.000E+05
 * Min # of t-steps per cell; max # of t-steps; timeout
GLAGTS =     5 ;GSTEMX =    -20
```

```
GTIMMX  = 5.00E-1
 *--------------------------------------------------
 * GENTRA GROUP 4: Output controls
 *--------------------------------------------------
 * Restart-file, history-file and frequency for output
GRSFIL  ='NONE'
GHFILE  ='ghis'
GOUTFR  =      1
 * The identifier of the individual history and
   trajectory files
GH1STC  ='NONE'
GT1STC  ='NONE'
 * The first, last particles and the interval for
   writing history and trajectory files
NGWSTR  =      1 ;NGWEND =      1 ;NGWINT =      1
GSWOUT  =     10
 * Particle number for residence-time calculation
GRESTI  =      0
L(GENSET
 ***************************************************************
 Group 20. Preliminary Printout
ECHO    =   T
 ***************************************************************
 Group 21. Print-out of Variables
 ***************************************************************
 Group 22. Monitor Print-Out
IXMON   =     13 ;IYMON =     15 ;IZMON =     15
NPRMNT  =      1
 ***************************************************************
 Group 23.Field Print-Out & Plot Control
  No PATCHes used for this Group
 ***************************************************************
 Group 24. Dumps For Restarts
NOWIPE  =   T
 ***************************************************************
MENSAV(S,RELX,DEF,9.3000E-03,27,1.0000E-02)
MENSAV(S,PHSPROP,DEF,200,0,8.3730E-01,1.5440E-05)
MENSAV(S,FLPRP,DEF,CONSTANT_EFFECTIVE,IDEAL_GAS_LAW)
m
STOP
```

B - Inlet data for the Q1-file for specific configuration

Nozzel Configuration	Inlet temp [°C]	[°K]	$Cp_{a(t)}$ [kJ/kg K]	Air enthalpy [J/Kg]	Air dens. [kg/m3]	Air mass flow [kg/s]	Air velocity [m/s]
9a20	152.14	425.1	1017	4.323E+05	0.831	0.04404	1.607E+01
	151.91	424.9	1017	4.320E+05	0.831	0.04406	1.607E+01
	152.06	425.1	1017	4.322E+05	0.831	0.04407	1.608E+01
	152.98	426.0	1017	4.332E+05	0.829	0.04407	1.611E+01
	153.28	426.3	1017	4.335E+05	0.828	0.04407	1.613E+01
9a26	150.33	423.3	1017	4.303E+05	0.834	0.04375	1.590E+01
	150.87	423.9	1017	4.309E+05	0.833	0.04368	1.589E+01
	150.74	423.7	1017	4.308E+05	0.833	0.04371	1.590E+01
	151.04	424.0	1017	4.311E+05	0.833	0.04364	1.589E+01
	151.53	424.5	1017	4.316E+05	0.832	0.04364	1.590E+01
27a20	151.45	424.5	1017	4.315E+05	0.832	0.04336	1.580E+01
	150.46	423.5	1017	4.305E+05	0.834	0.04337	1.577E+01
	150.37	423.4	1017	4.304E+05	0.834	0.04338	1.577E+01
	148.78	421.8	1016	4.287E+05	0.837	0.04338	1.571E+01
	149.51	422.5	1016	4.295E+05	0.836	0.04359	1.581E+01
27a26	149.17	422.2	1016	4.291E+05	0.836	0.04388	1.590E+01
	150.18	423.2	1017	4.302E+05	0.834	0.04388	1.594E+01
	149.72	422.7	1016	4.297E+05	0.835	0.04389	1.593E+01
	149.39	422.4	1016	4.293E+05	0.836	0.04389	1.592E+01
	150.68	423.7	1017	4.307E+05	0.833	0.04390	1.597E+01

C - FORTRAN program to generate Data-Inlet-File

```
INTEGER  NT,SPR,TT,S,L,R,K
REAL     X1,X2,XP,YP,ZP,VD,TETAZ,DTETA,DI,MDOTT,&
REAL     LDEN,TEM,DTETAT,T1
REAL  UP,VP,WP,MDOT,MDOT1,MDOT2,MDOT3,MDOT4,D1,D2,D3
PI=3.1415
OPEN(1,STATUS="UNKNOWN",FILE="drop")
print*,'This program writes the Inlet-data file for&
PHOENICS'
print*,'into a polar coordinated domain'
print*,'Please insert the following values'
print*,'X-position'
read*,XP
print*,'Start sprading at X-angle'
read*,X1
print*,'End sprading at X-angle'
read*,X2
print*,'No. of spreadings in this area'
read*,SPR
print*,'Y-position '
read*,YP
```

```
      print*,'Z-position '
      read*,ZP
      print*,'Velocity of droplets [m/s]'
      read*,VD
      print*,'Half spray angle from Z-axis [°Deg]'
      read*,TETAZ
      print*,'Scatta [°Deg]'
      read*,DTETA
      IF (DTETA.LE.0.0) THEN
      NT=0
      ELSE
      print*,'No. of trajectories  [-]'
      read*,NT
      ENDIF
      print*,'Diameter of particles [μm]'
      read*,DI
      print*,'Density of particles '
      read*,LDEN
      print*,'Total mass flow rate per second [kg/s]'
      read*,MDOTT
      print*,'Temperature [°C]'
      read*,TEM
      TEM=TEM+273
!     BEGIN OF CALCULATION OF VELOCITYS IN U, V & W
!     DIRECTION
      IF (NT.LT.1) THEN
      DTETAT=0
      ELSE
      DTETAT=DTETA/NT
      ENDIF
      TT=2*NT+1
      T1=TETAZ-DTETA
      MDOT=MDOTT/((SPR+2)*TT)
      DX=(X2-X1)/(SPR+1)
!     Size groups of particles
!     D1=0.10 DI ; D2=0.70 DI ; D3=1.0 DI ; D3=1.369 DI
      DI=DI/10**6
      D1=0.10*DI
      D2=0.70*DI
      D3=1.00*DI
      D4=1.341*DI

!     Mass concentration
!     D1=10% ; D2=20% ; D3=40% ; D3=30%
      MDOT1=0.10*MDOT
      MDOT2=0.20*MDOT
      MDOT3=0.40*MDOT
      MDOT4=0.30*MDOT

!     LOOP TO CALCULATE U & W VELOCITY COMPONENTS
      DO R=1,TT
```

```
      K=R-1
      WP=VD*COSD(180-T1+K*DTETAT)
      VW=SQRT(VD**2-WP**2)

      DO S=1,(SPR+2)
      L=S-1
      UP=VW*COSD(X1+L*DX)
      VP=VW*SIND(X1+L*DX)

      WRITE(1,10)XP,YP,ZP,UP,VP,WP,D1,LDEN,MDOT1,TEM
      WRITE(1,10)XP,YP,ZP,UP,VP,WP,D2,LDEN,MDOT2,TEM
      WRITE(1,10)XP,YP,ZP,UP,VP,WP,D3,LDEN,MDOT3,TEM
      WRITE(1,10)XP,YP,ZP,UP,VP,WP,D4,LDEN,MDOT4,TEM

10    FORMAT(1X,F7.3,1X,F7.3,1X,F7.3,1X,F8.3,1X,F8.3,1X,&
      F8.3,1X,ES9.2,1X,F7.1,1X,ES10.3,1X,F7.2)

      END DO
      END DO
      STOP
      END
```

D - Equation used for analysis of the runs

Ambient conditions

Value	Unit	Equation
p_{amb}	[mmHG]	average result
t_{amb}	[°C]	average result
p_{amb}	[mbar]	$p_{amb} = \rho_{HG}\ g\ h_{HG}$
ρ_{air}	[kg/m^3]	$\rho_{air} = \rho_n \frac{p_{amb}\ T_n}{p_n\ T_{amb}}$

Calculation of the average amounts

All values are the average results of each test run

Calculation of necessary values

Δt_w	[K]	$\Delta t_w = t_{wo} - t_{wi}$
Δt_a	[K]	$\Delta t_a = t_{ai} - t_{ao}$
φ_2	[%]	$\varphi_2 = \varphi_{2m}\left(1.041 - 3.6\,10^{-3} t_{ao} + 8.3\,10^{-5} t_{ao}^2 - 3.5\,10^{-7} t_{ao}^3\right)$
p_{1e}	[mbar]	$p_{1e} = \rho_w\ g\ h_1\ 10^{-2}$
Δp_2	[mbar]	$p_2 = \rho_w\ g\ h_2\ 10^{-2}$
$\dot{m}_{w1}$	[kg/s]	$\dot{m}_w = \frac{V_{w1}\ \rho_{w1}}{60\ \ 1000}$
$\dot{m}_a^M$	[kg/s]	See "Calculation of mass and volume flow rate after BS 1042 Section 1.1"
$\dot{V}_a^M$	10^{-3}[kg/s]	See "Calculation of mass and volume flow rate after BS 1042 Section 1.1"
$\dot{m}_a^E$	[kg/s]	$\dot{m}_a^E = \frac{p_a^E\ T_n\ V_a^E\ \rho_n}{p_n\ T_a^E\ 60\ 1000}$
$\dot{m}_a$	[kg/s]	$\dot{m}_a = \dot{m}_a^M + \dot{m}_a^E$
t_a	[°C]	$t_a = \frac{t_a^M \dot{m}_a^M + t_a^E \dot{m}_a^E}{\dot{m}_a^M + \dot{m}_a^E}$
ω_1	$\left[\frac{\text{kg H}_2\text{O}}{\text{kg Dry air}}\right]$	$\omega_1 = \frac{\omega_1^M \dot{m}_a^M + \omega_1^E \dot{m}_a^E}{\dot{m}_a^M + \dot{m}_a^E}$
ALR	[-]	$ALR = \frac{\dot{m}_a^E}{\dot{m}_{w1}}$

Calculation of mass and volume flow rate after BS 1042 Section 1.1

β	[-]	$\beta = \frac{d}{D}$
R_e	[-]	$R_e = \frac{4\,\dot{m}_a}{\pi\,\mu_{a1}\,D}$ (Iteration)
ε_1	[-]	$\varepsilon_1 = 1-\left(0.41+0.35\,\beta^4\right)\frac{\Delta p_e}{\kappa\,p_1}$
C	[-]	$C = 0.5959 + 0.0312\,\beta^{2.1} - 0.184\,\beta^8 + 0.0029\,\beta^{2.5}\left(\frac{10^6}{R_e}\right)^{0.75} + 0.090\,L_1\,\beta^4\left(1-\beta^4\right)^{-1} - 0.0337\,L_2'\beta^3$
ρ_1	[kg/m³]	$\rho_1 = \rho_n\frac{\left(p_{1e}+p_{amb}\right)T_1}{p_n T_n}$
$\dot{m}_a^M$	[kg/s]	$\dot{m}_a^M = \frac{C}{\sqrt{1-\beta^4}}\varepsilon_1\;0.025\pi\;d^2\sqrt{2\,\Delta p_2\rho_1}$
$\dot{V}_a^M$	[m³/s]	$\dot{V}_a^M = \frac{\dot{m}_a^M\,p_n\,T_n}{\rho_n\,p_{amb}\,T_{a1}}$

Calculation of the necessary values for the energy balance

Air inlet conditions

p_{v1}	[bar]	$p_{v1} = f\left(t_{w1}\right)$ *
ω_1	$\left[\frac{kg\,H_20}{kg\,dry\,air}\right]$	$\omega_1 = 0.622\,\frac{\varphi\,p_{v_{(t_{a1})}}}{p_{amb}-\varphi\,p_{v_{(t_{a1})}}}$
h_{g1}	$\left[\frac{kJ}{kg}\right]$	$h_{g1} = f\left(t_{a1}\right)$ *
h_{v1}	$\left[\frac{kJ}{kg}\right]$	$h_{v1} = f\left(t_{a1}\right)$ *
$T_{sat\,1}$	[°C]	$T_{sat\,1} = 18.952\,\ln\left(\frac{\omega_1\,p_{amb}}{\left(0.622+\omega_1\right)p_{v1}}\right)+92.271$
c_{pa1}	$\left[\frac{kJ}{kg\,K}\right]$	$c_{v1} = f\left(t_{a1}\right)$ *

Air outlet conditions

---

* for equation see Chapter SI-Units

p_{v2}	[bar]	$p_{v2} = f(t_{a2})$ *
ω_2	$\left[\frac{kg\,H_20}{kg\,dry\,air}\right]$	$\omega_2 = 0.622\,\frac{\varphi\,p_{v_{(t_{a2})}}}{p_{amb} - \varphi\,p_{v_{(t_{a2})}}}$
h_{g2}	$\left[\frac{kJ}{kg}\right]$	$h_{g2} = f(t_{a2})$ *
h_{v2}	$\left[\frac{kJ}{kg}\right]$	$h_{v2} = f(t_{a2})$ *
T_{sat2}	[°C]	$T_{sat2} = 18.952\,\ln\left(\frac{\omega_2\;p_{amb}}{(0.622+\omega_2)p_{v2}}\right) + 92.271$
c_{pa2}	$\left[\frac{kJ}{kg\;K}\right]$	$c_{v2} = f(t_{a2})$ *

Water inlet

$\dot{m}_{w1}$	$\left[\frac{kg}{s}\right]$	$\dot{m}_{w1} = \dot{V}_w\;\rho_{(t_{a1})}$
h_{w1}	$\left[\frac{kJ}{kg}\right]$	$h_{w1} = f(t_{w2})$ *

Water outlet

$\dot{m}_{w2}$	$\left[\frac{kg}{s}\right]$	$\dot{m}_{w2} = \dot{V}_w\;\rho_{(t_{a2})}$
h_{w2}	$\left[\frac{kJ}{kg}\right]$	$h_{w2} = f(t_{w2})$ *
$\dot{m}_e$	$\left[\frac{kg\,H_20}{kg\,dry\,air}\right]$	$\dot{m}_e = \omega_2 - \omega_1$

Energy balance

Q_w	[W]	$Q_w = \dot{m}_{w_2}\;h_{w_2} - \dot{m}_{w_1}\;h_{w_1}$
Q_v	[W]	$Q_v = \dot{m}_a\left(\omega_2\,h_{v_2} - \omega_1\,h_{v_1}\right)$
Q_a	[W]	$Q_a = \dot{m}_a\left(c_{p_2}\,t_{a_2} - c_{p_1}\,t_{a_1}\right)$
Q	[W]	$Q = Q_w + Q_v + Q_a$

Energy absorbed in total by water and air

$Q_{w\,in}$	[W]	$Q_{w_{in}} = \dot{m}_{w_1}\;h_{w_1}$
$Q_{w\,out}$	[W]	$Q_{w_{out}} = \dot{m}_{w_2}\;h_{w_2} + \dot{m}_a(\omega_2 - \omega_1)h_{v_2}$
ΔQ_w	[W]	$\Delta Q_w = Q_{w_{out}} - Q_{w_{in}}$

* for equation see SI-Units

$Q_{a\,in}$	[W]	$Q_{a_{in}} = \dot{m}_a\left(c_{p_1} t_{a_1} + \omega_1 h_{v_1}\right)$
$Q_{a\,out}$	[W]	$Q_{a_{out}} = \dot{m}_a\left(c_{p_2} t_{a_2} + \omega_1 h_{v_2}\right)$
ΔQ_a	[W]	$\Delta Q_a = Q_{a\,out} - Q_{a\,in}$
ΔQ	[W]	$Q = Q_w + Q_a$
Error	[%]	$Error = \frac{\Delta Q}{\Delta Q_w}$

Theoretical comparison

Non-dimensional numbers

FN	[-]	$FN = 0.395\frac{A_p^{0.5} D_e^{1.25}}{D_s^{0.25}}$
CD	[-]	$C_D = 0.35\left(\frac{A_p}{D_e D_s}\right)^{0.5}\left(\frac{D_s}{D_e}\right)^{0.25}$
K	[-]	$K = \frac{A_p}{D_e D_s}$

Depending on pressure

t_L	[m]	$t_L = 3.66\left[\frac{D_e FN\mu_W}{(\Delta p_W \rho_W)}\right]^{0.25}$
D_A	[m]	$D_A = D_e - 2t_L$
X (ratio of air core and exit orifice)	[-]	$X = \frac{A_A}{A_e}$
K_v	[-]	$K_v = 0.0367K^{0.29}\left(\frac{\Delta p_w \rho_w}{\mu_w}\right)$
θ	[°Deg]	$\theta = \arccos\left(\frac{0.00805\rho_w^{0.5} FN}{D_e t_L}\right)$
SMD	[m]	$SMD = 2.25\rho_w^{0.25}\mu_w^{0.25}\dot{m}_w^{0.25}\Delta p_w^{-0.5}\rho_a^{-0.25}$

U_u	[m/s]	$U_u = \frac{\dot{m}_w}{\rho_w (A_e - A_A)}$
U_v	[m/s]	$U_v = \frac{\dot{m}_w R_s}{\rho_w A_p R_a}$
U_D	[m/s]	$U_D = \sqrt{U_u^2 + U_v^2}$
P_w	[W]	$P_w = \frac{\Delta p_w \dot{m}_{w1}}{\rho_{w1}}$
P_a^E	[W]	$P_a^E = \dot{m}_a^E \int_{p_{a1}}^{p_{a2}} \frac{dp}{\rho_a}$
P	[W]	$P = P_a^E + P_w$
v_i	[m/s]	$v_i = \frac{\dot{m}_w}{\rho_w A_p}$
ψ	[-]	$\psi = \frac{\Delta Q_a}{P_w}$
ε	[-]	$\varepsilon = \frac{T_{a1} - T_{a2}}{T_{a1} - T_{w1}}$
q_a	[W/kg]	$\dot{q}_a = \frac{\dot{Q}_a}{\dot{m}_a}$
$R_{a/w}$	[-]	$\dot{R}_{a/w} = \frac{\dot{m}_a}{\dot{m}_w}$
ϕ	[1/K]	$\phi = \frac{m_a (h_{a1} - h_{a2}) \rho_w}{(T_{a1} - T_{w1}) \Delta p_w m_{w1}}$
C	[W/K]	$\phi = \frac{m_a (h_{a1} - h_{a2})}{T_{a1} - T_{w1}}$

E - Drawings of designed parts for pressure swirl nozzle and effervescent atomisers

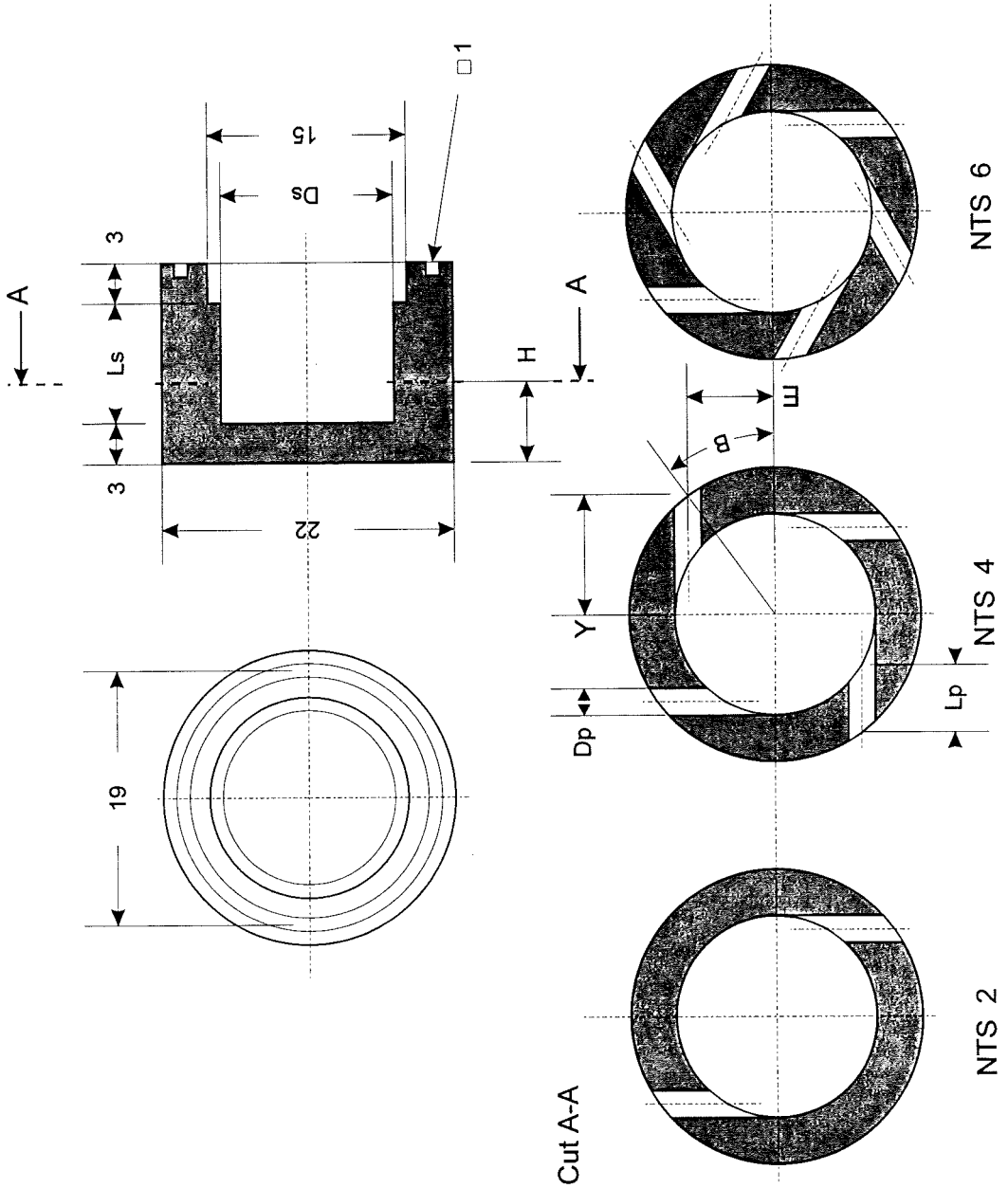
A
3
Ls
3
22
15
Ds
□1
H
A
19
NTS 6
E
B
Y
Dp
NTS 4
Lp
Cut A-A
NTS 2
DRG.NO.
TITLE
PROJECTION
First angle
Brass
DRAWN BY O. Schmidt MATERIAL

Diameter of the tangential inlet slots and height of the spray chamber

No	NTS	Ds	Ds/De	Dp	Lp	B	H	Ls a	Ls b	Ls c
1			3	4.98	8.42	25.26	5.49			
2		15	2.2	5.82	8.13	23.27	5.91	12.00	9.00	6.00
3			1.6	6.82	7.85	20.83	6.41			
4			3	3.52	12.93	18.14	4.76			
5	2	10.606	2.2	4.11	12.63	16.67	5.06	8.48	6.36	4.24
6			1.6	4.82	12.34	14.89	5.41			
7			3	2.49	15.84	12.93	4.25			
8		7.5	2.2	2.91	15.58	11.87	4.45	6.00	4.50	3.00
9			1.6	3.41	15.33	10.59	4.71			
10			3	3.52	9.11	28.68	4.76			
11		15	2.2	4.11	8.80	27.30	5.06	12.00	9.00	6.00
12			1.6	4.82	8.48	25.64	5.41			
13			3	2.49	13.62	20.68	4.25			
14	4	10.606	2.2	2.91	13.31	19.66	4.45	8.48	6.36	4.24
15			1.6	3.41	13.00	18.42	4.71			
16			3	1.76	16.41	14.78	3.88			
17		7.5	2.2	2.06	16.16	14.03	4.03	6.00	4.50	3.00
18			1.6	2.41	15.89	13.13	4.21			
19			3	2.88	9.52	30.16	4.44			
20		15	2.2	3.36	9.21	29.05	4.68	12.00	9.00	6.00
21			1.6	3.94	8.89	27.71	4.97			
22			3	2.03	14.02	21.79	4.02			
23	6	10.606	2.2	2.38	13.71	20.96	4.19	8.48	6.36	4.24
24			1.6	2.79	13.40	19.96	4.39			
25			3	1.44	16.73	15.59	3.72			
26		7.5	2.2	1.68	16.49	14.99	3.84	6.00	4.50	3.00
27			1.6	1.97	16.23	14.26	3.98			

DRAWN BY O.Schmidt MATERIAL Brass | PROJECTION -- | TITLE Dimensions of | DRG.NO.

COURSE Research TREATMENT

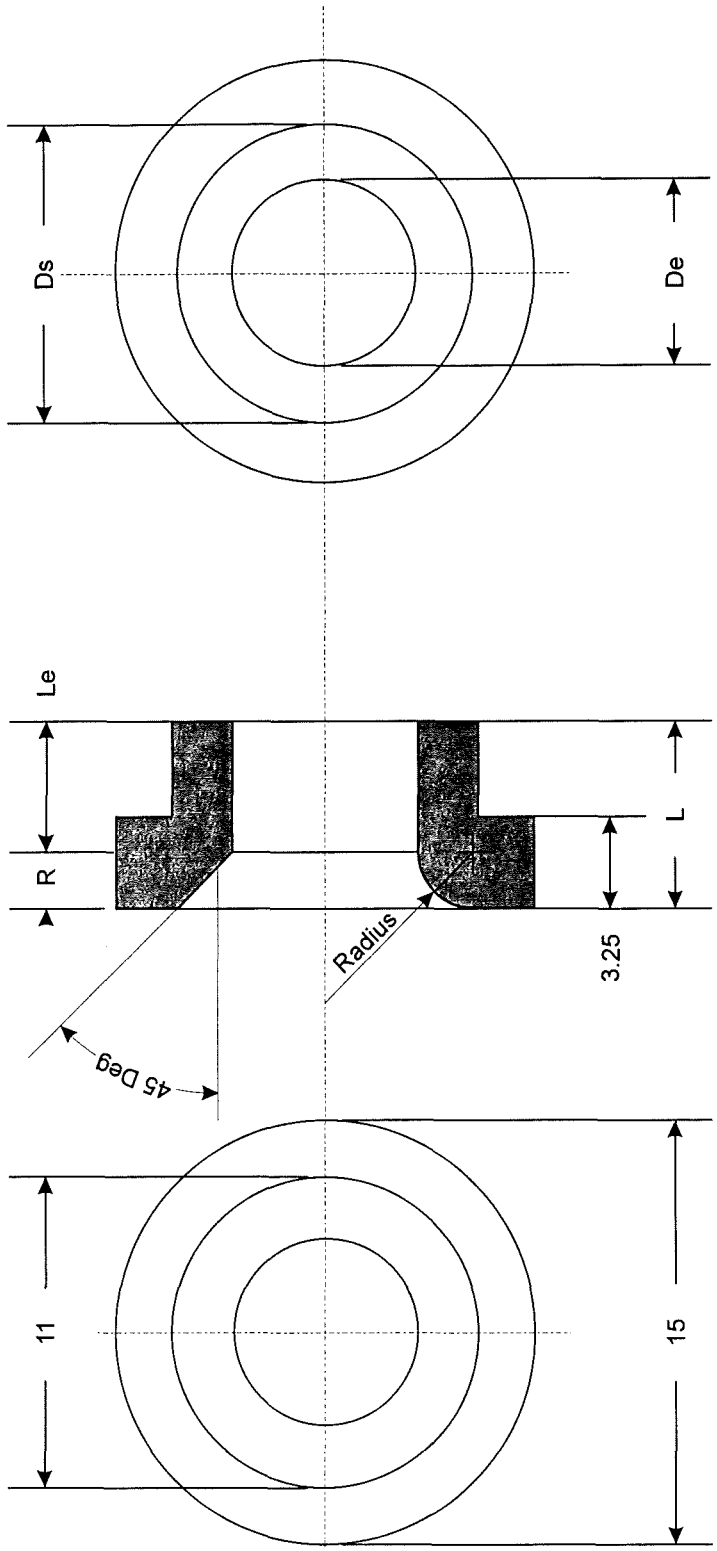

DRAWN BY O. Schmidt | MATERIAL Brass | PROJECTION First angle | TITLE | DRG NO.

List of measurements for the different nozzles

Ratio of :

	NTS (1)	Ds (2)	Ls/Ds (3)	Ds/De (5)	Le/De (6)	CD
a)	2	15	0.8	3	0.7	st = straight
b)	4	10.606	0.6	2.2	0.5	ro = rounded
c)	6	7.5	0.4	1.6	0.3	

Measurement values of the discharge orifices

				for rounded type
Ds	De	Le	L	R
15.00	5.00	3.50	8.50	5.00
		2.50	7.50	5.00
		1.50	6.50	5.00
	6.82	4.77	8.86	4.09
		3.41	7.50	4.09
		2.05	6.14	4.09
	9.38	6.56	9.38	2.81
		4.69	7.50	2.81
		2.81	5.63	2.81
10.61	3.54	2.47	6.01	3.54
		1.77	5.30	3.54
		1.06	4.60	3.54
	4.82	3.37	6.27	2.89
		2.41	5.30	2.89
		1.45	4.34	2.89
	6.63	4.64	6.63	1.99
		3.31	5.30	1.99
		1.99	3.98	1.99
7.50	2.50	1.75	4.25	2.50
		1.25	3.75	2.50
		0.75	3.25	2.50
	3.41	2.39	4.43	2.05
		1.70	3.75	2.05
		1.02	3.07	2.05
	4.69	3.28	4.69	1.41
		2.34	3.75	1.41
		1.41	2.81	1.41

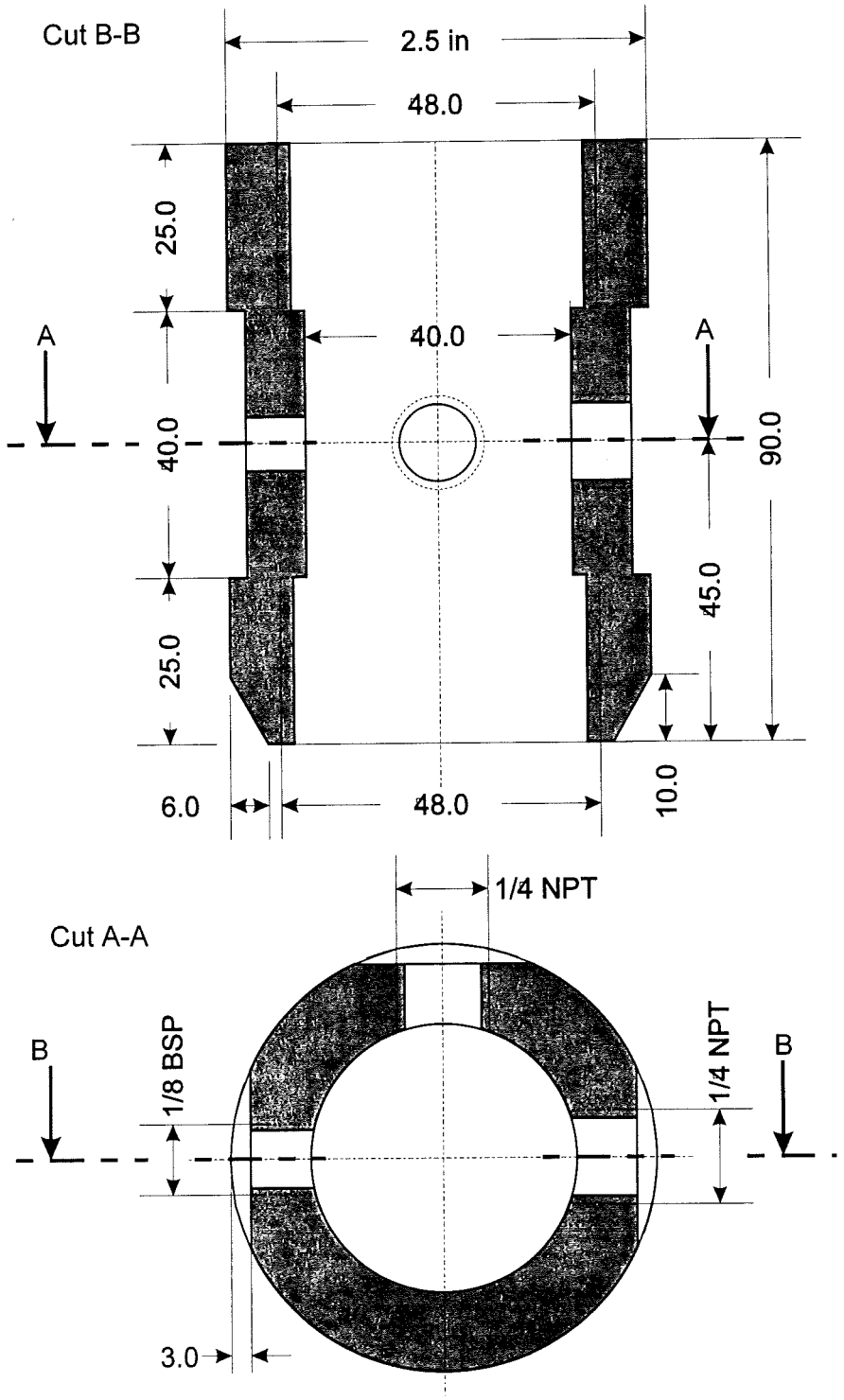

TITLE Multipurpose
DRG.NO.
PROJECTION First angle
DRAWN BY O.Schmidt MATERIAL Brass

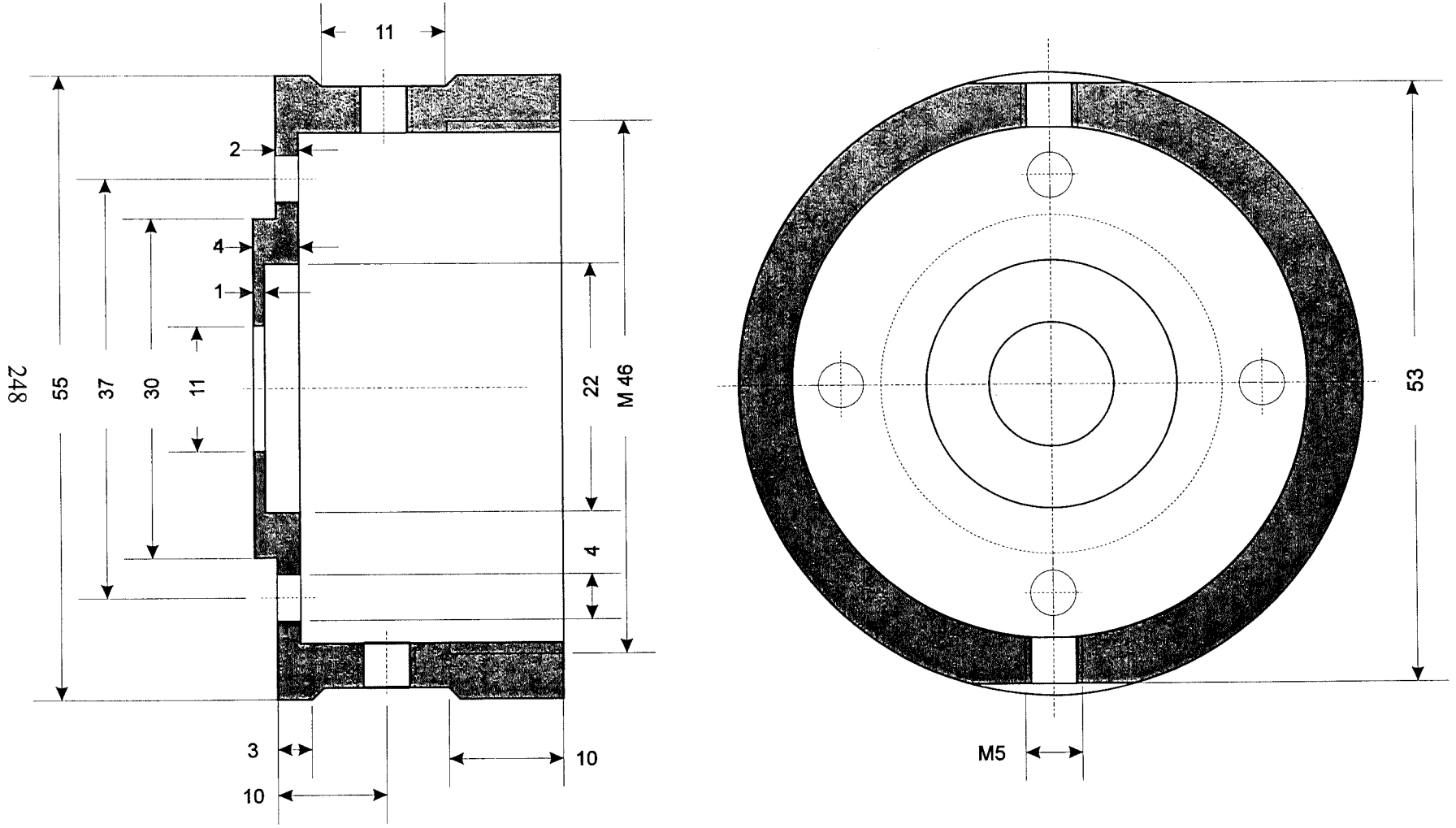

DRAWN BY O.Schmidt	MATERIAL Brass	PROJECTION First angle	TITLE Bottomplate for
COURSE Research	TREATMENT	TOLERANCE 0.1 0.1	DRG.NO.

Appendix

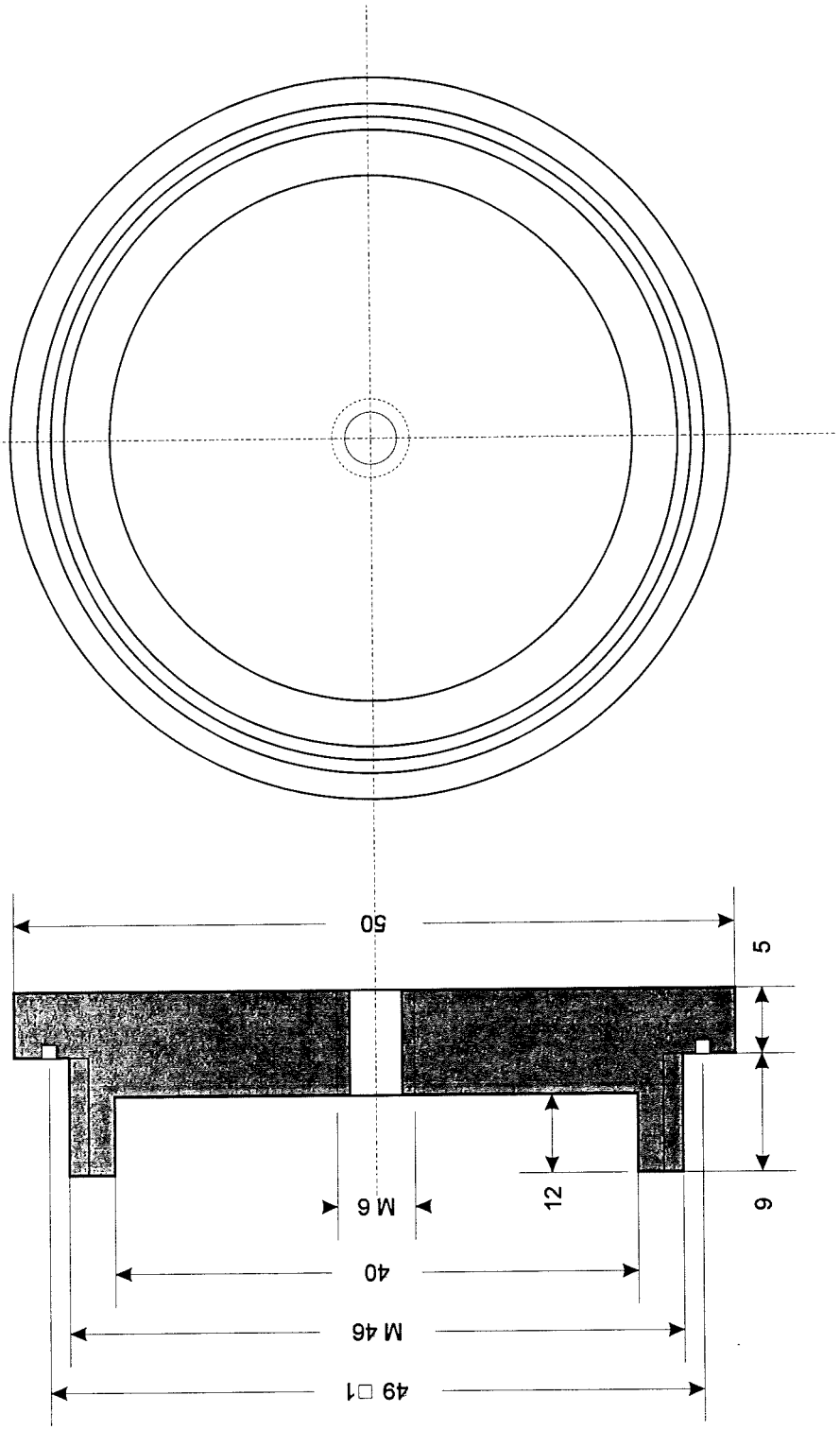

DRAWN BY O.Schmidt | MATERIAL Brass | PROJECTION First angle | TITLE Topplate for
COURSE Research | TREATMENT | TOLERANCE -0.1 - 0.1 | DRG.NO. | ISSUE | DATE | CHANGE

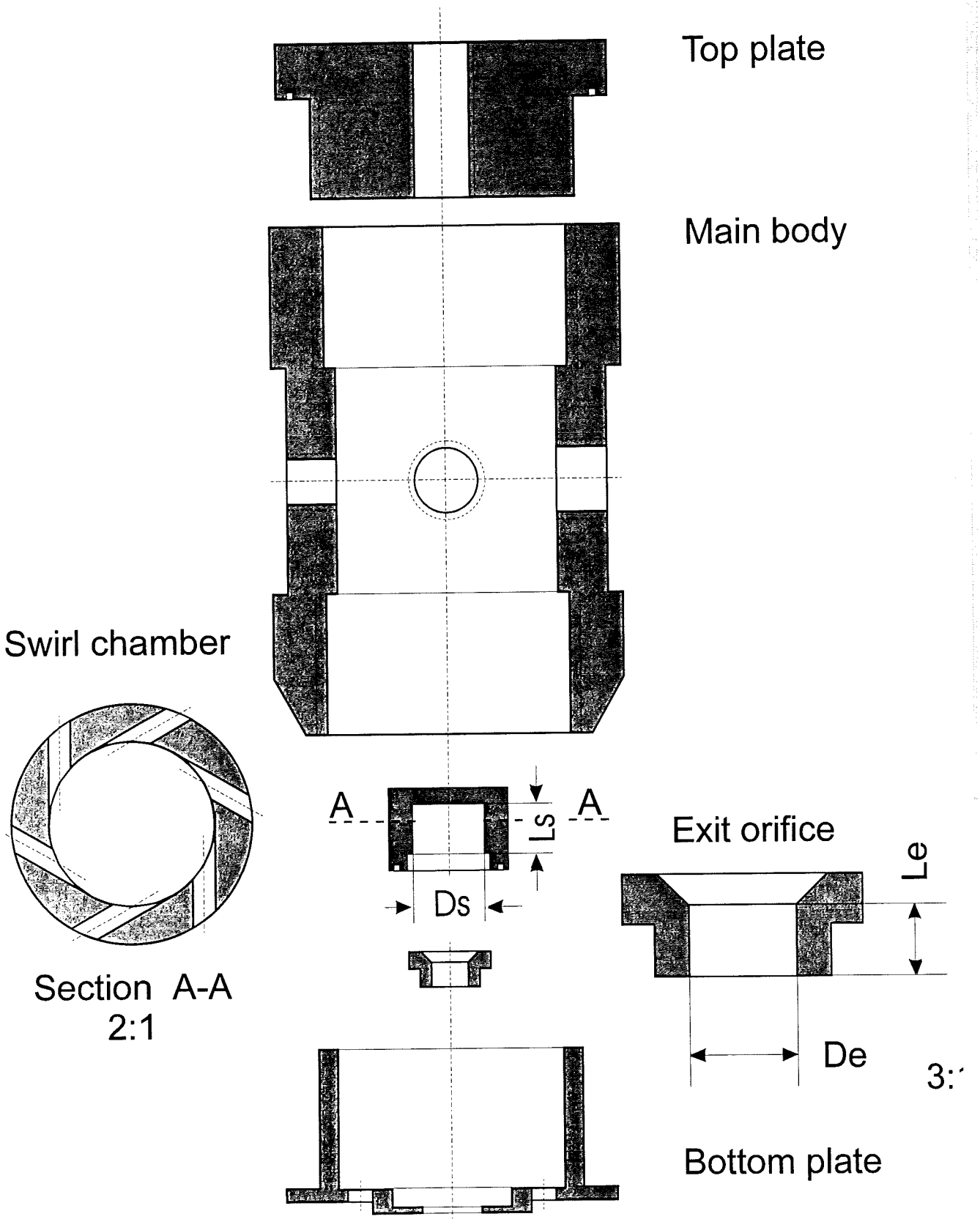
Top plate
Main body
Swirl chamber
A
A
Ls
Ds
Exit orifice
Le
De
Section A-A
2:1
Bottom plate

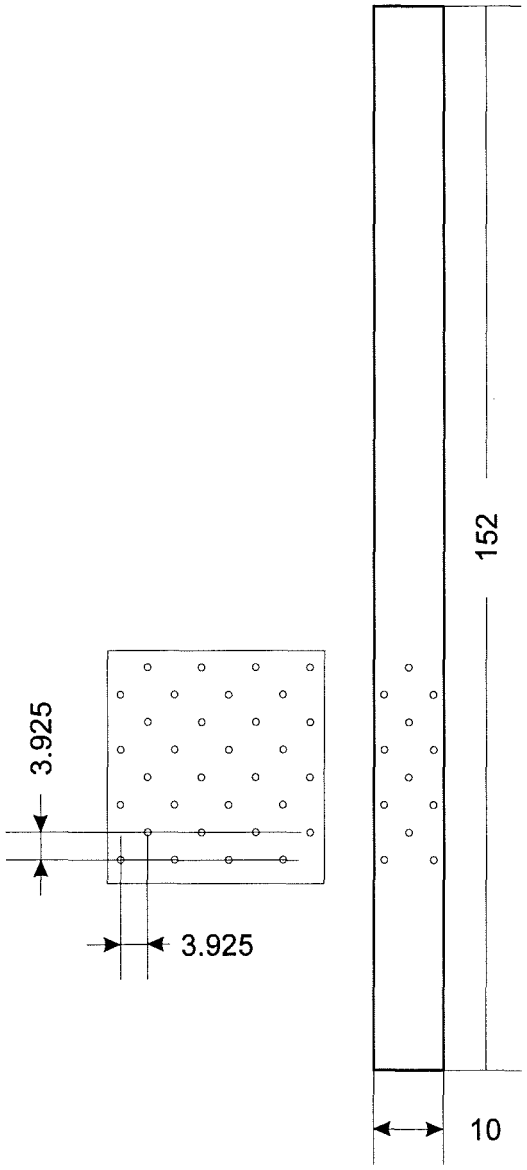

The diameter of the holes are

1.) 0.5 mm
2.) 0.7 mm
3.) 0.9 mm
4.) 1.1 mm
5.) 1.3 mm

DRAWN BY O.Schmidt | MATERIAL Stainles Steel | PROJECTION First angle | TITLE Innertube of
COURSE Research | TREATMENT | TOLERANCE +0.01 mm | DRG.NO. | ISSUE | DATE | CHANGE

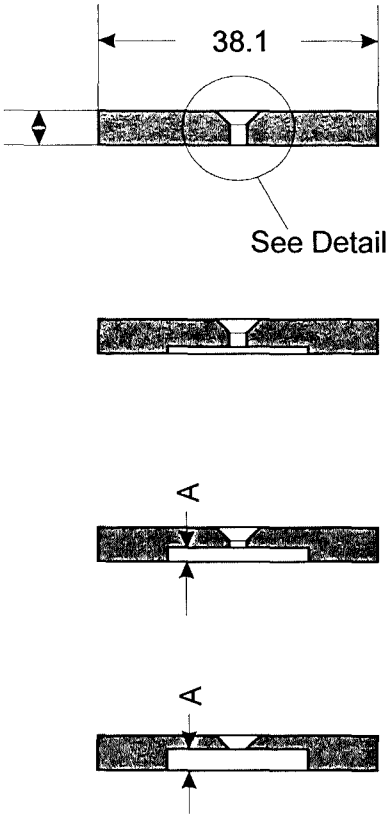

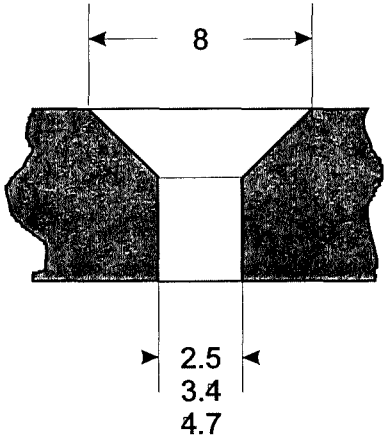

\De	2.50	3.40	4.70
A \	0.50	0.32	0.06
	1.00	1.00	1.00
	1.50	1.68	1.94
	2.25	2.70	3.35

DRAWN BY O.Schmidt	MATERIAL Brass	PROJECTION First angle	TITLE Exit orifice for	DRG.NO.
COURSE Research	TREATMENT	TOLERANCE +0.1 mm		ISSUE DATE CHANGE

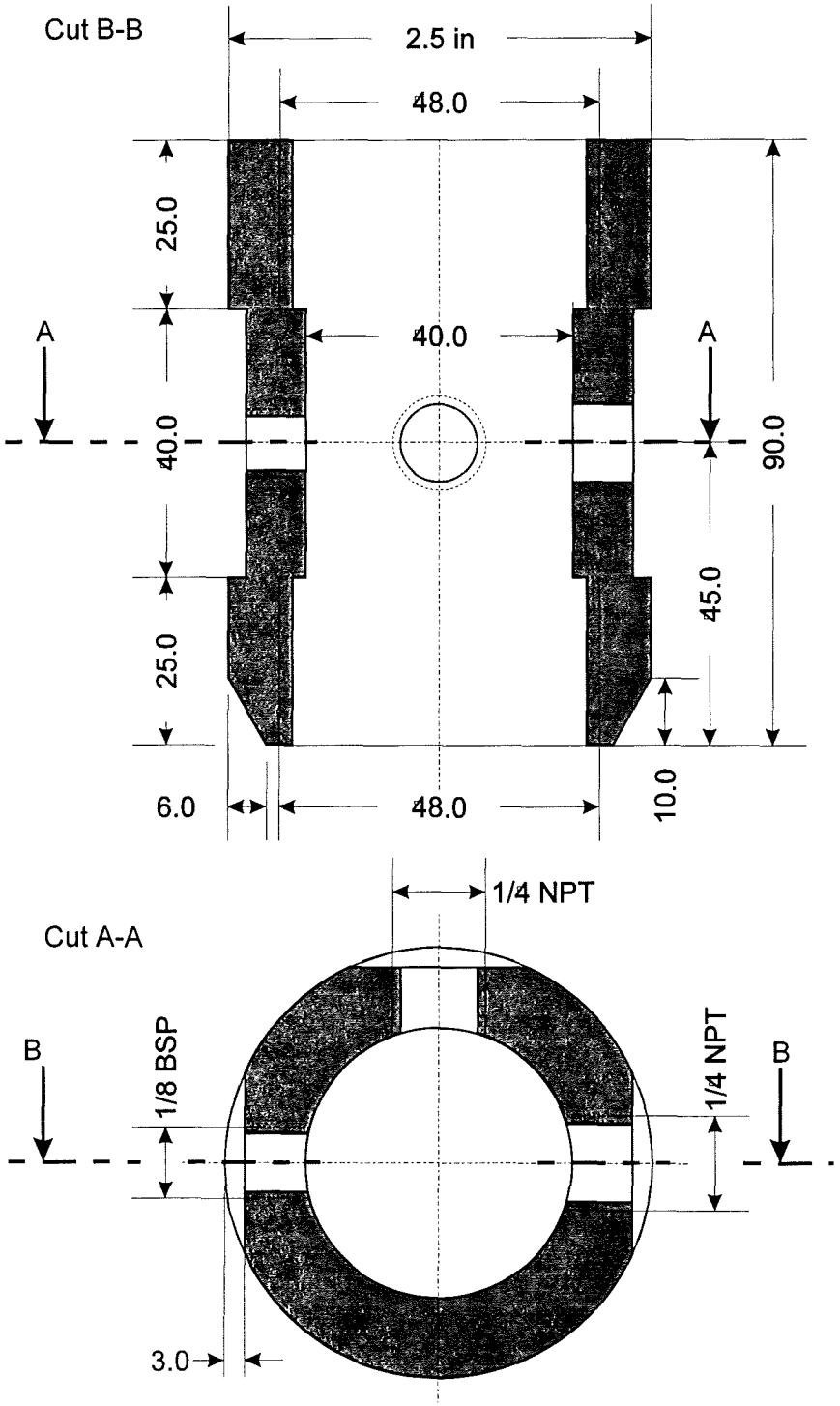

DRAWN BY O.Schmidt	MATERIAL Brass	PROJECTION First angle	TITLE Multipurpose main body	DRG.NO.	ISSUE DATE CHANGE
COURSE Research	TREATMENT	TOLERANCE -0.1 - 0.1			

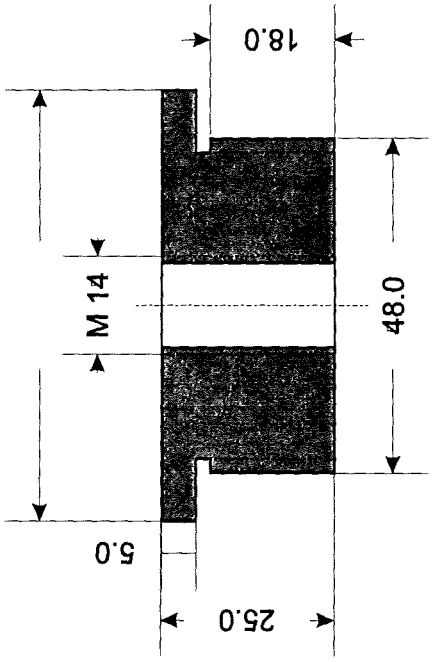

DRAWN BY O.Schmidt | MATERIAL Brass
COURSE Research | TREATMENT
PROJECTION First angle | TOLERANCE + 0.1 mm
TITLE Template for
DRG.NO.
ISSUE | DATE | CHANGE

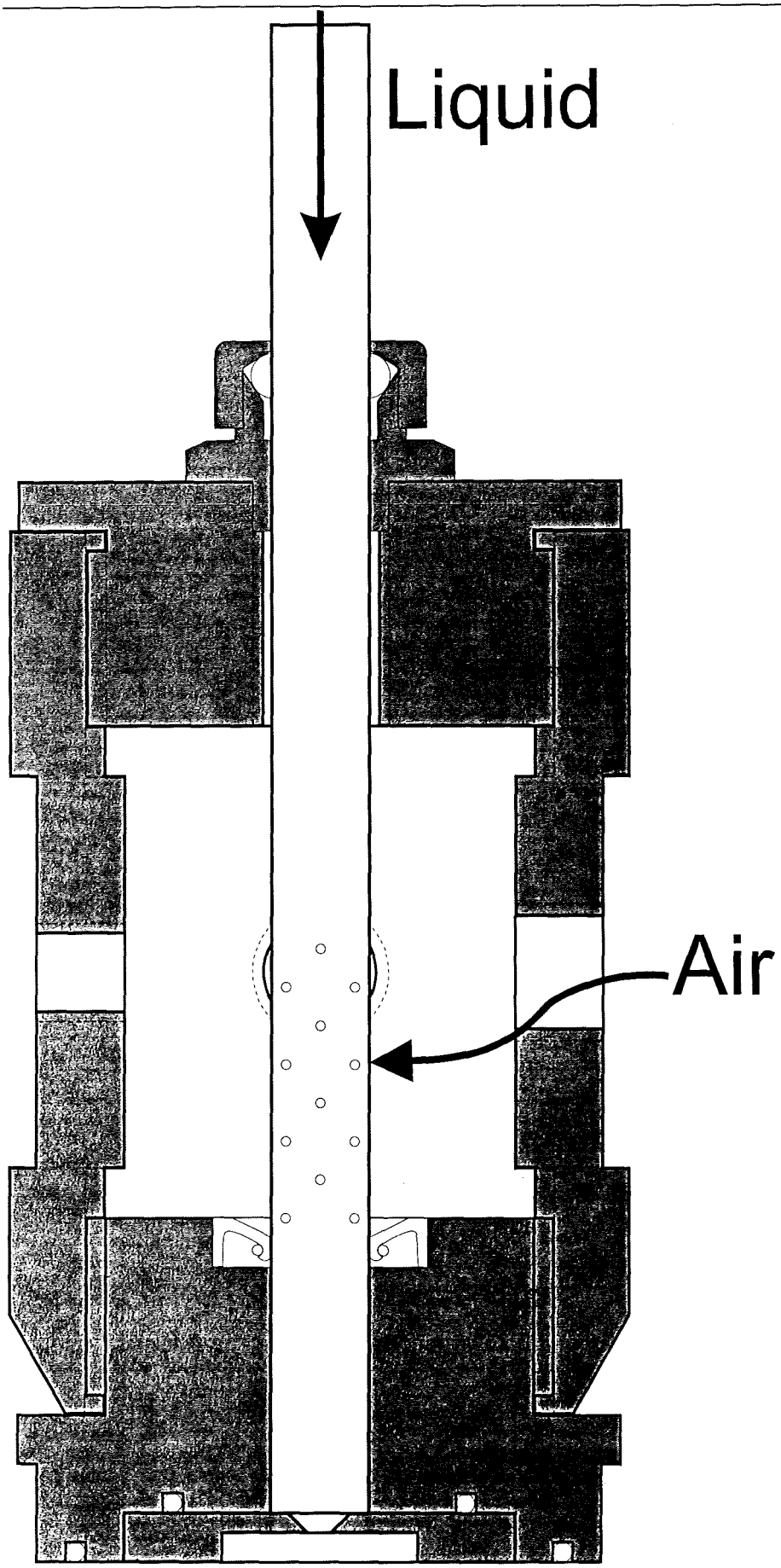
Liquid
Air